MUTE: A Program for High-Precision Calculations of Underground and Underwater Muon Intensities

by

William James Woodley

A thesis submitted in partial fulfillment of the requirements for the degree of
Doctor of Philosophy

Department of Physics
University of Alberta

Abstract

High-energy atmospheric muons originating from cosmic ray interactions in Earth's atmosphere have played a vital role in the field of astroparticle physics for nearly a century. Because the properties of the muons reflect the primary cosmic rays that produce them, they serve as a unique probe for understanding the cosmic ray spectrum as well as hadronic interactions at energies beyond the reach of current accelerator experiments. However, these muons also pose a significant challenge in rare event search experiments aiming to detect dark matter and neutrinos. These experiments are typically placed deep underground to escape atmospheric muons, using the rock overburden as natural shielding. However, while travelling through the rock, high-energy muons can induce backgrounds that mimic signals of interest in these detectors. Therefore, large-scale rare event search experiments rely on precise calculations of underground muon fluxes in order to properly characterise their expected backgrounds to develop effective shielding strategies.

This work presents a computational code, MUTE (MUon inTensity codE), which calculates forward-predictions for underground and underwater muons by combining the latest computational tools available: MCEQ and DAEMONFLUX for surface muon fluxes, and the Monte Carlo code PROPOSAL for transport through matter. The computational scheme is explained, outlining how MUTE achieves a full description of underground and underwater muons up to depths of 14 km.w.e., including calculations for muon intensities, energy spectra, angular distributions, and total fluxes. This method achieves excellent agreement with experimental data from a wide variety of detectors around the world, with precision surpassing previous error estimates. Applications of the MUTE code are also discussed, including its functionality in cross-checking data analyses and its ability to compute high-precision seasonal variations of total underground muon fluxes.

Preface

Some of the research conducted for this thesis was published or is in the process of being prepared for submission for publication. It was done under the supervision of Prof. Marie-Cécile Piro at the University of Alberta and we collaborated with Dr Anatoli Fedynitch at Academia Sinica in Taipei, Taiwan. Work from Sections 6.3, 6.4, 6.5.1, 7.1 and 7.4.1 was published previously in *The Astrophysical Journal* [1]:

[1] A. Fedynitch, W. Woodley and M.-C. Piro, *On the Accuracy of Underground Muon Intensity Calculations*, *Astrophys. J.* **928** (2022) 27 [`2109.11559`].

I was responsible for the creation and development of MUTE, producing the plots showing the main results, analysing the results, and composing the manuscript. M.-C. Piro and A. Fedynitch also contributed to the analysis of the results and the composition of the manuscript of the paper. All text that appears in this thesis is original.

Work from Sections 7.3 and 7.4 and Chapter 8 is currently being prepared for submission. This work is being led by myself, including upgrading the MUTE code to service the new calculations in these sections, the production and analysis of the results, managing the content of the paper, the writing, and the coordination of the work as a whole.

Acknowledgements

I would like to give thanks foremost to my Lord and Creator, who intricately and perfectly devised the Laws of Physics and created a human intellect capable of discovering them.

I want to give my sincerest gratitude to my invaluable supervisor, Professor Marie-Cécile Piro, for the indispensable support she has given me over my time in this programme. The completion of this work would not have been possible without her unceasing patience and encouragement at every step along the way. Her mentorship and advice over the years have been instrumental in shaping my research and she has taught me so much. I would also like to extend my deepest thanks to my collaborator, Dr Anatoli Fedynitch, for his involvement through to the completion of this work, and for sharing his extensive expertise of cosmic ray physics and programming with me. The knowledge I have gained from both Prof. Piro and Dr Fedynitch is immeasurable, and I am infinitely grateful for all they have done for me.

Throughout my academic journey, there have been a number of additional people that have been foundational to my scientific, professional, and personal growth that I have taken great example of, including Profs. Ben Newling, Abdelhaq Hamza, and Carsten Krauss. I would not be where I am today without their continual guidance, mentorship, and inspiration and their investment in my success in and beyond academia.

Thank you to my parents, Murray and Darlene Woodley, for instilling in me a desire to learn and supporting me in every way possible throughout my education. I am grateful for the sacrifices you have made to give me the opportunities to reach this stage, and for being supportive and accepting of my decisions each step along the way. I am also immensely grateful to my friends from New Brunswick — Ema Balihodzic, Dustin Fraser, Amy Higgins, Doyeon Kim, and Mondana Roustaian — without whom I would not have made it this far.

The friends I have made since moving to Edmonton have also been integral to my success, including everybody in the Piro Group. I want to specially thank Kyle Hayes and Catherine Bina for the kindness they have shown me and for their frequent encouragement and reassurances. My experience in Edmonton has been shaped by you and I will forever be grateful for it. Lastly, I want to express heartfelt gratitude to my campus minister, Theresa Robinson, and the whole worshipping community at St Joseph's College for enriching my time in Edmonton by providing

me with a second home and a deep sense of connection within the community, which has made all the difference in the long and often strenuous pursuit of this degree.

I would also like to extend thanks to the examination committee for the time they have dedicated to my thesis. The work in this thesis has been supported financially by the Arthur B. McDonald Canadian Astroparticle Physics Research Institute, as well as the Alberta Graduate Excellence Scholarship and the Queen Elizabeth II Graduate Scholarship. This research was also enabled in part by support provided by the Digital Research Alliance of Canada and the Academia Sinica Grid-Computing Centre.

Contents

List of Tables

List of Figures

List of Acronyms

AIRES	AIR shower Extended Simulations
AIRS	Atmospheric InfraRed Sounder
ALICE	A Large Ion Collider Experiment
ALLM	Abramowicz-Levin-Levy-Maor
AMANDA	Antarctic Muon And Neutrino Detector Array
ANAIS-112	Annual modulation with NaI Scintillators 112.5 kg
ANDES	Agua Negra Deep Experiment Site
ANTARES	Astronomy with a Neutrino Telescope and Abyss environmental RESearch project
ARCA	Astroparticle Research with Cosmics in the Abyss
ARF	Astroparticle Research Laboratory
BDUNT	Baikal Deep Underwater Neutrino Telescope
BESS	Balloon-borne Experiment with Superconducting Spectrometer
BNO	Baksan Neutrino Observatory
Borexino	BORon solar neutrino EXperiment (BOREX) + -ino
CDMS	Cryogenic Dark Matter Search
CERN	Conseil Européen pour la Recherche Nucléaire
CJPL	China Jinping Underground Laboratory
CMS	Compact Muon Solenoid
CORSIKA	COsmic Ray SImulations for KAscade
COSINUS	Cryogenic Observatory for SIgnals seen in Next-generation Underground Searches
CRESST	Cryogenic Rare Event Search using Superconducting Thermometers
CSDA	Continuous-Slowing-Down Approximation
CUPP	Centre for Underground Physics in Pyhäsalmi
DAEMONFLUX	DAta-drivEn MuOn-calibrated atmospheric Neutrino FLUX
DAMA/LIBRA	DArk MAtter Large sodium Iodide Bulk for RAre processes

DARWIN	DARk matter WIMP search with liquid xenoN
DD	Double-Differential
DDM	Data-Driven Model
DIR	Depth-Intensity Relation
DPM	Dual Parton Model
DPMJET	Dual Parton Model JET
EDELWEISS	Expérience pour DEtecter Les WIMPs En Site Souterrain
EECR	Extreme-Energy Cosmic Ray
EPOS-LHC	Event generator for the Propagation of the Objects in Simulated Large Hadron Collider collisions
EQ	Vertical-EQuivalent
EXO	Enriched Xenon Observatory
FLUKA	FLUktuierende KAskade
GALLEX	GALLium EXperiment
Geant4	GEometry ANd Tracking v4
GERDA	GERmanium Detector Array
GH	Gaisser-Honda model
GRAPES-3	Gamma Ray Astronomy PeV EnergieS phase-3
GSF	Global Spline Fit
GST3	Gaisser-Stanev-Tilav 3-generation model
GST4	Gaisser-Stanev-Tilav 4-generation model
GZK	Greisen-Zatsepin-Kuzmin
H3a	Hillas-Gaisser 3-Peters cycles model
H4a	Hillas-Gaisser 3-Peters cycles model (protons only in the third component)
HAWC	High Altitude Water Cherenkov observatory
HiRes	HIgh RESolution fly's eye
IMB	Irvine-Michigan-Brookhaven detector
INO	India-based Neutrino Observatory
INTEGRAL	INTErnational Gamma-Ray Astrophysics Laboratory
ISR	Intersecting Storage Rings
JNE	Jinping Neutrino Experiment
JUNO	Jiangmen Underground Neutrino Observatory
KamLAND	KAMioka Liquid scintillator ANtineutrino Detector
KGF	Kolar Gold Fields
KIMS	Korea Invisible Mass Search
KM3NeT	Cubic KiloMetre NEutrino Telescope

KURF	Kimballton Underground Research Facility
L3+C	Third LEP experiment + Cosmic
LEP	Large Electron-Positron collider
LHAASO	Large High Altitude Air Shower Observatory
LHC	Large Hadron Collider
LNGS	Laboratori Nazionali del Gran Sasso
LSC	Laboratorio Subterráneo de Canfranc
LSM	Laboratoire Souterrain de Modane
LVD	Large Volume Detector
MCEq	Matrix Cascade EQuation
MCNP	Monte Carlo N-Particle Transport Code
MINOS	Main Injector Neutrino Oscillation Search
MMC	Muon Monte Carlo
MST	Muon Scattering Tomography
MUM	MUons + Medium
MUPAGE	MUon GEnerator from PArametric formulas
MUSIC	MUon SImulation Code
MUSUN	MUon Simulations UNderground
MUTE	MUon inTensity codE
NASA	National Aeronautics and Space Administration
NEMO	Neutrino Ettore Majorana Observatory
NEMO	NEutrino Mediterranean Observatory
NEVOD	Neutrino Water Detector (Russian)
NOνA	Neutrinos at the main injector Off-axis ν_e Appearance
NRLMSISE-00	United States Naval Research Laboratory Mass Spectrometer and Incoherent Scattering radar-Exosphere 2000
OPERA	Oscillation Project with Emulsion-tRacking Apparatus
ORCA	Oscillation Research with Cosmics in the Abyss
PAO	Pierre Auger Observatory
PAUL	Paarl Africa Underground Laboratory
PDG	Particle Data Group
PHITS	Particle and Heavy Ion Transport code System
PL27	Power Law $\gamma = 2.7$
P-ONE	Pacific Ocean Neutrino Experiment
PROPOSAL	PRopagator with Optimal Precision and Optimised Speed for All Leptons
QCD	Quantum Chromodynamics

QED	Quantum Electrodynamics
QGS	Quark-Gluon String
QGSJET	Quark-Gluon String model for JET hadronisation
SABRE	Sodium iodide with Active Background Rejection Experiment
SD	Single-Differential
SHINE	SPS Heavy Ion and Neutrino Experiment
SNO	Sudbury Neutrino Observatory
SNOLAB	Sudbury Neutrino Observatory LABoratory
SR	Standard Rock
SUL	Solotvina Underground Laboratory
SUPL	Stawell Underground Physics Laboratory
SURF	Sanford Underground Research Facility
TA	Telescope Array
TR	TRue vertical
UHECR	Ultra-High Energy Cosmic Ray
USStd	United States STandarD atmosphere
WIMP	Weakly Interacting Massive Particle
WIPP	Waste Isolation Pilot Plant
Y2L	Yangyang Laboratory
ZePLiN	ZonEd Proportional scintillation in LIquid Noble gases
ZS	Zatsepin-Sokolskaya model
ZSP	Zatsepin-Sokolskaya (PAMELA) model

1 Introduction

Underground muons have been a topic of interest in physics for many decades, with the first study on them being published by P. H. Barrett, et al. in 1952 [2]. Over the decades, studies of underground muons continued, driven in part by their importance to underground particle physics experiments. Cosmic-ray muons are vital in astroparticle physics, but pose challenges in rare event search experiments like those observing neutrinos or aiming to discover dark matter. In these experiments, muons can induce backgrounds whose signals mimic events the detectors are searching for. For this reason, a number of calculations, parameterisations, and programs were devised, especially between the 1960s and 1980s, to predict muon fluxes underground. However, in the recent decades, not much work has been done to expand our knowledge in this field. This is despite the fact that underground muons remain crucial for underground experiments, and more precise knowledge of their physics is needed as detectors increase their sensitivity. Additionally, our knowledge of cosmic ray physics remains minimal in some key areas, including the composition of cosmic rays. These high-energy atmospheric muons that originate from cosmic rays serve as a unique probe for understanding cosmic ray properties and interactions at extreme energies, especially because underground data tends to be more consistent than surface muon data [3]. Because it is high-energy muons that reach underground laboratories, an in-depth study of these muons deep underground has the potential to reveal information about the primary spectrum in this energy range that is normally inaccessible to experiments. Therefore, the motivation behind an updated detailed study of atmospheric muons is great. The goal of this research was to develop a program using state-of-the-art tools that do not rely on parametric fits, like many previous methods, to perform a detailed study on underground and underwater muons. Therefore, in this thesis, the MUTE code (MUon inTensity codE) is introduced, offering precise calculations of underground muon fluxes up to 14 km.w.e., achieving excellent agreement with experimental data worldwide.

Chapters 2 to 5 review the physics and current literature in the field of cosmic rays and underground muons. Specifically, Chapters 2 and 3 give an overview of the physics of cosmic rays and air showers that lead to the production of atmospheric muons and their propagation through the atmosphere. Chapter 4 gives an overview of the physics of energy loss in matter and the relevant energy loss processes for muons. Chapter 5 provides a review of the current status of the field, including comments on why underground muons are a topic of importance, as well as previous methods of estimating muon fluxes underground and underwater.

Chapters 6 to 8 describe the work unique to this thesis. Chapter 6 gives an overview of the specific goals of the MUTE code and a technical explanation with details of how MCEQ, DAEMONFLUX, and PROPOSAL are used in MUTE. It also contains a summary of the models available for the primary cosmic ray flux, hadronic interactions, atmosphere, and energy loss interaction cross-sections, and how the defaults were chosen. Chapters 7 and 8 present the main physics results obtained by MUTE concerning underground and underwater muon intensities and total fluxes, along with discussions of the uncertainties and applications of the program in astroparticle physics.

Chapter 9 summarises the important results obtained in this thesis and their relevance for the dark matter and neutrino communities. It also gives a summary of future possible expansions to the program and further applications outside the scope of this study.

2 Cosmic Rays

Cosmic rays were first discovered in 1912 by Victor Hess, who took an ionisation chamber up into the atmosphere in a balloon and observed the number of charged particles in the chamber decrease as the balloon's altitude increased and then start to increase again as the balloon continued to get higher [4]. He reasoned that the charged particles at low altitudes were radiation coming from the Earth, and he attributed the origin of the charged particles higher in the atmosphere to be what he termed "cosmic rays."

A cosmic ray is broadly defined as any charged particle entering Earth's atmosphere from outer space. The vast majority of cosmic rays are protons (90%), with the second most abundant species being helium nuclei (9%), and the last portion being heavier nuclei (1%), such as ^{12}C, ^{18}O, and ^{56}Fe [5]. Some definitions also consider electrons to be cosmic rays, but the most common description of a cosmic ray is a high-energy atomic nucleus.

Despite over a century of research into cosmic rays, cosmic ray physics continues to be a field of research with many open questions remaining, including fundamental questions about their origin and composition. One aspect of cosmic ray physics relevant to dark matter and neutrino physics is cosmic-ray muons (also "cosmogenic muons" or "atmospheric muons"). Cosmic rays interact in the Earth's atmosphere to produce air showers containing muons. These muons can penetrate the Earth and travel multiple kilometres, during which they can produce high-energy neutrons, which act as backgrounds for sensitive dark matter and neutrino experiments. A diagram summarising these processes is given in Figure 2.1. This chapter will focus on the physics of the cosmic rays as it relates to these underground atmospheric muons.

2.1 The Standard Model

The Standard Model of particle physics is the current best and most complete description of the fundamental particles and their interactions. The Standard Model is made up of a total of 61 particles, four fundamental forces, and is fit to 26 free parameters. Despite this large number of free parameters, it successfully describes all current experimental data, and has been used in the past to predict new particles before they were discovered, such as the top quark and the Higgs

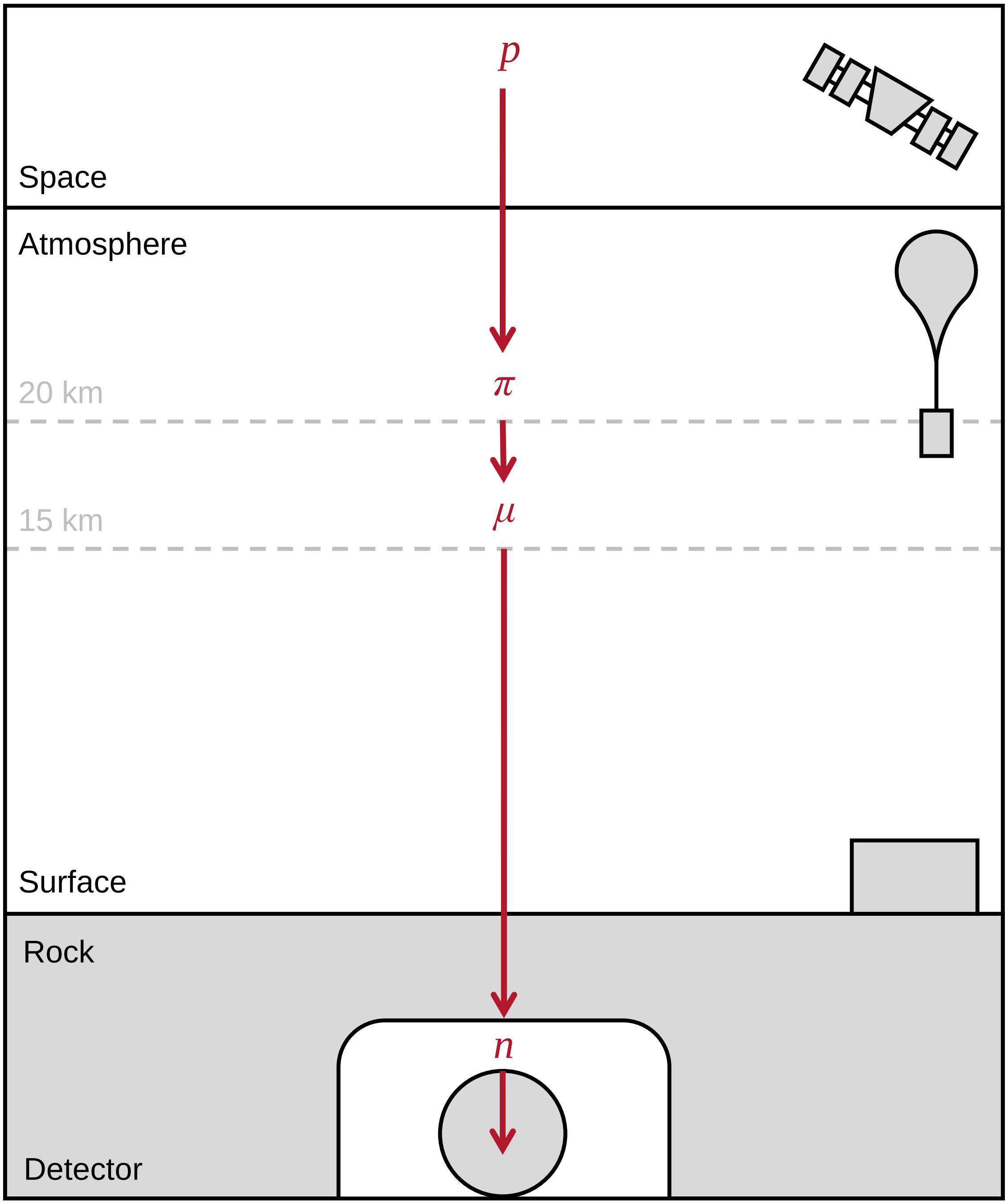

Figure 2.1: An overview of the chain of processes of interest for this work: first, the primary cosmic ray (p) coming from space, then interacting approximately 20 km up into the atmosphere to produce pions (π) in air showers, which travel for 5 km on average before decaying into muons (μ), which propagate through the atmosphere and into the ground, where they finally produce neutrons (n), which can be background signals for dark matter and neutrino detectors. Also shown are some common detector types in the field of cosmic ray physics: space-borne satellites, balloon-borne detectors, and surface detectors.

boson [6].

The fundamental particles are divided into two classes: fermions, particles with half-integer spins that obey the Fermi exclusion principle; and bosons, particles with integer spins which do not obey this principle. Fermions are further categorised into quarks, which have colour charge, and leptons, which do not have colour charge. Both quarks and leptons are split into three generations of particles, and make up what is typically thought of as physical matter, such as atoms, whereas fundamental bosons in the Standard Model are force-mediating particles. The elementary particles of the Standard Model are listed in Table 2.1 with their defining properties of charge, mass, and spin. The muon, the focus of the majority of this work, is highlighted in grey. The muon is a second-generation lepton with charge -1, mass 105.7 MeV (approximately 200 times more massive than the electron), and spin $1/2$ [6, 7].

Interactions between particles of the Standard Model are governed by four fundamental forces, which obey various quantum number conservation laws based on certain symmetries of the forces. In order from strongest to weakest, these forces are:

- **The Strong Force:** A force that acts between particles with colour charge (quarks), mediated by gluons. The physics of the strong force is described by quantum chromodynamics (QCD).
- **The Electromagnetic Force:** A force that acts between particles with electric charge, mediated by the photon. The physics of the electromagnetic force is described by quantum electrodynamics (QED).
- **The Weak Force:** A force that acts between all quarks and leptons, mediated by the Z^0 (neutral current) or $W^{\pm}$ (charged current) bosons.
- **The Gravitational Force:** A force that acts between particles with mass. Gravity is far too weak to be observed on the particle level except by the most sensitive detectors, and the unification of gravity with quantum physics is one of the largest unsolved problems of modern physics.

One feature of the strong force is that coloured particles cannot be free particles, resulting in the fact that no free quark has ever been experimentally observed. All quarks have been observed in bound systems where the overall colour charges cancel out. Colour charges come in three types: red (r), green (g), and blue (b). Therefore, this cancelling of the colour charge can be achieved in two ways: either with a quark bound to an antiquark (in which the colour of the quark and the anti-colour of the antiquark cancel each other to produce a colourless particle; $b\bar{b}$, for example), known as “mesons,” or with three quarks or three antiquarks (in which the three colours or three anticolours add together to give a colourless “white” particle as in additive colour theory; rgb, for

Table 2.1: The elementary particles of the Standard Model with their symbols, electric charges in units of the elementary charge e, masses, and spins, taken from [8]. Quark masses are given with large uncertainties because of the difficulty of measuring them due to colour confinement. All quarks and leptons — with the possible exception of the neutrinos — have antiparticles with electric charges of the opposite polarities (written either with an overline, such as $\overline{u}$ for an anti-up quark, or with the polarity indicated as a superscript, such as μ^+ for an anti-muon), and all quarks (and antiquarks) have three variations for the three colour charges (red, green, and blue).

Generation	**Particle**	**Charge, q (e)**	**Mass, m (MeV)**	**Spin**
		Quarks		
First	Up (u)	2/3	$2.16^{+0.49}_{-0.26}$	1/2
	Down (d)	−1/3	$4.67^{+0.48}_{-0.17}$	1/2
Second	Strange (s)	−1/3	$93.4^{+8.6}_{-3.4}$	1/2
	Charm (c)	2/3	1270 ± 20	1/2
Third	Bottom (b)	−1/3	4180^{+30}_{-20}	1/2
	Top (t)	2/3	$(1.727 \pm 0.003) \times 10^5$	1/2
		Leptons		
First	Electron (e^-)	-1	0.511	1/2
	Electron Neutrino (ν_e)	0	$< 10^{-6}$	1/2
Second	Muon (μ^-)	-1	105.658	1/2
	Muon Neutrino (ν_μ)	0	$< 10^{-6}$	1/2
Third	Tau (τ^-)	-1	1776.86 ± 0.12	1/2
	Tau Neutrino (ν_τ)	0	$< 10^{-6}$	1/2
		Bosons		
	Higgs (H)	0	1.25×10^5	0
	Gluon (g)	0	0	1
	Photon (γ)	0	0	1
	Z^0 boson	0	9.12×10^5	1
	$W^\pm$ bosons	± 1	8.04×10^5	1

example), known as “baryons.” Together, mesons and baryons form a class of particles known as “hadrons” [6, 7].

Because muons are leptons that have electric charge, they interact both electromagnetically and weakly, though because they do not have colour charge, they do not interact via the strong force. However, the particles that produce them — charged pions ($\pi^+ = u\overline{d}$; $\pi^- = d\overline{u}$) and kaons ($K^+ = u\overline{s}$; $K^- = s\overline{u}$) — are mesons, and so their interactions must be described with QCD.

2.2 Cosmic Ray Energy Spectrum

Despite 110 years of research, the central question to cosmic ray physics remains how cosmic rays are accelerated to such high energies. The two typical features of interest for cosmic rays are their composition and their energy spectrum. While it is well-known that the cosmic rays reaching Earth's upper atmosphere are composed of ionised nuclei, mainly protons, they arrive with a very large range of energies, from as low as 10^9 eV to as high as $> 10^{20}$ eV [5]. The energy spectrum is given by a power law:

$$\frac{\mathrm{d}N}{\mathrm{d}E} \propto E^{-\gamma}, \tag{2.1}$$

where γ is known as the spectral index. Up to $E = 10^{12}$ eV $= 1$ PeV, the spectral index is $\gamma \approx 2.7$. Beyond this, it is $\gamma \approx 3.0$ [5]. The cosmic ray energy spectrum is shown in Figure 2.2 with data from multiple experiments.

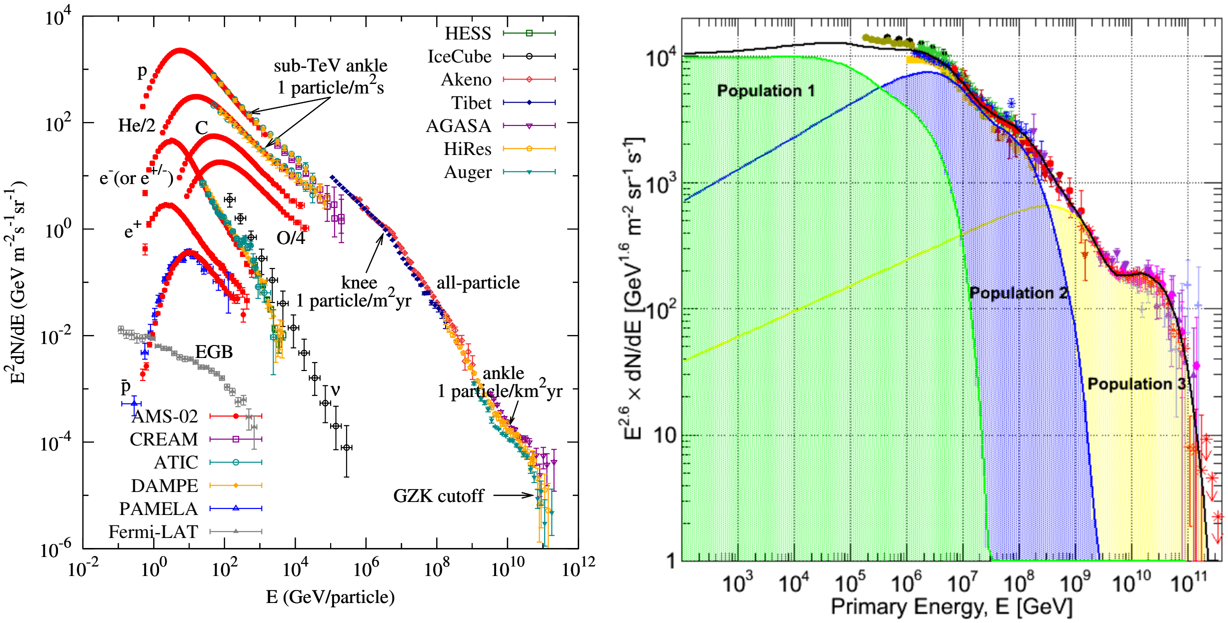

Figure 2.2: The cosmic ray energy spectrum against energy, showing the spectrum broken up into different components (left, taken from [9], which also contains the citations for the data shown), and three overlapping populations of different cosmic ray sources (right, taken from [10]). It is typical to multiply the cosmic ray flux on the y-axis by E^γ in order to reveal more structure in the plot.

The origin of cosmic rays is difficult to understand because cosmic rays, by definition, are charged particles, which means that, while travelling through space, they get deflected by magnetic fields, and so their directions when they arrive at Earth do not point back to their origins. Tracing the trajectory of a very high-energy cosmic ray back to its origin could be possible, because it would experience less deflection by magnetic fields, but there are so few of them that a constant stream coming from one direction cannot be detected.

In general, however, it is known that different ranges of the energy spectrum correspond to different astrophysical sources for the cosmic rays, given the accelerations that would be achievable in the relative distances travelled to reach the Earth. These ranges are split into three populations in the plot of the cosmic ray spectrum against energy (right) in Figure 2.2. Population 1 includes low-energy cosmic rays, which are known to be produced within the solar system by solar activity and within the galaxy by supernova remnants (SNRs). Population 2 contains high-energy cosmic rays produced outside the solar system but within the galaxy, but of inconclusive origin. Population 3 includes still higher-energy cosmic rays, which are thought to be produced outside the galaxy, though the exact astrophysical sources and the mechanisms by which they are accelerated are still unknown [5].

There are two additional important features of the cosmic ray spectrum in Figure 2.2:

- **The Knee:** Beginning around 10^6 GeV = 1 PeV, the spectrum softens, and the spectral index goes from –2.7 to –3.0 to produce what is known as "the knee." Below the knee, cosmic rays mostly come from galactic SNRs.
- **The Ankle:** Beginning around 10^9 GeV = 1 EeV, the spectrum hardens, and the spectral index goes from –3.0 to –2.0 to –2.7. This transition is thought to correspond to the transition from galactic to extragalactic sources, such as gamma-ray bursts.

2.3 Cosmic Ray Acceleration

It is thought that, below around 100 TeV (below the knee), cosmic rays are accelerated by supernova explosions inside the galaxy. This would provide an explanation for both the high energies seen in cosmic rays, as well as their power law spectrum [5]. In order to account for the cosmic ray flux in this range, galactic supernovas would have to explode approximately every 50 years, and while the rate of supernova events is not exactly known, it is thought that, within the galaxy, explosions happen sufficiently often, in the range of every 10 to 100 years, with the International Gamma-Ray Astrophysics Laboratory (INTEGRAL) experiment predicting a rate of one supernova in the galaxy every (53 ± 46) years [11].

The idea that SNRs were a source of cosmic ray acceleration was first proposed by E. Fermi in 1949 [12] in what is now referred to as the "Fermi mechanism" or "Fermi acceleration." There are two types of Fermi acceleration:

1. **First-Order Fermi Acceleration:** Also called "diffusive shock wave acceleration"; a shock can form when the speed of the matter from the supernova explosion travels through the

interstellar medium gas faster than the speed of sound in the medium. After thousands of years, the shock will eventually start to slow down, and it is possible for particles to escape upstream.

2. **Second-Order Fermi Acceleration:** The original phenomenon proposed by E. Fermi in which charged particles are accelerated by colliding with moving clouds of gas in the interstellar medium. This process is less efficient at accelerating particles than the first-order mechanism.

In both cases, the cosmic rays gain energy when passing into and out of the respective medium (the shock for first-order, and the cloud for second-order) [5].

The first-order Fermi mechanism works by transferring macroscopic kinetic energy of moving magnetised plasma to individual charged particles, increasing the individual particles' energies to many times their original values. The shock wave from a supernova explosion can travel outwards at tens of thousands of kilometres per second and can compress and strengthen the magnetic fields of surrounding gases. At the edge of the shock wave, charged particles, including protons, can increase their energy by scattering off magnetic fields while bouncing back and forth across the shock wave. Their energies eventually increase to a level high enough such that the particles can break free from the shock wave entirely, and be ejected into space at very high speeds. This mechanism results in a non-thermal energy distribution that is characteristic of cosmic rays. The cosmic ray particles get caught up in the plasma of the shock wave multiple times and gain energy each time they pass through it. If a particle enters the accelerator with energy E_0, then the energy it leaves with will be:

$$E \leq E_0(1+\xi)^{1/T_{\text{cycle}}}. \tag{2.2}$$

where ξ is the amount of energy gained in each pass across the shock, and T_{cycle} is the time taken for one cycle of acceleration [5]. This is referred to as "first-order Fermi acceleration" because the fraction of energy gained per encounter, ξ, is first-order in its proportionality to $\beta = v/c$ (where v is the speed of the medium and c is the speed of light), as opposed to second-order Fermi acceleration in which $\xi \propto \beta^2$ [5]. Most supernova models are simplistic in that they assume a spherical shock wave, when, in reality, the shock wave has fluctuations in its shape and is not isotropic. However, the model does give the beginning of an explanation for the origin of low-energy cosmic rays.

One notable feature of the Fermi mechanisms is that Fermi accelerators with limited lifetimes have a maximum energy they can accelerate particles to. In general, all cosmic rays have a theoretical upper limit on their possible energy of 5×10^{19} eV $= 50$ EeV. This is known as the Greisen-Zatsepin-Kuzmin (GZK) limit, named after K. Greisen, G. Zatsepin, and V. Kuzmin, who proposed this limit in 1966 [13, 14]. Beyond this energy, cosmic rays should interact with the cosmic microwave background radiation within a distance of 150 million lightyears, reducing the cosmic rays' energies to be below the GZK limit, through these interactions:

$$\begin{gathered} p+\gamma \longrightarrow \Delta^{+} \longrightarrow p+e^{+}+e^{-}, \\ p+\gamma \longrightarrow \Delta^{+} \longrightarrow p+\pi^{0}, \\ p+\gamma \longrightarrow \Delta^{+} \longrightarrow n+\pi^{+}. \end{gathered} \tag{2.3}$$

Cosmic rays should continue to lose energy via these processes until their energies fall below the cut-off for pion production, meaning no particle with energy above 50 EeV should ever be observed [15]. However, this is not the case, as will be discussed in Section 3.2.3.

2.4 Primary Flux Experiments and Models

Modelling the primary cosmic ray flux is necessary for studying the muons that are produced as a result of it, and in order to model the flux, experimental data is required from cosmic ray detection experiments. Cosmic ray experiments are divided into two categories: direct detection and indirect detection.

Direct detection experiments include space-borne satellites and balloon-borne detectors. Balloon experiments are the oldest type of cosmic ray detection experiments, as this was the type of experiment carried out by V. Hess in his discovery of cosmic rays. A modern example is the BESS-TeV experiment [16, 17]. Direct detection experiments are good for measuring cosmic rays with low energies (below 10^6 GeV), but not for those with higher energies. This is because high-energy cosmic rays are very rare, and so in order to have a better chance of observing one, the area of the detectors needs to be very large. However, experiments launched into orbit are limited in both weight and volume, and so are usually quite small, which leads to large statistical uncertainties on high-energy cosmic ray fluxes [5].

For higher energies, indirect detection experiments are better suited for cosmic ray measurements. There are four major types of indirect experiments, all of which are arranged in arrays on Earth's surface: Cherenkov detectors, scintillation detectors, fluorescence detectors, and radio detectors. In each case, the detector measures charged particles from the air showers produced by cosmic rays in order to infer details about the original cosmic ray itself. The largest indirect experiments are water Cherenkov experiments, examples of which include the Pierre Auger Observatory (PAO) [18] in Argentina, the Large High Altitude Air Shower Observatory (LHAASO) [19] in China, and the High Altitude Water Cherenkov Observatory (HAWC) [20] in Mexico. More detailed reviews of direct and indirect cosmic ray detectors are found in [21, 22, 23].

Historically, the primary spectrum has been modelled as a collection of multiple nuclei that follow a power-law spectrum, fitting the scaling factor and spectral index to data from multiple experiments that were not always in agreement. A number of models exist, including the Gaisser-Honda model developed by T. K. Gaisser and M. Honda in 2002 [24], the Hillas-Gaisser model developed by A. M. Hillas and T. K. Gaisser in 2012 [25], the Zatsepin-Sokolskaya model developed by V. I. Zatsepin and N. V. Sokolskaya in 2006 [26], as well as others. The most recent model is the Global Spline Fit.

2.4.1 Global Spline Fit

The Global Spline Fit (GSF) model [27] is a data-driven model that compiles direct and indirect measurements of cosmic ray primaries to produce the flux of nucleons at the top of the atmosphere. Compared to other models, it relies on theoretical assumptions as little as possible; the only assumption made is that the primary flux varies smoothly. It splits the primary spectrum composition into four mass groups — p, He, O, and Fe, shown in Figure 2.3 — spaced equally in $\ln(A)$, where A is the atomic number of the mass group. The model then uses a spline to parameterise data as well as statistical and systematic uncertainties from satellite and balloon experiments, and different cosmic ray experiments are cross-calibrated through a combined fit. Despite having many parameters (80–100), GSF is able to calculate fluxes spanning a range from 10 GeV to 10^{11} GeV.

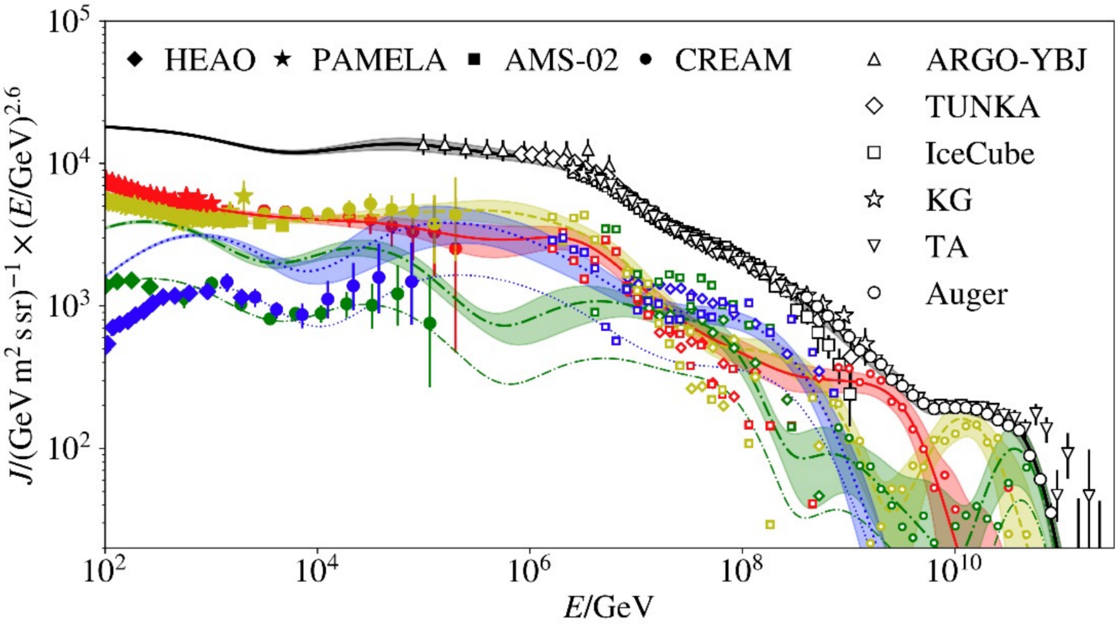

Figure 2.3: Primary cosmic ray flux vs energy. The four mass groups are shown by the colours: red (p), yellow (He), green (O), and blue (Fe), with the sum of all groups in black.

3 Air Showers

Air showers were first discovered by Pierre Auger in 1939, who noticed coincidences in charged particles in laterally separated particle counters that he had suspended in air [28]. When cosmic rays reach Earth's atmosphere, they interact with particles in the atmosphere (such as nitrogen and oxygen) in hadronic interactions and undergo spallation interactions in which multitudes of daughter particles are produced. These daughter particles go on to create further charged and neutral secondaries, which similarly go on to create more particles, resulting in the phenomenon of an extensive air shower cascade of secondary particles.

Depending on the energy and zenith angle of the primary cosmic ray, most hadronic interactions occur at altitudes between 15 km and 35 km [21]. There are a number of different interactions that can occur in the production of an air shower, but the basic interaction is represented by a proton, p, colliding with a nucleon in an air molecule, N:

$$p + N \longrightarrow p,\ n,\ \pi^{\pm},\ \pi^{0},\ K^{\pm},\ K^{0},\ \ldots \tag{3.1}$$

This process starts a chain of subcascades of multiple types of charged and neutral particles interacting and decaying. A schematic diagram giving an overview of the processes in an air shower is shown in Figure 3.1. Air showers are composed of three components. The first is the hadronic component, made up of hadrons originating from the initial interaction in Equation (3.1). The second is a muonic component, made up of muons and muon neutrinos, coming mainly from the decays of low-energy charged pions and kaons. The third is an electromagnetic (EM) component, made up of electrons, positrons, and photons. This component is fed by all air shower components: the hadronic component feeds the EM component via decays of neutral pions into photons; the muonic component via the decays of muons into electrons; and the EM component itself via electron-positron pair production of high-energy photons, which is described by the Heitler model [29]. The focus of this work will be on the hadronic and muonic components, covered in Sections 3.1 and 3.2 respectively.

A comparison between the fluxes of different types of secondary cosmic-ray particles at different altitudes is given in Figure 3.2. At high altitudes above 7 km, protons and neutrons are the most abundant. The pion flux is lowest at all altitudes because pions have a short lifetime, and so

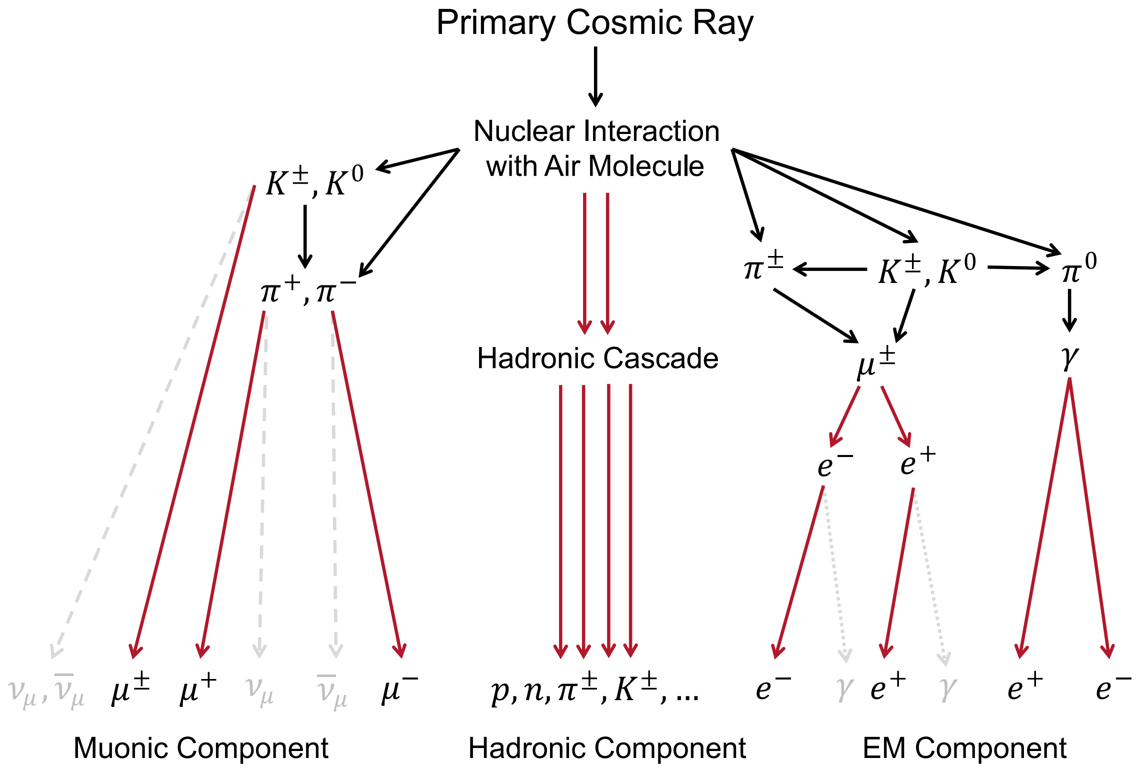

Figure 3.1: A diagram of the development of an air shower cascade in the atmosphere starting from a single proton, showing the hadronic core along with the muonic component and the electromagnetic component. Adapted from [22, 30].

decay very quickly. Because pions are the most abundantly produced hadrons, however, and most pions decay into muons, whereas most muons reach the surface of the Earth without decaying into electrons, the muonic component of an air shower is greater than the EM component at the surface. Therefore, the muon and muon neutrino fluxes dominate at lower altitudes (the flux of muon neutrinos is higher than that of muons because muon neutrinos are produced in the decays of both pions and muons). Aside from muons and muon neutrinos, the fluxes of secondary particles more or less follow the shape of the primary cosmic rays, whose slope is given approximately by the power law in Equation (2.1).

As the particles propagate through the atmosphere, they spread out laterally from the trajectory of the incident primary cosmic ray due to multiple Coulomb scattering. Low-energy cosmic rays tend to produce extensive air showers with large lateral spreads, approaching tens of kilometres, compared to high-energy cosmic rays, which can produce extensive air showers with lateral spreads of only a few metres surrounding the core. Because muons are typically produced by the decays of low-energy pions, the lateral spread of muons in any air shower is typically larger than that of electrons, which are produced in highest abundance by the decays of π^0. Because of this large lateral spread, surface array detectors that perform indirect observations of cosmic rays, such as

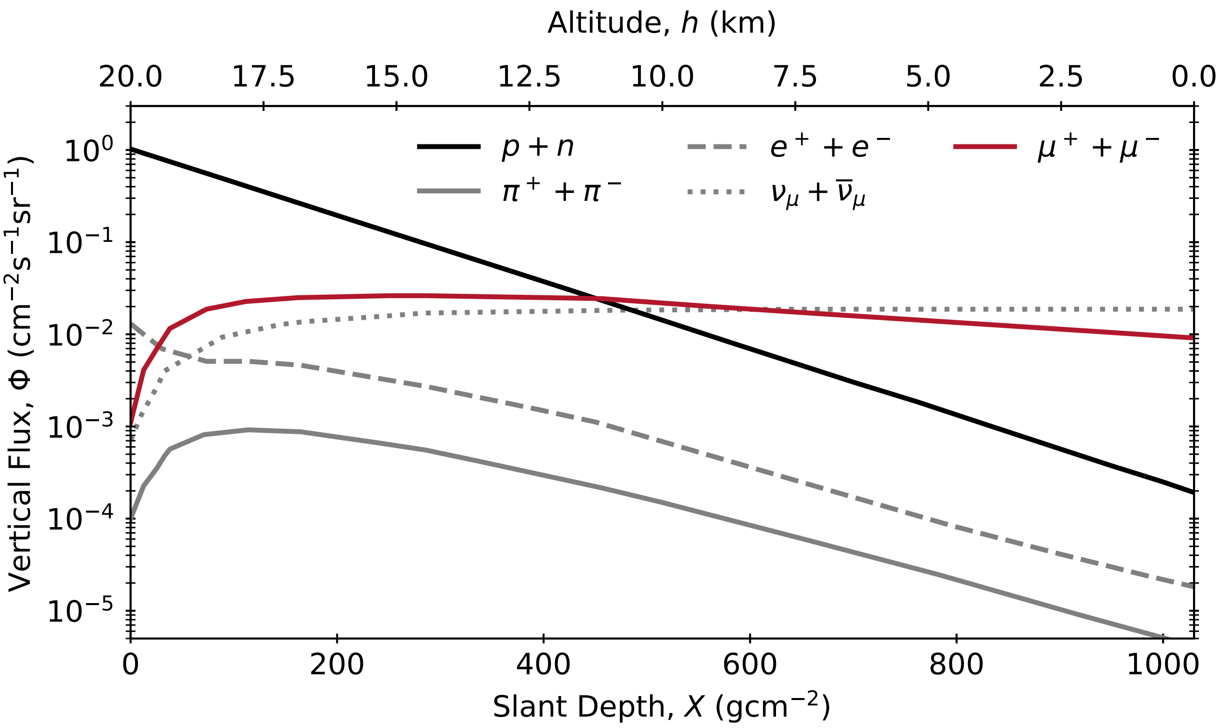

Figure 3.2: Vertical particle fluxes in the atmosphere, taken from [8], showing comparisons above 1 GeV between secondary protons and neutrons, pions, electron, muon neutrinos, and muons. [8] includes experimental data for negatively charged muons from [17, 31, 32, 33, 34, 35].

the Pierre Auger Observatory (PAO) in Argentina, are spread out across a large distance (3000 km^2 in the case of the PAO) [18].

3.1 Hadronic Component

In order to analyse the hadronic component of air showers in the atmosphere, some conventions for the treatment of the atmosphere must first be established. The geometrical variables that will be used are shown in Figure 3.3.

For zenith angles below 60°, thus neglecting the curvature of the Earth, the vertical altitude h can be approximated as:

$$h \approx \ell \cos(\theta). \tag{3.2}$$

The total vertical altitude of the atmosphere is $h_{\text{tot}} = 1030$ gcm^{-2}, which is equivalent to about 10.3 metres of water in terms of energy loss. When considering the curvature of the Earth, from the barometric formula, which describes how the density of the air changes as altitude changes, the vertical slant depth is given in relation to the atmospheric slant depth and vertical altitude by:

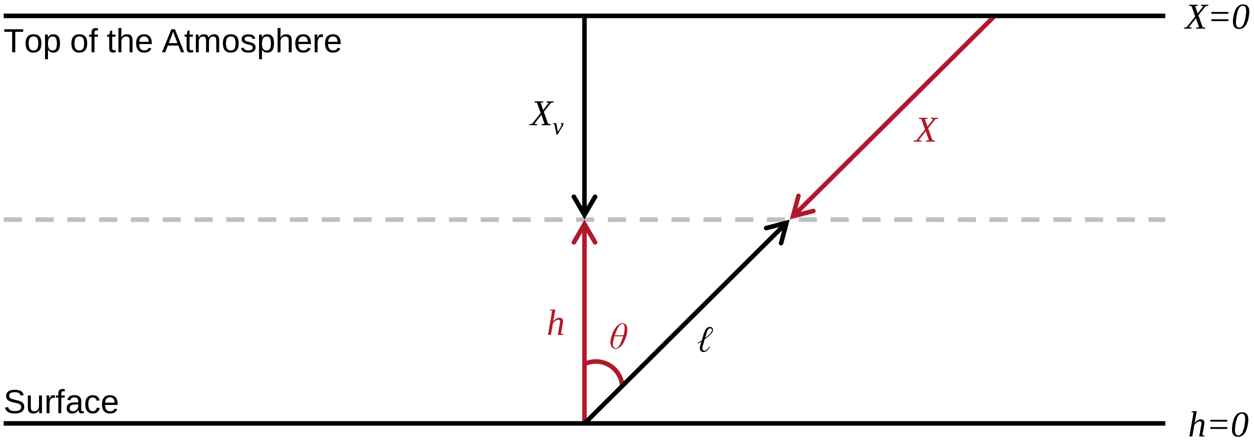

Figure 3.3: Geometry of the atmosphere, based on [5], showing the atmospheric slant depth, X, the particle trajectory length (which is along the trajectory of the cosmic ray), ℓ, the vertical slant depth, X_v, the vertical altitude, h, and the zenith angle of the incoming cosmic ray trajectory, θ. The variables used most often — X, h, and θ — are shown in red.

$$X_v = X e^{h/h_0(T)}, \tag{3.3}$$

where $h_0(T)$ is a temperature-dependent scale height, and T is the atmospheric temperature at height h [5]. The geometry defined in Figure 3.3, then, implies that $e^{h/h_0(T)} \approx \cos(\theta)$ in the approximation that the Earth is flat. The slant depth and vertical slant depth are given by integrals over the atmospheric density of the air, ρ_{air}, at different altitudes, integrated over the particle trajectory length and the vertical altitude respectively [36]:

$$\begin{aligned} X &= \int_{\ell}^{\infty} \rho_{\text{air}}(h(\ell'))\mathrm{d}\ell', \\ X_v &= \int_{h}^{\infty} \rho_{\text{air}}(h')\mathrm{d}h'. \end{aligned} \tag{3.4}$$

From Equations (3.2) to (3.4), the density can be calculated as:

$$\begin{aligned} \rho_{\text{air}} &= \frac{\mathrm{d}X_v}{\mathrm{d}h} \\ &= \frac{X\cos(\theta)}{h}. \end{aligned} \tag{3.5}$$

The density is related to the energy-dependent interaction and decay mean free paths of the particles in the atmosphere. In general, for a particle of type i with energy E_i, the interaction mean free path is:

$$\lambda^{i}_{\text{int}}(E_i) = \frac{\rho_{\text{air}}}{n_{\text{air}}\sigma_i^{\text{air}}(E_i)} = \frac{m_{\text{air}}}{\sigma_i^{\text{air}}(E_i)} = \frac{Am_p}{\sigma_i^{\text{air}}(E_i)}, \tag{3.6}$$

where $\rho_{\text{air}} = n_{\text{air}} m_{\text{air}}$ is the density of air, n_{air} is the number density of air, m_{air} is the mass of air nuclei, $\sigma_i^{\text{air}}(E_i)$ is the energy-dependent cross-section of a particle of type i to interact with an air molecule, A is the average mass number of the nuclei in the air, and m_p is the proton mass. The decay mean free path for a particle of type i with energy E_i is:

$$\begin{aligned}\lambda_{\text{dec}}^{i}(E_i, X) &= \frac{E_i X \cos(\theta) c\tau_i}{m_i c^2 h_0} \\ &= \frac{E_i X \cos(\theta)}{\varepsilon_i},\end{aligned} \tag{3.7}$$

where c is the speed of light, m_i is the mass of the particle, and τ_i is the particle's mean lifetime. In the second line of Equation (3.7), some terms have been gathered into a single variable, ε_i. This is the critical energy of the particle:

$$\varepsilon_i = \frac{m_i c^2 h_0}{c\tau_i}. \tag{3.8}$$

The critical energy is defined as the energy at which the probability a particle will interact is equal to the probability it will decay. When $E_i > \varepsilon_i$, interaction dominates; when $E_i < \varepsilon_i$, decay dominates. The critical energy, and therefore the decay mean free path, contains a factor of $c\tau_i$ which is the average proper decay length. This, along with some other notable decay constants for air shower particles, is given in Table 3.1 for comparison [5].

Table 3.1: Decay constants for the main particles of interest in air showers, including critical energy, ε, mean lifetime, τ, mean proper decay length, $c\tau$, and mean boosted decay length, $c\gamma\tau$. It can be noted that the critical energy of the kaon is much greater than that of the pion because the kaon's mass is higher and its mean lifetime is shorter than those of the pion. Additionally, the mean distances travelled by neutrons and muons before decaying, given in the fourth and fifth columns, are significantly larger than those of pions and kaons.

Particle	**ε (GeV)** [5]	**τ (s)** [8]	**cτ (cm)** [5]	**c$\gamma\tau$ (km)** [21]
Neutron (n)	-	878	2.69×10^{13}	2×10^{11}
Pion ($\pi^{\pm}$)	115	2.60×10^{-8}	780	5.6
Kaon ($K^{\pm}$)	850	1.24×10^{-8}	371	2.7
Muon ($\mu^{\pm}$)	1	2.20×10^{-6}	6.59×10^{4}	480

The most common interaction products from Equation (3.1), and thus the most abundant particles in the hadronic component of air showers, are pions, which have a typical production altitude of around 20 km up into the atmosphere. Depending on their energy, pions can either interact again, if their interaction mean free path is less than their decay mean free path, or they will decay. From the average boosted decay length in Table 3.1, pions will travel, on average, 5.6 km through the atmosphere before decaying when their energy reaches around 30 GeV [21], meaning the average production altitude of muons is around 15 km. Higher-mass hadrons can also be produced by the interaction given in Equation (3.1) (such as the Λ^0 baryon in associated kaon production, $p+N \to \Lambda^0 + K^+$, for example), but these quickly decay either into pions (the lightest hadron) or directly into muons. These particles provide the air shower with a consistent hadronic core, which feeds both the EM component (through decays of neutral pions: $\pi^0 \to 2\gamma$) and the muonic component (through decays of charged pions and kaons).

3.1.1 Cascade Equations

The cascade equations (or "transport equations") are a set of coupled analytical integro-differential equations that describe the propagation of hadrons and the linear development of air showers through the atmosphere:

$$\begin{aligned}\frac{\mathrm{d}\Phi^A_{E_i}(E_i,X)}{\mathrm{d}X} = &-\frac{\Phi^A_{E_i}}{\lambda^A_{\text{int},\,E_i}} - \frac{\Phi^A_{E_i}}{\lambda^A_{\text{dec},E_i}(X)} + \\ &+ \sum_{E_k \geq E_i} \sum_{l} \frac{c_{l(E_k)\to A(E_i)}}{\lambda^l_{\text{int},\,E_k}} \Phi^l_{E_k} + \sum_{E_k \geq E_i} \sum_{l} \frac{d_{l(E_k)\to A(E_i)}}{\lambda^l_{\text{dec},E_k}(X)} \Phi^l_{E_k},\end{aligned} \tag{3.9}$$

where A indicates the particle species, such as $\pi^\pm$ or $K^\pm$, and E_i is a discrete energy bin [37]. The reason the equations are coupled is because an energetic interacting hadron can produce other types of hadrons (for example, an interacting proton can produce a pion).

The first two terms of Equation (3.9) are "sink terms," describing, respectively, the absorption of particles in the air via interaction and their loss due to decay. Their role in the reduction of the particle species A flux is represented by the negative signs in front of them. The other terms are the "source terms," describing the feeding of the cascades by secondary particles, either from interactions that produce particles of type A or by other particles decaying into particles of type A [37]. Boundary conditions are imposed such that the flux at $X = 0$ is equal to the primary cosmic ray flux for the relevant energy range [5].

3.2 Muonic Component

The muonic component of air showers is made up of muons and neutrinos that are produced in the decays of charged pions and kaons. The muons produced in these decays are commonly referred to as "atmospheric muons." The muonic component of an air shower is, in some ways, the most important component, because it has the highest inclusive flux at the surface (see Figure 3.2) and because muons are long-lived and highly-penetrating particles. This also makes muons very easy to detect, because they can be easily distinguished from other charged particles, all of which are less penetrating, and so they can be used as tools of measurement to study the properties of an air shower, including the shower's direction, lateral spread, and energy spectrum [38].

3.2.1 Muon Production

Charged pions and kaons decay into muons through the following interactions:

$$\begin{aligned} \pi^{+(-)} &\longrightarrow \mu^{+(-)} + \nu_\mu(\overline{\nu}_\mu), \\ K^{+(-)} &\longrightarrow \mu^{+(-)} + \nu_\mu(\overline{\nu}_\mu). \end{aligned} \tag{3.10}$$

The Feynman diagram for the decay of a negatively charged pion into a muon and muon neutrino is shown in Figure 3.4. Nearly 100% of charged pions decay into muons. About 63.5% of the time, charged kaons decay into muons directly, whereas the other 36.5% of the time, they will decay either into charged pions or a neutral pion and an electron.

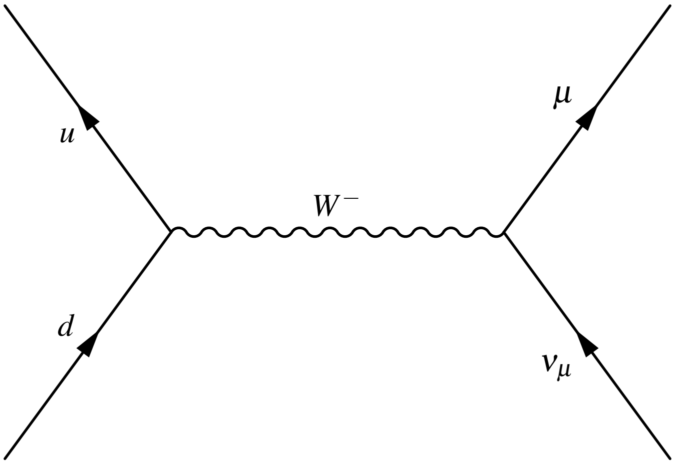

Figure 3.4: The decay of a negatively charged pion into a muon and an anti-muon neutrino via a charged-current weak interaction.

The reason pions decay to muons rather than electrons is because of helicity suppression. The decay proceeds via a charged-current weak interaction, as in Figure 3.4. The π^- is made up of $d\bar{u}$, and has spin 0, and, from conservation of angular momentum, spin must be conserved in the products. This means the spins of μ^- and $\overline{\nu}_\mu$ must be opposite. Because all antineutrinos (antiparticles) are right-handed, the μ^- (particle) must be left-handed. A particle's helicity (whether it is right-handed or left-handed) is the projection of the particle's spin onto the particle's direction of linear momentum. The W^- boson only couples to right-handed particles and left-handed antiparticles, however, there is some mixing, and the W^- boson can couple to left-handed particles and right-handed antiparticles, though much more weakly. The strength of this mixing increases as the mass of the particle increases, making the e^- the least likely decay product of the π^-. Because the τ^- is more massive than the pion, the pion cannot decay into it, and so the most likely decay product is then the μ^-. The result is that the branching ratio for a charged pion to decay into a muon is nearly 100%.

In addition to the conventional decays of pions and kaons into muons, there are also so-called "prompt" semileptonic decays of charmed mesons with short lifetimes, which are much less common but still contribute small amounts to the production of muons at high energies. Some examples include [39, 40]:

$$\begin{aligned} D^+ &\longrightarrow \overline{K}^0 + \mu^+ + \nu_\mu, \\ D^0 &\longrightarrow K^- + \mu^+ + \nu_\mu, \\ \Lambda_c^+ &\longrightarrow \Lambda^0 + \mu^+ + \nu_\mu, \\ \eta &\longrightarrow \mu^+ + \mu^- + \gamma. \end{aligned} \tag{3.11}$$

The exact magnitude of the contribution of the charm component of prompt fluxes is currently unknown and is an active area of research in the field of cosmic ray physics (see [41, 42]).

Similar to the cascade equations in Section 3.1.1, the muon flux at any given energy and atmospheric depth is determined by how many muons are being produced by pion and kaon decays compared to how many muons are decaying. The only experimentally observed decay mode of a muon is into an electron and two neutrinos:

$$\begin{aligned} \mu^+ &\longrightarrow e^+ + \nu_e + \overline{\nu}_\mu, \\ \mu^- &\longrightarrow e^- + \overline{\nu}_e + \nu_\mu. \end{aligned} \tag{3.12}$$

These are represented by the Feynman diagram in Figure 3.5.

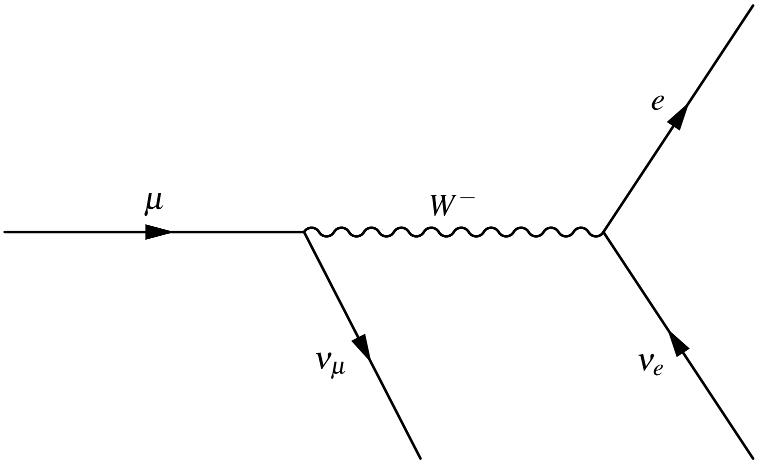

Figure 3.5: The decay of a negatively charged muon into an electron and two neutrinos via a charged-current weak interaction.

From Equation (3.7), the decay mean free path of muons is:

$$\lambda^{\mu}_{\mathrm{dec}}(E_\mu, X) = \frac{E_\mu X \cos(\theta)}{\varepsilon_\mu}, \tag{3.13}$$

where E_μ is the muon energy and ε_μ is the muon critical energy from Table 3.1. This gives the decay rate of muons per infinitesimally small slice of the atmosphere:

$$\begin{aligned} \frac{\mathrm{d}N_\mu}{\mathrm{d}X} &= -\frac{1}{\lambda^{\mu}_{\mathrm{dec}}} N_\mu(E_\mu, X) \\ &= -\frac{\varepsilon_\mu}{E_\mu X \cos(\theta)} N_\mu(E_\mu, X). \end{aligned} \tag{3.14}$$

Integrating the decay rate over the muon energy gives the muon intensity. From Equation (3.14), then, the muon intensity has an angular dependence [5]:

$$\begin{aligned} I_\mu(\cos(\theta)) &= \int_{m_\mu c^2}^{\infty} \frac{\mathrm{d}N_\mu}{\mathrm{d}E_\mu} \mathrm{d}E_\mu \\ &= -\frac{\varepsilon_\mu}{X\cos(\theta)} \int_{m_\mu c^2}^{\infty} \frac{N_\mu(E_\mu, X)}{E_\mu} \mathrm{d}E_\mu \\ &\propto \frac{1}{\cos(\theta)}. \end{aligned} \tag{3.15}$$

Therefore, the muon flux approximately scales as $1/\cos(\theta)$. However, it is important to keep in mind that this is under the assumptions laid out by Equations (3.2) to (3.5) of a flat Earth and an isothermal atmosphere, and is therefore only an approximation at larger zenith angles.

3.2.2 Muon Charge Ratio

Muons are not produced in equal amounts of μ^+ and μ^-. For low energies in the GeV range, the muon charge ratio is:

$$\frac{\Phi^s_{\mu^+}}{\Phi^s_{\mu^-}} \approx 1.28, \tag{3.16}$$

meaning positively charged muons are more common than negatively charged muons. This corresponds to the excess of π^+ and K^+ mesons over π^- and K^- mesons in the atmosphere due to the fact that stable nuclei in the atmosphere have more protons than neutrons. However, this is energy-dependent. As energy increases, the ratio of positively charged muons relative to negatively charged muons also increases. At higher energies, above 1 TeV, the ratio starts sharply increasing again, reflecting the increasing importance of kaons from $p + N \rightarrow \Lambda^0 + K^+$ interactions over pion interactions at these energies.

Experimental measurements of the muon charge ratio from surface muon spectrometers are shown in Figure 3.6. As shown in this figure, the charge ratio remains nearly constant for a range of energies spanning approximately 100 MeV to 100 GeV.

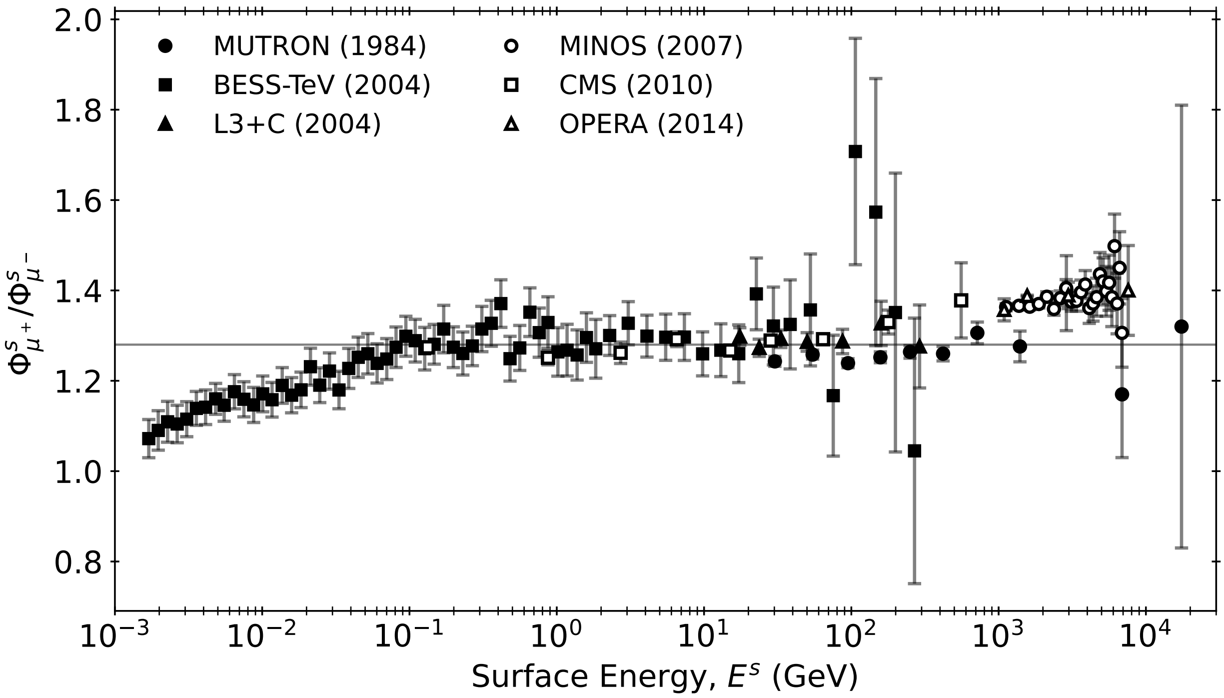

Figure 3.6: Muon charge ratio vs surface energy, with a constant line drawn at 1.28. Experimental data is taken from MUTRON [43], BESS-TeV [17], L3+C [44], MINOS [45], CMS [46], and OPERA [47], and is converted from muon momentum to muon kinetic energy where required, for consistent comparison.

The muon charge ratio can be important for muon-induced background studies because positively- and negatively charged muons can undergo different interactions in rock, leading to different neutron yields (see Section 5.1.1). For this reason, although the difference in energy loss between the two polarities is low at the relevant energy ranges, the energy loss must be modelled properly. Additionally, the muon charge ratio is useful because the measurements given in Figure 3.6 provide sets of data spanning a wide energy range that can be used to calibrate hadronic interaction models, as will be explained in Section 6.3.

3.2.3 High-Energy Muons

Most cosmic rays have energies between 10 MeV and 10 GeV. However, as discussed in Chapter 2, cosmic rays can reach incredibly high energies. Ultra-high-energy cosmic rays (UHECRs) are defined as cosmic rays with energy greater than 1 EeV (10^{18} eV). Extreme-energy cosmic rays (EECRs) are those with energies above the GZK limit of 50 EeV, of which many have been observed by the High Resolution Fly's Eye (HiRes) detector [48, 49, 50], the PAO [51, 52], and the Telescope Array (TA) [53]. The most powerful cosmic ray ever detected was observed by the HiRes detector in 1991 with an energy of (320 ± 90) EeV [54]. For comparison, the highest energy produced on Earth is 6.8 TeV (beam energy) by the Large Hadron Collider at CERN, the most powerful particle accelerator in the world.

High-energy cosmic rays produce high-energy muons, and these muons have certain properties by nature of their high energies that make them not only necessary and useful to study but also convenient. First, it must be established how these muons can survive their trip to the surface of the Earth in the first place. From Table 3.1, the mean lifetime of a muon is $\tau = 2.2\ \mu$s. Even for the highest-energy muons, using classical physics, this would not be long enough for the muon to travel an average length through the atmosphere of $\langle h \rangle = 15$ km to reach the Earth.

$$v = \frac{\langle h \rangle}{\tau} = \frac{1.5 \times 10^4\ \mathrm{m}}{2.2 \times 10^{-6}\ \mathrm{s}} = 6 \times 10^9\ \mathrm{ms}^{-1} > c. \tag{3.17}$$

However, it is possible for muons to reach the surface of the Earth, and even penetrate it by multiple kilometres, under the physics of special relativity. Atmospheric muons, especially those at energy levels relevant to this work, are relativistic particles, meaning they experience special relativistic effects. In special relativity, particles travelling close to the speed of light experience two non-classical effects:

- **Time Dilation:** The slowing down of time in a moving frame of reference as perceived by an observer at rest. The interval of time spanning an event concerning an object moving near the speed of light, Δt, will be measured to be longer than the interval of time spanning the same event in the object's own rest frame, Δt_0.
- **Length Contraction:** The shortening of the length of a moving object as measured by an observer at rest. The length of an object moving near the speed of light, L, will be measured to be shorter than its proper length, L_0 (the length measured in the object's own rest frame).

For time dilation above, "object" in the case of atmospheric muons refers to the relativistic muon, whereas, for length contraction, it refers to the atmosphere.

This means muons, from their own point of view, experience length contraction of the atmosphere, meaning the muon views the length it has to travel to reach the surface of the Earth as being shorter than in our rest frame. The contracted length is represented by the proper length divided by the Lorentz factor, γ:

$$\gamma = \frac{E}{m_\mu} + 1, \tag{3.18}$$

in natural units (where the speed of light is $c = 1$), where E is the muon's kinetic energy and m_μ is the mass of the muon. For a muon with energy 100 GeV, for example, the Lorentz factor is $\gamma = 947$. The length of the atmosphere, then, is contracted from 15 km down to:

$$\begin{aligned} L &= \frac{L_0}{\gamma} \\ &= \frac{15 \text{ km}}{947} \\ &= 0.016 \text{ km} = 16 \text{ m}. \end{aligned} \tag{3.19}$$

This means, from the muon's perspective, it only needs to travel, on average, 16 m to reach the surface of the Earth, instead of 15 km. Its mean lifetime of 2.2 μs gives it more than enough time to travel this distance and far further into the Earth.

Conversely, in the atmosphere's frame of reference, time dilation is calculated as the muon's proper time multiplied by the Lorentz factor. Therefore, the time interval of the muon's lifetime from our rest frame is:

$$\begin{aligned} \Delta t &= \gamma \Delta t_0 \\ &= 947 \cdot 2.2 \times 10^{-6} \text{ s} \\ &= 2.1 \times 10^{-3} \text{ s} = 2.1 \text{ ms}. \end{aligned} \tag{3.20}$$

Correspondingly, this also gives the muon more than enough time to travel 15 km and reach the surface of the Earth before decaying. Therefore, because of relativistic effects, muons are observed not only at sea level, but also deep underground. This has served as very strong evidence of special relativity.

Another important feature of high-energy muons is their gyroradius. Gyroradius, also called the "Larmor radius," is the radius of the circular motion that charged particles travel in when in the presence of a magnetic field. It is given by:

$$r_g = \frac{m v_\perp}{qB}, \tag{3.21}$$

where r_g is the gyroradius, m is the mass of the particle (in this case, m_μ), $v_\perp$ is the particle's speed perpendicular to the magnetic field, q is the charge (in this case, e, the elementary charge), and B is the strength of the magnetic field. The gyroradius of atmospheric muons is an important consideration because they are in the presence of Earth's magnetic field when they are produced. However, for high-energy muons relevant for underground muon studies, the gyroradius is large enough (because $v_\perp$ is large for high-energy muons) that the circular motion they experience due to the Earth's field can be ignored. For the purposes of this study, the effects of the magnetic field are completely neglected, greatly simplifying the calculations.

A last feature of high-energy muons that makes them convenient to study is that they are unaffected by solar cycles. Solar cycles are cycles of 11-year periods in which the activity of the sun (the number of sunspots) changes. While low-energy cosmic rays less than 10 GeV in energy can be affected by solar modulations due to changing conditions of the solar wind [55], high-energy cosmic rays relevant for underground physics are not.

3.2.4 Seasonal Variations

The Earth experiences seasons due to the fact that it is tilted 23.4° on its rotation axis. Therefore, in January, less of the Earth's northern hemisphere is exposed to the sun, meaning it experiences lower temperature, whereas more of the southern hemisphere is exposed to the sun and thus experiences higher temperature, and vice versa for July.

A long-known feature of the atmospheric muon flux is its variation over these seasons [2]. This is primarily caused by the change in temperature of the stratosphere between winter and summer, and the resulting effect on the muon flux is driven by the two competing options for pions and kaons to either interact or decay. From Equation (3.6), the interaction mean free path of pions (and similarly for kaons, K) is given by:

$$\lambda_{\mathrm{int}}^{\pi}(E_\pi) = \frac{\rho_{\mathrm{air}}}{n_{\mathrm{air}}\sigma_{\pi}^{\mathrm{air}}(E_\pi)}, \tag{3.22}$$

where E_π is the energy of the pion. Additionally, from Equation (3.7), the decay mean free path of pions is given by:

$$\lambda_{\mathrm{dec}}^{\pi}(E_\pi, X) = \frac{E_\pi X\cos(\theta)}{\varepsilon_\pi}, \tag{3.23}$$

where m_π is the mass of the pion, τ_π is the mean lifetime of the pion, and ε_π is the critical energy of the pion. When $E_\pi > \varepsilon_\pi$, interaction dominates, and when $E_\pi < \varepsilon_\pi$, decay dominates.

As the atmosphere warms during summer, its temperature increases and it expands, becoming less dense. According to Equation (3.22), when density decreases, the pion interaction mean free path will decrease (and $1/\lambda_{\mathrm{int}}^{\pi}$ will increase), meaning pions will have further to travel before interacting with an air molecule, and so will interact less often. This means they will be more likely instead to decay into muons, overall increasing the muon flux at the surface. However, the expansion of the atmosphere in summer (by about 1 km) also causes the altitude of the production level of pions and kaons to increase. Because of this, the muons they decay into have further to travel before reaching the surface of the Earth, and the probability of these muons to decay increases [5, 56]. The overall result is in favour of decay over interaction, resulting in a drop in the muon flux at the surface of the Earth during summer and a peak during winter. These effects on low-energy and high-energy muons are summarised in Table 3.2.

Table 3.2: Summary of the effects of the atmosphere warming during summer on the processes pions and kaons can undergo. When interaction decreases, decay increases, and so the muon flux increases, and vice versa.

	Lower Density	**Higher Production Level**
Interaction	Less Likely	More Likely
Low-Energy Muons	Increase	Decrease
High-Energy Muons	Increase	Decrease
Decay	More Likely	More Likely
Low-Energy Muons	Decrease	Decrease
High-Energy Muons	Decrease	Increase
Overall Flux	Decrease	

However, this process is energy-dependent [37]. This is shown in the plots of the total muon surface flux against surface energy for vertical and horizontal muons in January and July in Figure 3.7. Because the decay of pions and kaons into muons is delayed in summer, the energy distribution of the muons at sea level is shifted to higher energies. Higher-energy muons can reach deeper depths underground, resulting in a peak in the single muon flux underground in the summer despite the peak at the surface in the winter. Because the variations in the atmosphere across the seasons is small, the amplitude of the modulations at sea level is generally small, while the effect tends to be amplified at large depths, making underground detectors a good probe of the seasonal variations and, in turn, energy distributions of atmospheric muons.

3.3 Hadronic Interaction Models

Properly modelling the hadronic interactions that lead to the production of muons is crucial for calculating muon fluxes underground and underwater. In the present-day literature, there are three typical ways of performing hadronic interaction calculations: the Gaisser parameterisation, Monte Carlo event generators, and, more recently, data-driven models. A short overview will be given in this section, and further comparisons will be done in Section 6.3.

3.3.1 Analytical Formulas

Although it is not possible to solve the coupled cascade equations in Equation (3.9) analytically, T. K. Gaisser proposed an approximation via a parametric formula in [5]. The Gaisser parameterisa-

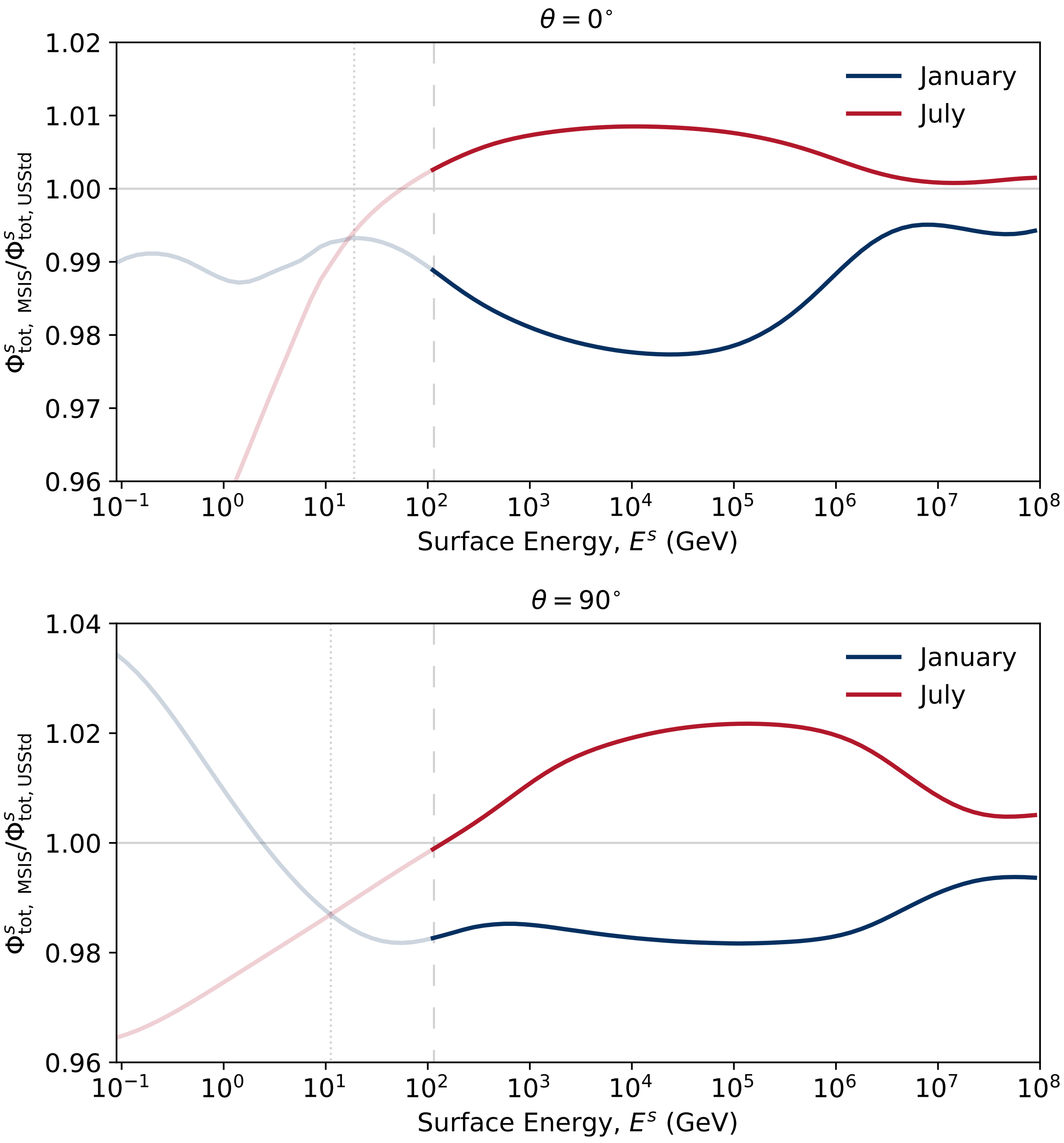

Figure 3.7: The ratio of the surface flux for the LNGS location (see Section 5.2) using SIBYLL-2.3C (see Section 3.3.2) and GSF to the surface flux for USStd (see Section 6.3.3) against surface energy for vertical muons (top) and horizontal muons (bottom). The blue curve shows the flux in January, and the red curve shows the flux in July. The dotted grey vertical line shows the energy at which the flux becomes higher in July than in January (19 GeV and 11 GeV for vertical and horizontal muons respectively), showing that, although the total muon flux is higher in January, the high-energy muon flux is higher in July. The grey dashed vertical line shows the critical energy of pions in the atmosphere, 115 GeV. See also Figure 5 in [37].

tion has since become a commonly used method for estimating the number of cosmic-ray muons, N_μ, per surface energy, E^s, as a function of energy and zenith angle, θ^s, at sea level:

$$\frac{\mathrm{d}N_\mu}{\mathrm{d}E} \approx (E^s)^{-\gamma}\left(\frac{1}{1+\frac{1.11E^s\cos(\theta^p)}{115\text{ GeV}}}+\frac{0.054}{1+\frac{1.11E^s\cos(\theta^p)}{850\text{ GeV}}}\right), \tag{3.24}$$

where, θ^p is the zenith angle of the muon at production [5, 57]. Here, 115 GeV and 850 GeV are the critical energies of pions and kaons respectively, from Table 3.1. This parameterisation is based on several assumptions. Full lists of the assumptions can be found in [5, 36], but some of note are:

1. The net flux of incoming cosmic rays is described by a power law, with a spectral index that is independent of energy, as in Equation (2.1).
2. The Earth is flat, as in Section 3.1. This means the parameterisation is only valid up to zenith angles of around 60°, beyond which the curvature of the Earth is non-negligible.
3. The atmosphere is isothermal, as in Section 3.1.
4. Muon energy loss in the atmosphere is negligible.

Because of these assumptions and approximations, the Gaisser parameterisation is only valid for a certain range of energies and zenith angles and it has limited applicability compared to more recent methods. However, it remains a convenient formula to use for fast and non-intensive approximations of the muon flux.

Aside from the Gaisser parameterisation, an empirical formula was proposed by S. Miyake in 1973 in [58] to calculate the vertical muon intensity at sea level, I_v^s, in units of [$\mathrm{m}^{-2}\mathrm{s}^{-1}\mathrm{sr}^{-1}$]:

$$I_v^s(E^s,\theta^p) = \frac{1.74\times 10^6}{5E^s\cos(\theta^p)+400}(5E^s+10\sec(\theta^p))^{-1.57}\frac{E^s+15}{E^s+10+5\sec\theta^p}. \tag{3.25}$$

Here, E^s is the muon energy at the surface, and θ^p is the muon's zenith angle when it is produced. This formula describes the surface muon intensity well, but was based on data from underground muon experiments [59].

Multiple other analytical calculations have been published over the decades. L. V. Volkova, G. T. Zatsepin, and L. A. Kuzmichev calculated muon fluxes at sea level in 1979 in [60], with a follow-up work in 2001 found in [61] focussing on atmospheric neutrino fluxes using a semi-analytical solution to the cascade equations. An analytical calculation of muon fluxes was also published by P. Lipari in 1993 in [62]. Most recently, E. V. Bugaev, et al. presented a theoretical calculation for muon fluxes at sea level, underground, and underwater in 1998 in [3]. They claim earlier calculations used less advanced phenomenological approaches that relied on extrapolations to energy levels orders of magnitude higher than the accelerator data they were based on.

3.3.2 Event Generators

Because the cascade equations in Section 3.1.1 are impossible to solve analytically, Monte Carlo generators have become a standard method of calculating hadronic interactions. These are implemented in particle propagation and air shower development programs such as COsmic Ray SImulations for KAscade (CORSIKA) [63] and FLUktuierende KAskade (Fluctuating Cascade; FLUKA) [64, 65]. Some common event generators, and those referenced in this work, include:

- **EPOS-LHC:** The Event generator for the Propagation of the Objects in Simulated Large Hadron Collider collisions (EPOS-LHC) [66] is an event generator based on the parton-based Gribov-Regge theory from [67].

- **QSGJET:** The Quark-Gluon String model for JET hadronisation (QGSJET) [68] is based on the Quark-Gluon String (QGS) model from [69] and uses the Gribov-Regge formalism to simulate inelastic hadronic interactions. The latest version is QGSJET-II-04.

- **DPMJET:** The Dual Parton Model JET (DPMJET) is based on the Dual Parton Model (DPM) from [70] and uses Gribov-Regge theory to simulate hadron-hadron interactions. DPMJET-III was published in 2000 and is able to simulate hadron-hadron, photon-hadron, and photon-photon interactions from as low as a few GeV up to the highest cosmic ray energies [71, 72]. An overview of the model is given in [73]. The latest version is DPMJET-III-19.3, released in 2022.

- **SIBYLL:** SIBYLL is a minijet model written specifically for simulations of hadronic interactions from high-energy cosmic rays [74]. Because it focusses on high energies, it naturally produces more events at higher energies and fewer events at lower energies, making it an appropriate model choice for deep underground laboratories. The latest version is SIBYLL-2.3D, released in 2019 [75].

3.3.3 Data-Driven Models

More recently, data-driven models have been published by A. Fedynitch, J. P. Yañez, and M. Huber. Compared to event generators, these achieve significantly smaller uncertainties on muon fluxes. At the moment, the two available data-driven models are:

- **DDM:** The Data-Driven Model (DDM) [76] is an inclusive model based on data from the NA49 [77, 78] and NA61/SHINE [79] accelerator experiments at CERN. These experiments have a maximum beam momentum of 158 GeV. Higher TeV- and PeV-scale energies relevant for underground muons coming from cosmic rays are extrapolated to under the assumption of Feynman scaling of the scattering processes. Because it is driven by lower-energy data, DDM is an appropriate model choice for shallower underground laboratories.

- **DAEMONFLUX:** DAta-drivEn MuOn-calibrated atmospheric Neutrino FLUX (DAEMONFLUX) [80] is a recent model for muon and neutrino fluxes based on DDM and GSF which has been calibrated to muon surface flux and charge ratio data (including the data presented in Figure 3.6) and uses constraints from fixed-target near-horizontal measurements at the highest energies. With this calibration, it can achieve muon flux uncertainties at the percent level up to 1 TeV. DAEMONFLUX is currently the hadronic interaction model with the smallest uncertainties.

3.3.4 Uncertainties

The dominant uncertainties throughout this work are those coming from the hadronic interaction model. Uncertainties on these models are typically high because of the lack of accelerator measurements in the relevant very forward (low scattering angle) region that simulates cosmic ray interactions. This is the region of non-perturbative QCD, which means there are no robust methods to compute particle production yields from these processes from first principles. Before DAEMONFLUX, uncertainties on both pion and kaon production were high, but they were higher for kaons ($\sim$40%) because kaons are produced in hadronic interactions less often than pions, and so there is very little data from high-energy fixed-target experiments. This means errors had to be extrapolated from low-energy experiments for the modelling forward kaon production, as is the case in DDM.

This is relevant for underground muons, because deep underground muons are those that had high energies at the surface, and the contribution of kaons to the muon flux at the surface increases as energy increases. This is because kaons typically decay quickly before they can interact and lose much energy due to their short lifetime (see the values in Table 3.1). This means the large uncertainties on kaon production become more important the deeper the underground laboratory.

As a note, this is particularly important for atmospheric neutrino uncertainties. The large uncertainties on hadron production turn into large uncertainties in muon and neutrino production, being 20% and 40% respectively [81], before the publication of DAEMONFLUX. They are higher for neutrinos than they are for muons because of the kinematics of the interactions that produce

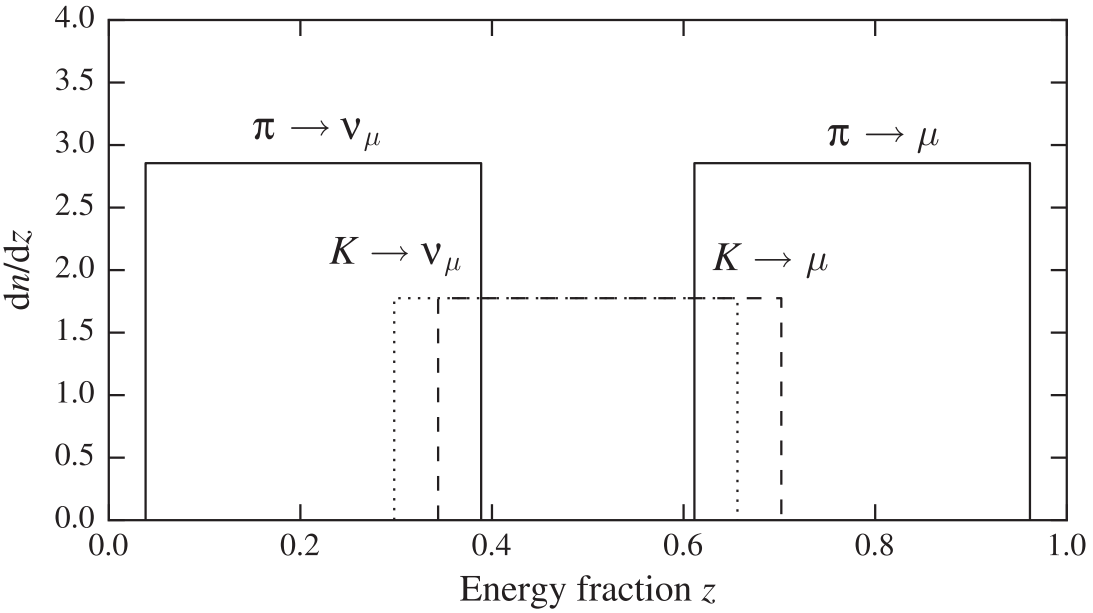

Figure 3.8: Energy distributions of muons and neutrinos in the decay of pions and kaons, taken from [5].

them. This is seen in the plot of the energy fractions in Figure 3.8. For muons, the energy limits are:

$$\left(\frac{m_\mu}{m_\pi}\right)^2 \leq E_\pi \leq 1. \tag{3.26}$$

For neutrinos, they are:

$$0 \leq E_\pi \leq 1 - \left(\frac{m_\mu}{m_\pi}\right)^2. \tag{3.27}$$

According to the decay kinematics, in pion decays, neutrinos only receive 21% of the initial energy of the pion, whereas they receive 48% of the energy in kaon decays [5]. This is because the ratio of masses between the muon and kaon is small, so the energy given to the muon is smaller. In summary, then, because kaons are less common than pions, there is less data available on them, and so they are more difficult to model, leading to high kaon uncertainties, leading to higher neutrino uncertainties.

This is important because modern detectors are so precise that the flux uncertainties are now showing up as a dominant uncertainty, particularly in measurements of astrophysical neutrinos, for which atmospheric neutrinos are a main background. If the atmospheric neutrino flux were known well, with small uncertainties, then it could be accounted for more easily.

4 Muon Energy Loss in Matter

After muons travel through the atmosphere and reach the surface of the Earth, either land or water, they will keep travelling through the Earth for multiple kilometres. As they do this, they lose energy via multiple different processes, which must be well-understood in order to simulate their propagation. This chapter will establish important fundamental concepts for the passage of high-energy charged particles through matter that will be necessary for Chapter 6. A summary of the variables used throughout this chapter is given in Table 4.1.

Table 4.1: Summary of symbols used throughout this chapter and their values taken from [8] and rounded where applicable.

Variable Symbol	Definition	Formula	Value
ε_0	Permittivity of free space		5.526×10^{13} MeV^{-1}m$^{-1}e^2$
$\hbar$	Planck's reduced constant		6.582×10^{-16} eVs
c	Speed of light in vacuum		2.998×10^{8} ms^{-1}
e	Elementary electric charge		1.602×10^{-19} C
m_e	Electron mass		0.511 MeVc^{-2}
m_μ	Muon mass		105.658 MeVc^{-2}
r_e	Classical electron radius	$e^2/4\pi\varepsilon_0 m_e c^2$	2.817 fm
α	Fine structure constant	$e^2/4\pi\varepsilon_0\hbar c$	$1/137$
N_A	Avogadro's number		6.022×10^{23} mol^{-1}
K	Ionisation constant	$4\pi N_A r_e^2 m_e c^2$	0.307 MeVmol^{-1}cm^2
v_μ	Muon velocity		
β	Velocity factor	v_μ/c	
γ	Lorentz factor	$1/\sqrt{1-\beta^2}$	
E	Muon energy	$\gamma m_\mu c^2$	
T	Muon kinetic energy	$(\gamma-1)m_\mu c^2$	
ν	Fractional energy loss	$\Delta E/E$	
q	Momentum transfer		
Q^2	Virtuality	$-q^2$	
Z	Atomic number of medium		
A	Atomic mass of medium		
X_0	Radiation length		

Energy loss is described in terms of energy lost per unit distance, $\mathrm{d}E/\mathrm{d}X$, also called the "stopping power." Because energy loss is largely a stochastic process, especially at higher energies, this is typically given as an average, $-\langle \mathrm{d}E/\mathrm{d}X \rangle$ (with a negative sign because energy is being lost). An overview of muon energy loss at different scales is shown in Figure 4.1 as the stopping power of a positively charged muon in copper as a function of muon kinetic energy. Below 1 MeV, there is a difference between the losses of μ^+ and μ^- because low-energy negatively charged muons are susceptible to being captured by atoms to form muonic hydrogen (a proton with a bound muon instead of an electron). This is known as the Barkas effect, named after W. H. Barkas [82, 83].

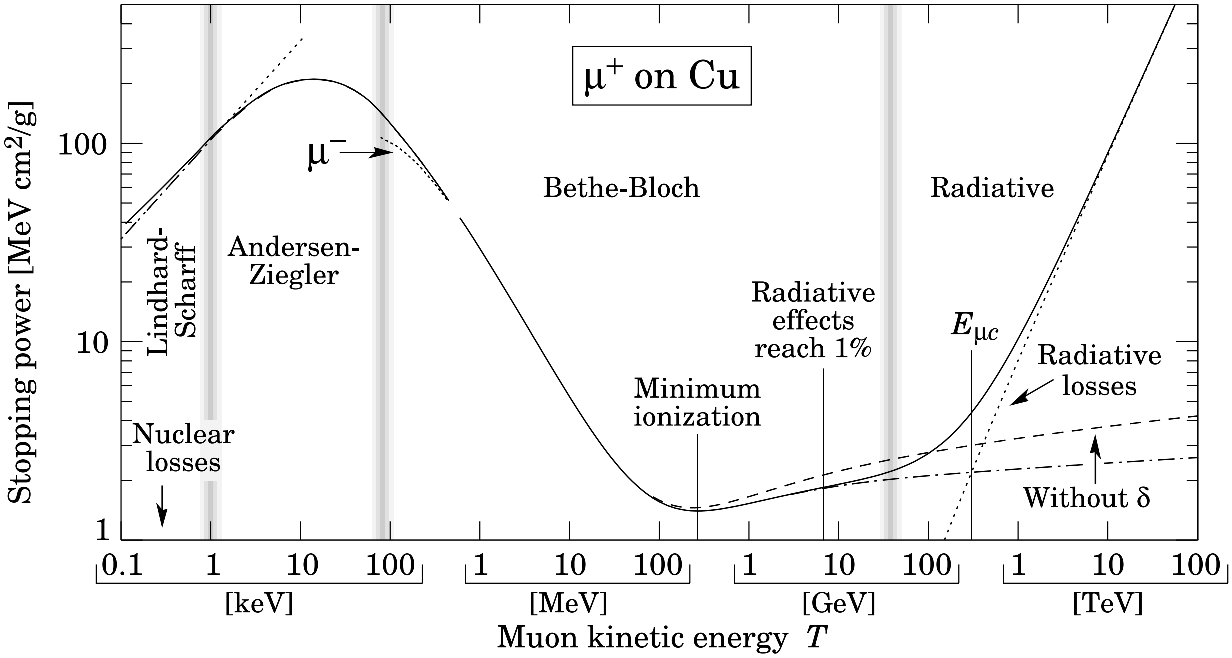

Figure 4.1: Energy loss of μ^+ in copper against muon kinetic energy, taken from [8]. Note that the rate of energy loss is dependent on the material the muon is travelling through.

Four energy ranges are shown in Figure 4.1, divided by vertical grey bars in the plot. Below 1 keV, the stopping power increases with energy. In this region, energy is lost mainly to nuclear recoils, as the velocity of the muon is less than the velocity of the valence electrons of the material's atoms. Between 1 keV and 1 MeV, the theory is not well-understood, and calculations usually depend on phenomenological fitting formulas developed by H. H. Andersen and J. F. Ziegler in [84] for proton stopping powers (usually scaled down to the mass of muons). Some sources claim, however, that these formulas overestimate the stopping power in this region [85, 86, 87].

High energies above 1 MeV are relevant for underground and underwater muons. Between 1 MeV and 500 GeV, ionisation losses dominate, and the stopping power is described by the Bethe-Bloch equation. The energy loss decreases with energy to a minimum ionisation point before increasing due to radiative losses. By 500 GeV, labelled $E_{\mu c}$ in Figure 4.1, radiative losses dominate, and the stopping power continues to rise logarithmically with muon energy.

4.1 Variables and Units

Before further describing the handling of muon propagation at different laboratories, certain conventions for the variables and units used throughout must first be established. The main variable of interest when dealing with muon propagation and energy loss in matter is the slant depth. In general, the slant depth, X (similar in concept to but defined differently from the atmospheric slant depth of Section 3.1), is defined geometrically in terms of the vertical depth, h:

$$X = \frac{h}{\cos(\theta)}, \tag{4.1}$$

where θ is the zenith angle of the incoming muon. Here, X is the hypotenuse of the right-angle triangle created by the trajectory of the muon and the vertical distance, h, to the lab the muon is travelling towards. The meanings of vertical depth (valid only for laboratories under flat overburdens) and slant depth are visualised in the diagrams in Figure 4.2.

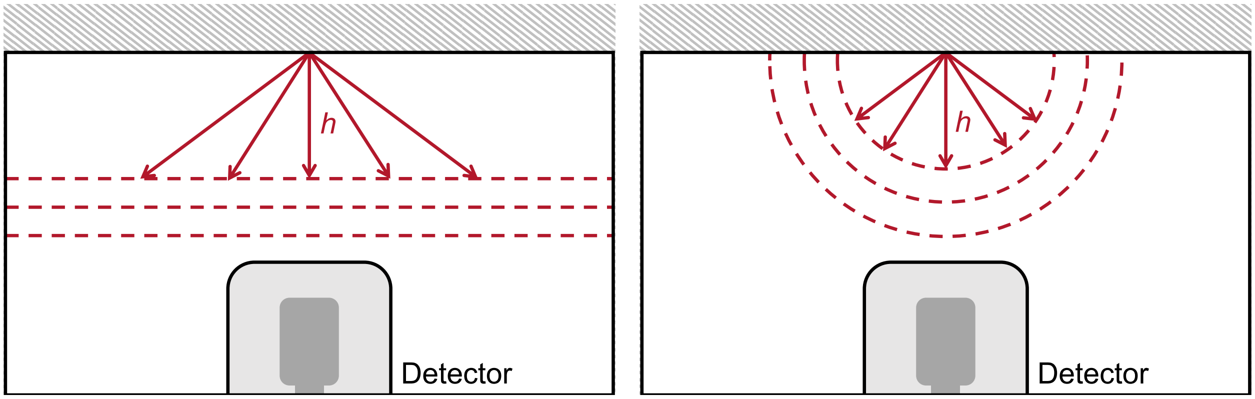

Figure 4.2: Dashed lines of varying vertical depth (left) and varying slant depth (right) for different zenith angles. The magnitude of the arrows defining the slant depth in the right diagram is constant no matter the zenith angle.

The standard unit of the slant depth is kilometres water equivalent (abbreviated as [km.w.e.]). Another common unit, however, is radiation units of either [gcm^{-2}] or [hgcm^{-2}]. The three are easily converted between each other:

$$1 \text{ km.w.e.} = 1 \text{ hgcm}^{-2} = 10^5 \text{ gcm}^{-2}. \tag{4.2}$$

If h is given in units of [km.w.e.], as it always is in this work, then Equation (4.1) is valid. If, instead, h is given in units of [cm], it must be multiplied by the density of the medium, such as the density of the rock, ρ_{rock}, to convert to [km.w.e.]:

$$X_{[\text{km.w.e.}]} = \rho_{\text{rock}} \frac{h_{[\text{cm}]}}{\cos(\theta)}. \tag{4.3}$$

The purpose of using kilometres water equivalent to measure depths underground instead of just kilometres is to account for the differences in density of the different types of rock above laboratories around the world so that the muon fluxes underground can be compared in a meaningful way. This is because denser rock will provide stronger shielding of atmospheric muons. For example, a lab at a vertical depth of 2 km with a rock overburden that has a density of 3 gcm^{-3} and a lab at a physically deeper vertical depth of 3 km under rock of a lower density of 2 gcm^{-3} are both under the equivalent of 6 km of water, so they are both, in effect, equally deep in terms of their suppression of the muon flux. The slant depth is best thought of as a measure of the effective total amount of matter a muon has to travel through. From Equation (4.3), the slant depth can increase due to increases in the density of the medium, the physical vertical depth of the lab, or the zenith angle of the incoming muon, all of which increase the effective total amount of rock the muon ends up travelling through.

It is often necessary to convert between slant depths defined with respect to different types of rock and in different units. The value of the physical slant depth in units of [km] is given by the value in [km.w.e.] of the given lab i, from Equation (4.1) or Equation (4.3), divided by the density of the rock:

$$X_{[\text{km}]} = \frac{X^{i}_{[\text{km.w.e.}]}}{\rho_i}. \tag{4.4}$$

Therefore, in order to convert a slant depth directly from units of [km] to units of [km.w.e.], because of the conversion between [km.w.e.] and [gcm^{-2}] from Equation (4.2), the value is simply multiplied by the density of rock.

Another useful concept in the field of muon propagation and energy loss is that of standard rock. Standard rock (SR) is defined as an isotope of sodium ($Z = 11$, $A = 22$)[1] with a density of $\rho_{\text{SR}} = 2.65\ \text{gcm}^{-3}$ [8, 90]. This is the definition of the Cayuga Rock Salt Mine near Ithaca, New York, and its use dates back to the first studies of underground muons (see [2]). To convert from a slant depth in [km] of standard rock to a slant depth in [km.w.e.], one can do:

---

[1] In some cases, standard rock is alternatively considered to be CaCO_3 (calcium carbonate; a type of limestone), originating from assumptions made by W. Lohmann, R. Kopp, and R. Voss in [88]. The standard mass density of CaCO_3 is 2.8 gcm^{-3}, but this is adjusted to 2.65 gcm^{-3} when considered as standard rock. This definition is used, for example, by the SNO Collaboration in [89].

$$X^{\mathrm{SR}}_{[\mathrm{km.w.e.}]} = \rho_{\mathrm{SR}} X_{[\mathrm{km}]}, \tag{4.5}$$

This is valid for any type of rock. Thus, after some slight rearranging:

$$X_{[\mathrm{km}]} = \frac{X^{\mathrm{SR}}_{[\mathrm{km.w.e.}]}}{\rho_{\mathrm{SR}}} = \frac{X^{\mathrm{lab}}_{[\mathrm{km.w.e.}]}}{\rho_{\mathrm{lab}}}. \tag{4.6}$$

Further rearranging the right-hand side of Equation (4.6) and putting it in terms of the physical variables h and θ:

$$\begin{aligned} X^{\mathrm{lab}}_{[\mathrm{km.w.e.}]} &= \left(\frac{\rho_{\mathrm{lab}}}{\rho_{\mathrm{SR}}}\right) X^{\mathrm{SR}}_{[\mathrm{km.w.e.}]} \\ &= \left(\frac{\rho_{\mathrm{lab}}}{\cancel{\rho_{\mathrm{SR}}}}\right) \cancel{\rho_{\mathrm{SR}}} X_{[\mathrm{km}]} \\ &= \rho_{\mathrm{lab}} X_{[\mathrm{km}]} \\ &= \rho_{\mathrm{lab}} \frac{h_{[\mathrm{km}]}}{\cos(\theta)}. \end{aligned} \tag{4.7}$$

Because h for laboratories under flat overburdens is a special case of X for $\theta = 0^\circ$, Equations (4.4) to (4.7) apply to vertical depths as well. Therefore, the vertical depth of SNOLAB, for example, can be converted from [km] to [km.w.e.] in this way:

$$\begin{aligned} h^{\mathrm{SNO}}_{[\mathrm{km.w.e.}]} &= \rho_{\mathrm{SNO}} h^{\mathrm{SNO}}_{[\mathrm{km}]} \\ &= (2.83\ \mathrm{gcm}^{-3})(2.092\ \mathrm{km}) \\ &= (2.83\ \mathrm{gcm}^{-3})(2.092 \times 10^5\ \mathrm{cm}) \\ &= 5.92 \times 10^5\ \mathrm{gcm}^{-2} \\ &= 5.92\ \mathrm{km.w.e.} \end{aligned} \tag{4.8}$$

This is close to SNO's given value of 5.89 km.w.e. in [89] (the exact reason for the discrepancy is unknown but is likely found in the details of the chemical composition of the rock and possibly variations in the rock density at different locations above the lab; see Equation (6.10) and the discussion in Section 8.2).

4.2 Energy Loss Processes

Above 1 GeV, muons will lose energy by interaction with atoms through four main energy loss processes: ionisation, pair production, bremsstrahlung, and photonuclear interactions. The process a muon undergoes is random, and therefore must be treated stochastically (as "stochastic losses"), but depends on the energy scale of the muon as well as the distance of approach of the muon to the atom it is interacting with.

Ionisation is referred to as a type of continuous loss because the muon loses small amounts of energy due to ionisation at a frequency so high that the loss of energy is nearly continuous. Conversely, pair production, bremsstrahlung, and photonuclear interactions are referred to as discrete losses (also "radiative losses" or "catastrophic losses") because the muon undergoes these interactions less frequently, but, when it does, it typically loses large amounts of energy at once. Continuous losses are dominant at low energies, whereas discrete losses are dominant at high energies. Their relative frequencies are energy-dependent, but, at high energies, pair production is the most important process in terms of the amount of energy lost, while bremsstrahlung is nearly as important but slightly less so, and photonuclear interactions are 3 times less important than ionisation [5].

The mean energy loss rate for these processes over distance travelled is generally proportional to the energy:

$$-\left\langle \frac{\mathrm{d}E}{\mathrm{d}X} \right\rangle \propto E. \tag{4.9}$$

It is also proportional to the integral of the cross-section differential in the relative energy loss, ν: $\mathrm{d}\sigma/\mathrm{d}\nu$. For this reason, cross-sections will be shown as differential cross-sections in the following sections. These sections will give an overview of some basic concepts and will explain these energy loss processes and how the muon interacts in each of them in more detail.

In addition to these four main interactions, there are also other rarer processes, such as $\mu^+\mu^-$ pair production, or charged or neutral current weak nuclear interactions (including equivalent interactions to those described in the following sections with the photon replaced with the heavier — and therefore suppressed — Z^0 boson). These will not be focussed on in this work, because they contribute very little to the overall energy loss.

4.2.1 Radiation Length and the Critical Energy

The radiation length, written X_0 — though often expressed in terms of $1/X_0$ — is the distance (in radiation units of [gcm^{-2}]) a muon will travel before losing $1/e$ of its initial energy due to bremsstrahlung. In other words, it is the length X_0 at which the muon's energy is equal to:

$$E = E^s e^{-X/X_0}, \tag{4.10}$$

where E^s is the muon's initial energy at the surface of the Earth. This is a characteristic length for a given species of particle in a given material. A higher radiation length indicates that a particle will travel further before losing the same amount of energy as a particle of a lower radiation length. X_0 decreases as the atomic number Z of the medium the particle is travelling through increases. For this reason, the values of $\langle Z/A \rangle$ and $\langle Z^2/A \rangle$ are important when considering and comparing different propagation media. A common parameterisation for the radiation length for different materials is given by Y.-S. Tsai in [91].

The muon critical energy, ε_μ, is the threshold energy at which energy losses due to ionisation are equal to those due to radiation, which is important for quantifying the energy loss when simulating the propagation of muons through matter [5, 8, 92]. This is the standard definition of the critical energy, and is a completely independent concept from the pion and kaon critical energy for hadronic interactions and decays in the atmosphere discussed in Section 3.1.1. For muons in standard rock, the critical energy is often quoted as 500 GeV [5], but D. E. Groom, N. V. Mokhov, and S. I. Striganov give the value of 693 GeV in [93]. Alternatively, B. Rossi, in [94], defines the critical energy as the energy at which losses by ionisation per radiation length are equal to the energy of the electron. For low Z, the standard critical energy is equal to the Rossi critical energy, but they diverge at larger Z, with the Rossi critical energy being 4.6% lower for electrons in lead ($Z = 84$) [8]. For muons in rock and water, the difference between the two definitions is less than 1%. Throughout the rest of this work, the standard definition is used.

4.2.2 Ionisation

Ionisation refers to the creation of atomic ions when muons interact with atoms in the rock or water and release electrons (this term typically includes the excitation of atomic electrons as well). At low energies, below 500 GeV, muons lose energy mainly via ionisation. When a muon approaches an atom at a large distance compared to the scale of the atom, it will generally interact coherently, meaning it will interact with the atom as a whole, and the result is that the muon will ionise the atom, either by exciting an electron to an upper shell or by a knock-on process in which an electron is knocked out of the atomic orbital entirely.

The differential cross-section for ionisation is given by [95] to be:

$$\frac{\mathrm{d}\sigma}{\mathrm{d}\nu} = \frac{1}{2} K \frac{Z}{A} \frac{1}{(\beta E \nu)^2} \left(1 - \beta^2 \left(\frac{\nu}{\nu_{\max}} \right) + \frac{1}{2} \left(\frac{\nu}{1 + 1/\gamma} \right)^2 \right). \tag{4.11}$$

In general, the rate of energy loss to ionisation of a charged particle travelling through matter is given by the Bethe-Bloch equation, named after H. Bethe and F. Bloch and derived from the cross-section above [8, 96]:

$$-\left\langle \frac{dE}{dX} \right\rangle = K \frac{Z}{A} \frac{1}{\beta^2} \left(\frac{1}{2} \ln \left(\frac{2 m_e c^2 \beta^2 \gamma^2 T_{\max}}{I^2} \right) - \beta^2 - \frac{\delta}{2} \right). \tag{4.12}$$

where $T_{\max}$ is the maximum possible amount of energy transferred from the muon to an electron in a single collision, given by:

$$T_{\max} = \frac{2m_e c^2 \beta^2 \gamma^2}{1 + 2\gamma(m_e/m_\mu) + (m_e/m_\mu)^2}, \tag{4.13}$$

I is the mean excitation energy, and δ is a density effect correction parameter. This density correction is introduced in order to counteract against the logarithmic rise with $\beta^2\gamma^2$ at high energies, where media become polarised and ionisation is reduced, and is dependent on the energy parameter $x = \log_{10}(\beta\gamma)$:

$$\delta = \begin{cases} \delta_0 10^{2(x-x_0)} & \text{if } x < x_0, \\ 2\ln(10)x + c + a(x_1 - x)^b & \text{if } x_0 \le x \le x_1, \\ 2\ln(10)x + c & \text{if } x > x_1, \end{cases} \tag{4.14}$$

where x_0 and x_1 simply demarcate the transition regions of the function form of the δ parameter [97]. Here, δ_0, a, b, and c are additional empirical parameters, termed the “Sternheimer parameters” after R. M. Sternheimer, specific for a given material. The strength of this density effect increases as energy increases, as seen in the comparison between the solid curve and the dashed “without δ” curve below the critical energy in Figure 4.1.

4.2.3 Pair Production

If a photon that is being exchanged between a muon and an atomic nucleus has enough energy, it can produce an electron-positron pair. When this happens, the muon loses energy to the creation and transfer of energy to this pair. The minimum amount of energy required for this is at least twice the mass of the electron, in order to convert enough energy into the production of the electron and the positron:

$$E_\gamma \ge 2m_e = 1.02\ \text{MeV}. \tag{4.15}$$

This process can proceed in two ways: either the electron-positron pair can couple to the nucleus, or the muon can couple to the nucleus. Feynman diagrams for both of these processes are shown in Figure 4.3.

Calculations for pair production by a relativistic muon were first performed by S. R. Kelner and Y. D. Kotov in [98]. These calculations were later expanded upon by R. P. Kokoulin and A. A. Petrukhin in [99], who give the differential cross-section as:

$$\frac{\mathrm{d}^2\sigma}{\mathrm{d}\nu\,\mathrm{d}\rho} = \frac{2}{3\pi}(Z\alpha r_e)^2 \frac{1-\nu}{\nu}\left(\Phi_e + \left(\frac{m_e}{m_\mu}\right)^2 \Phi_\mu\right). \tag{4.16}$$

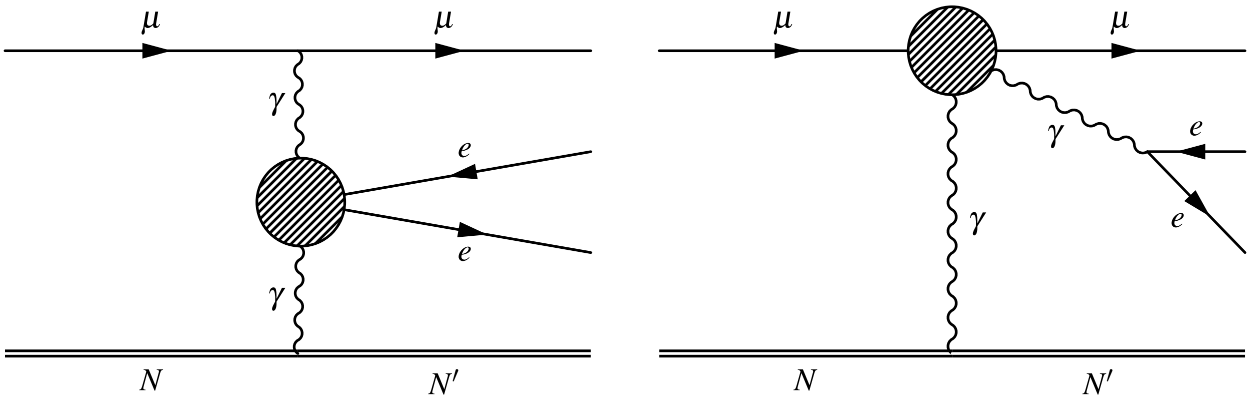

Figure 4.3: Feynman diagrams for the production of an electron-positron pair from a high-energy photon being exchanged between a propagation muon and an atomic nucleus. The nucleus can couple either to the pair (left; "electron diagram") or to the muon (right; "muon diagram").

In addition to being differential in the relative energy loss, ν, the cross-section is also differential in an asymmetry coefficient, ρ, which accounts for the energy distribution of the electron-positron pair, and is defined as:

$$\rho = \frac{E_{e^+} - E_{e^-}}{E_{e^+} + E_{e^-}}, \tag{4.17}$$

where E_{e^+} is the amount of energy transferred to the positron and E_{e^-} is the amount of energy transferred to the electron. Φ_e and Φ_μ in Equation (4.16) quantify the contribution from the electron and muon diagrams in Figure 4.3 respectively [99]. The Φ_μ term is suppressed by multiple orders of magnitude by the ratio of the electron mass to the muon mass, meaning energy loss via pair production is driven by the electron diagram for all but the highest energies.

The radiation length for pair production, X_{pair}, is comparable to that of bremsstrahlung [5]:

$$\frac{1}{X_{\mathrm{pair}}} = \frac{7}{9}\frac{1}{X_0}. \tag{4.18}$$

This comes from the approximation of the high-energy limit for the pair production cross-section, $\sigma = (7/9)(A/X_0 N_A)$, based on calculations of the bremsstrahlung cross-section by Y.-S. Tsai [8, 91]. Because the radiation length is slightly lower for pair production, muons will lose energy due to pair production more often than they will to bremsstrahlung radiation, making it the largest contributor to energy loss above the critical energy [5].

4.2.4 Bremsstrahlung

At high energies above 500 GeV, muons lose energy mainly via bremsstrahlung ("braking radiation"). When any charged particle accelerates or decelerates, it emits an electromagnetic wave.

This happens to muons travelling through matter when the muons are deflected by the electric fields of the nuclei in the atoms that make the matter up. The leading-order Feynman diagrams for this process are shown in Figure 4.4. When a muon approaches an atom at a small distance compared to the scale of the atom, the deflection of the muon by the atomic nucleus becomes most significant, and so bremsstrahlung becomes more likely.

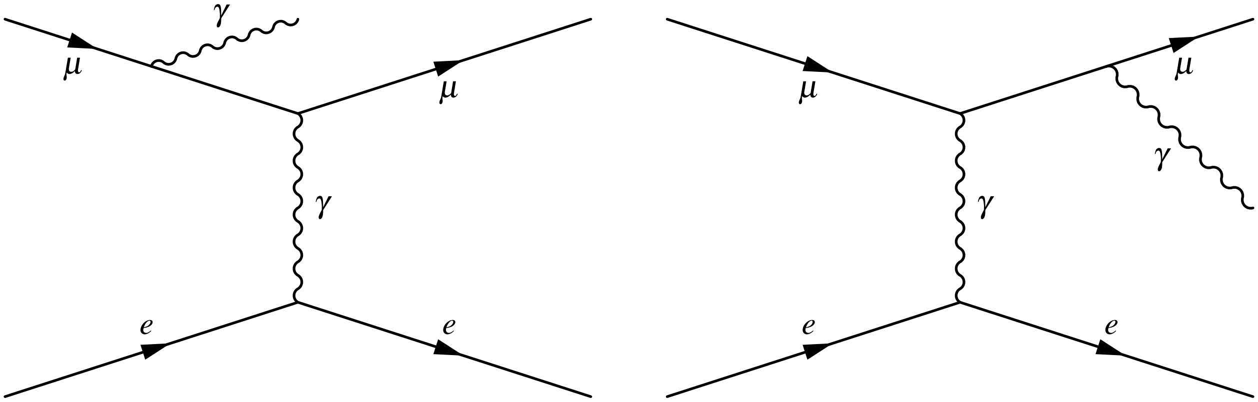

Figure 4.4: Feynman diagrams for inelastic bremsstrahlung interactions. There are two additional diagrams in which the outgoing photon is emitted by the electron. Because both bremsstrahlung and pair production involve the exchange of a photon between the muon and an atomic nucleus, their Feynman diagrams are variants of one another, and so the calculations for both are similar [8].

The differential cross-section for bremsstrahlung is given by [95] to be:

$$\frac{\mathrm{d}\sigma}{\mathrm{d}\nu} = \frac{\alpha}{\nu}\left(2Zr_e\frac{m_e}{m_\mu}\right)^2\left((2-2\nu+\nu^2)\Phi_1 - \frac{2}{3}(1-\nu)\Phi_2\right), \tag{4.19}$$

where Φ_1 and Φ_2 are electric-field screening functions (a technique that interprets the Coulomb force repulsion of like-polarity muons creating a small physical vacuum region around each muon as a screen of positive charges). The contribution of bremsstrahlung as an energy loss mechanism to the overall amount of energy lost by a muon is proportional to the square of the atomic number of the medium, as seen by the dependence on Z^2 in Equation (4.19). For low-atomic number media, such as aluminum (with $Z = 13$), bremsstrahlung is nearly insignificant for MeV-scale muons, whereas it is more significant for higher-atomic number media, like lead (with $Z = 82$).

Because the muon can come in towards the nucleus at any distance, it can be deflected at any angle, releasing a photon of the corresponding energy and wavelength. This leads to a continuous energy spectrum emitted by bremsstrahlung interactions. The maximum amount of energy that can be emitted occurs when the muon directly strikes the nucleus and loses all of its kinetic energy, leading to the maximum frequency (f) of the emitted photon, and the shortest wavelength (λ), is:

$$E_{\gamma,\,\mathrm{max}} = hf_{\mathrm{max}} = \frac{hc}{\lambda_{\mathrm{min}}}. \tag{4.20}$$

where h is Planck's constant.

From Equation (4.10), the average energy loss due to bremsstrahlung can be written as an approximation in terms of the radiation length, X_0:

$$-\left\langle \frac{\mathrm{d}E}{\mathrm{d}X} \right\rangle \approx \frac{E}{X_0}, \tag{4.21}$$

where E is the muon's energy from Equation (4.10). Note that, with this approximation, the two definitions of critical energy given in Section 4.2.1 become equal. From Equation (4.21), bremsstrahlung radiation is proportional to the muon's energy and is inversely proportional to the radiation length. By Equation (4.19), then, the radiation length is, in turn, proportional to the square of the radiating particle's mass. This means that, as the particle mass increases, the radiation length increases (so the particle has to travel further before losing its energy), and the amount of energy lost via bremsstrahlung is less. Therefore, in comparing the energy loss of muons to electrons, the muon's radiation length is larger than that of an electron by a factor of

$$\left(\frac{m_\mu}{m_e}\right)^2 = 4.28 \times 10^4. \tag{4.22}$$

Because of this, bremsstrahlung for muons is suppressed compared to electrons, and so muons travel further than electrons before losing the same proportion of energy. For example, the radiation length of electrons in air is 37 gcm^{-2}, whereas it is 1.48×10^6 gcm^{-2} for muons [5]. It follows, then, that bremsstrahlung radiation in the atmosphere is completely negligible for muons (despite being crucial for electrons). However, as rock and water have higher average Z values and higher densities than air, energy losses due to bremsstrahlung in rock and water are still significant.

4.2.5 Photonuclear Interactions

Photonuclear interactions are the inelastic collisions of muons with atomic nuclei. In this type of interaction, a muon exchanges a virtual photon with an atomic nucleus which leads to hadronic production. This is shown in the Feynman diagram in Figure 4.5. This process is a combination of electromagnetic and quantum chromodynamic interactions. Because most interactions of this type occur in the low-Q^2 region, which is typically described in terms of the absorption by the nucleus of a photon, this process is termed "photonuclear."

There are multiple parameterisations available for photonuclear interactions, including those by L. B. Bezrukov and E. V. Bugaev in [100] and A. V. Butkevich and S. P. Mikhailov in [101]. One parameterisation that describes experimental data well over a large range of Q^2 is that of H. Abramowicz, E. M. Levin, A. Levy, and U. Maor (the "ALLM parameterisation") from [95, 102]. The differential cross-section is given as:

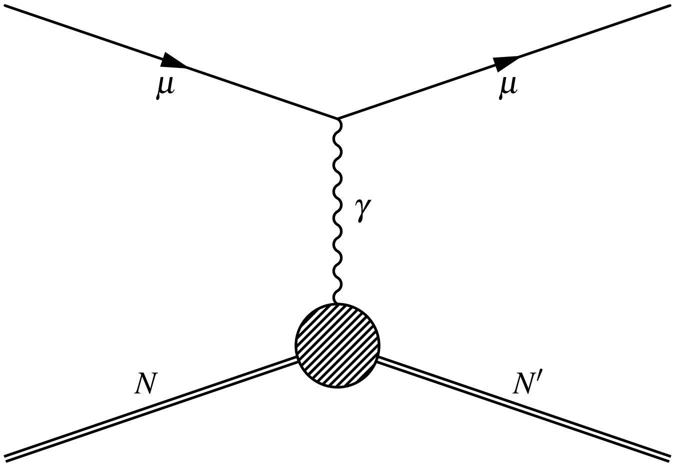

Figure 4.5: A Feynman of a photonuclear interaction in which a propagating muon exchanges a virtual photon with an atomic nucleus.

$$\frac{\mathrm{d}^2\sigma}{\mathrm{d}\nu\mathrm{d}Q^2} = \frac{4\pi\alpha^2}{Q^4}\frac{F_2}{\nu}\left(1-\nu-\frac{m_N x_{\mathrm{Bj}}\nu}{2E}+\left(1-\frac{2m_\mu^2}{Q^2}\right)\frac{\nu^2(1+4m_N^2x_{\mathrm{Bj}}^2/Q^2)}{2(1+R)}\right). \tag{4.23}$$

F_2 is the dimensionless proton structure function, which describes the distribution of parton momenta in the proton, $x_{\mathrm{Bj}} = Q^2/2m_N E\nu$ is a kinematic scale variable referred to as “Bjorken-x,” named after its discoverer J. D. Bjorken, which describes the invariance of F_2 to scale transformations at large Q^2, m_N is the mass of the nucleon, and R is the ratio of the transverse to longitudinal components of the cross-section. The ALLM parameterisation was first published in 1991 and was followed by an update in 1997. This update fit the 23 free parameters that make up the structure function to additional data, almost doubling the number of data points and decreasing the reduced χ^2 from 1.5 down to 0.97, resulting in the ALLM97 parameterisation in [103].

Despite describing experimental data well over a large range of Q^2, the uncertainties for photonuclear cross-sections are the largest out of any of the muon energy loss processes, reaching up to 10–20%, depending on the energy range, compared to the other interaction cross-sections, which are closer to 2–3% up to 10 TeV [95, 104]. This is because of the difficult nature of performing quantum chromodynamics (QCD) calculations, particularly in the non-perturbative low-Q^2 region, where not much experimental data is available.

4.3 Energy Loss Parameterisation

The average energy loss by muons in rock can be approximated by a simple yet highly useful parameterisation:

$$-\left\langle \frac{\mathrm{d}E}{\mathrm{d}X} \right\rangle = a(E) + b(E)E, \tag{4.24}$$

where $a(E)$ describes continuous energy losses from ionisation (Section 4.2.2), and $b(E)$ describes discrete energy losses from e^+e^- pair production (Section 4.2.3), bremsstrahlung (Section 4.2.4), and photonuclear processes (Section 4.2.5). $b(E)$ is given as the sum of coefficients for each process: $b(E) = b_{\text{pair}} + b_{\text{brems}} + b_{\text{photo}}$. With these definitions, the critical energy of muons, ε_μ, is the ratio of a to b:

$$\varepsilon_\mu = \frac{a}{b}. \tag{4.25}$$

Values for ε_μ and b for standard rock, as well as γ_μ, the spectral index for muons, were fit by P. Lipari and T. Stanev in [105], and by D. E. Groom, N. V. Mokhov, and S. I. Striganov in [93, 106], with values listed in [107]:

$$\text{Lipari}\begin{cases}\varepsilon_\mu = 618\ \text{GeV},\\ b = 0.383\ \text{km.w.e.}^{-1},\\ \gamma_\mu = 3.7.\end{cases} \qquad \text{Groom}\begin{cases}\varepsilon_\mu = 693\ \text{GeV},\\ b = 0.4\ \text{km.w.e.}^{-1},\\ \gamma_\mu = 3.77.\end{cases} \tag{4.26}$$

These values can be used to compute a number of physical values, such as the mean surface energy a muon needs to propagate a certain depth underground and the mean underground energy. As described, the tails of the distributions must be obtained via Monte Carlo simulations for precise results, and so Equation (4.26) is of limited use. However, although these parameters are not used directly in this work, they can still provide many convenient and useful comparisons that will be presented in Chapter 7.

5 Underground and Underwater Muons

5.1 Rare Event Searches

As previously stated, of all the particles produced in cosmic-ray air showers, muons are of particular interest because they are massive and long-lived. This means they can penetrate matter much more deeply than other types of particles, usually multiple kilometres, before decaying. This is important for rare-event searches like dark matter and neutrino experiments, because, as muons travel underground, they can interact with the rock to produce backgrounds that contaminate the detectors or have detection signatures that fall exactly within the range of the expected dark matter or neutrino signals. Detectors are typically installed in deep underground laboratories under mountains or in mines to shield from these muon-induced backgrounds, and they rely on accurate muon flux estimations in order to determine effective shielding strategies from them, especially in cases of future experiments, where background estimates from data are not yet available [108]. The importance of reducing cosmic-ray backgrounds motivates the expensive and effortful construction and operation of deep underground laboratories.

5.1.1 Muon-Induced Backgrounds

While muons themselves are often not a problem for rare event experiments, as they are easily identified by their charge and large energy and can be vetoed, the particles they produce — namely neutrons and the decay products of radioisotopes — are a problem. These background particles can be produced in a number of different ways, including quasi-elastic muon spallation, negative muon capture, electromagnetic showers, and photo-neutron production through virtual photon exchange [109].

Muon spallation involves a high-energy muon colliding with a nucleus and breaking the nucleus apart:

$$\mu + N \longrightarrow \mu + N' + X, \tag{5.1}$$

where N' and X can be any number of nuclei of smaller atomic number than the original N, including high-energy neutrons. In this way, high-energy cosmic ray muons can form neutrons as well as radioisotopes, which can both act as backgrounds to rare event experiments.

Negative muon capture is very similar to electron-induced inverse beta decay, where a negatively charged muon is captured by a proton and produces a neutron and a muon neutrino via the weak interaction:

$$\mu^- + p \longrightarrow \nu_\mu + n + \gamma. \tag{5.2}$$

It can be either radiative or non-radiative. The non-radiative process is shown by a Feynman diagram in Figure 5.1.

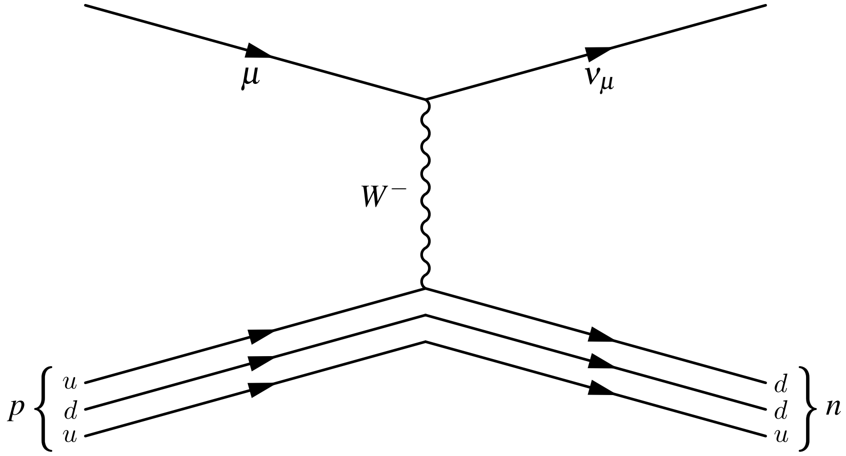

Figure 5.1: The Feynman diagram for negative muon capture.

In this process, a high-energy muon can cause the production of a free neutron, which can then propagate through the laboratory space and enter dark matter or neutrino detectors, causing the detectors to trigger.

5.1.2 Dark Matter Experiments

Although the existence of dark matter has been known for nearly a century by means of cosmological evidence, the exact nature of dark matter is still unknown. One of the most popular candidates for dark matter is the Weakly Interacting Massive Particle (WIMP), which is theorised to be a neutral non-baryonic particle beyond the current Standard Model. Because WIMPS, by definition, interact weakly with visible matter, they are difficult to detect. There are three main detection channels detectors use when searching for WIMPs, shown in Figure 5.2. They are interactions in particle colliders, direct detection, and indirect detection.

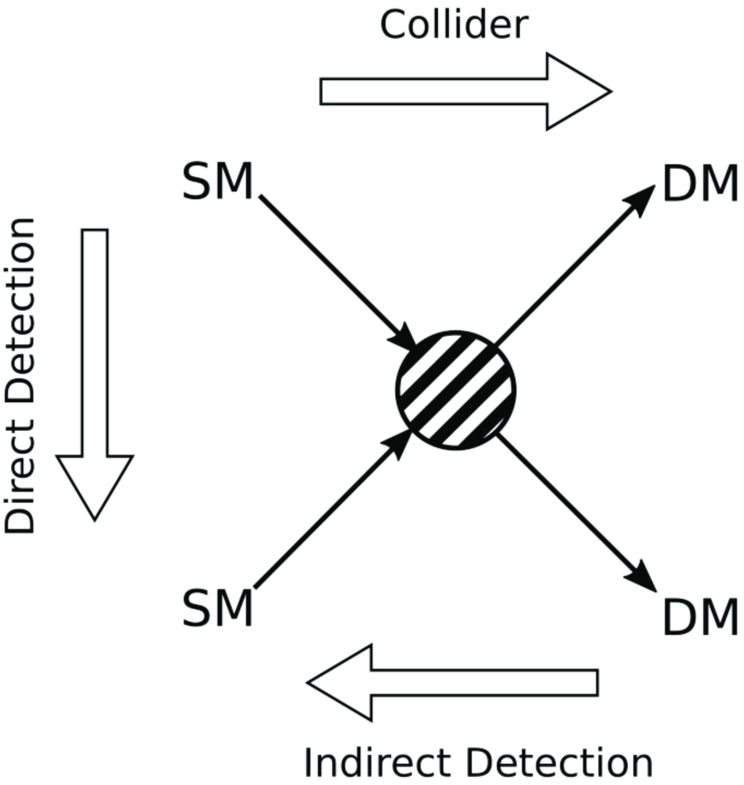

Figure 5.2: A Feynman diagram showing the possible channels for the detection of WIMPs (dark matter) interacting with Standard Model particles. The collider channel involves colliding two Standard Model particles to produce dark matter; the direct detection channel involves observing a dark matter particle interact directly with a Standard Model particle, as in a nuclear recoil [110]; and the indirect detection channel involves dark matter particles interacting with each other to produce Standard Model particles.

Any WIMP signal in a particle detector will be very low. To achieve an acceptable signal-to-noise ratio then, the noise must also be very low. Noise in this context comes from any particle that can create a signal similar to WIMPs in a dark matter detector, including charged and neutral particles of internal radioactive origins or external sources. Neutrons produced by cosmic-ray muons are one of the most important backgrounds in WIMP search experiments, because they can mimic the signature of WIMPs in nuclear recoils due to their similar properties: like WIMPS, neutrons are massive and electrically neutral. Muon-induced neutron backgrounds, therefore, are very important backgrounds to understand for the design and operation of dark matter experiments.

5.1.3 Neutrino Experiments

Muon-induced backgrounds are also crucial for neutrino experiments, such as astrophysical neutrino observatories or neutrinoless double beta decay ($0\nu\beta\beta$) experiments. $0\nu\beta\beta$ experiments aim to discover whether neutrinos are Dirac particles (meaning neutrinos, ν, and their antiparticles, $\overline{\nu}$, are distinct particles), or Majorana particles (meaning that neutrinos are their own antiparticles and $\nu \leftrightarrow \overline{\nu}$). They hope to do this by observing a rare event in which an unstable atomic nucleus decays by emission of two beta particles and no observable neutrino, because the neutrino will have annihilated with the antineutrino. A Feynman diagram for this process is shown in Figure 5.3.

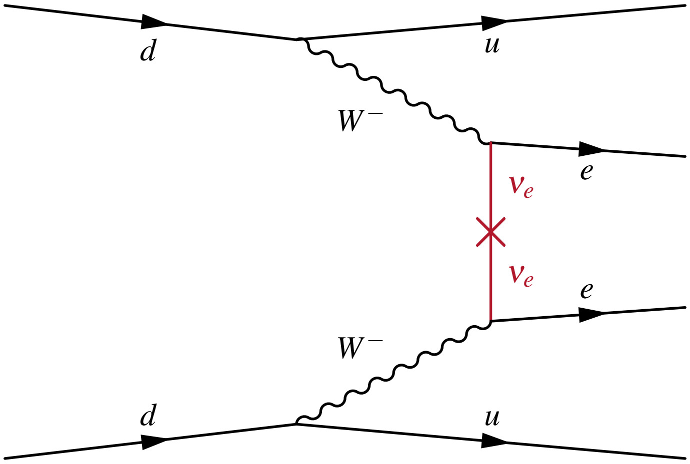

Figure 5.3: A Feynman diagram of neutrinoless double beta decay, showing the annihilation of the neutrinos and the emission of two beta particles (electrons).

The KamLAND-Zen [111] and the Enriched Xenon Observatory (EXO) [112], as well as its successor nEXO [113], along with the proposed DARWIN experiment [114], are experiments searching for $0\nu\beta\beta$ in the beta decay of xenon-136. A contaminant for this experiment is the beta decay of other xenon isotopes. Muons can produce neutrons that will collide with xenon atoms and create xenon isotopes like xenon-137, which can then decay into caesium via beta decay:

$$
\begin{aligned}
{}^{136}_{54}\mathrm{Xe} + \mathrm{n} \longrightarrow {}^{137}_{54}\,\mathrm{Xe}& \\
&\hookrightarrow {}^{137}_{55}\mathrm{Cs} + e^- + \gamma.
\end{aligned}
$$

This beta decay has a Q-value spectrum that overlaps with that of $0\nu\beta\beta$ [113, 114], and so the presence of xenon-137 as a muon-induced background must be mitigated. For this reason, knowledge of the muon spectrum underground around the detector is crucial for the success of the experiment.

5.2 Overview of Underground and Underwater Sites

Deep underground laboratories are laboratories located at least 1 km underground. There are multiple underground laboratories around the world, with reviews of current labs given in [115, 116, 117, 118]. They host a number of dark matter and neutrino experiments, as well as other types of experiments, such as those performing research in astrobiology and photonics [119]. There are also many experiments — mainly neutrino telescopes — located underwater in lakes, seas, or oceans, where they can make use of large volumes of materials that are dark yet optically transparent, so Cherenkov light from neutrino events can be easily detected.

The underground and underwater laboratories considered for this study are listed in Table 5.1 along with their locations, depths, and densities. KM3NeT is made up of multiple detectors placed in three different locations: KM3NeT-Fr (ORCA) off the coast of Toulon, France, KM3NeT-It (ARCA) off the coast of Sicily, Italy, and KM3NeT-Gr off the coast of Pylos, Greece. The site of ORCA is near the site of the ANTARES neutrino telescope, and the site of ARCA is near the site of the now-decommissioned NEMO neutrinoless double beta decay experiment [120, 121].[1]

The labs in Table 5.1 will be used for calculations throughout Chapters 7 and 8, and a short overview of some laboratories of note are given in this section. The locations of the labs in Table 5.1 are shown on a map in Figure 5.4 for reference.

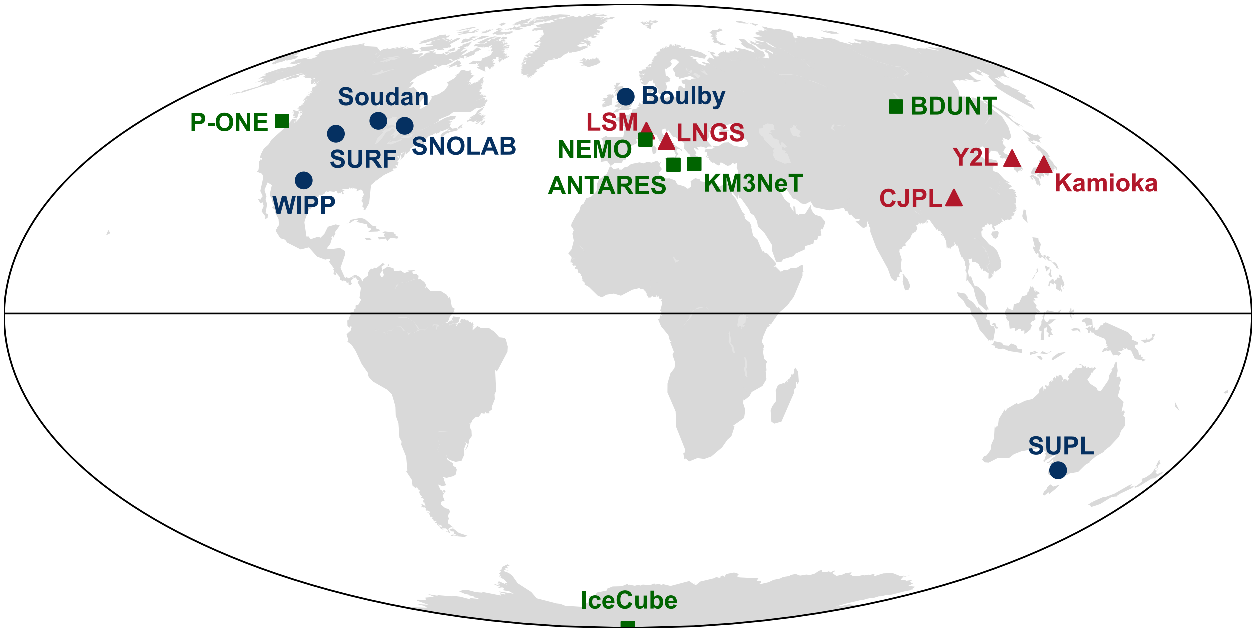

Figure 5.4: Locations of underground laboratories around the world. Those with flat overburdens are shown by blue circles, those under mountains are shown by red triangles, and those underwater (or under ice) are shown by green squares. For this work, there are 6 laboratories with flat overburdens, 5 under mountains, and 8 underwater or under ice, and there are 17 laboratories in the northern hemisphere, and 2 in the southern hemisphere.

To perform calculations for labs under mountains, additional information about the mountain profile is required. Maps in spherical coordinates of slant depth as a function of zenith and azimuthal angle, $X(\theta, \phi)$, produced either from satellite images or detector data, were obtained for each laboratory, and are shown in Figure 5.5.

---

[1] The NEMO experiment referred to here is the Neutrino Mediterranean Observatory (NEMO) located in the

Table 5.1: Summary of underground and underwater sites relevant for this work, their locations and coordinates, their depths, h, and their average rock densities, ρ. Depths remain undefined for laboratories under mountains. Depths are given as a range for some underwater detectors because they are made up of long strings that can reach over a kilometre in length. For underwater labs, although some variation is expected in the water density due to different minerals and salinity levels, the nominal density of sea water is assumed for each lab because information on the water's density at a lab's location is usually limited. There are a number of additional deep underground laboratories around the world given in Table A.1 in Appendix A that are not under consideration for the present study, but are still relevant for dark matter and neutrino experiments.

Laboratory	**Location**	**Coordinates (°)**	**Depth, h (km.w.e.)**	**Density, ρ (gcm^{-3})**
		Underground		
WIPP	U.S.	(32.372, -103.794)	$1.585^{+0.011}_{-0.006}$ [122]	2.3 ± 0.2 [122]
Y2L	S. Korea	(38.010, 128.543)	Mountain	2.7 [123]
Soudan	U.S.	(47.823, -92.237)	2.09 [124]	2.80 ± 0.05 [124]
Kamioka	Japan	(36.423, 137.315)	Mountain	2.70 ± 0.05 [125, 126]
Boulby	England	(54.553, -0.825)	2.805 ± 0.045 [127]	2.62 ± 0.03 [127]
SUPL	Australia	(-37.070, 142.810)	2.88 [128]	2.86 [129]
LNGS	Italy	(42.400, 13.500)	Mountain	2.72 ± 0.05 [130]
LSM	France	(45.179, 6.689)	Mountain	2.73 ± 0.01 [131]
SURF	U.S.	(44.353, -103.744)	4.26 [132]	2.86 ± 0.11 [132, 133]
SNOLAB	Canada	(46.472, -81.187)	6.065 ± 0.095 [89]	2.83 ± 0.05 [89]
CJPL	China	(28.153, 101.711)	Mountain	2.8 [134]
		Underwater		
BDUNT	Lake Baikal	(51.765, 104.415)	0.75–1.275 [135]	1.03975
AMANDA	South Pole	(-90.000, 0.000)	1.5–2.35 [136]	
IceCube	South Pole	(-90.000, 0.000)	1.5–2.5 [136]	
KM3NeT-Fr	Med. Sea	(42.800, 6.033)	2.475 [120]	
ANTARES	Med. Sea	(42.800, 6.167)	2.5 [137]	
P-ONE	Pac. Ocean	(47.763, -127.759)	2.66 [138]	
KM3NeT-Gr	Ionian Sea	(36.517, 21.983)	3.00–4.55 [139]	
KM3NeT-It	Med. Sea	(36.267, 16.100)	3.4 [120]	
NEMO	Med. Sea	(36.297, 15.083)	3.5 [140]	

Kamioka Observatory

The Kamioka Observatory is located at (36.423° N, 137.315° E) in a mine under the Ikeno mountain in the Kamioka region of Hida in the Gifu Prefecture of Japan. The laboratory is located at a depth of approximately 1000 m underground with an overburden made up of inishi rock, standard rock, and generic skarn, giving a rock density ranging from 2.65 gcm^{-3} to 2.75 gcm^{-3}. This gives

---

Mediterranean Sea, not the Neutrino Ettore Majorana Observatory (NEMO) located at LVD.

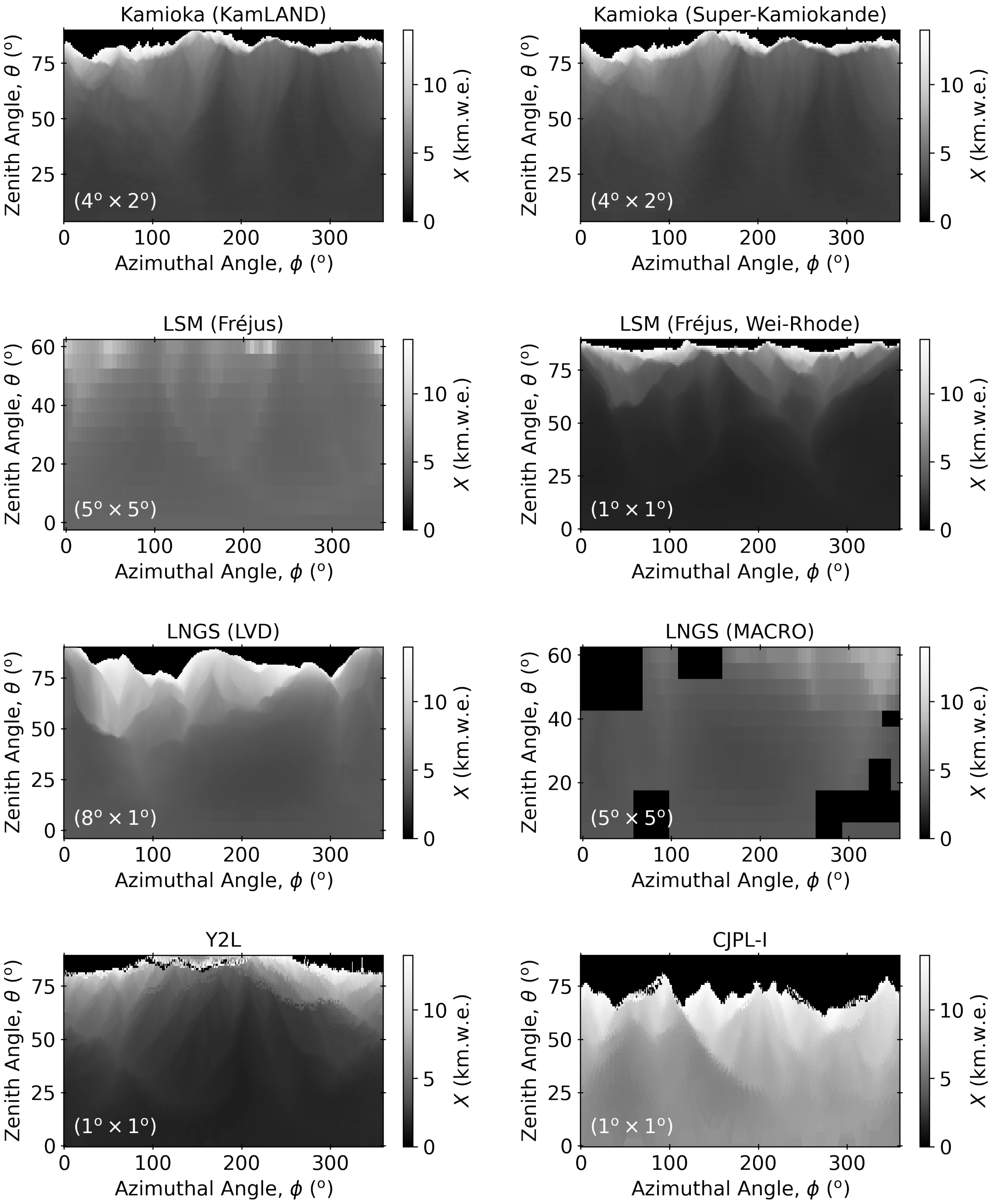

Figure 5.5: $X(\theta, \phi)$ plots of mountain maps received from KamLAND [125], Super-Kamiokande [125, 141], Fréjus [131], Y. Wei and W. Rhode [142], LVD [143], MACRO [144], Y2L, and CJPL-I [145]. The (θ, ϕ) resolution of each map is shown in the bottom left corner. The black rectangles in the MACRO map are masked bins for which the slant depth is not reported.

it an average coverage of approximately 2.7 km.w.e. [125]. It hosts several experiments, including KamLAND [125], Super-Kamiokande, and Hyper-Kamiokande [126].

A map of the laboratory is shown in Figure 5.6, with the locations of KamLAND and Super-Kamiokande indicated. Because these two experiments are located in different parts of the lab, with slightly different rock coverage, their muon flux will slightly differ. For this reason, two separate Kamioka maps were obtained: one centered on KamLAND [125], and one centered on Super-Kamiokande [125, 141]. The maps are very similar to each other, as seen in Figure 5.5, though lead to slightly different results because the detectors are in slightly different locations. Because both maps are available, results will be presented for KamLAND and Super-Kamiokande separately.

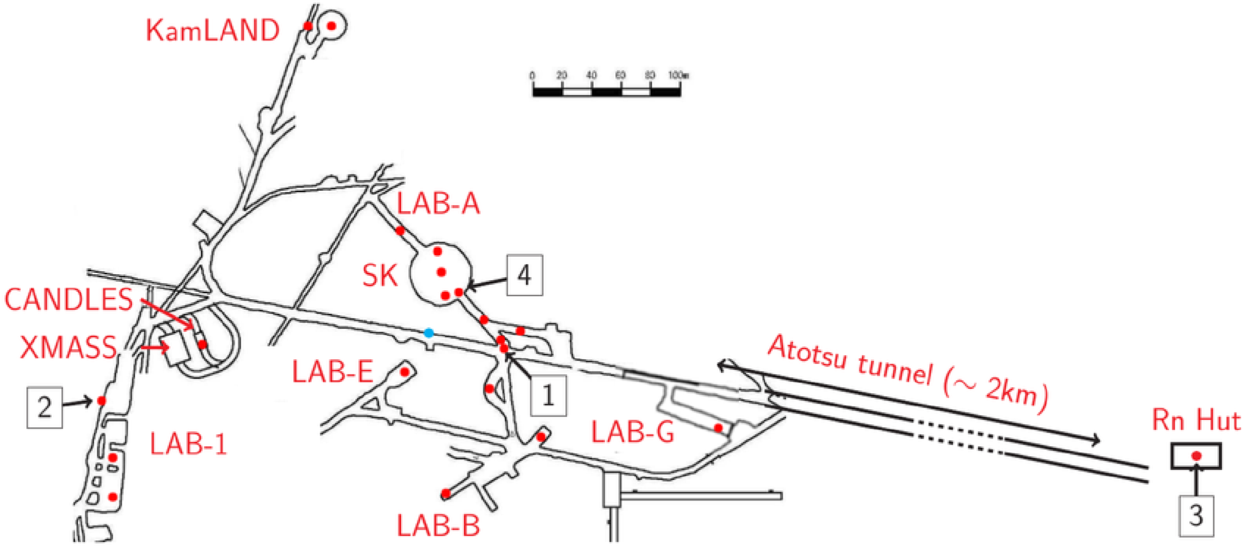

Figure 5.6: Map of the Kamioka labs from [146]. The location of KamLAND is shown at the top most part of the lab, and the location of Super-Kamiokande is shown as “SK” in LAB-A.

Stawell Underground Physics Laboratory

Stawell Underground Physics Laboratory (SUPL) is a new laboratory located in Stawell Gold Mines at (37.070° S, 142.810° E) in Stawell, Victoria, Australia, outside Melbourne. The lab is approximately 1 km underground, with an overburdened rock density of 2.86 gcm^{-3}, giving it 2.88 km.w.e. of coverage [128, 129]. SUPL is significant because it is the first deep underground laboratory in the southern hemisphere (with the exception of IceCube under ice at the South Pole). Construction began in 2019, and the laboratory opened in August 2022. The first experiment planned for SUPL is the Sodium iodide with Active Background REjection (SABRE) experiment, which will have twin detectors in LNGS and SUPL aiming to provide a model-independent test of the DAMA/LIBRA dark matter annual modulation results [128].

Laboratori Nazionali del Gran Sasso

The Gran Sasso National Laboratory (LNGS) is located at (42.400° N, 13.500° E) in a tunnel under the Gran Sasso mountain in Italy. The tunnel is at an average depth of a little over 1 km under the mountain, with an overburdened rock density of (2.72 ± 0.05) gcm^{-3} [130], resulting in an average coverage of 3.65 km.w.e. [107]. LNGS is the largest underground laboratory in the world, hosting several experiments located in three main halls, shown in Figure 5.7. The experiments mentioned in this work and their locations and statuses are summarised in Table 5.2. There are two available mountain profile maps for LNGS from the LVD and MACRO Collaborations, shown in Figure 5.5. Because the angular resolution and zenith angle range are poor for the MACRO map and it has significant masking of regions across all zenith and azimuthal angles, the LVD map is used for all calculations for LNGS in this work.

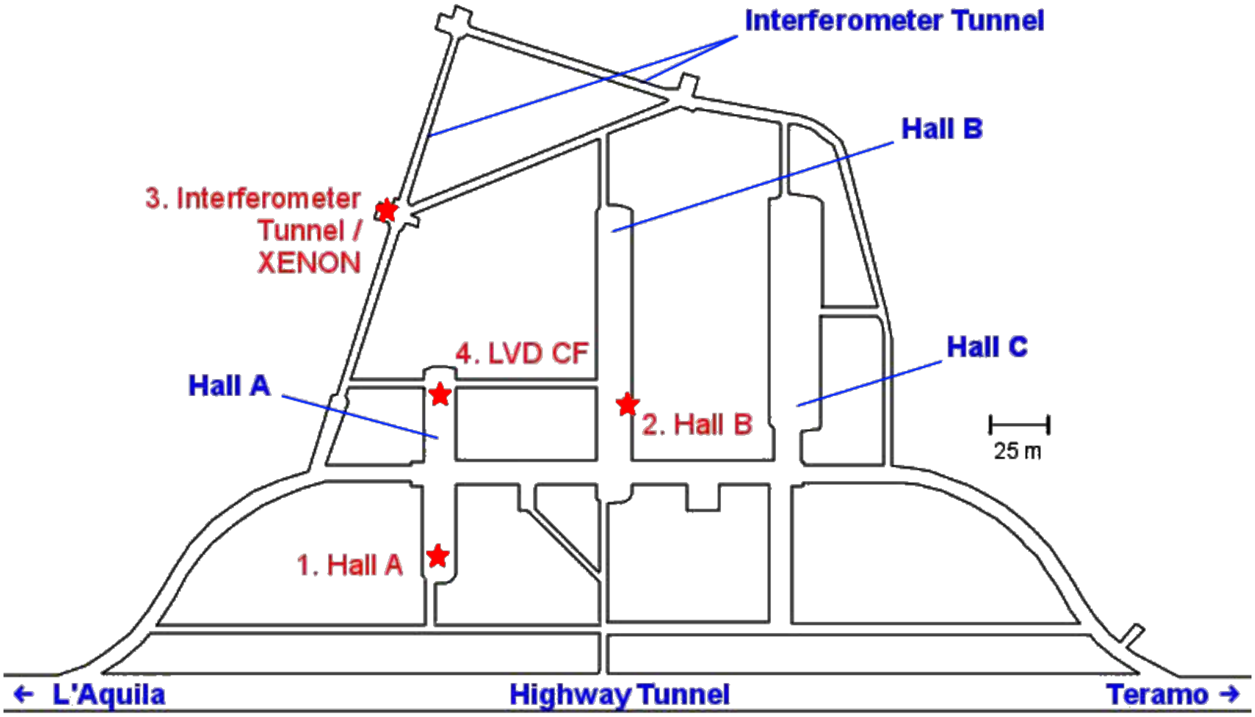

Figure 5.7: A map of LNGS showing the main halls that hold the experiments (Hall A, Hall B, and Hall C) from [147].

Table 5.2: A summary of the experiments mentioned in this work that are located at LNGS, including their location in the lab, their primary physics goals, and their statuses of being either actively running or retired and decommissioned.

Experiment	Hall	Primary Physics Goal	Status	Reference
LVD	A	Supernova Neutrinos	Running	[148]
GERDA	A	Neutrinoless Double Beta Decay	Decommissioned	[149]
GALLEX	A	Solar Neutrinos	Decommissioned	[150]
COSINUS	B	Direct Dark Matter	Running	[151]
CRESST	B	Direct Dark Matter	Running	[152]
DAMA/LIBRA	B	Direct Dark Matter	Running	[153]
MACRO	B	Magnetic Monopoles	Decommissioned	[144]
SABRE	C	Direct Dark Matter	Running	[128]
Borexino	C	Solar Neutrinos	Decommissioned	[154]
OPERA	C	Tau Neutrinos	Decommissioned	[155]

Laboratoire Souterrain de Modane

The Modane Underground Laboratory (LSM) is located at (45.179° N, 6.689° E) in the Fréjus Road Tunnel under the Col du Fréjus in the Cottian Alps between Modane, France and Bardonecchia, Italy. It is the deepest lab in Europe at an average depth of 1.7 km with a rock density of (2.73 ± 0.01) gcm^{-3}, providing an average coverage of 4.8 km.w.e. [131, 156]. It holds the EDELWEISS direct dark matter detection experiment [156] as well as the now-retired Fréjus nucleon decay experiment [131], amongst others. LSM is one of the only laboratories for which a complete description of the rock overburden including Sternheimer parameters exists, given in [131]. There are two available mountain maps from the Fréjus experiment, shown in Figure 5.5. Although the map from Y. Wei and W. Rhode ("Wei-Rhode map") has better resolution and a full zenith angle range compared to the Fréjus map from [131] which has a resolution of $(5^\circ \times 5^\circ)$ and only goes up to $\theta = 60^\circ$, the Wei-Rhode map seems to be less accurate, possibly due to mispositioning of the detector in the coordinate system, as suggested by comparisons between the angular distributions obtained from both maps compared to data. For this reason, the map from [131] is used for all LSM calculations.

SNOLAB

SNOLAB is located at (46.472° N, 81.187° W) in a nickle mine Sudbury, Ontario, Canada. It was first built in 1990 for the Sudbury Neutrino Observatory (SNO) solar neutrino experiment [89], and is one of the deepest laboratories in the world, being approximately 2 km deep, under dense norite rock that has an average density of 2.83 gcm^{-3}. It is stated in [89] that this gives SNOLAB a coverage of (5.890 ± 0.094) km.w.e. of rock. However, this value is in terms of SNO rock, and must be converted to standard rock for proper comparison with other laboratories. Using the empirical conversion formula given by Equation (4) in [89], this depth becomes (6.065 ± 0.095) km.w.e. The minimum depth in [89] is given in Table IV to be 6.225 km.w.e. of standard rock, rather than the value calculated here, which has a maximum of 6.160 km.w.e. The reason for this discrepancy is unknown, but may have implications for comparisons to the muon intensity and flux measurements for SNOLAB, which will be discussed in Section 8.2. (6.065 ± 0.095) km.w.e. is the value that has been used for all SNOLAB calculations in this work.

China Jinping Underground Laboratory

The China Jinping Underground Laboratory (CJPL) is located at (28.153° N, 101.711° E) under the Jinping mountain in Sichuan, China. The lab is 2400 m under the peak of the mountain, with an overburdened rock density of 2.8 gcm^{-3}, making it the deepest operating underground laboratory in the world at a maximum depth of 6.72 km.w.e. [145]. The lab holds the Jinping Neutrino Experiment (JNE) [145], amongst others, in its CJPL-I hall. Currently, the lab is expanding to a new CJPL-II hall, much larger and deeper than CJPL-I, which will also make it the largest deep underground laboratory in the world.

5.3 Current Methods

There are three main ways of performing calculations for underground and underwater muons, namely analytical calculations, depth-intensity parameterisations, and Monte Carlo programs. The latest comprehensive analyses of underground muon measurements were a theoretical calculation performed 25 years ago by E. V. Bugaev, et al. [3], and a parameterisation from 18 years ago by D.-M. Mei and A. Hime [107]. In the experimental dark matter and neutrino communities, the D.-M. Mei and A. Hime parameterisation of underground muon fluxes and angular distributions has long been a standard for simulating muon fluxes underground in particle transport codes like GEANT4 and MCNP. An overview of the existing methods in the literature will be given here.

5.3.1 Analytical Calculations

An early parameterisation specifically for underwater muons between the depths of 0.5 km.w.e. and 14 km.w.e. was given by A. Okada in [59]. It is based on the Miyake empirical formula described in Section 3.3.1 from [58], and is given by:

$$I^u(E^u, h, \theta) = \frac{c_1(e^{c_2 X} - c_3)^{\beta}}{(\cos(\theta))^{G_0(E^u, X)}} \frac{(1 + E^u/G_1(X))^{1-\beta}}{1 + E^u/G_2(X)}. \tag{5.3}$$

The parameters c_1, c_2, c_3, β, and the expressions for $G_0(E^u, X)$, $G_1(X)$, and $G_2(X)$ are given in [59].

The Bugaev analysis in [3] presents a theoretical calculation for muon fluxes underground and underwater. It uses inputs derived from data collected by the Intersecting Storage Rings (ISR) accelerator at CERN in the 1970s for conventional muon fluxes. The calculation provides a semi-analytical solution to the muon transport equations:

$$I^u(h) = \int_{E_{\text{th}}}^{\infty} D(E,h)\mathrm{d}E, \tag{5.4}$$

where $D(E,h)$ is a transport equation for muons through matter, defined by a chain of equations in [3]. For energies above 1 TeV, a semi-empirical parameterisation of data derived by S. I. Nikolsky, J. N. Stamenov, and S. Z. Ushev in 1984 in [157]. The analysis presents comparisons with multiple data sets at various depths underground and sees good agreement at all depths. A. A. Lagutin and A. V. Yushkov attribute this agreement to the surface muon spectrum at TeV energies in [158]. However, given the quality and age of the data and analysis, the prediction must be accompanied by modelling uncertainties that have not been estimated by [3].

Although calculations like these can describe the data well, their biggest limitation is that they lack rigorous treatments of the uncertainties, and so it is difficult to do proper comparisons between these calculations and experimental data or other methods.

5.3.2 Depth-Intensity Relations

For practical applications, the muon intensity at a certain depth underground is often calculated using a parametric model, termed a Depth-Intensity Relation (DIR). Groom, et al. [107] give the following DIR for depth ranges between 1 and 10 km.w.e.:

$$I^u(h) = I_1 e^{(-h/\lambda_1)} + I_2 e^{(-h/\lambda_2)}, \tag{5.5}$$

where h is the vertical depth of the lab, and $I_1 = (8.60 \pm 0.53) \times 10^{-6}$ cm^{-2}s^{-1}sr^{-1}, $I_2 = (0.44 \pm 0.06) \times 10^{-6}$, $\lambda_1 = (0.45 \pm 0.01)$ km.w.e., and $\lambda_2 = (0.87 \pm 0.02)$ km.w.e. are determined by fitting to experimental data. With this fit function, [107] achieve a fit within approximately 3% of the data across the full range of depths. This is similar in form to the parameterisation used by M. Crouch in the “Crouch World Survey” from [159]:

$$I^u(h) = e^{(A_1 + A_2 h)} + e^{(A_3 + A_4 h)} + A_5, \tag{5.6}$$

where $A_1 = (-11.22 \pm 0.17)$, $A_2 = (-0.00262 \pm 0.00013)$ km.w.e.$^{-1}$, $A_3 = (-14.10 \pm 0.14)$, and $A_4 = (-0.001213 \pm 0.000021)$ km.w.e.$^{-1}$ are fit parameters, and A_5 is an additional constant term for neutrino-induced muons.

The two exponential terms in Equations (5.5) and (5.6) correspond to the two terms in Equation (4.24). This is clear if the equation is written $I^u(h) = A + B$ and the two terms are plotted separately, as in Figure 5.8. Because of the visible bend in the intensity curve when plotted with a logarithmic y-axis, the data cannot be fit exactly using only one exponential. From the plot, the red line contributes most at lower slant depths. It is low-energy muons that dominate the intensity at low slant depths, and at low energies, muons are most likely to lose energy via ionisation. Therefore, the red line, and so the I_1 term in Equation (5.5), corresponds to the $a(E)$ term in Equation (4.24). Similarly, the blue line contributes most at higher slant depths. It is high-energy muons that dominate the intensity at high slant depths, and at high energies, muons are most likely to lose energy via pair production. Therefore, the blue line, and so the I_2 term in Equation (5.5), corresponds to the $b(E)$ term in Equation (4.24).

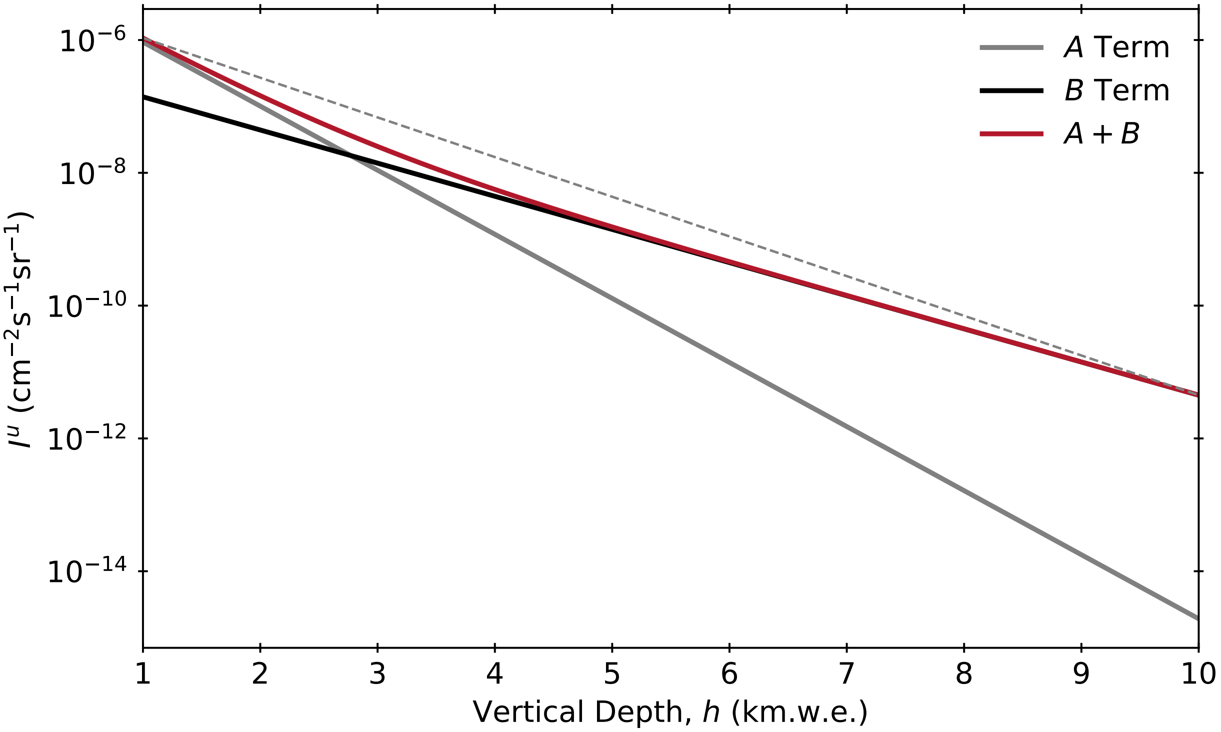

Figure 5.8: The two terms of Equation (5.5) plotted separately, along with their sum, giving the full DIR of [107]. A grey dashed line is included to emphasise the curvature of the red intensity curve. The two terms cover two separate energy ranges of muon energy loss.

Comparatively, the Fréjus [131], MACRO [144, 160], LVD [143], and SNO [89] Collaborations give the following three-parameter single-exponential relation:

$$I^u(h) = A\left(\frac{h_0}{h}\right)^{\alpha} e^{-h/h_0}, \tag{5.7}$$

where A, h_0, and α are fit from data (α is fixed to 2 in the Fréjus parameterisation). Here, the power term multiplying the exponential accounts for energy loss due to ionisation in the shallow-X depths. This is similar to an early depth-intensity relation that was proposed by S. Miyake in 1963 in [161] for the vertical intensity:

$$I_v^u(h) = \frac{K}{h+H}(h+a)^{-\alpha}e^{-\beta h}. \tag{5.8}$$

The values of H, K, a, α, and β were fit to data obtained from experiments at the Kolar Gold Fields (KGF) Mine and are given in [161].

Parametric fits can provide good estimates for underground labs, as demonstrated in [107]. However, because the fits are done to vertical-equivalent underground intensity data, which is known to be a poor approximation to the true vertical intensity at high zenith angles (see Section 7.1.2 and [1]), they introduce unnecessary systematic errors. Another downside is that, because they are fit to entire data sets at a time, they are influenced heavily by the large statistical errors on measurements at deep depths where the muon flux is low. Lastly, they are also limited in the sense that they cannot provide additional physical information about the muons underground, such as their energy and angular distributions, and entirely separate parameterisations are needed to calculate those quantities. Therefore, while the previous methods have sufficed for some simulations and analyses, there is room for improvement for more in-depth studies into underground muons and their physics implications, which has been the motivation behind this thesis.

5.3.3 Muon Propagation Programs

There are many general particle transport codes and toolkits that can propagate muons, the most popular being GEANT4 [162], FLUKA [64, 65], MCNP [163], MARS [164], and PHITS [165]. However, a small number of dedicated muon propagation programs have been developed over the past few decades as well. Reviews of and comparisons between some of the codes can be found in, for example, [166, 167]. The list below gives a summary of those that have been most widely used:

- **PROPMU:** The PROPMU code is a Monte Carlo algorithm written in Fortran that was developed by P. Lipari and T. Stanev in 1991 [105] for the propagation of muons through rock.
- **MUM:** The MUons + Medium (MUM) code was developed by I. A. Sokalski, E. V. Bugaev, and S. I. Klimushin in 2001 [166]. This is based on the analytical calculations of E. V. Bugaev in [3] mentioned in Section 5.3.1 and is a one-dimensional algorithm for muon transport.
- **MMC:** The Muon Monte Carlo (MMC) program was developed by D. Chirkin and W. Rhode in 2004 [168]. It is a C++ code that was originally made for the AMANDA experiment, and

is the precursor to the PRopagator with Optimal Precision and Optimised Speed for All Leptons (PROPOSAL) code developed for IceCube (see Section 6.4) [95].

- **MUPAGE:** The MUon GEnerator from PArametric formulas (MUPAGE) code was developed by G. Carminati, A. Margiotta, M. Spurio in 2008 [169]. It is based on parametric formulas given in [170] for single and multiple muons, which matches the Okada parameterisation from [59] to within 1%. It is a C++ code written specifically for underwater neutrino telescopes (and therefore does not provide calculations for underground labs) with a maximum depth of 5 km.w.e.
- **MUSIC and MUSUN:** The MUon SImulation Code (MUSIC) and the MUon Simulations UNderground (MUSUN) programs were developed by P. Antonioli, et al. in 1997 [171] and V. Kudryavtsev in 2008 [172] respectively. MUSIC provides muon energy spectra and angular distributions underground (under either flat earth or mountains) and underwater, which can be used as input into MUSUN to simulate muons in or around laboratories. Although MUSIC and MUSUN are flexible codes, there are disadvantages. The muon spectrum at the surface is defined in MUSIC using either a modified Gaisser parameterisation based on Equation (3.24) for shallow depths or the LVD parameterisation from Equation (5.7) for deep depths. Moreover, it is written in Fortran, and is not open-source or publicly available, and therefore is difficult to access.

While the program presented in this work is not the first of its kind, the motivation behind its development is the improvement on previous programs, which are sufficient for some studies of underground and underwater muons but leave room for improvement. In particular, previous muon propagation programs rely heavily on limited parameterisations described in Sections 3.3.1 and 5.3.2, and have lacked characterisation of the systematic uncertainties of their results in most cases. In this way, they give only partial descriptions of the muons they simulate and are not easily adaptable to new models and methods. These are limitations which the MUon inTensity codE (MUTE) was developed to overcome.

6 MUTE

This thesis presents a program written over the course of four years to calculate muon fluxes and intensities underground and underwater called MUTE (MUon inTensity codE) [1, 173]. This chapter will discuss the development of MUTE with a focus on the technical details before presenting and discussing the physical results that are obtained with MUTE in Chapters 7 and 8. The main variables of interest for the next three chapters are listed in Table 6.1.

Table 6.1: Summary of symbols used for the main variables and surface and underground physical observables in Chapters 6 to 8 with their definitions. A superscript s will be used to denote that the quantity is measured at the surface of the Earth, and a superscript u will be used to denote that the quantity is measured underground or underwater. Because all quantities in these chapters will be referring to muons, the μ subscript on all symbols will now be dropped.

	Symbol	**Definition**	**Units**
Variables	E	Energy	[MeV]
	X	Slant depth	[km.w.e.]
	θ	Zenith angle	[°]
	ϕ	Azimuthal angle	[°]
Observables	Φ	Flux	[$\text{cm}^{-2}\text{s}^{-1}\text{sr}^{-1}\text{MeV}^{-1}$]
	I	Intensity	[$\text{cm}^{-2}\text{s}^{-1}\text{sr}^{-1}$]
	Φ_{Ω}	Energy Spectrum	[$\text{cm}^{-2}\text{s}^{-1}\text{MeV}^{-1}$]
	Φ_{θ}	Azimuthal Angular Distribution	[$\text{cm}^{-2}\text{s}^{-1}\text{rad}^{-1}$]
	Φ_{ϕ}	Zenith Angular Distribution	[$\text{cm}^{-2}\text{s}^{-1}$]
	Φ_{tot}	Total flux	[$\text{cm}^{-2}\text{s}^{-1}$]

6.1 Development of MUTE

Development of MUTE began in 2019, with the first official release of v1.0.0 on 19 December 2021 [174]. The release of v2.0.0 on 15 July 2022 [173] expanded the scope of MUTE to include calculations for laboratories under mountains, and the release of v3.0.0 will see the interfacing of MUTE with DAEMONFLUX as well as the introduction of functions to calculate muon energy and angular spectra underground, a function to calculate equivalent vertical depths for mountains, and the ability to set Z and A values for specific rock types. MUTE is written in Python and is offered as an open-source code under a BSD-3-Clause license on GitHub at `https://github.com/wjwoodley/mute`.

6.1.1 Goals

The goal of MUTE was to write a program that could calculate muon fluxes underground and underwater with high precision and efficiency. After testing the feasibility of the code to produce good preliminary results, there were several objectives that were set for the final product, namely that it should be:

- **Complete:** It should be able to give a complete definition of the muon spectrum underground in physical units with uncertainties based on physical models.
- **Data-Independent:** It should be able to make forward predictions without needing to fit to already-existing underground or underwater data.
- **Precise:** It should give errors on muon fluxes that are smaller than current muon propagation programs.
- **Flexible:** It should allow the user to change several models and parameters (for current as well as future models that have not been developed yet), including:
    - The primary cosmic ray flux model.
    - The hadronic interaction model.
    - The atmospheric density model (including coordinates and month).
    - The propagation medium.
    - The propagation density.
    - The overburden geometry.
- **Efficient:** It should be fast enough to provide results in a reasonable amount of time and should be able to perform the propagation of muons quickly, if required.
- **Easy:** It should be written in a popular language (Python), and the interface should be easy to use.
- **Accessible:** It should be practically accessible to the scientific community, meaning it should be open-source with a license that will allow others to perpetually modify it and improve upon it.

6.1.2 Overview of the Program

In general, the algorithm in MUTE separates the calculations of underground (or underwater) muon fluxes into three steps: surface calculations, muon propagation, and underground (or underwater) calculations. The first step calculates surface fluxes using Matrix Cascade EQuation (MCEQ) [40, 175] or DAta-drivEn MuOn-calibrated atmospheric Neutrino Flux (DAEMONFLUX) [80], and the second step calculates surface-to-underground transfer tensors using PRopagator with Optimal Precision and Optimised Speed for All Leptons (PROPOSAL) [95]. In both cases, rather than interacting with them directly, the user accesses MCEQ and PROPOSAL through the MUTE interface.

MUTE is made up of four modules that keep track of the constants and take care of the three steps of the calculations: `constants`, `surface`, `propagation`, and `underground`. These are abbreviated in MUTE documentation as `mtc`, `mts`, `mtp`, and `mtu` respectively. The relationships between these modules are shown in Figure 6.1.

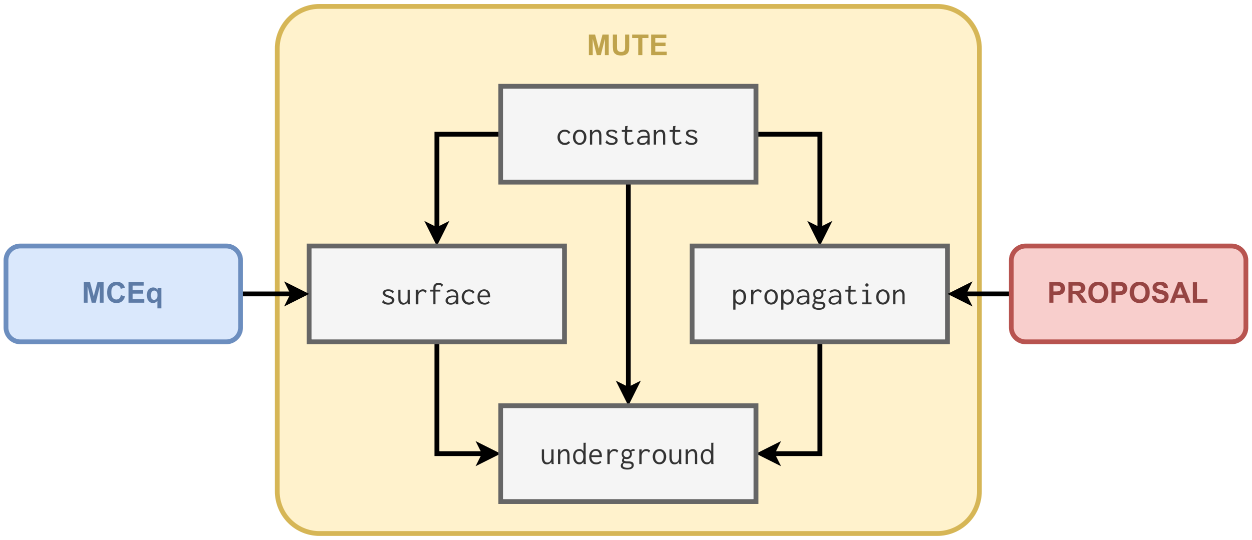

Figure 6.1: A flowchart of the four modules of the MUTE code and their relationships to each other and MCEQ and PROPOSAL. The `constants` module is used by all three of the other modules, and the `underground` module uses all three other modules.

The main functions in MUTE are calculation functions, which compute a number of physical observables at the surface and underground or underwater. These are listed by module in Table 6.2. The units used for each physical observable are also given in Table 6.2. The default units throughout all of MUTE are [MeV] for energies, [km.w.e.] for distances, and degrees for angles (but radians and steradians for output). In addition to the calculation functions, there are also load functions, with which the user can load in results from MUTE output files. The relationship between the different functions is summarised by the flowchart in Figure 6.2.

Table 6.2: The calculation functions available in each of the three main modules of MUTE and what they return. The name of the `mtp.calc_survival_probability_tensor()` function has been abbreviated to `mtp.calc_sp_tensor()`. Symbol definitions are given in Table 6.1.

Calculation Function	**Returned Observable**	**Returned Observable Units**
	`surface`	
`mts.calc_s_fluxes()`	$\Phi^s(E^s,\theta)$	$[\mathrm{cm}^{-2}\mathrm{s}^{-1}\mathrm{sr}^{-1}\mathrm{MeV}^{-1}]$
`mts.calc_s_intensities()`	$I^s(\theta)$	$[\mathrm{cm}^{-2}\mathrm{s}^{-1}\mathrm{sr}^{-1}]$
`mts.calc_s_e_spect()`	$\Phi^s_\Omega(E^s)$	$[\mathrm{cm}^{-2}\mathrm{s}^{-1}\mathrm{MeV}^{-1}]$
`mts.calc_s_tot_flux()`	Φ^s_{tot}	$[\mathrm{cm}^{-2}\mathrm{s}^{-1}]$
	`propagation`	
`mtp.propagate_muons()`	E^u	[MeV]
`mtp.calc_sp_tensor()`	$U(E^s,E^u,X)$	$[\mathrm{MeV}^{-2}\mathrm{km.w.e.}^{-1}]$
	`underground`	
`mtu.calc_u_fluxes()`	$\Phi^u(E^u,X,\theta)$	$[\mathrm{cm}^{-2}\mathrm{s}^{-1}\mathrm{sr}^{-1}\mathrm{MeV}^{-1}\mathrm{km.w.e.}^{-1}]$
`mtu.calc_u_intensities()`	$I^u(\theta)$	$[\mathrm{cm}^{-2}\mathrm{s}^{-1}\mathrm{sr}^{-1}]$
	$I^u(\theta,\phi)$	$[\mathrm{cm}^{-2}\mathrm{s}^{-1}\mathrm{sr}^{-1}]$
`mtu.calc_u_e_spect()`	$\Phi^u_\Omega(E^u)$	$[\mathrm{cm}^{-2}\mathrm{s}^{-1}\mathrm{MeV}^{-1}]$
`mtu.calc_u_ang_spect()`	$\Phi^u_\phi(\theta)$	$[\mathrm{cm}^{-2}\mathrm{s}^{-1}]$
	$\Phi^u_\theta(\phi)$	$[\mathrm{cm}^{-2}\mathrm{s}^{-1}\mathrm{rad}^{-1}]$
`mtu.calc_u_tot_flux()`	Φ^u_{tot}	$[\mathrm{cm}^{-2}\mathrm{s}^{-1}]$

6.2 Constants

The code is written in order to be flexible for the end user, and, as such, has a number of local and global variables that can be set by the user. The local constants are function parameters that can be used to change, for example, the atmospheric models or set an energy threshold, whereas the global constants are held in the `constants` module. This module is made up of a number of static grid definitions for the independent variables of MUTE (mainly energy, slant depth, and zenith angle), as well as user-set constants and basic functions that maintain the variable and unit checks when the code is running.

The following are the grid constants defined in MUTE that are used throughout all calculations:

- **`mtc.ENERGIES`:** A constant grid of 91 log-spaced energies in [MeV] used throughout all MUTE modules and functions. This energy grid is derived from that used by MCEQ, with a cut off at approximately 89 PeV. This cut was chosen because higher energies greatly increase the computation time for the Monte Carlo simulations in PROPOSAL, and cutting energies above 89 PeV resulted in a change of less than 5% in the results because surface fluxes at

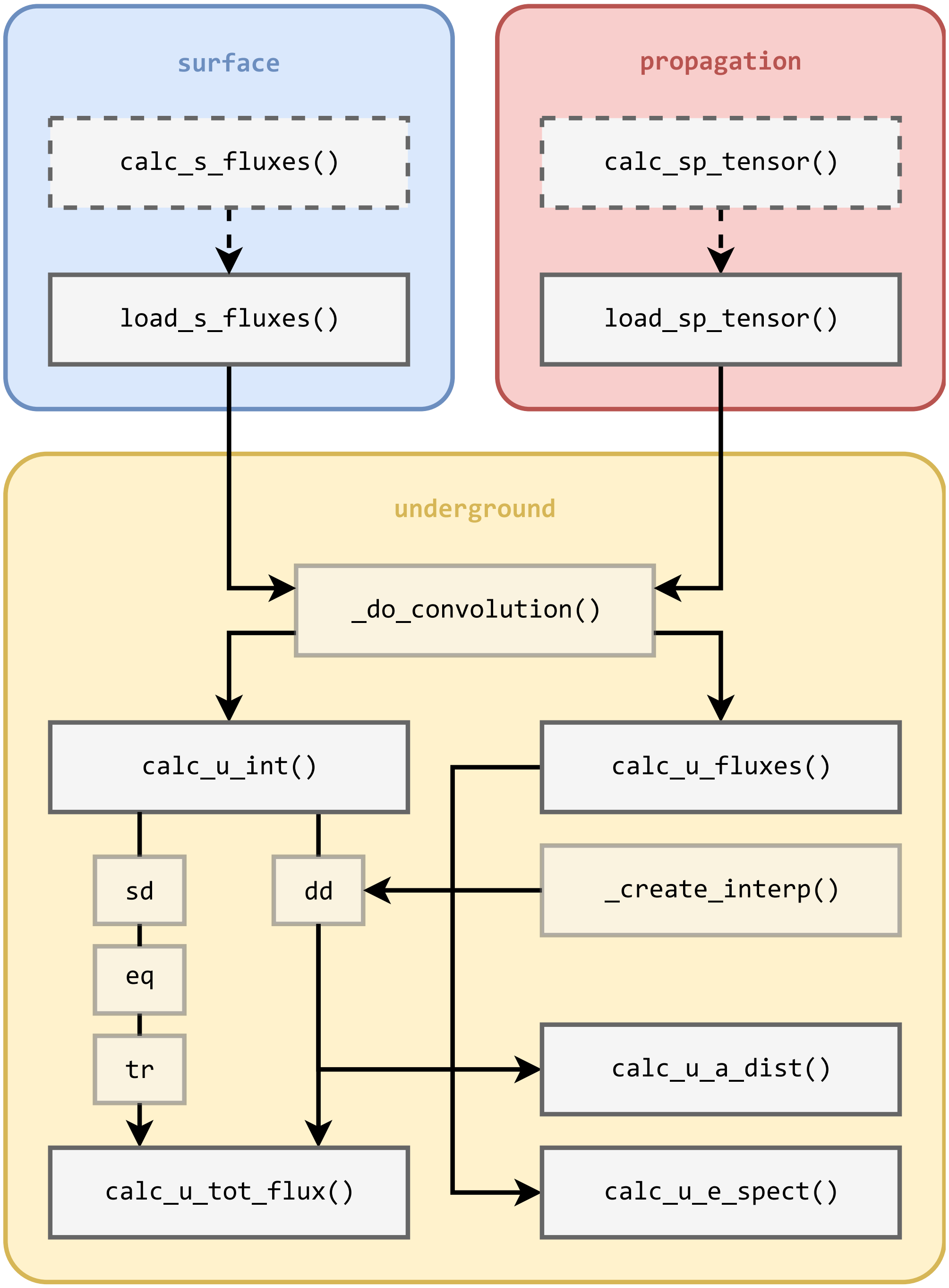

Figure 6.2: A flowchart of the main functions used in MUTE (with abbreviated function names). Those with dashed borders are not necessarily called, as `mts.load_s_fluxes_from_file()` and `mtp.load_survival_probability_tensor_from_file()` will only call them if files corresponding to the requested matrices cannot be found (and will not be called at all if the `s_fluxes` and/or `survival_probability_tensor` parameters are set in any of the `underground` functions). Translucent functions are those hidden from the user. All three modules are constantly interacting with the `constants` module, as shown in Figure 6.1.

this energy range and above are so small ($< 10^{-31}$ cm^{-2}s^{-1}sr^{-1}MeV^{-1}) and contribute so little to the overall flux.

- **`mtc._SLANT_DEPTHS`:** A constant grid of 28 linearly-spaced slant depths in [km.w.e.] used in the propagation of muons in the Monte Carlo. The initial convolution calculation in the `underground` module uses this grid, then later functions interpolate to the values in `mtc.slant_depths`. The grid consists of depths starting at 0.5 km.w.e. and going up to 14 km.w.e. in steps of 0.5 km.w.e. This resolution in slant depth is enough to give a smooth interpolation between grid depths when calculating underground variables at off-grid depths.
- **`mtc._ANGLES`:** A constant grid of 28 zenith angles in degrees that directly correspond to the slant depths in `mtc._SLANT_DEPTHS`. These are only used for labs under flat overburdens.
- **`mtc.slant_depths`:** An array of slant depths based on the values in `mtc._SLANT_DEPTHS` but adjusted according to the user-set vertical depth. These are only used for labs under flat overburdens; for labs under mountains, users use an `mtc.mountain.slant_depths` matrix that contains values of $X(\theta,\phi)$.
- **`mtc.angles`:** An array of zenith angles that directly correspond to the slant depths in `mtc.slant_depths`. These are only used for labs under flat overburdens.
- **`mtc.ANGLES_FOR_S_FLUXES`:** A constant grid of 20 linearly-spaced zenith angles in degrees that are used only for the calculation of surface fluxes. Because interpolations are done to the surface fluxes using these angles in order to calculate the underground fluxes, the angles in `mtc._ANGLES` are not suitable because their values are governed by the linear spacing of the slant depths, which results in $1/\cos(\theta)$ spacing for the zenith angles. This means the first value in `mtc._ANGLES` is 0°, but the second is 60°, because the slant depths go from 0.5 km.w.e. to 1.0 km.w.e. This $1/\cos(\theta)$ spacing is ill-suited for a smooth interpolation, and so a separate variable is used for linearly spaced zenith angles.

MUTE follows PEP8 naming styles from [176] in that variables that are written in all uppercase letters with underscores between words are constants, and are not meant to be changed by the user (but can be accessed by the user), such as `mtc.ANGLES_FOR_S_FLUXES`. Single underscores at the beginning of variable names are used as internal use indicators, meaning the user should not access these variables, as with the static `mtc._SLANT_DEPTHS` (where users are expected to use — but not change — the dynamic `mtc.slant_depths` variable instead).

In addition to the grid constants, the `constants` module also holds the global user-set constants, which are listed in Listing 6.1.

Listing 6.1: The global constants that can be set in MUTE with the `mute.constants` module, their default values, and their descriptions.

```python
import mute.constants as mtc

mtc.set_verbose(2)              # Verbosity of the calculation steps
mtc.set_output(True)            # Whether output is written to files
mtc.set_directory("mute/data")  # The directory data files are stored in
mtc.set_lab("Default")          # The name of the lab for output files
mtc.set_medium("rock")          # The propagation medium
mtc.set_reference_density(2.65) # The density of the propagation medium
mtc.set_n_muon(1000000)         # The Monte Carlo statistics level
mtc.set_overburden("flat")      # The type of overburden geometry
mtc.set_vertical_depth(0.5)     # The depth of a lab for flat overburdens
```

These global constants can be sorted into three categories: those related to output, those related to propagation, and those related to underground calculations.

Output Global Constants

Below is an explanation of those related to output.

- **`set_verbose()`:** There are three available verbosity levels: `0` prints nothing to the terminal or notebook; `1` prints `tqdm` progress bars for the calculation of surface fluxes or the propagation of muons; `2` prints all information about what has been loaded, what calculations have started, what calculations have finished, and where any output is stored.

- **`set_output()`:** The user can choose whether to have any output from the calculation functions written to a file or not. Local parameters are also available in each individual calculation function, but the default values for each local parameter are drawn from this global constant.

- **`set_directory()`:** The user can specify a directory to load files from (for all of the “load” functions in the `surface`, `propagation`, and `underground` modules) and to write output files to. The default directory is the `data` directory that is located wherever MUTE is installed.

- **`set_lab()`:** Multiple output files can be stored for any calculated underground variable, and they can be distinguished between by setting the lab, which is included in the name of the output file. The purpose of this is to provide a way to ensure multiple output files (for different vertical depths or different reference densities, for example) are not involuntarily overwritten. However, this will likely be replaced by a more sophisticated method of organisation in a theoretical future major release of MUTE.

Propagation Global Constants

Below is an explanation of the global constants related to propagation.

- **`set_medium()`:** The available media in MUTE are `["rock", "water", "sea_water", "ice", "air"]`. When MUTE is installed and imported for the first time (or the data directory is changed), pre-computed transfer tensors are supplied for standard rock ($\rho = 2.65$ gcm^{-3}), fresh water ($\rho = 0.997$ gcm^{-3}), and sea water ("ANTARES water"; $\rho = 1.03975$ gcm^{-3}; see Section 6.4.2) with 10^6 muons per bin. Although `"ice"` and `"air"` are available as options as well, they are not prioritised in MUTE.

- **`set_reference_density()`:** The reference density corresponds to the set medium and is used to locate which transfer tensor to load whenever a calculation is done in MUTE. This is named in contrast to a scale density parameter available in the `mtc.load_mountain()` function. Changing the reference density from 2.65 gcm^{-3} for rock, 0.997 gcm^{-3} for fresh water, or 1.03975 gcm^{-3} for sea water to anything else will prompt (or trigger, if any local `force` parameters are set to `True`) the calculation of new transfer tensors with PROPOSAL in the `mtp.calc_survival_probability_tensor()` function.

- **`set_n_muon()`:** This function sets the number of muons to be propagated per surface energy-zenith angle bin in the PROPOSAL Monte Carlo ran by the `mtp.propagate_muons()` function. The default value is 10^6 in order to give a level of statistics such that the pre-computed transfer tensors are smooth and there is negligible statistical uncertainty in the results. This value is used to locate and identify files containing underground energies and survival probability tensors when calling the calculate and load functions.

Underground Calculation Global Constants

Lastly, below is an explanation of the global constants related to underground calculations.

- **`set_overburden()`:** Since v2.0.0, MUTE can be ran in two modes for the two cases of overburden type — flat or mountain — which is set with the `mtc.set_overburden()` setter function. If the overburden type is set to `"flat"`, the user will have access to the `mtc.set_vertical_depth()` function, with which the vertical depth of the lab in [km.w.e.] can be set. If the overburden type is set to `"mountain"`, the user will have access to the `mtc.load_mountain()` function, with which the mountain profile file can be loaded. This function will then read the file and create the `mtc.mountain.zenith`, `mtc.mountain.azimuthal`, and `mtc.mountain.slant_depths` arrays in the `mountain` namedtuple, which hold, respectively, the θ, ϕ, and X variables that are used throughout the calculations of the underground fluxes and intensities.

- **`set_vertical_depth()`:** The vertical depth can be set to any value between 0.5 km.w.e. and 14 km.w.e., which are the minimum and maximum possible slant depths available in MUTE calculations, independent of overburden type. If a vertical depth is set outside this range, the function will throw an error. The user has the option to set vertical depths below 0.5 km.w.e. by first setting `mtc.shallow_extrapolation = True`, but this raises a warning and is not recommended, as the results are not guaranteed to be stable or precise. When the vertical depth is set, the slant depths and zenith angles held in `mtc.slant_depths` and `mtc.angles` are automatically adjusted. The slant depth array is sliced at the user-set vertical depth, which is then appended to the beginning of the array if it is not already an on-grid point. The zenith angles are then set according to the following:

  $$\theta = \arccos\left(\frac{h}{X}\right), \tag{6.1}$$

  from Equation (4.1), where h is the vertical depth, and X are the slant depths in `mtc.slant_depths`. For example, if the vertical depth is set by the user to 3.4 km.w.e., then the slant depths will then be set to `[3.4, 3.5, 4.0, 4.5, ...]` and the zenith angles will be set to `[0, 13.73, 31.79, 40.93, ...]`. These adjustments are done by the `mtc.set_vertical_depth()` function, and this ensures physical and computational consistency at every stage of the calculations between the vertical depth, slant depths, zenith angles, and all output physical variables.

6.3 MCEq and DAEMONFLUX

In order to calculate atmospheric muon fluxes at the surface of the Earth, MUTE makes use of the codes MCEQ [40, 175], which is a one-dimensional fast cascade equation solver program written in Python, and DAEMONFLUX [80], which is a recent refined surface flux calculation code that uses GSF and DDM calibrated to high-energy surface muon and neutrino flux and charge ratio data.

MCEQ and DAEMONFLUX calculate muon fluxes at the surface of the Earth, Φ^s, as a function of muon surface energy, E^s, and zenith angle, θ. MCEQ provides results with an accuracy comparable to previously established cosmic-ray air shower simulation codes, including CORSIKA [177, 178], CONEX [179], and AIRES [180]. Recent comparisons between Monte Carlo simulations and MCEQ can be found in, for example, [63, 181, 182]. By calibrating data-driven inputs to surface flux and ratio data, DAEMONFLUX exceeds this level of accuracy, and provides surface muon and neutrino fluxes with uncertainties of as low as below 10% up to 1 TeV. It can do this within a fraction of the computational time of the previous codes, making it the optimal calculation for surface fluxes for MUTE. However, because DAEMONFLUX is limited to GSF for the primary flux model and DDM for the hadronic interaction model, MUTE also implements MCEQ, in order to provide users with access to various additional models.

In MCEQ, the user has the ability to select from a number of supplied models for the primary cosmic ray flux, the hadronic interactions, and the atmospheric density. In order to easily compare results from different models, these are left as local parameters that can be set in any function in the `surface` or `underground` modules. Listing 6.2 shows a few examples of how they can be set.

Listing 6.2: Calculating surface and underground variables for varying primary, interaction, and density models. The abbreviation `"GH"` for the `primary_model` parameter in line 5 is for the Gaisser-Honda model from [24].

```
1  import mute.surface as mts
2  import mute.underground as mtu
3
4  mts.calc_s_fluxes(interaction_model = "SIBYLL-2.3c", atmosphere = "MSIS",
    ↪  location = (10, 10), month = "July")
5  mtu.calc_u_intensities(method = "eq", primary_model = "GH")
6  mtu.calc_u_tot_flux(interaction_model = "DDM")
```

After the user sets the input models, MCEQ solves the cascade equations, and returns a matrix of muon fluxes at the surface of the Earth, $\Phi^s(E^s, \theta)$. An MCEQ calculation can run in a matter of minutes, but in order to further reduce the computation time on the user's end, several pre-calculated surface flux matrices are supplied along with the code when MUTE is installed. MUTE provides matrices for the SIBYLL-2.3C, SIBYLL-2.3D, and DDM hadronic interaction models (along with their uncertainties) with the GSF primary flux model and US Standard Atmosphere.

The next three sections will provide an overview of the results obtained with the different models to motivate the selection of the default models.

6.3.1 Primary Flux Models

The primary model is the model that describes the primary all-particle cosmic ray flux at the top of the atmosphere. The switching of the primary flux models in MUTE is done through MCEQ, where the models are handled by the `crflux` [183] package. This package provides access to available models, the most recent of which is Global Spline Fit (GSF) [27]. This is a data-driven parameterisation of the cosmic ray flux, as described in Section 2.4.1, and is the default model in MUTE. Users, however, have the ability to change the model by setting the `primary_model` parameter in any of the `surface` or `underground` functions.[1]

Because of the complexity of the cosmic ray composition and energy spectrum and discrepancies between different experiments reaching above 30%, especially at low energies in the GeV range and high energies in the hundreds of PeV range (see, for example, [9, 184]), there can be significant differences between the results obtained from different primary models. Results for the primary nucleon flux, total surface muon flux, and underground muon intensities are shown in Figure 6.3 for nine different models. These are GSF, H3a and H4a (Hillas models; [25]), GH (Gaisser-Honda; [24]), ZS and ZSP (Zatsepin-Sokolskaya (PAMELA); [26, 185]), GST3 and GST4 (Gaisser-Stanev-Tilav 3- and 4-generation; [10]), and PL27 (a simple power law containing only protons, no heavier nuclei, with a spectral index of $\gamma = 2.7$, based on [42]).

The top panel of Figure 6.3 shows the primary flux multiplied by the primary energy per nucleon to the power of 2.7 against the primary energy per nucleon. Some curves, like those for H3a and ZSP, match the shape of the experimental data well, showing features of the knee and ankle of the spectrum, whereas others, like ZS and PL27 show less structure. The constant form of PL27 is expected, because the flux is being multiplied by $(E^p)^{2.7}$. The comparison between the models and to the experimental data is discussed more fully in [183, 186].

The middle panel of Figure 6.3 shows the surface muon flux multiplied by the surface energy to the power of 3 against the surface energy, with a mean around 100 GeV. In this plot, it can be seen that PL27 seems to give the best description of the data, despite its simple definition. In the same way, ZSP clearly gives the worst agreement with the data, despite its better overall agreement in the top panel. The reason ZSP fails to match the surface data is because the model does not include enough protons in its calculation of the primary flux, where protons are the most abundant component of cosmic rays, accounting for up to 90% of the flux. Another point to note is that different primary models have been designed for different energy ranges; for example, GH is not intended for energies above 10^6 GeV. However, different energies are relevant for the atmospheric, surface, and underground fluxes, because the mean energy shifts as the particles lose energy as

---

[1] However, this cannot be done for the most recent hadronic interaction models: DAEMONFLUX, DDM, and SIBYLL-2.3D, all of which use GSF. The most recent hadronic interaction model that is available for calculations with different primary models in MCEQ is SIBYLL-2.3C.

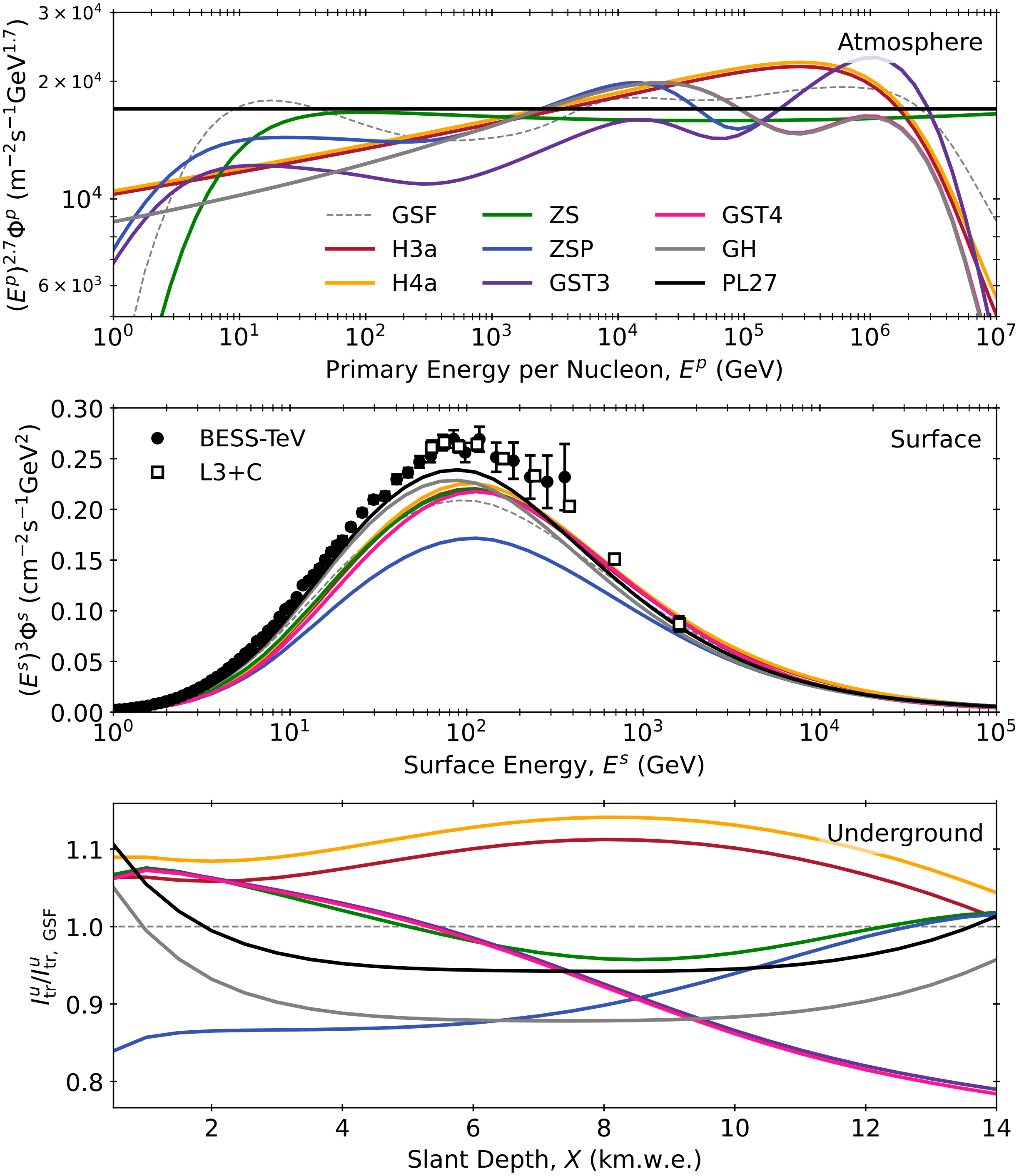

Figure 6.3: Total particle (top) and muon (middle and bottom) flux for various primary models. All calculations were done using SIBYLL-2.3C for the hadronic interaction model, and US Standard Atmosphere for the density model. Experimental data is shown in the surface panel for BESS-TeV [17] and L3+C [44]. The curves in the underground panel were computed using a vertical depth of 0.5 km.w.e.

they propagate. Therefore, models that describe the cosmic ray data well in certain energy ranges in the atmosphere are not necessarily expected to describe the data equally well for surface or underground muon fluxes.

The bottom panel of Figure 6.3 shows the ratio of the underground muon intensity (integrated over underground energy, as explained in Chapter 7) to GSF against slant depth. Here, there is variation between the models by up to 20%. This discrepancy is a reflection of the difficulty of measuring the primary flux of cosmic rays in the top panel.

6.3.2 Hadronic Interaction Models

The default hadronic interaction model in MUTE is SIBYLL-2.3C, which is a Monte Carlo event generator written specifically for interpreting cosmic ray data [175, 187]. This is the most recent model that is publicly available with MCEQ; however, there are two newer models, namely SIBYLL-2.3D [75, 186] and DDM (Data-Driven Model) [76]. SIBYLL-2.3D is an update to SIBYLL-2.3C informed by recent higher-precision measurements, while DDM is a recent fit to fixed-target accelerator data on particle production in hadronic interactions.

In addition to the models available for the provided matrices, a number of additional hadronic interaction models are available to be used with MCEQ through MUTE, including SIBYLL-2.3 [188], SIBYLL-2.1 [189], EPOS-LHC [66], and several versions of QGSJET [190] and DPMJET [40, 71], all of which are Monte Carlo event generators. These are currently the most accurate particle interaction models for cosmic ray cascades, and their comparison to surface muon spectrometer data is shown in Figure 6.4.

There are no uncertainty calculations for EPOS-LHC, QGSJET, or DPMJET, but the fluxes calculated by all of the models are confined by the error bands from DDM and SIBYLL-2.3D, which are both around 20%. The upper end of the SIBYLL-2.3D error band is about 10–15% lower than the data, without including systematic uncertainties on the data. The DDM prediction is closer to describing the data, but is similarly off 10–15%, despite being directly constrained by accelerator data, though it does agree with the data to the extent of its error band. Conversely, the DAEMONFLUX prediction (DDM + GSF with calibration to surface data) describes the surface data very well, as expected, and has significantly smaller errors than the two previous models. For this reason, DAEMONFLUX has been chosen as the new default surface flux model in MUTE v3.0.0, replacing the previous SIBYLL-2.3C.

6.3.3 Atmospheric Density Models

As from Chapters 2 and 3, the definition and modelling of the atmosphere are very important in calculating the production of muons in air showers. The most important quantity to model is the den-

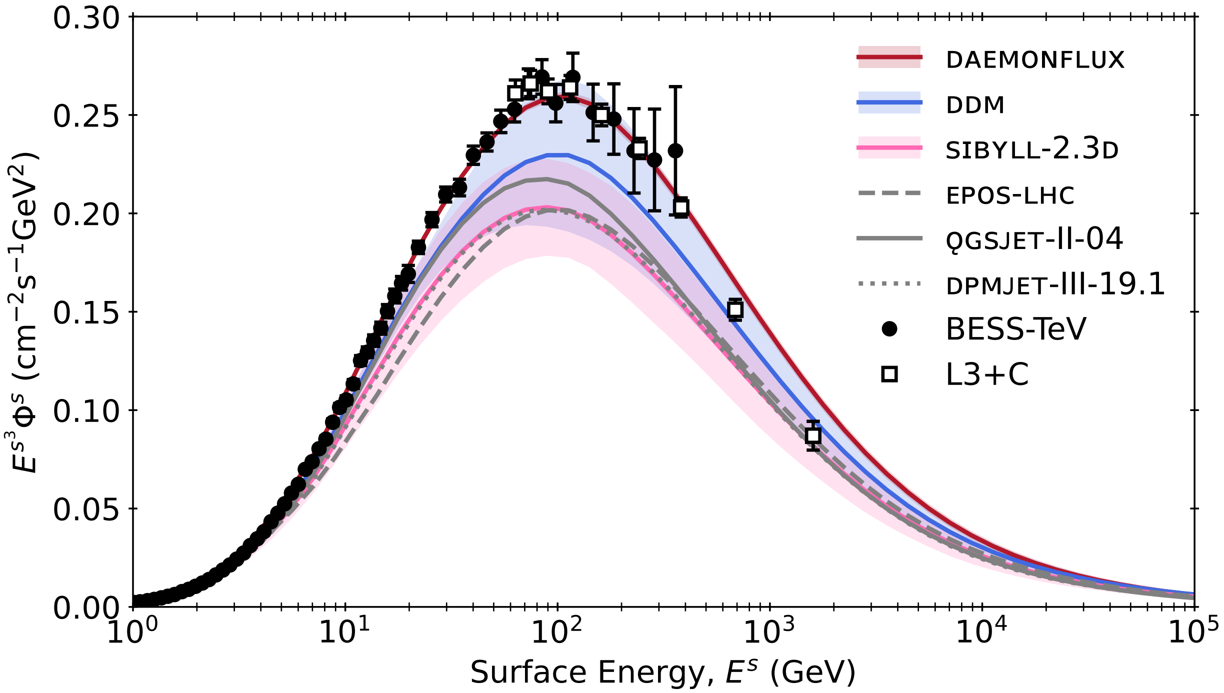

Figure 6.4: Surface muon flux multiplied by the cube of the surface energies vs surface energy for a near-vertical zenith angle of $\theta \approx 18°$. Curves are shown for DAEMONFLUX, DDM, and SIBYLL-2.3D with error bands for hadronic uncertainties, as well as for EPOS-LHC, QGSJET-II-04, and DPMJET-III-19.1. Experimental data is shown for the surface spectrometer experiments BESS-TeV [17] and L3+C [44]. GSF was used as the primary flux model in all calculations.

sity of the atmosphere, as this influences the development of extensive air showers through the ρ_{air}-dependence of the interaction mean free paths of pions and muons, as in Equation (3.22). MCEQ, and thereby MUTE, offers two models for the atmospheric density: a CORSIKA implementation of U.S. Standard Atmosphere (USStd) [177, 191], and the U.S. Naval Research Laboratory Mass Spectrometer and Incoherent Scattering radar-Exosphere 2000 (NRLMSISE-00) model [192].

USStd

Unless otherwise stated, the MCEQ density model used in MUTE in this work is the default USStd based on a parameterisation developed by J. Linsley (the “Linsley model”) to reproduce the 1976 USStd average density profile [177, 193]. This models the atmosphere as an idealised steady-state representation, with air being composed homogeneously of 78.1% N_2, 21.0% O_2, and 0.9% Ar. In CORSIKA, the atmosphere is split into five isothermal ranges of altitudes, and the mass overburden of the atmosphere in each of these five layers is defined in terms of three fit parameters, a, b, and c. For the four lower levels, the mass overburden, $X(h)$ (the slant depth), has an exponential decay dependence on altitude, h, whereas for the fifth level (for $h > 100$ km), it scales linearly with altitude [177]:

$$X(h) = \begin{cases} a_i + b_i e^{-h/c_i} & \text{if } i \in \{1,2,3,4\}, \\ a_i - b_i \left(\frac{h}{c_i}\right) & \text{if } i = 5, \\ 0 & \text{otherwise.} \end{cases} \tag{6.2}$$

The values of $\{a_i\}$ in [gcm^{-2}], $\{b_i\}$ in [gcm^{-2}], and $\{c_i\}$ in [cm] for all i that are used in CORSIKA are given in [177], where boundary conditions are imposed on them such that $X(h)$ is a continuous function. The maximum altitude is $h = 112.8$ km, and while the original USStd model in [191] extends out to 1000 km, this maximum altitude is sufficient for air shower calculations. However, because USStd provides a standard average atmosphere around the globe, it has no inputs for specific locations or times of the year, meaning it cannot be used to investigate the seasonal variations of the muon flux at the surface or underground.

NRLMSISE-00

To calculate the flux for different months of the year, as is done in Section 8.3 to study the seasonal variations of the muon flux, the NRLMSISE-00 model, which has a numerical representation available in MCEQ, is used instead of the otherwise default USStd. This is a static empirical model of the Earth's atmosphere around the globe that extends from the surface of the Earth up to the exosphere. It uses data from ground-, rocket-, and satellite-based observations and it is based on spherical harmonics, which it uses to represent spatial variability of the density profile and temperature parameters [192].

The NRLMSISE-00 model takes in as input the location in (latitude, longitude, altitude) coordinates as well as the day of the year, and returns the total mass density and atmospheric temperature. MCEQ then uses this information about the density $\rho(X)$ to calculate the one-dimensional development of air showers and solve the cascade equations, returning the surface muon flux. It is an atmospheric model that describes how the mass density of the atmosphere, ρ, develops along the slant depth, X. However, X is needed explicitly because X is in the decay terms of the cascade equations in Equation (3.9):

$$X_i(\theta) = \int_0^{l_i} \rho(h(l', \theta))\mathrm{d}l'. \tag{6.3}$$

Density as a function of slant depth can be calculated with the `X2rho()` function in MCEQ. The result is shown in Figure 6.5, where density increases as slant depth increases (according to the definition of X in Figure 3.3), and decreases as altitude increases, as expected.

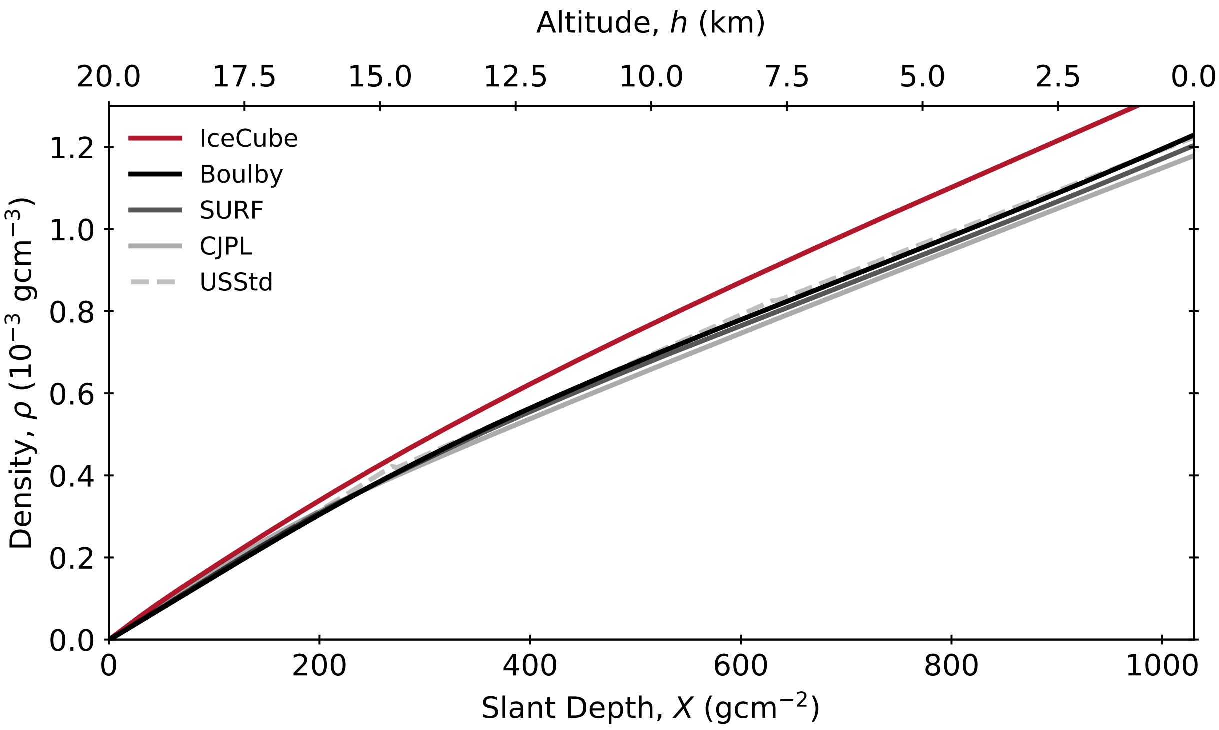

Figure 6.5: Atmospheric density vs altitude and slant depth. The solid curves were calculated using NRLMSISE-00, and the dashed curve for USStd, representing a mean density profile, is shown for comparison. Curves are shown for select laboratories to demonstrate the span of variation due to location (refer to Figure 5.4 for the locations of the labs). Variation will also occur across months and zenith angles.

6.3.4 Results for Atmospheric Muons at the Surface

Although MUTE is mainly intended for underground and underwater calculations, there are surface muon equivalents for almost all underground calculation functions that are in the `underground` module in the `surface` module (with the only exception being that there is no function to calculate a surface angular spectrum because the zenith angle distribution at the surface is trivial when the intensity is provided). These functions are listed in Table 6.2, and their results are summarised in this section.

`mts.calc_s_fluxes()` is the standard `surface` function that returns the surface fluxes as a function of surface energy and zenith angle, $\Phi^s(E^s, \theta)$. The surface fluxes are output from MCEQ and DAEMONFLUX and a simple unit conversion is done to put them into the appropriate units for MUTE (following PROPOSAL, MUTE uses [MeV] as its energy unit, whereas MCEQ and DAEMONFLUX use the more common [GeV]). The surface fluxes returned by DAEMONFLUX are shown in Figure 6.6 against surface energy for vertical and horizontal muons.

`mts.calc_u_intensities()` integrates the surface fluxes over surface energy:

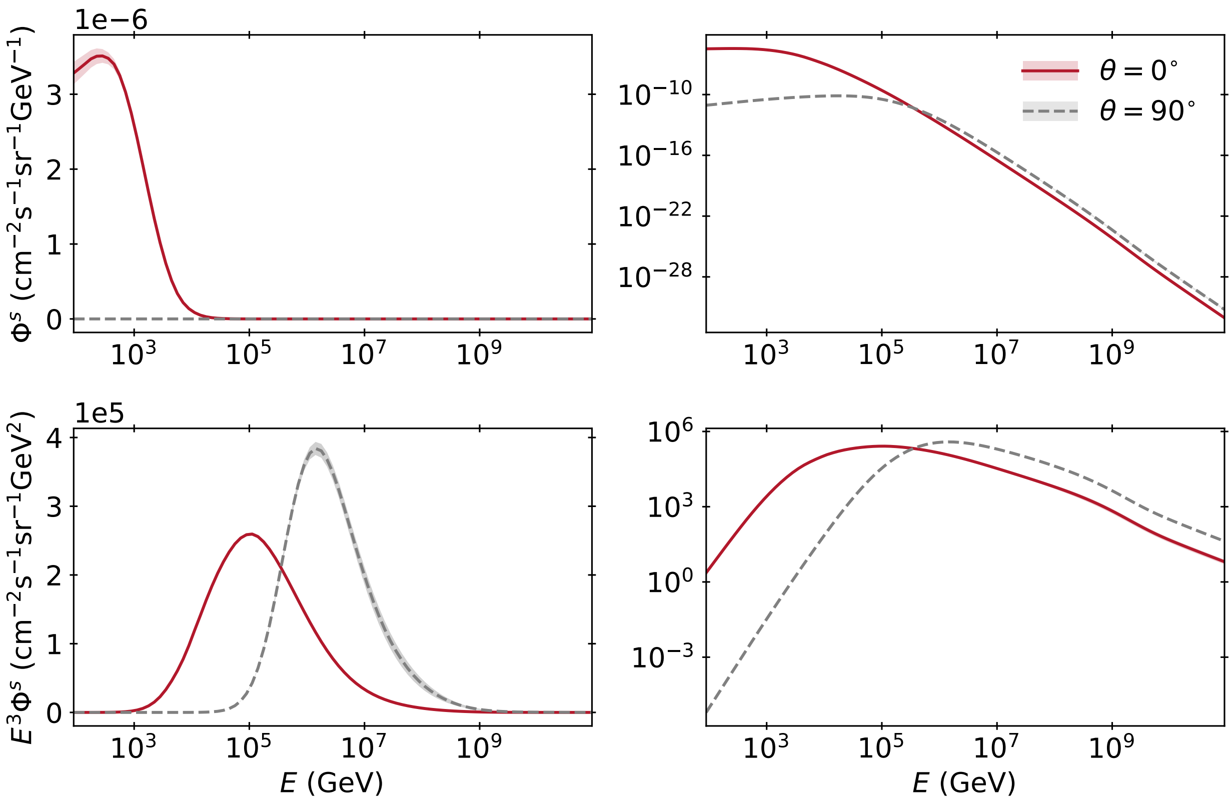

Figure 6.6: Surface muon flux vs surface energy calculated using DAEMONFLUX displayed in different ways for vertical (solid red) and horizontal (dashed grey) muons. The top row of plots shows the surface flux whereas the bottom row shows the surface flux multiplied by the cube of the surface energies to reveal more structure. The left column of plots shows a linear scale for the y-axis whereas the right column shows a logarithmic scale. The horizontal muon flux is five orders of magnitude lower than the vertical muon flux, and so no peak is visible for the horizontal flux in the upper left plot on the linear y-axis.

$$I^s(\theta) = \int_{E^s_{\text{min}}}^{E^s_{\text{max}}} \Phi^s(E^s, \theta) \mathrm{d}E^s. \tag{6.4}$$

It returns the surface intensities as a function of zenith angle, $I^s(\theta)$, in units of [cm^{-2}s^{-1}sr^{-1}]. These intensities are plotted against zenith angle in Figure 6.7. In the top left panel, it can be seen that, for high energies, the surface flux increases as zenith angle increases, peaks at near-horizontal, and then decreases again slightly for the directly horizontal direction. The reason the muon flux is low for vertical angles is because, although the slant depth is at a minimum, the density of the air column is at a maximum. From Equation (3.22), when the density of air increases, the interaction mean free path of pions and kaons increases (particularly for high-energy pions and kaons above 1 TeV, as plotted in the top panels in Figure 6.7, which are more likely to interact than decay), which in turn results in a lower muon flux. Conversely, for a horizontal zenith angle, the air column density is at a minimum, but the slant depth is at a maximum, meaning the pions and muons have further to travel before reaching the surface of the Earth, and more decay before being able to do so, again resulting in a lower muon flux. This competition between the inverse effects of the density and slant depth balances out at near-horizontal angles, around 80°, and so a peak in the muon flux is observed here in Figure 6.7. The shape in the surface flux zenith angle distribution changes as energy increases, and this peak is only observed for energies above approximately 100 GeV. The shape of the distribution at other energy scales can be seen in, for example, [175].

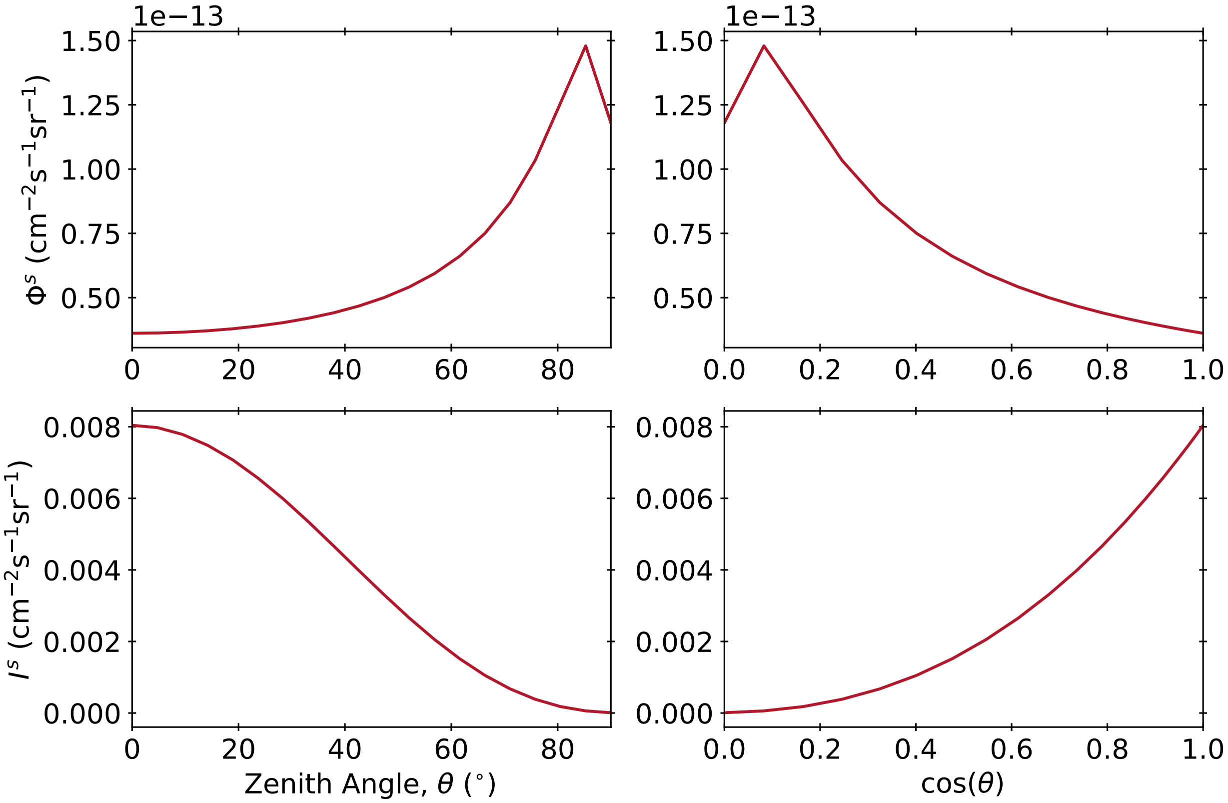

Figure 6.7: Surface muon intensity vs zenith angle calculated using DDM. The top row of plots shows the surface flux for $E^s \approx 1$ TeV, whereas the bottom row shows the intensity integrated over all energies as in Equation (6.4). The left column of plots shows the spectra against zenith angle, θ, whereas the right column shows against cosine of the zenith angle, $\cos(\theta)$.

`mts.calc_s_e_spect()` integrates the surface fluxes over the solid angle and returns the surface energy spectrum as a function of surface energy, $\mathrm{d}\Phi^s/\mathrm{d}E^s$:

$$\frac{\mathrm{d}\Phi^s}{\mathrm{d}E^s} = 2\pi \int_0^1 \Phi^s(E^s, \theta)\mathrm{d}\cos(\theta). \tag{6.5}$$

Lastly, `mts.calc_s_tot_flux()` integrates the surface intensities over the solid angle and returns the total surface flux, Φ^s_{tot}:

$$\Phi^s_{\text{tot}} = 2\pi \int_0^1 I^s(\theta)\,\mathrm{d}\cos(\theta). \tag{6.6}$$

Using the default models (DAEMONFLUX and US Standard Atmosphere), this returns a value of (0.0155 ± 0.0008) cm^{-2}s^{-1}. This is equal to (0.930 ± 0.048) cm^{-2}min^{-1}, which is comparable to the often conveniently quoted value of one muon per square centimetre per minute at sea level.

6.4 PROPOSAL

To simulate the propagation of muons through rock, water, and ice, MUTE makes use of PROPOSAL [95, 194]. PROPOSAL is a recently developed Monte Carlo code that transports leptons through long ranges of matter quickly with high precision, and is a successor program of the MMC code developed originally for the AMANDA experiment at the South Pole by [168]. It is written in C++, but a Python interface is available, through which it interacts with MUTE in the `propagation` module.

For muon propagation, one of the most important variables is the slant depth, which can be thought of as the total amount of matter in radiation units of [km.w.e.] that a muon travels through, and is defined in Equation (4.1) as:

$$X = \frac{h}{\cos(\theta)}, \tag{6.7}$$

h is the vertical depth in units of [km.w.e.], and θ is the incoming muon's zenith angle at the surface. This slant depth, as well as the muon's energy at the surface, E^s, are input into PROPOSAL, which returns the muon's energy underground, E^u, at the depth X.

The main job of PROPOSAL is to create surface-to-underground transfer tensors, $U(E^s, E^u, X)$, which associate a muon's energy at the surface with a distribution of underground energies for a given slant depth. To do this, the propagation medium has to be properly set up in terms of its geometry and definition.

6.4.1 Geometry

In order to propagate muons, PROPOSAL requires a geometry to provide the setting of the propagation. The default geometry used by MUTE is a large sphere of homogeneous, isotropic standard rock ($Z = 11$, $A = 22$, $\rho = 2.65$ gcm^{-3}), shown in Figure 6.8 (shown also for water). Muons are initially placed at $(0,0,0)$, the center of the sphere, and are propagated downwards for initial surface energies as defined in `mtc.ENERGIES`. Because the surface fluxes obey azimuthal symmetry in the relevant energy range of E^s, the number of angular bins in the PROPOSAL calculations is reduced to a set of zenith angles within $[0,\ 90)^\circ$, where 0° describes downward-going muons, and 90° describes horizontal muons. Although the distinction between surface zenith angle and underground zenith angle is possible to be made in PROPOSAL because the average angular deviation from surface to underground is $\langle|\theta^u - \theta^s|\rangle < 1^\circ$, the distinction is not drawn, and so the simulations are only one-dimensional, and, for computational efficiency, scattering is turned off.

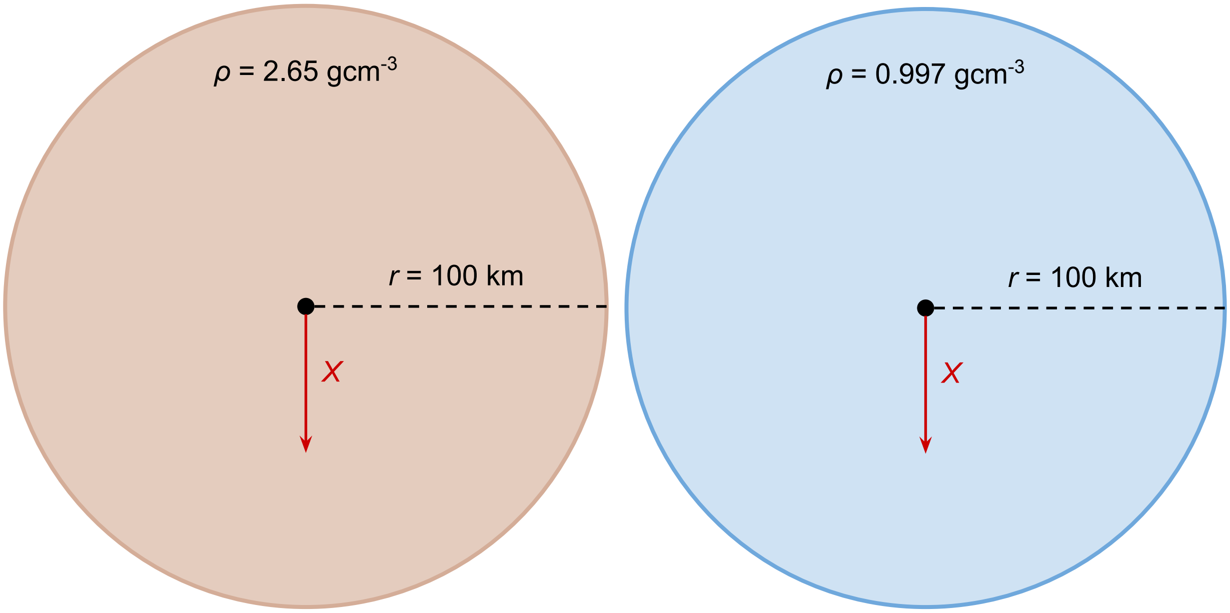

Figure 6.8: PROPOSAL geometry for rock (left; with a density of $\rho = 2.65$ gcm^{-3}) and fresh water (right; with a density of $\rho = 0.997$ gcm^{-3}). In all cases, the geometry in PROPOSAL is a solid homogeneous and isotropic sphere of radius 100 km. Muons are always propagated straight down along the red arrow from the center of the sphere until they either decay or reach the end of the set propagation length. The only difference between calculations for rock and calculations for water in MUTE is the definition and density of the propagation medium.

6.4.2 Media in PROPOSAL

When defining the geometry of the propagation medium, in addition to the shape, the details of the medium itself must also be given. Media in PROPOSAL are made up of components, which are defined by their Z and A values. In addition to this, media also require the empirical Sternheimer parameters from Equation (4.14): I, x_0, x_1, a, b, c, and δ_0. PROPOSAL offers 18 media by default, some of which are listed in Table 6.3 with their values to demonstrate the differences between the Sternheimer parameters between different materials. Other media available in PROPOSAL include hydrogen, copper, calcium carbonate, paraffin, and liquid argon [95].

Although the Sternheimer parameters are important for calculating energy losses of muons travelling through media due to ionisation in the Bethe-Bloch equation, Equation (4.12), they are not reported for most rock types. In addition to being reported for standard rock, Sternheimer

Table 6.3: The Sternheimer parameters for select media defined by default in PROPOSAL, as given in [88, 93, 195]. The values for water and ice are taken from PDG 2020 (values from PDG 2001 are also available in PROPOSAL).

Medium	I (eV)	x_0	x_1	a	b	$-c$	δ_0
Air	85.7	1.7418	4.2759	0.10914	3.3994	10.5961	0
Fresh Water	79.7	0.2400	2.9004	0.09116	3.4773	3.5017	0
Sea Water	75.0	0.2400	2.8004	0.09116	3.4773	3.5017	0
Ice	79.7	0.2586	2.8190	0.09116	3.4773	3.5873	0
Standard Rock	136.4	0.0492	3.0549	0.08301	3.4120	3.7738	0
Fréjus Rock	149.0	0.288	3.196	0.078	3.645	5.053	0
Salt	175.3	0.2	3.0	0.1632	3	4.5041	0
Lead	823.0	0.3776	3.8073	0.09359	3.1608	6.2018	9.14
Iron	286.0	-0.0012	3.1531	0.14680	2.9632	4.2911	0.12
Uranium	890.0	0.2260	3.3721	0.19677	2.8171	5.8694	0.14

parameters are published only for Fréjus rock — the rock above LSM, also called glossy schist — in, for example, [168] (and are listed in Table 6.3). The differences in energy loss between standard rock and Fréjus rock from the Sternheimer parameters alone account for differences of up to 10% in the total underground muon flux. For this reason, the calculations for LSM presented in this work were done using the full definition of Fréjus rock. For other laboratories, however, because values for the Sternheimer parameters do not exist in the literature, all calculations with MUTE use the Sternheimer parameters for standard rock as an approximation.

Energy Loss in Different Rock Types

The definition of the medium, and in particular the Z and A values, of different rock types is one of the most significant factors affecting the energy loss of muons travelling through rock and therefore the total muon flux underground. The average atomic number and average atomic weight are important because the cross-sections for the energy loss processes in Chapter 4 are proportional to Z/A and Z^2/A. As these values increase, the cross-sections increase, meaning the number of interactions the muons undergo increases, leading to more energy loss, and therefore fewer muons surviving to deep depths underground.

Detailed information on the compositions of the different rock types above the underground labs listed in Table 5.1 was gathered and is shown in Table 6.4. The chemical composition of Fréjus rock in terms of elemental abundances by weight is given in [196], with a recent review of the existing measurements in [36]. Similarly, the chemical composition of the rock above Y2L, Yangyang rock, is given in [197], for LNGS, Gran Sasso rock, in [198] and [144] (which report the same composition though give different $\langle A \rangle$ values), and for the rock above CJPL, Jinping rock, in [199], though Sternheimer parameters are not provided for any of these.

Table 6.4: Chemical compositions of rocks above various laboratories, given in terms of mass fractions (%). Note that the totals do not always add up to 100% because not all elements are reported for all rock types. Hydrogen, for example, is often not reported, though it remains important for simulating neutron transport in muon-induced neutron studies [197].

Laboratory	**H**	**C**	**O**	**Na**	**Mg**	**Al**	**Si**	**K**	**Ca**	**Fe**	**Reference**
Z	1	6	8	11	12	13	14	19	20	26	
A	1	12	16	23	24	27	28	39	40	56	
Y2L	-	-	48	2.6	2.4	8.4	26	1.9	4.2	5.2	[197]
Kamioka 1	-	-	39	0.01	0.6	6.0	17	-	28	7.6	[197, 200]
Kamioka 2	-	-	47	2.7	1.2	7.5	32	-	2.5	2.6	[197, 200]
LNGS 1	-	11.88	47.91	-	5.58	1.03	1.27	1.0	30.29	-	[152, 197]
LNGS 2	0.03	12.17	50.77	-	8.32	0.63	1.05	0.1	26.89	-	[144, 198]
LSM	-	-	24	-	5.6	1.0	1.3	0.1	30	-	[196, 197]
SNOLAB	0.15	0.04	46.0	2.2	3.3	9.0	26.2	1.2	5.2	6.2	[201]
CJPL	-	9.59	46.42	0.01	11.5	0.15	0.19	0.07	31.96	0.1	[199]

These chemical compositions were then used to calculate $\langle Z/A \rangle$ and $\langle Z^2/A \rangle$ values when these values were not otherwise found in the literature. This was done by taking a weighted average across all elements using the mass fractions as the weights. The resulting values for each rock type are given in Table 6.5 along with the rocks' densities. These values were used to define new components and media in PROPOSAL to use in simulations for each individual laboratory.

More careful study of the various rock types is required in order to maximise the accuracy of the simulations in reproducing the environments above each laboratory. For example, fuller details on the rock composition, as well as the different types of rocks above a given lab, should be obtained, with uncertainties, in order to ensure the correct $\langle Z/A \rangle$ and $\langle Z^2/A \rangle$ values are being simulated. Additionally, it would be better to use the number fraction rather than the mass fraction in Table 6.4, because it is the relative number of atoms in a given molecule, not the relative weight of the elements, that is important in simulating particle interactions stochastically. Furthermore, while some labs publish full chemical compositions, as in Table 6.4, others publish $\langle Z/A \rangle$ and $\langle Z^2/A \rangle$ values, while others still publish only $\langle Z \rangle$ and $\langle A \rangle$ values. It is largely $\langle Z/A \rangle$ and $\langle Z^2/A \rangle$ that are important for calculating energy losses, but it is not always possible to calculate $\langle Z/A \rangle$ and $\langle Z^2/A \rangle$ with simple algebra when given $\langle Z \rangle$ and $\langle A \rangle$, because, in general,

$$\left\langle \frac{Z}{A} \right\rangle \neq \frac{\langle Z \rangle}{\langle A \rangle}. \tag{6.8}$$

An approximation cannot usually be made because the difference between the left-hand side and right-hand side of Equation (6.8) can reach nearly 20% in some cases. Lastly, as stated above, the

Table 6.5: Comparison of further physical parameters between standard rock and other types of rock relevant to underground laboratories. When not stated directly in the literature, the $\langle Z/A \rangle$ and $\left\langle Z^2/A \right\rangle$ values were calculated using the chemical compositions in Table 6.4. Characteristic Sternheimer parameters for standard rock and Fréjus rock are given in Table 6.3.

Medium	**Density, ρ (gcm^{-3})**	$\langle Z/A \rangle$	$\left\langle Z^2/A \right\rangle$	**Reference**
Standard Rock	2.65	0.50	5.5	[8]
WIPP Rock	2.3 ± 0.2	0.488	7.14	[202]
Yangyang Rock	2.7	0.498	7.45	[197]
Soudan Rock	2.80 ± 0.05	0.495	6.10	[45, 203]
Kamioka Rock	2.70 ± 0.05	0.50	5.08	[125]
Boulby Rock	2.62 ± 0.03	0.496 ± 0.030	5.80 ± 0.55	[127]
Gran Sasso Rock (1994)	2.71	0.51	5.79	[198]
Gran Sasso Rock (1995)	2.71 ± 0.05	0.50	5.69	[144, 160]
Fréjus Rock	2.72 ± 0.01	0.50	5.87 ± 0.02	[131]
SNOLAB Norite	2.83 ± 0.10	0.491	6.01	[204]
Jinping Rock	2.8	0.50	6.07	[199]
KGF Rock	3.02	0.49	6.32	[161]

lack of Sternheimer parameters for every rock type aside from Fréjus rock means there will always be an estimated 10% systematic uncertainty on the results.

From Table 6.5, the value of $\left\langle Z^2/A \right\rangle$ can vary by up to approximately 47% or higher, which can have significant effects on the energy loss, as radiative losses — which are proportional to Z^2 — become more significant at higher energies and therefore deeper depths. Due to the described chemical differences in the rock types, converting between rock types by simply multiplying by the ratio of the densities, as in Equation (4.6), is often not enough, because these differences can result in different shapes of the intensity and total flux curves for the given rock types (similar to the differences between the shapes of the curves for rock and water in Figure 6.10 below). Therefore, depths in terms of the different rocks types are sometimes converted between each other using more complicated empirical formulas constructed by comparing underground intensity vs depth data in different depth units. To convert from depths in [km.w.e.] measured in Gran Sasso rock, X_{GS}, to those measured in standard rock, X_{SR}, the LVD Collaboration provides the following formula [143]:

$$X_{\mathrm{SR}} = -9.344 + 1.0063 X_{\mathrm{GS}} + (1.7835 \times 10^{-6}) X_{\mathrm{GS}}^2 - (5.7146 \times 10^{-11}) X_{\mathrm{GS}}^3. \tag{6.9}$$

A similar formula is provided by the SNO collaboration in [89] for conversion in [m.w.e.] from depths measured in SNO rock, X_{SNO}:

$$X_{\mathrm{SR}} = 1.015 X_{\mathrm{SNO}} + (2.5 \times 10^{-6}) X_{\mathrm{SNO}}^2. \tag{6.10}$$

Differences between using Equation (4.6) and Equation (6.10) to convert depths between standard and SNO rock amount to 5.3%, nearly constant at all depths, with the values from Equation (4.6) being lower. They are 1.6% with Equation (6.9) for Gran Sasso rock (when omitting the first term of Equation (6.9)). The fact that these differences are constant at all depths suggests the shapes of the underground intensity and total flux curves do not vary significantly, and so simply applying a correction based on the density alone, as with Equation (4.6), may suffice to convert between rock types, especially for laboratories for which formulas like Equations (6.9) and (6.10) are not given in the literature. However, it is still more accurate to use the proper $\langle Z/A \rangle$ and $\left\langle Z^2/A \right\rangle$ values for a given rock type. One solution that may be implemented in MUTE in the future is to calculate energy losses for a fine grid of Z and A values and perform a two-dimensional interpolation to any set of Z and A values that the user defines when running the program. Like this, the efficiency of MUTE can be maintained while also expanding its flexibility to service any laboratory.

Energy Loss in Standard Rock vs Water

Although all calculations are done in terms of kilometres of water equivalent, energy loss through rock is not equivalent to energy loss through water because of the physical and chemical differences between the two. In addition to the different elemental abundances, they also have vastly different densities. Therefore, a comparison between the energy loss processes was performed and is shown in Figure 6.9. There is a clear difference seen between the processes for rock compared to those for fresh water, where pair production is more abundant for rock than it is for water across all tested surface energies, and ionisation is more abundant for water. For this reason, MUTE differentiates between propagation through rock and water.

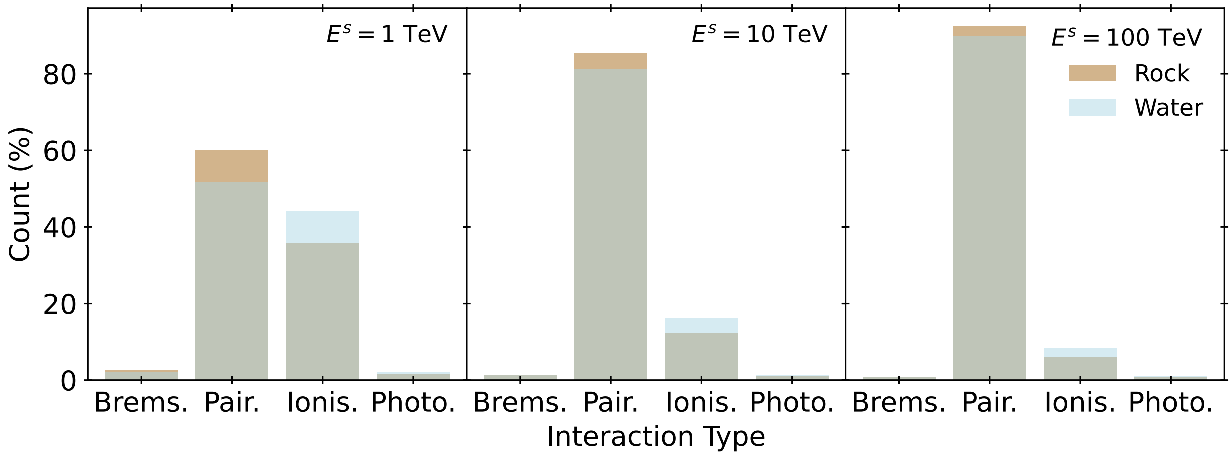

Figure 6.9: Numbers of energy loss interactions as simulated by PROPOSAL for at surface energies of 1 TeV (left), 10 TeV (middle), and 100 TeV (right) for standard rock and fresh water.

Figure 6.10 shows the direct comparison between standard rock and fresh water for underground intensity and total underground flux. This shows the effects in the final muon fluxes underground as a result of the different densities and compositions of rock and water. Although results for both media are plotted against units of [km.w.e.], the water curves are higher than those for rock in both cases because of these differences.

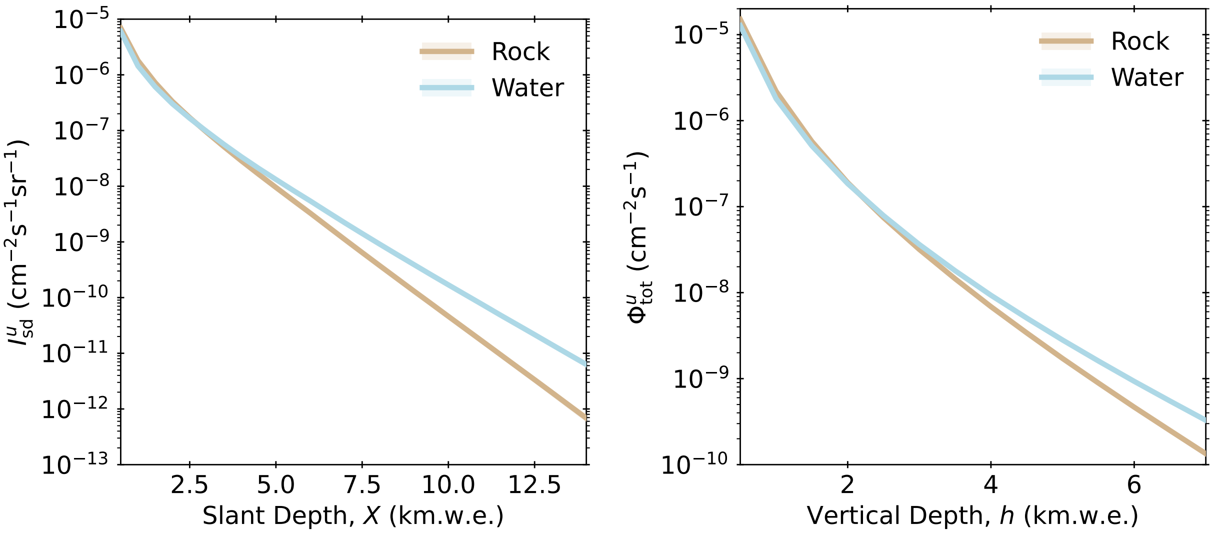

Figure 6.10: Underground intensity (left) and total underground flux (right) against depth underground for rock and fresh water.

Energy Loss in Fresh Water vs Sea Water

The definitions of fresh water and sea water are very similar with respect to their Sternheimer parameters, as seen in Table 6.3. However, their mass densities and chemical compositions are different. The mass density of fresh water is 1.000 gcm^{-3} and it is made up of H_2O, whereas the mass density of sea water is 1.03975 gcm^{-3} for ANTARES sea water and 1.0400322 gcm^{-3} for Cascadia Basin sea water. In addition to H_2O, sea water is also made up of small amounts of chlorine, sodium, sulphur, magnesium, potassium, and calcium [59]. The result of these differences is that total fluxes calculated with sea water are constantly about 5% lower than those calculated with fresh water. For this reason, both `"water"` and `"sea_water"` are offered as separate media in MUTE. All results presented in this work were calculated using the sea water transfer tensor.

6.4.3 Cross-Section Models

The cross-sections for muon energy loss interactions are described by different theoretical models in PROPOSAL. For the simulations done in MUTE, the Bethe-Bloch-Rossi model [94] described in Section 4.2.2 is used to describe ionisation, the Kelner-Kokoulin-Petrukhin models are used for electron-positron pair production [205] as described in Section 4.2.3 and bremsstrahlung [206] as described in Section 4.2.4, and the updated 1997 parameterisation by Abramowicz, Levin, Levy, and Maor [102, 103] described in Section 4.2.5 is used for photonuclear interactions. While the accuracy of the models is not perfect and some cross-sections remain uncertain, the impact is assumed to be negligible on the underground intensity calculation, reaching at most a few percent [104, 166, 167].

6.4.4 Simplifications of Energy Loss Simulations

In order to simplify the simulations that need to be performed, a number of decisions were made regarding which particles and details of the media were important for describing the propagation and energy loss of muons through rock and water, which will be summarised in this section.

Energy Loss of μ^- vs μ^+

Although there is a difference in the abundances of the positively charged and negatively charged muons produced in the atmosphere and they can undergo different interactions in the matter at low energies, theoretically, the energy loss in matter of both at high energies should be described identically. In order to ensure this, simulations were done in PROPOSAL for both polarities, and the energy loss output was analysed for three different energies in the TeV range. With these results, it was verified that PROPOSAL discerns no practical differences between μ^- and μ^+ in its propagation simulations, which is as expected from Figure 4.1, where the difference between the two polarities is only seen below 1 MeV, where slow negatively charged muons undergo muon capture. For this reason, only negatively charged muons are simulated in MUTE, and the resulting survival probabilities are taken to apply to both polarities.

Energy Loss in Water vs Ice

Because water and ice are the same compound and are even more similar to each other in their definitions in Table 6.3 than standard and Fréjus rock, it can be concluded that, although `"ice"` is available as a medium option in MUTE, the energy losses between water and ice will be nearly identical, and so separate transfer tensors for ice are not needed. Any discrepancies between the energy losses in water and ice are assumed to be completely negligible.

6.4.5 Surface-to-Underground Transfer Tensors

PROPOSAL propagates the muons one by one in a Monte Carlo simulation until the muon decays, loses all of its energy, or reaches the end of the set propagation length. Muons can lose energy via multiple different processes, and PROPOSAL uses tables generated by the Bethe-Bloch equation in order to calculate the energy losses. If a muon survives for the entirety of the length of the slant depth X without decaying, its final underground energy, E^u, is filled into a histogram of $\mathrm{d}N/\mathrm{d}E^u$, which is then normalised by the number of simulated events (the default number of simulated events per surface energy-slant depth bin in MUTE is 10^6). These histograms are arranged as columns of a surface-to-underground transfer tensor $U(E^s,E^u,X)$. The simulations are repeated for each surface energy bin E^s that enumerates the columns of $U(E^s,E^u,X)$. A two-dimensional image of slices of the transfer tensor $U(E^s,E^u,X)$ is shown in Figure 6.11.

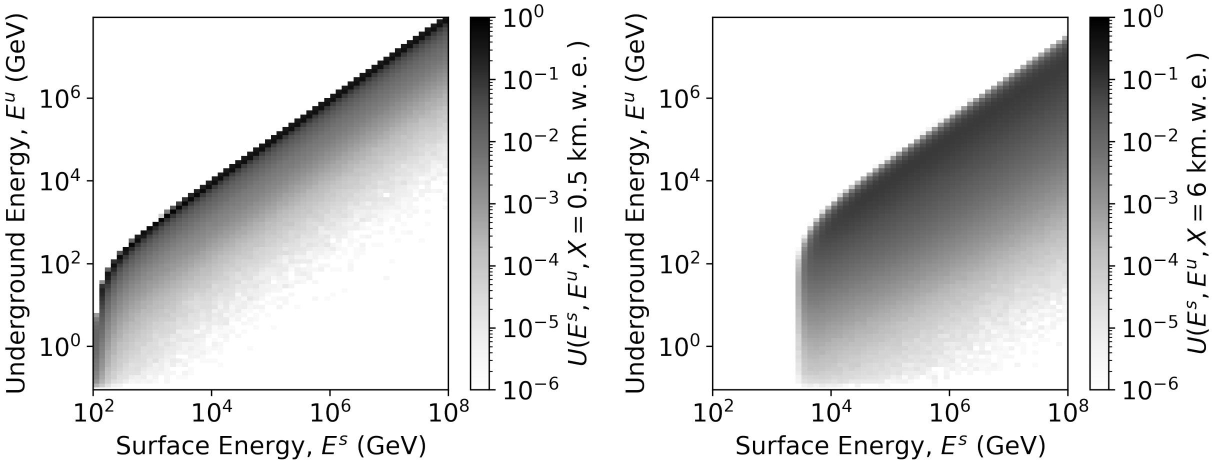

Figure 6.11: A slice of the surface-to-underground transfer tensor (a transfer matrix) for depths of 0.5 km.w.e. (left) and 6 km.w.e. (right) for standard rock, simulated with PROPOSAL for 10^6 initial muons per surface energy-slant depth bin.

By default, MUTE provides surface-to-underground transfer tensors for muon energy loss in standard rock, fresh water, and sea water for a range of slant depths spanning 0.5 km.w.e. to 14 km.w.e., going up in steps of 0.5 km.w.e. (the slant depths in `mtc._SLANT_DEPTHS`) so users do not have to run the time-consuming Monte Carlo simulation themselves.

6.4.6 Muon Survival Probabilities

In the literature, the survival probability $P(E^s,X)$ for a muon with surface energy E^s to reach a certain slant depth X is sometimes approximated analytically. One of these approximations is the continuous-slowing-down approximation (CSDA), given in [93] as derived from Equation (4.24):

$$\langle X(E)\rangle = \int_{E^s}^{E} \frac{\mathrm{d}E'}{a(E')+b(E')E'}. \tag{6.11}$$

Here, $\langle X(E)\rangle$ is the mean slant depth a muon can travel when it loses an amount $E-E^s$ of energy, where E^s is the muon's energy at the surface [36]. This is given as a mean due to range straggling (or fluctuations), referring to the fact that not all muons travel the exact same range due to the statistical nature of energy loss by radiation [94]. At high energies, $a(E)=a$ and $b(E)=b$ are nearly constant, and Equation (6.11) can be approximated further as:

$$\langle X(E)\rangle \approx \left(\frac{1}{b}\right)\ln\left(1+\frac{E}{\varepsilon_\mu}\right), \tag{6.12}$$

where ε_μ is the critical energy of the muon, defined in Equation (4.25). At low energies, it is generally true that $\langle X(E)\rangle < X(\langle E\rangle)$ [105]. Thus, if the fluctuations in the energy loss are taken to be negligible such that the fluctuations in underground muon energy due to the large range of energies in the spectrum are lower than those due to range straggling, as proposed by T. K. Gaisser in [5], the survival probability can be written as a step function, Θ [207]:

$$P(E^s,X) = \Theta(E^s - E^s_{\mathrm{min}}(X)), \tag{6.13}$$

where E^s_{min} is the minimum energy a muon must have at the surface in order to reach a depth X underground. This allows for a semiquantitative calculation of muon fluxes underground, as has been carried out by P. Lipari and T. Stanev in [105] for the PROPMU code.

However, this treatment of the survival probabilities as a step function is a rough approximation, and breaks down for underground laboratories deeper than a few kilometres water equivalent. Because of the larger propagation depths to these deep labs, range straggling is not negligible, and the CSDA results in underground muon energies far above experimental values [36, 105]. More recently, analytical calculations of muon survival probabilities through matter, taking into account energy loss via ionisation, bremsstrahlung, pair production, and photonuclear interactions, have been proposed (see [208, 209]). However, these calculations are only presented for very shallow ranges of matter ($\ll 0.1$ km.w.e.) for the purposes of muon tomography, and so are not applicable to deep underground analyses.

The only suitable method for accurately calculating survival probability at deep depths, therefore, remains Monte Carlo simulations. MUTE derives its survival probabilities from the surface-to-underground transfer tensors calculated by PROPOSAL and explained in Section 6.4.5. $P(E^s,X)$ values can be obtained by integrating the transfer tensor over the underground energies:

$$P(E^s,X) = \int_0^\infty U(E^s,E^u,X)\mathrm{d}E^u. \tag{6.14}$$

The integrals over the columns of the transfer matrices, such as the one illustrated in Figure 6.11, are shown as survival probabilities in Figure 6.12 for multiple values of X. As shown, as surface energy increases, the survival probability increases, as muons with higher energies have more of a chance to survive the propagation. In addition to this, as slant depth increases, survival probability decreases, as the muons have more rock (or water) to travel through, and so undergo more interactions and lose more energy, and are thus more likely to decay.

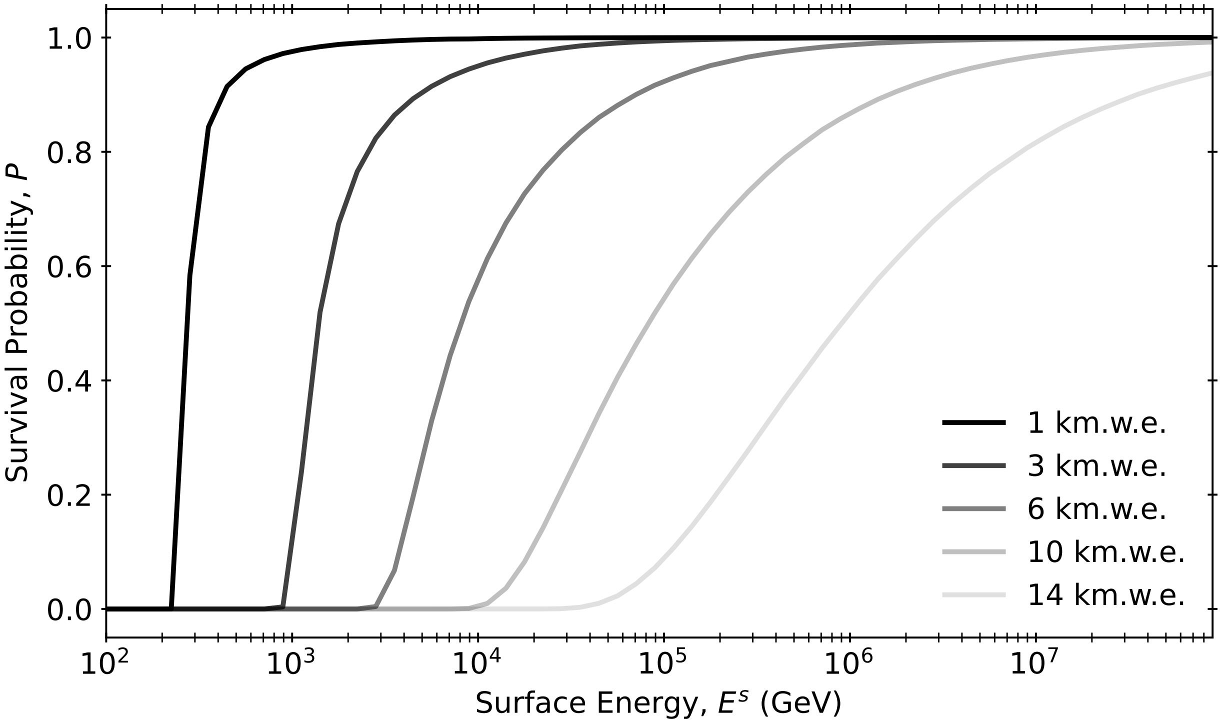

Figure 6.12: Survival probability against surface energy for various slant depths. At low depths, the survival probability curve seems to approximate a step function, as given in Equation (6.13). However, at lower depths, where the mean muon surface energy is higher and range straggling becomes more significant, a step function is ill-suited to describe the shape of the curve, demonstrating the need for Monte Carlo simulations.

6.5 Computational Method

After loading or calculating the surface flux matrix, $\Phi^s(E^s, \theta)$, and transfer tensor, $U(E^s, E^u, X)$, using the `surface` and `propagation` modules respectively, the first step in the `underground` module is to perform a convolution between the two in order to calculate a tensor of underground fluxes, $\Phi^u(E^u, X, \theta)$, given mathematically by a simple discrete linear algebraic operation:

$$\Phi^u(E_j^u, X_k, \theta_\ell) = \sum_i \Phi^s(E_i^s, \theta_\ell) U(E_i^s, E_j^u, X_k) \left(\frac{\Delta E_i^s}{\Delta E_j^u} \right). \tag{6.15}$$

where X is the depth along the initial trajectory and depends on the zenith angle, as defined in Equation (6.7). The ratio of surface and underground energy bin widths, $(\Delta E_i^s / \Delta E_j^u)$, is to account for the fact that muons starting in the same energy bin at the surface can end up in different energy bins underground, as muons do not always lose the same amount of energy while travelling through the rock or water.

After this convolution is performed and MUTE has the underground flux tensor, according to the flowchart in Figure 6.2, the program diverges based on what output the user wants. In particular, there is a divergence between calculation methods and output for labs under flat overburden and those under mountains.

6.5.1 Flat Overburdens

In the case of a flat overburden, symmetry is assumed in the azimuthal angle, which reduces the number of dimensions of most variables from the general case by one, as there is no longer dependence on ϕ. Labs under a flat overburden have a well-defined and fixed vertical depth, h, and so, through Equation (6.7), there is a one-to-one correspondence between zenith angle and slant depth, meaning observables are returned either as a function of X or as θ, but not both. This fact is used to optimise the linear algebraic calculations in the code.

The `mtu.calc_u_fluxes()` function returns a matrix $\Phi^u(E^u, \theta)$. It does this by first performing the convolution in Equation (6.15) to the grid constants `mtc.ANGLES_FOR_S_FLUXES` and `mtc._SLANT_DEPTHS` to obtain the tensor of shape $\Phi^u(X, E^u, \theta)$, then interpolating the tensor in θ from `mtc.ANGLES_FOR_S_FLUXES` to `mtc.angles` so that the angles and slant depths correspond to each other. The diagonal of the tensor along the X and θ axes is then taken, returning a two-dimensional $\Phi^u(E^u, \theta)$ matrix. The calculations for underground intensities and total underground fluxes begin as well with the full $\Phi^u(X, E^u, \theta)$ tensor from the convolution. These calculations are further explained in Chapters 7 and 8.

In all cases, when choosing which functions and routines to use for integration and interpolation, in-depth checks have been performed to ensure optimisation of the code in terms of both computation time and stability and precision of the results.

6.5.2 Mountain Profiles

For labs under mountains, the calculations are slightly more complicated; labs do not have well-defined vertical depths, and the amount of rock a muon has to travel through is dependent, in this case, on both the zenith angle and the azimuthal angle, and so the geometry of the mountain retaining information about the azimuthal angle has to be taken into account in the calculations. To do this, topographic maps of the mountains in terms of $X(\theta, \phi)$ data are obtained from the labs, such as the one for Gran Sasso in Figure 6.13, and those for the other labs from Table 5.1 in Figure 5.5. A text file containing a topographic map of the mountain's profile in these spherical coordinates must be loaded into the code with the `mtc.load_mountain()` function. This then sets the slant depths, zenith angles, and azimuthal angles for which the calculations in the `underground` module are performed, as explained in Section 6.2.

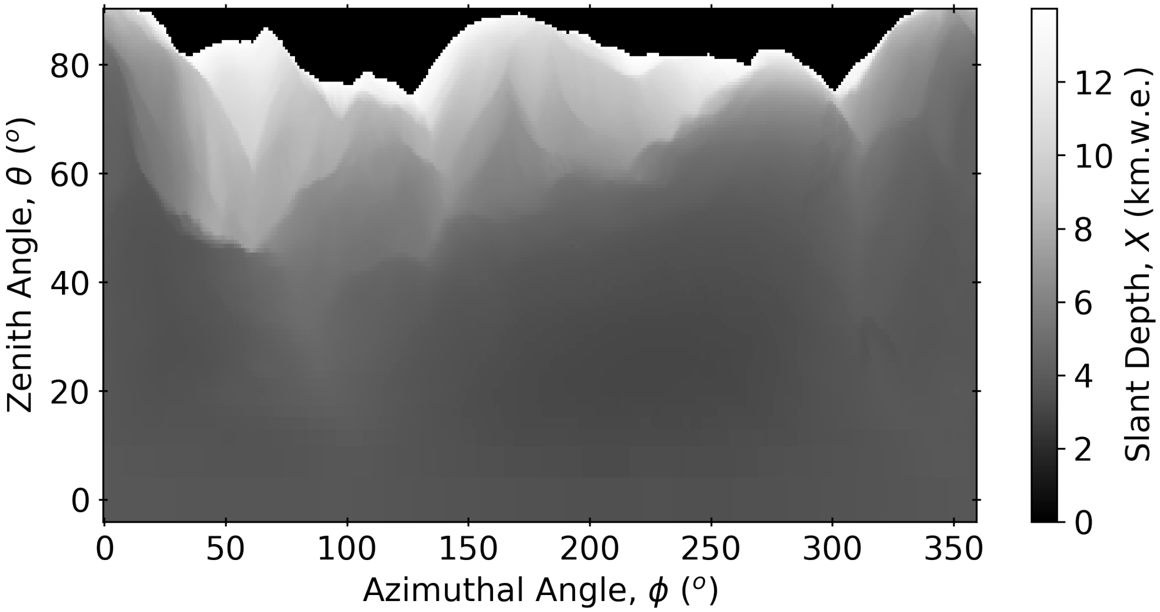

Figure 6.13: A plot of the slant depths of the Gran Sasso mountain, $X(\theta, \phi)$, in terms of zenith and azimuthal angle. Depths above 14 km.w.e. have been masked (shown in black), as 14 km.w.e. is the default maximum slant depth for which calculations can be done by MUTE.

Because the slant depth and zenith angle are related to each other but do not form a one-to-one correspondence for mountains, they are kept as separate variables, and the `mtu.calc_u_fluxes()` function returns the full $\Phi^u(X, E^u, \theta)$ tensor without any diagonalisation as in the case of flat overburdens. Because of this, the only underground intensity calculation available for mountains is double-differential (differential in slant depth and zenith angle):

$$I^u_{\mathrm{dd}}(X, \theta) = \frac{\mathrm{d}N}{\mathrm{d}X\,\mathrm{d}\cos(\theta)}. \tag{6.16}$$

To have this in physical units, this is further divided by infinitesimal units of area and time, $\mathrm{d}A\mathrm{d}t$. In practice, this is calculated from Φ^u in MUTE, which obtains its physical units from Φ^s from

MCEQ or DAEMONFLUX. The underground intensity, along with the total underground flux for mountains, is explained further in Chapters 7 and 8.

The variation in altitude for different points on the mountain for any given location is on the order of many kilometres. Although altitude is important in both the USStd and NRLMSISE-00 models, these variations in altitude along the surface of the mountains have been neglected throughout all calculations, as they are assumed to be negligible to the surface flux in this case.

7 Underground Intensity

The underground muon intensity, $I^u(\theta, \phi)$, also called the directional intensity, is the first physical observable of interest that can be calculated with MUTE. It is defined as the number of muons underground ($\mathrm{d}N_\mu^u$) that pass through a unit of area ($\mathrm{d}A$) per unit time ($\mathrm{d}t$) per unit solid angle ($\mathrm{d}\Omega$), and is typically measured in units of $[\mathrm{cm}^{-2}\mathrm{s}^{-1}\mathrm{sr}^{-1}]$ [56]:

$$I^u(\theta, \phi) = \frac{\mathrm{d}N_\mu^u}{\mathrm{d}A\mathrm{d}t\mathrm{d}\Omega}. \tag{7.1}$$

Throughout the decades, it has been common for experiments to publish measurements of the underground muon intensity and for parameterisations to be done in terms of vertical underground intensity. This is because the surface muon flux and the energy loss of muons in rock are both dependent on the zenith angle, so muons coming in at different angles have different energies. By converting directional intensity to vertical intensity, measurements done at different depths can be compared independent of their zenith angle dependence. This is especially useful for laboratories under mountains because using vertical intensity means the measured intensity can be compared to theoretical predictions without requiring knowledge of the mountain profile.

In MUTE, there are four types of intensities that can be calculated. For flat overburdens, there are single-differential, vertical-equivalent, and true vertical intensities, and for mountains, there are double-differential intensities that are available.

The maximum slant depth available in MUTE for both flat and mountainous overburdens is 14 km.w.e. This is because, beyond 14 km.w.e., the underground muon flux is dominated by neutrino-induced muons. Atmospheric and astrophysical neutrinos have energies low enough to travel through the Earth, and can interact with the rock to produce local muons. The flux of these muons is constant but is of the order of around 10^{-13} $\mathrm{cm}^{-2}\mathrm{s}^{-1}$, which only becomes significant compared to atmospheric muons at around 14 km.w.e.

7.1 Underground Intensities for Flat Overburdens

In MUTE, single-differential underground intensities as a function of zenith angle, $I^u(\theta)$, are calculated by integrating the underground flux, defined by Equation (6.15), over the underground energy:

$$I^u_{\text{sd}}(\theta) = \int_{E_{\text{th}}}^{\infty} \Phi^u(E^u, X, \theta)\mathrm{d}E^u, \tag{7.2}$$

where E_{th} is the threshold energy that a muon needs to survive the journey underground to the lab or a detection threshold of an experiment. This value can be set by the user (in which case MUTE, during the computation of the integral, will set the actual threshold energy to the value in the energy grid that is nearest to the user-set threshold), where the default is 0 GeV. Here, the value is set to 0 GeV for all labs, for generality. For deeper X, the dependence on E_{th} is small since the mean muon energy increases with depth. Rather than keeping the intensity as a function of multiple variables, $I^u(X, \theta, \phi)$, it is reduced to a function of one variable, the single-differential underground intensity, due to non-dependence on the azimuthal angle and the degeneracy between the zenith angle and slant depth for flat overburden geometries.

In MUTE, all four available types of underground intensities are calculated first by integrating the underground flux tensor as in Equation (7.2), which produces a matrix $I^u(X, \theta)$, shown in Figure 7.1 (left). This matrix is then used to compute the three types of underground intensities for flat overburdens. For single-differential intensities, a two-dimensional spline object is created from the matrix. This spline returns a callable function of two variables, which is then evaluated at the vertical depth-adjusted slant depth and zenith angle variables in the `constants` module of MUTE. This then returns an array of underground intensities.

An example of how single-differential underground intensities are calculated with MUTE for a laboratory under a flat overburden with vertical depth 2.7 km.w.e. is shown in Listing 7.1.

Listing 7.1: A MUTE script which calculates single-differential (`"sd"` in the code) underground muon intensities for a lab under 2.7 km.w.e. of flat earth. All of the parameters after `method` in the function call are optional, and are shown set to their default values here.

```python
import mute.constants as mtc
import mute.underground as mtu

mtc.set_vertical_depth(2.7)
mtu.calc_u_intensities(method="sd", angles=mtc.angles, E_th=0,
                       primary_model="GSF",
                       interaction_model="SIBYLL-2.3c",
                       atmosphere="CORSIKA", location="USStd")
```

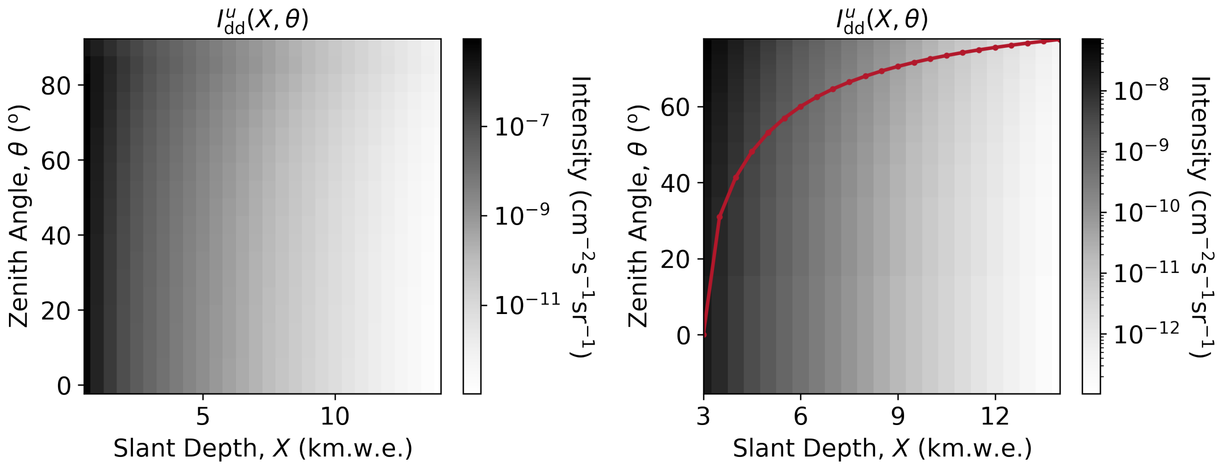

Figure 7.1: Underground intensity matrices as a function of slant depth and zenith angle. The calculations of these matrices are intermediate steps in the MUTE algorithm for calculating underground muon intensities for laboratories under flat overburdens. The left plot shows the default grid plotted against `mtc._SLANT_DEPTHS` and `mtc.ANGLES_FOR_S_FLUXES`. The right plot shows the interpolated matrix for a laboratory with a vertical depth of 3 km.w.e., plotted against `mtc.slant_depths` and `mtc.angles`. The red curve in the right plot shows the points at which the angles correspond to the slant depths. This curve is returned by the `mtu.calc_u_intensities(method = "sd")` function as an array.

7.1.1 Vertical Intensity

Although the single-differential intensity is provided by MUTE, it is not used frequently in the field of underground muons. What is used more frequently is the vertical-equivalent muon intensity. This is calculated by multiplying the muon intensity in Equation (7.2) by $\cos(\theta)$:

$$I^u_{\mathrm{eq}}(X) = I^u_{\mathrm{sd}}(\theta)\cos(\theta). \tag{7.3}$$

Here, I^u_{eq} can be a function of X through the relation $X = h/\cos(\theta)$. This is the form in which muon intensities are typically given in the literature (see [89, 143, 144, 210]), since detectors are located at a fixed vertical depth. The justification of this multiplication by $\cos(\theta)$ to approximate the vertical intensity comes from the approximation that the muon flux at the surface varies as $1/\cos(\theta)$, which is derived from the assumptions made about the atmosphere, leading to Equations (3.14) and (3.15). Substituting the definition of the decay rate from Equation (3.14) into Equation (3.15) and multiplying both sides by $\cos(\theta)$ results in:

$$I^u\cos(\theta) = \frac{\varepsilon_\mu}{X}\int_{m_\mu c^2}^{\infty}\frac{N_\mu(E_\mu, X)}{E_\mu X}\mathrm{d}E_\mu. \tag{7.4}$$

The measurements of the vertical-equivalent intensity from multiple experiments are shown in Figure 7.2.

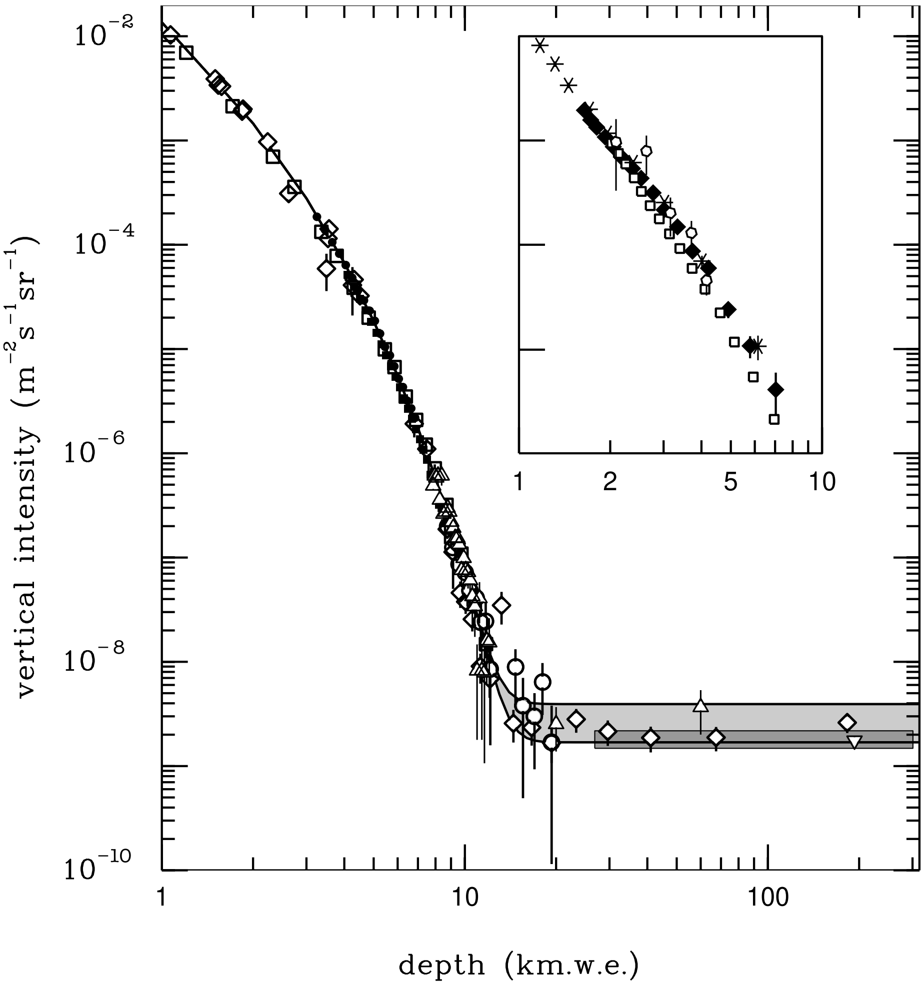

Figure 7.2: Vertical underground muon intensity vs depth, taken from [211]. This plot includes the classic Crouch "world survey data set" [159], which is a compilation of measurements from different laboratories (under flat earth, mountains, and underwater), and the data is accompanied by systematic uncertainties that are difficult to control. For this reason, this data set is excluded in further plots. Beyond 14 km.w.e., the intensity levels off at around 10^{-9} m^{-2}s^{-1}sr^{-1} due to neutrino-induced muons.

It is widely known that the relation in Equation (7.3) is only approximate [1, 3], and the deviation between the true vertical intensity, defined as

$$I^u_{\text{tr}}(X) = I^u(X, \theta = 0), \tag{7.5}$$

and the vertical-equivalent intensity becomes significant as θ increases.

The true vertical underground intensity from Equation (7.5) is provided in MUTE through the `mtu.calc_u_intensities(method = "tr")` function, where it is calculated by simply taking the bottom row of the matrix in Figure 7.1 for $\theta = 0$ and returning it as an array. The result using the DAEMONFLUX model is plotted against slant depth for standard rock in Figure 7.3. There is

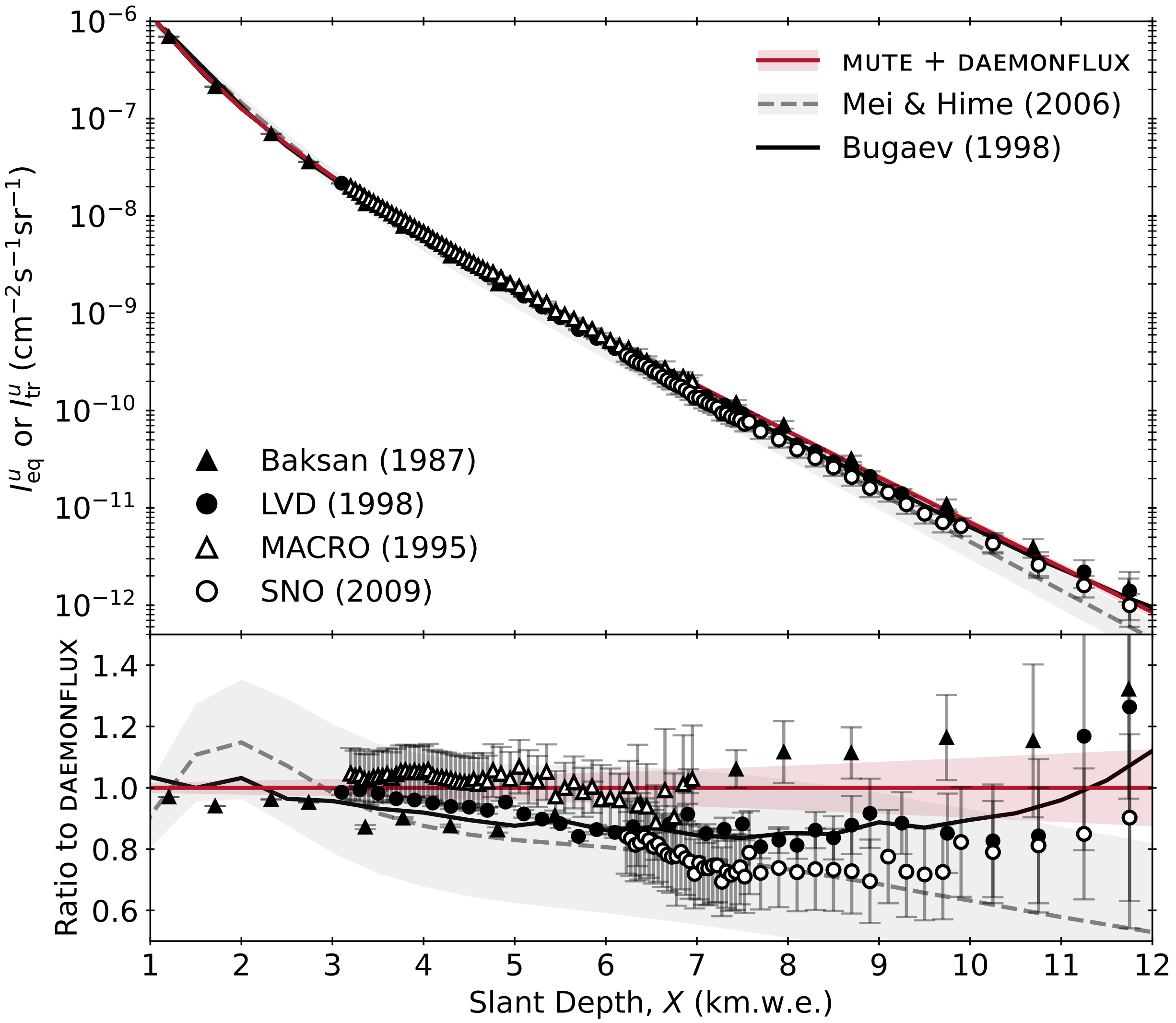

Figure 7.3: True vertical underground muon intensity calculated for standard rock with the DAEMONFLUX model (top) and ratio to DAEMONFLUX (bottom) vs slant depth. Curves are shown for the D.-M. Mei and A. Hime DIR [107], and the E. V. Bugaev, et al. calculation [3]. Experimental data is taken from Baksan [210], LVD [143], MACRO [144], and SNO [89]. Data and the curve from [107] are vertical-equivalent, whereas [3] and our calculations are for true vertical intensity. Systematic and statistical errors are geometrically summed for LVD, MACRO, and SNO. Other error bars denote solely statistical errors.

excellent agreement between the MUTE results and the experimental data over the entire depth range within uncertainties, which can be seen in higher detail in the bottom panel of Figure 7.3, which plots the ratio of the other curves and the data to the DAEMONFLUX curve for standard rock. Comparisons to additional hadronic interaction models are shown in Figure B.1 in Appendix B.

Visually, the data, without correction for systematics, is in good agreement with the fit by D.-M. Mei and A. Hime [107] and the Bugaev calculation [3]. However, the depth dependence of individual data sets follows that of MUTE more consistently. The difference in the slope between the D.-M. Mei and A. Hime band and the MUTE calculation is a result of the simple parameterisation by a sum of two exponential functions described in Section 5.3.2. The relatively large errors of D.-M. Mei and A. Hime are estimated from the fit to underground data and can exhibit bias from systematic uncertainties and the fixed form of the parameterisation.

The intensity has also been plotted for water in Figure 7.4. The curve here is slightly different from that of Figure 7.3 for standard rock because of the chemical differences between water and rock (see the definitions of the media in Table 6.3 and the rock and water curves in Figure 6.10). MUTE finds agreement here with all other predicted vertical intensities shown, including those by the MUM code and the Sinegovskaya calculations from [212], although neither estimates inclusive muon flux uncertainties.

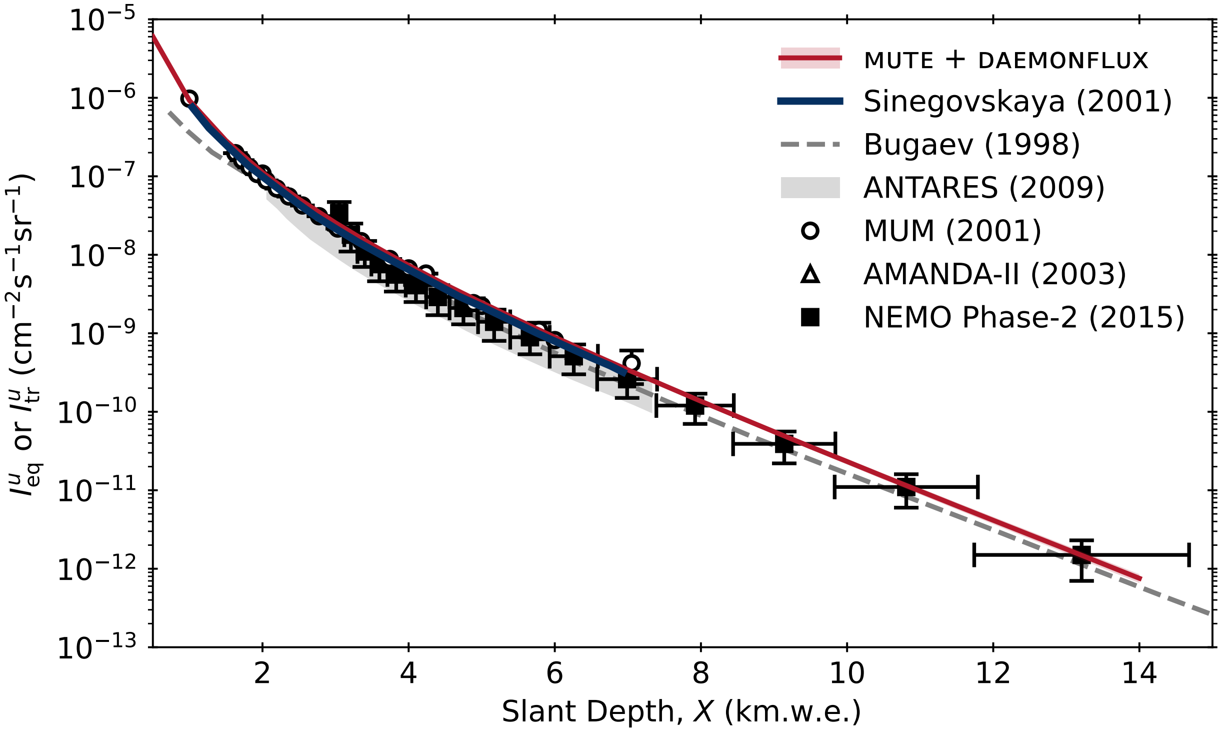

Figure 7.4: True vertical underground muon intensity calculated for sea water with the DAEMONFLUX model against slant depth, with experimental data from ANTARES [213], NEMO Phase-2 [214], and AMANDA-II [215], calculation from Sinegovskaya [212], and simulation from MUM [216]

7.1.2 Zenith-Angle Dependence

The difference between vertical-equivalent and true vertical intensities is demonstrated in Figure 7.5 by plotting the ratio of the two against the zenith angle. The vertical-equivalent approximation performs worse at larger zenith angles and shallower depths, as the deviation of the vertical-equivalent intensity from the true vertical intensity for an experiment located at a depth of 3 km.w.e. measuring muons coming in at a zenith angle of 60° is 5%, shown by the solid grey lines, whereas it rises to 15% for an experiment located at a depth of 1 km.w.e. The reason why this is the case is illustrated in Figure C.1 in Appendix C.

This ratio is plotted again in Figure 7.6, with the inclusion of the data and curves from Figure 7.3. This plot, like Figure 7.5, again shows that the deviation of vertical-equivalent intensity from true vertical intensity is worse for shallower vertical depths and deeper slant depths. The underground muon intensity data is seen to follow the trend of this deviation, as it is presented by the experiments in terms of vertical-equivalent intensities.

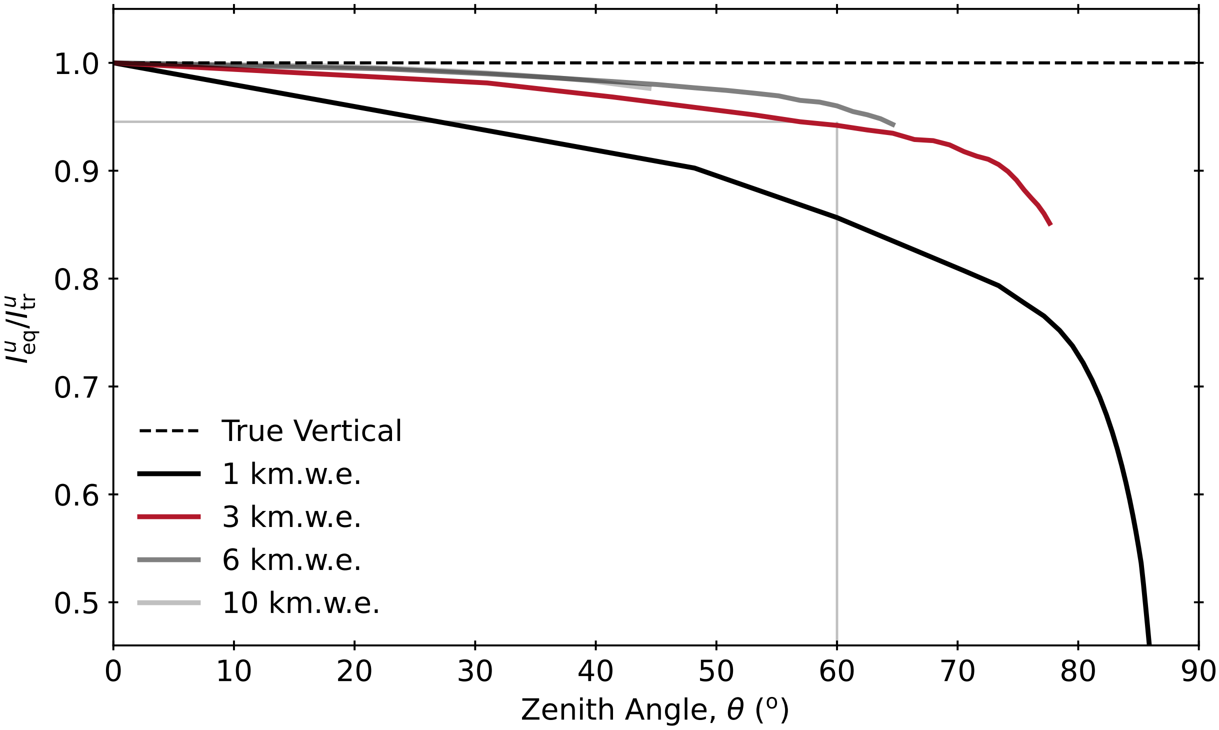

Figure 7.5: The ratio of vertical-equivalent to true vertical muon flux as a function of the zenith angle. The black dashed line is the expectation for the case of perfect agreement. The solid curves show deviation due to the approximation in Equation (7.3) from the true vertical intensity, and stop at slant depths of 14 km.w.e.

While MUTE is not the first instance of a distinction being drawn between vertical-equivalent and true vertical intensity, as this aspect has been discussed in classic literature (see [217], which acknowledges the systematic errors introduced in the approximation of vertical-equivalent intensity and uses true vertical intensity in their theoretical calculation, as well as the original Barrett study [2]), many experimental results are still reported under the assumption of the $1/\cos(\theta)$ ap-

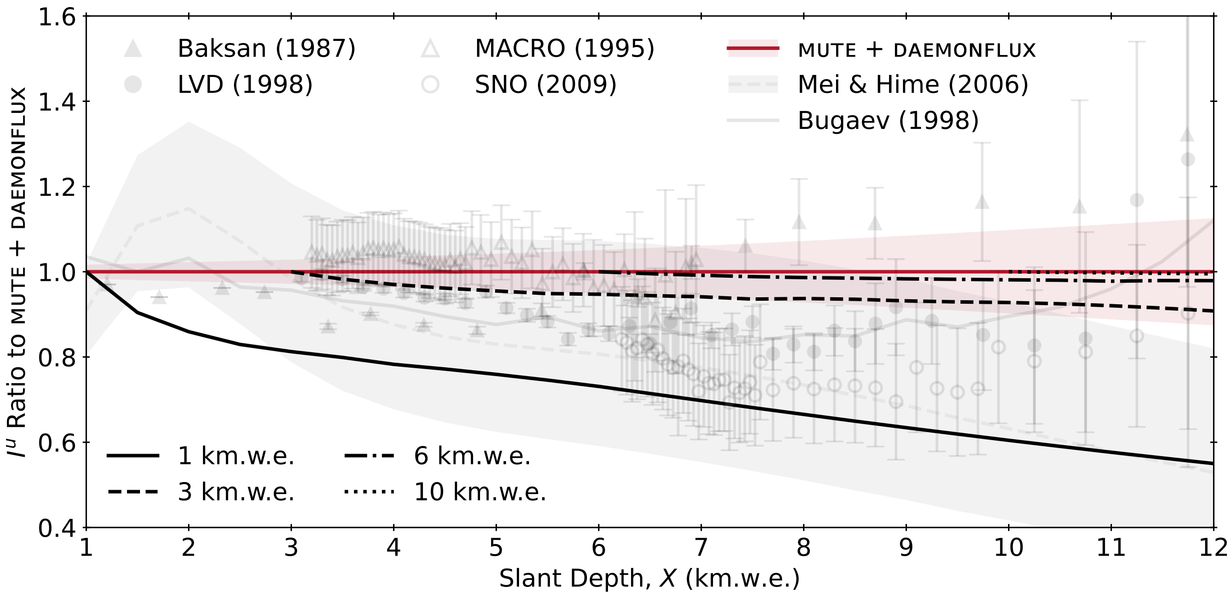

Figure 7.6: The ratio of the vertical-equivalent intensity to the true vertical intensity against slant depth for various initial vertical depths as calculated by MUTE for standard rock using DAEMONFLUX and GSF. Each curve starts at the vertical depth indicated in the legend for $\theta = 0$. All experimental data is referenced in Figure 7.3.

proximation at much larger zenith angles. MUTE calculations, however, suggest that Equation (7.3) should not be used for zenith angles significantly larger than 20°. Because the true vertical intensity is typically inaccessible for laboratories located at a fixed geometrical depth, though, reporting double-differential measurements in X and true zenith angle, θ, would be beneficial for the theoretical analysis of the data as, for example, in [218].

7.2 Underground Intensities for Mountains

For mountain profiles, the double-differential (“dd” in the code) muon intensity is given by integrating the underground flux over the underground energy:

$$I^u_{\mathrm{dd}}(X,\theta) = \int_{E_{\mathrm{th}}}^{\infty} \Phi^u(E^u, X, \theta)\mathrm{d}E^u, \tag{7.6}$$

This is calculated as a matrix of intensities, $I^u(X,\theta)$, or $I^u(\theta,\phi)$

To do these calculations, the intensities are first calculated by MUTE on a constant grid of default X and θ values, shown in Figure 7.7 (left). These intensities are then interpolated to the $X(\theta,\phi)$ given by the topographic map of the mountain obtained from the experiments (represented by `mtc.mountain.zenith` and `mtc.mountain.azimuthal` in MUTE respectively), and the resulting intensities are reshaped into a matrix of the form $I^u(\theta, \phi)$, which is returned by MUTE, shown in Figure 7.7 (right).

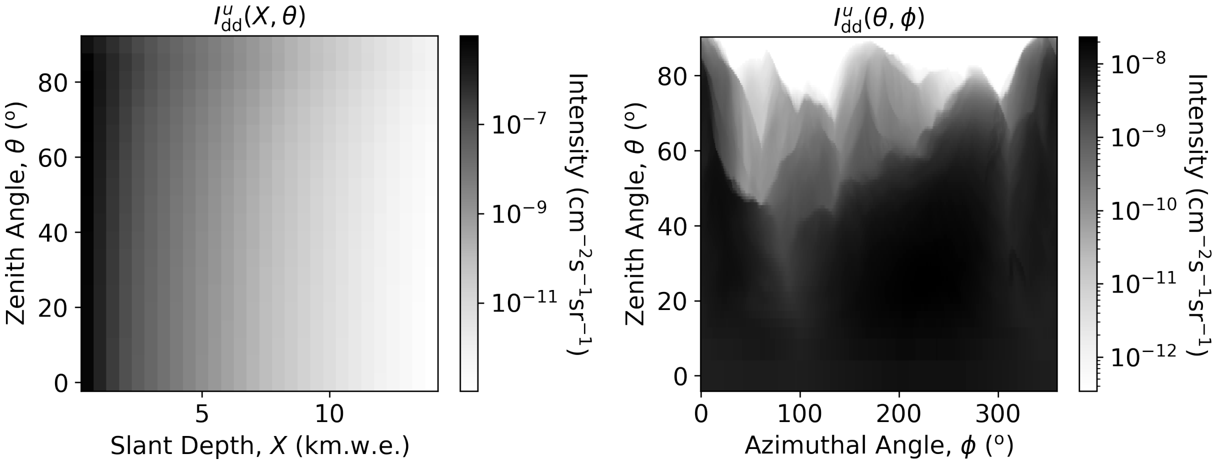

Figure 7.7: Underground intensity matrices calculated by MUTE as a function of slant depth and zenith angle (left), then interpolated and reshaped into a function of zenith angle and azimuthal angle for the Gran Sasso mountain (right). The matrix in the plot on the right is returned by the `mtu.calc_u_intensities("dd")` function as a two-dimensional array. This plot is comparable to that of the slant depths for LNGS in Figure 5.5.

7.3 Underground Angular Distributions

The underground angular distribution of muons under mountains is calculated from the double-differential underground intensity by integrating the intensity over one angle at a time, either the azimuthal angle to get the zenith distribution, or over the zenith angle to get the azimuthal distribution, represented respectively as:

$$\Phi^u_\phi = \frac{\mathrm{d}N^u_\mu}{\mathrm{d}A\mathrm{d}t\mathrm{d}\cos(\theta)} = \int_0^{2\pi} I^u(X(\theta,\phi),\theta)\mathrm{d}\phi, \tag{7.7}$$

$$\Phi^u_\theta = \frac{\mathrm{d}N^u_\mu}{\mathrm{d}A\mathrm{d}t\mathrm{d}\phi} = \int_0^1 I^u(X(\theta,\phi),\theta)\mathrm{d}\cos(\theta). \tag{7.8}$$

Many detectors can measure the one-dimensional or two-dimensional angular distribution of muons up to a certain angle, depending on the geometry of the detector, and some depend on it for data analyses, including event reconstruction or signal discrimination and rejection in the context of directionality studies.

7.3.1 Case Study with the LVD Experiment

The Large Volume Detector (LVD) is a neutrino telescope experiment located approximately 3 km.w.e. underground in Hall A of LNGS in Italy (shown in Figure 5.7). LVD is a modular detector divided into three towers, with a total of $3 \times 35 \times 8 = 840$ scintillation counters, each of which acts as its own sub-detector. Because of this highly modular design, it can measure the angular distribution of atmospheric muons with high resolution.

Double-differential data of raw muon counts and detector acceptance as a function of zenith and azimuthal angle, $n(\theta, \phi)$ and $\varepsilon(\theta, \phi)$ respectively, representing over 10 years of data collection, was obtained from the LVD experiment [143]. Using this data, experimental one-dimensional underground angular distributions were calculated, and were then compared with the predictions from MUTE that were calculated using the map of the Gran Sasso mountain in Figure 6.13. In MUTE this was simply done by first loading the mountain profile file into MUTE and running `mtu.calc_u_intensites(method = "dd")`, following the method described in Section 7.2, to calculate the MUTE intensities, $I^u_{\mathrm{MUTE}}(\theta, \phi)$. The result is shown in Figure 7.8 (top). After this, the integrations in Equations (7.7) and (7.8) were performed to calculate the angular distributions. Lastly, using `mtu.calc_u_tot_flux()` returned the MUTE prediction for the total flux, $\Phi^u_{\mathrm{MUTE,\ tot}}$.

For the calculations with the LVD data, the intensities, $I^u_{\mathrm{LVD}}(\theta, \phi)$, were first calculated according to the following equation:

$$\begin{aligned} I^u_{\mathrm{LVD}}(\theta, \phi) &= K \left(\frac{n(\theta, \phi)}{\varepsilon(\theta, \phi)} \right) \\ &= KF, \end{aligned} \tag{7.9}$$

where K is a normalisation constant representing the product of detector lifetime and effective area, used to convert the I^u_{LVD} values to physical units, and F is a convenience variable for the counts divided by acceptance, defined to simplify further calculations. Because the maximum slant depth available in MUTE is 14 km.w.e., in order to compare the LVD and MUTE results, the counts and acceptance matrices were masked for (θ, ϕ) coordinates at which $X(\theta, \phi) > 14$ km.w.e. After calculating F, K was then calculated by requiring the total integrated underground fluxes from MUTE and from the LVD data to be equal:

$$K = \frac{\Phi^u_{\mathrm{tot,\ MUTE}}}{\iint_{\Omega} \left(\frac{n(\theta,\phi)}{\varepsilon(\theta,\phi)} \right) \mathrm{d}\Omega}. \tag{7.10}$$

The comparison between the experimental and predicted intensities was performed by calculating the pulls for each (θ, ϕ)-bin of the data:

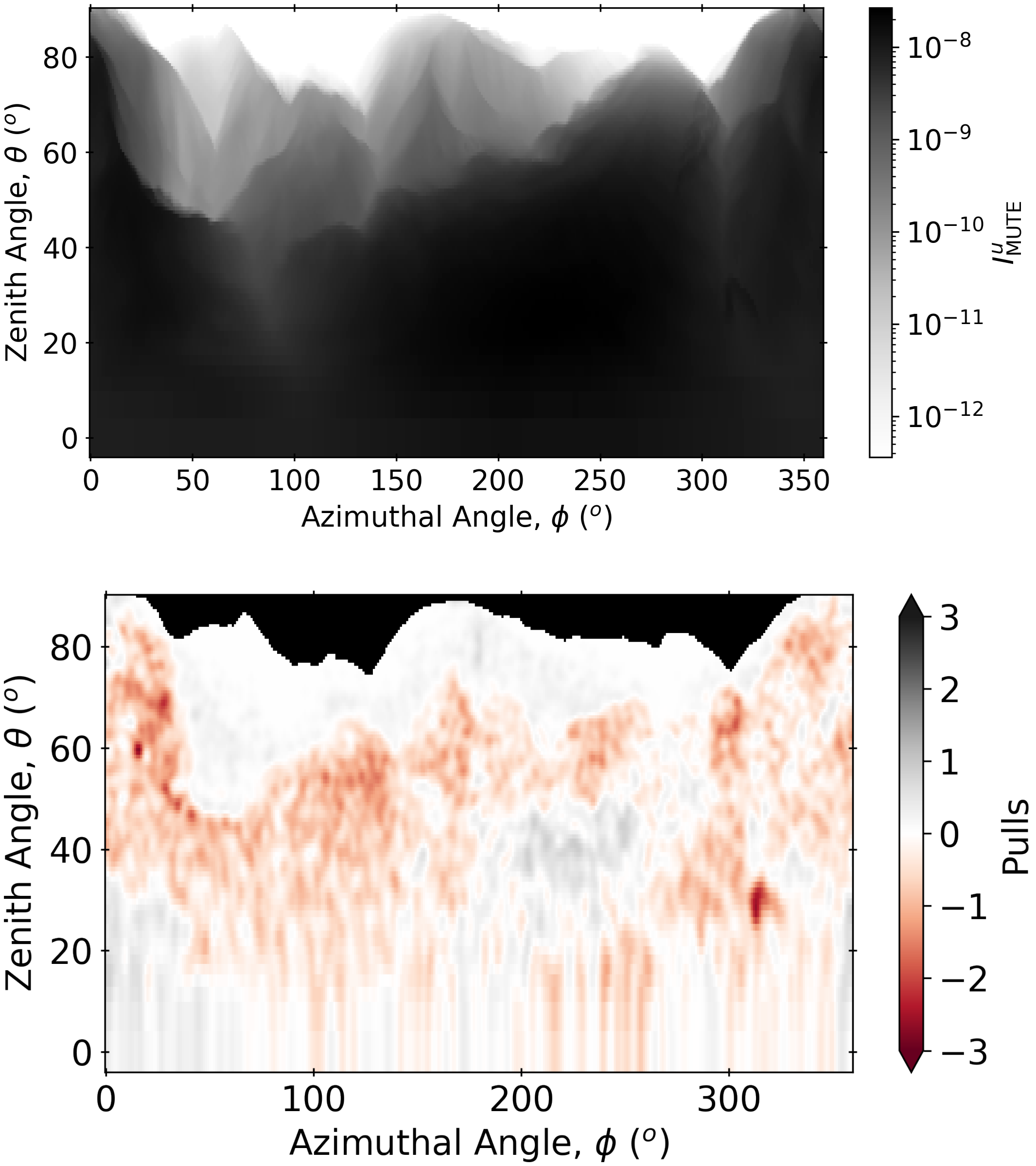

Figure 7.8: Underground double-differential muon intensities for the Gran Sasso mountain as calculated by MUTE (top) and the pulls of the LVD data (bottom) as a function of zenith and azimuthal angle. Because the binning on the map of the Gran Sasso mountain is very fine, with large bin-to-bin fluctuations in the pulls, a Gaussian filter ($\sigma = 1.5$) has been applied to help identify any characteristic trends. In the plot of the pulls, black indicates masked bins for which the slant depth is greater than 14 km.w.e.

$$\mathrm{Pull} = \frac{I^u_{\mathrm{LVD}} - I^u_{\mathrm{MUTE}}}{\delta I^u_{\mathrm{LVD}}}, \tag{7.11}$$

where $\delta I^u_{\mathrm{LVD}}$ is the statistical error in each angular bin, defined below in Equation (7.14). The result is shown in Figure 7.8 (bottom). Because the normalisation matches by construction, only relative trends can be observed. Although the pulls are mostly negative and some features are visible where they are above one standard deviation, there does not appear to be a significant characteristic trend, and it is noted that these features come from the LVD data rather than the mountain map or the MUTE calculation. The calculation is slightly below the data at near-vertical directions and above it for intermediate zenith angles, except for a small patch in the southwest direction ($\phi \approx 225^\circ$), where the situation is inverted. There is therefore some deviation from the LVD data, which claims high precision with small error estimates, and we estimate the χ^2/ndf to be 1.34, where ndf is assumed to be the number of non-zero bins ($\text{ndf} = 31756$). The LVD data was rebinned in terms of slant depth and zenith angle in order to explore the expected sea-level azimuthal symmetry of the muon flux. Values of I^u_{MUTE} and I^u_{LVD} with the same values of X and θ and varying ϕ should be the same — with small amounts of deviation expected due to bin size and interpolation error — meaning a narrow distribution is expected. We found that the spread of values in the data bins is higher than that from MUTE simulations, and they are also higher than what would be expected given the systematic errors on the data, which suggests there may be an imprecision in the mountain map that cannot be accounted for in the MUTE analysis.

Following the integrations in Equations (7.7) and (7.8), the one-dimensional projections of the angular distributions were calculated for the LVD data, and are shown in Figure 7.9 for the zenith (top) and azimuthal (bottom) directions, compared to the MUTE predictions. The error bars on the LVD data points represent errors that were propagated from the uncertainty from DAEMONFLUX and the uncertainties in the LVD counts and acceptance data using these equations:

$$\delta\Phi^u_{\phi,\,\text{LVD}} = \sqrt{\sum_j (\delta I^u_{\text{LVD},\,j}\Delta\phi)^2}, \tag{7.12}$$

$$\delta\Phi^u_{\theta,\,\text{LVD}} = \sqrt{\sum_i (\delta I^u_{\text{LVD},\,i}\Delta\cos(\theta))^2}, \tag{7.13}$$

where the indices i and j are, respectively, for the rows and columns of θ and ϕ values in the counts, acceptance, and intensity matrices, and $\Delta\cos(\theta)$ and $\Delta\phi$ are the constant step sizes in the numerical integrals for $\cos(\theta)$ and ϕ. These step sizes are defined by the granularity of the map in the mountain profile file for the Gran Sasso mountain in Figure 6.13. The uncertainty in the LVD data is given by the geometric sum of the relative errors of K and F:

$$\delta I^u_{\text{LVD}} = \sqrt{\left(\frac{\delta K}{K}\right)^2 + \left(\frac{\delta F}{F}\right)^2}. \tag{7.14}$$

Simplifying the numerator and denominator in the definition of K in Equation (7.10) to num/den, the uncertainties in K and F are given as:

$$\delta F = \frac{n}{\varepsilon}\sqrt{\left(\frac{\delta n}{n}\right)^2 + \left(\frac{\delta \varepsilon}{\varepsilon}\right)^2}, \tag{7.15}$$

$$\delta K = \delta\left(\frac{\text{num}}{\text{den}}\right) = K\sqrt{\left(\frac{\delta(\text{num})}{\text{num}}\right)^2 + \left(\frac{\delta(\text{den})}{\text{den}}\right)^2}, \tag{7.16}$$

where δn was taken as $\sqrt{n}$, and $\delta\varepsilon$ was given in the LVD data. The numerator and denominator in K are both calculated from numerical integrals. Therefore, their uncertainties will be given by the discrete matrix elements added in quadrature as:

$$\delta(\text{num}) = \sqrt{\sum_{ij}(\delta I^u_{\text{MUTE},\,ij}\Delta\cos(\theta)\Delta\phi)^2}, \tag{7.17}$$

$$\delta(\text{den}) = \sqrt{\sum_{ij}(\delta F_{ij}\Delta\cos(\theta)\Delta\phi)^2}. \tag{7.18}$$

We observe good compatibility with the result from MUTE within the small errors of the data, in particular for the zenith projection at near-horizontal directions. The shape of the underground zenith project reproduces that of a surface projection, as in Figure 6.7. The peak is around $\cos(\theta) = 0.9$, which corresponds to $\theta = 25°$. The flux is expected to drop off for low $\cos(\theta)$ values, because as the zenith angle increases, the muons have more rock to travel through, and so fewer survive. However, it also drops off as the zenith angle approaches vertical, because, although the muons have the least amount of rock to travel through at $\theta = 0$, the surface flux is lower here, due to the density of the vertical air column being higher than for the non-vertical direction. For the azimuthal projection, because the azimuthal angle wraps around the mountain, and the muon flux is inversely proportional to the amount of rock coverage, the shape of the mountain is roughly reproduced, with the flux peaking at approximately 10° and 250°, where the slant depths are the lowest, according to Figure 6.13. The agreement of the azimuthal projection is worse than that of the zenith projection, but since it is dominated by near-vertical zenith angles and shallower depths, it is consistent with what is otherwise observed for LVD. Therefore, there is good overall agreement between MUTE and the LVD data.

7.3.2 Implications for Data Analyses

Comparing the experimental and calculated angular distributions in Figures 7.8 and 7.9 can reveal important information about the accuracy of data analyses of underground experiments. While variables like the total underground flux or the amplitude of seasonal variations in the flux allow for comparisons to single data points for each laboratory, double-differential underground intensities

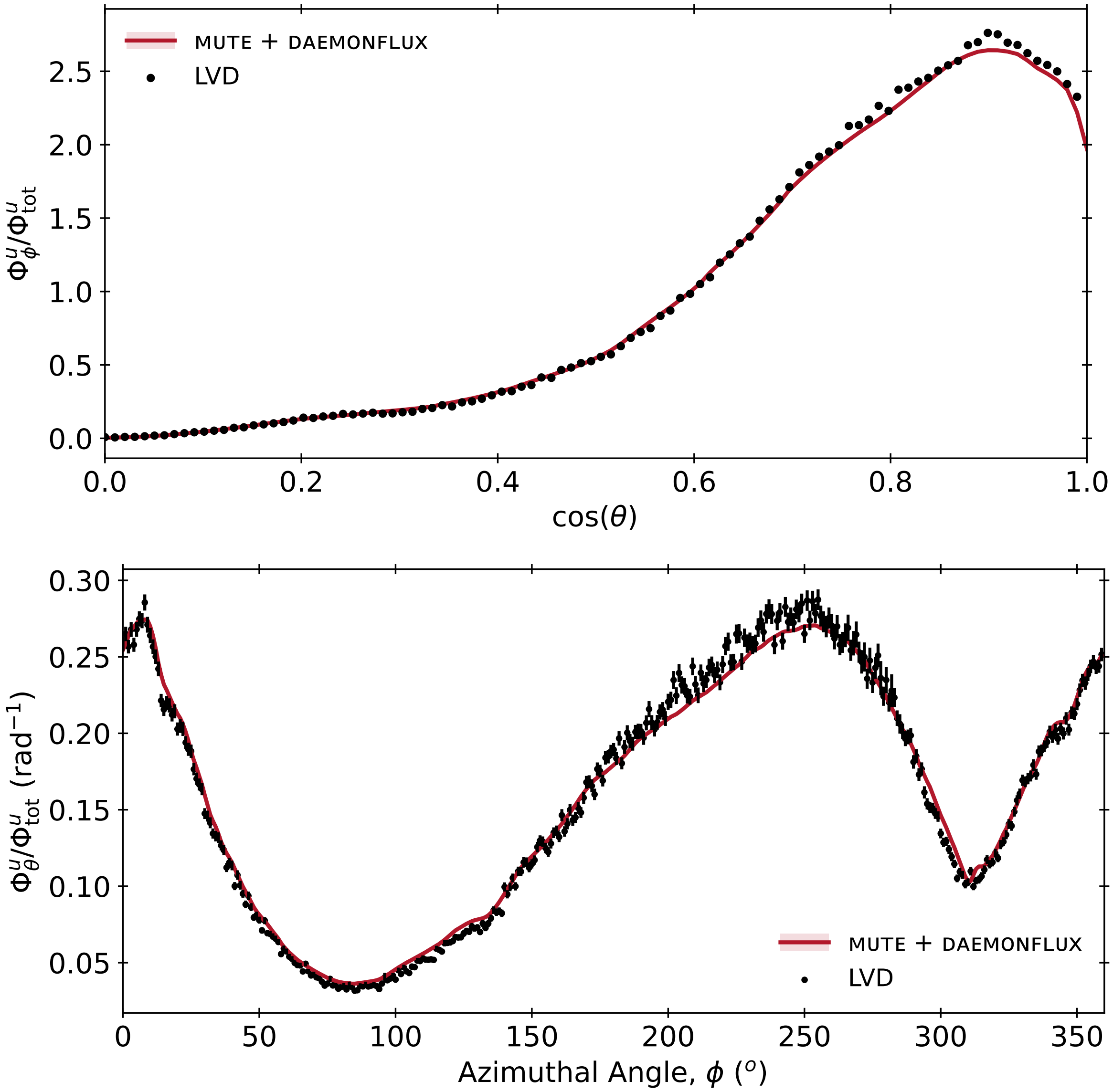

Figure 7.9: One-dimensional projections of the zenith (top) and azimuthal (bottom) angular distributions for the Gran Sasso mountain as calculated by MUTE, compared to data from the LVD detector [143]. The spectra have been normalised by the total underground muon flux in order to remove uncertainties coming from the hadronic and primary models. Error bars are present on the LVD data in the zenith angular distribution, as calculated by Equation (7.12), but are not visible.

and angular distributions allow for comparisons to a wider array of data, which can be much more revealing.

Continuing with the highly modular and well-resolved data from the LVD experiment, using the intensity matrix, a histogram of slant depths has been plotted in the top panel of Figure 7.10 (shown by the grey dashed curve), along with the red MUTE result for vertical-equivalent intensity for a vertical depth of 3 km.w.e., and published data from the LVD experiment from [143]. The bottom panel shows the ratio to the MUTE result.

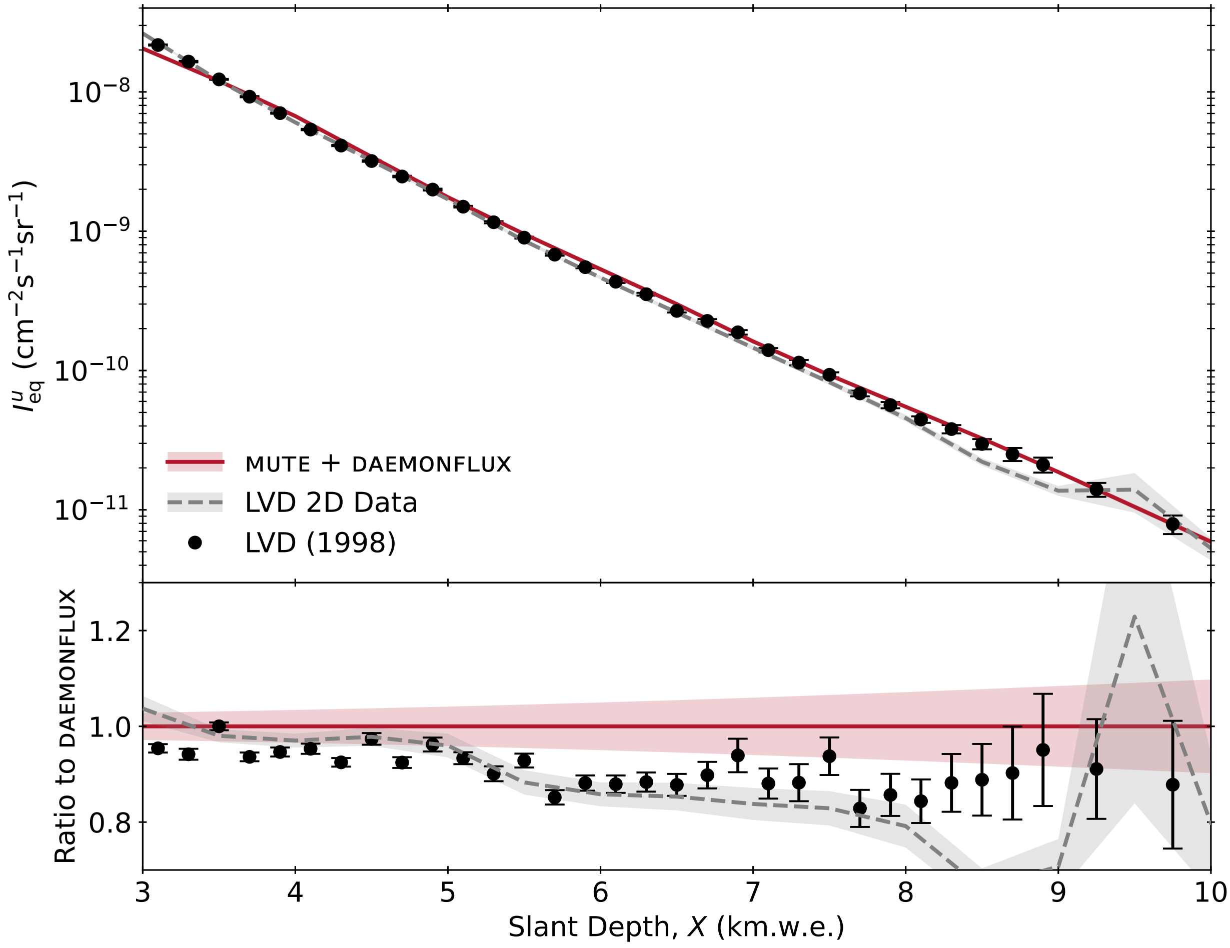

Figure 7.10: vertical-equivalent intensity vs slant depth (top) and ratio to DAEMONFLUX (bottom) for LVD data. The grey dashed curve is a weighted histogram calculated using the two-dimensional counts and acceptance data from LVD.

The histogram curve was constructed by binning the slant depths in the Gran Sasso mountain profile file, using the default slant depth grid from MUTE as bin centers. The intensities from the 2D plot in Figure 7.8 were used as weights, with the inclusion of a $\cos(\theta)$ factor for the comparison to vertical-equivalent data. The histogram was then normalised by the number of slant depths in each slant depth bin to avoid overcounting. Lastly, a correction factor, corr, was computed by taking the ratio of the MUTE result for flat overburdens to the result using the Gran Sasso map, in order to cancel out any discrepancies between the results originating from the mountain geometry:

$$\text{corr} = \frac{I^u_{\text{eq, MUTE}}}{I^u_{\text{dd, MUTE}}}. \tag{7.19}$$

This correction was then multiplied into the LVD histogram result, producing the grey dashed curve in Figure 7.10. The errors on the weighted histogram were taken as the square root of the histogram produced with the squares of the weights.

It can be observed that the histogram follows the published LVD data more closely than it does the MUTE result, but starts to deviate at around 7 km.w.e., corresponding to a zenith angle of approximately 64°. However, there is no trend visible, and the error bars on the LVD histogram and data points are both large. If a systematic trend had been seen in the deviation, this could suggest that the LVD detector reports more or fewer detections of muons than it actually does, pointing towards possible event misreconstruction in their data analysis. This could have a number of sources, for example, identifying delta electrons at large depths (large zenith angles and high energies) as muons.

Additionally, another issue experiments might encounter is the precision of their mountain profile file, for example, with the correct positioning of the detector or the lab under the mountain. If the lab is displaced by a significant amount in the file from its true position, then the prediction would report a higher flux of muons from one hemisphere of the sky and a lower flux from the other. This would be visible in both the plot of the pulls in Figure 7.8, which would be seen as one distinct hemisphere of positive pulls and one of negative pulls, as well as the azimuthal projection of the angular distribution in Figure 7.9.

In this way, in addition to providing forward predictions for muon spectra and fluxes, MUTE can also find application in cross-checking data analyses for underground and underwater detectors. With this case study, the LVD experiment was verified to have a well-composed mountain map, and its analysis was verified to have properly counted muon events.

7.4 Underground Energy Spectra

The differential underground energy spectrum is defined as the number of particles per unit area per unit time per energy interval, and is measured in units of [$\mathrm{cm}^{-2}\mathrm{s}^{-1}\mathrm{GeV}^{-1}$] [56]. It is crucial to have information on the energy distribution of muons for muon-induced background studies, as information about the energies of underground and underwater muons is required as input for Monte Carlo simulations.

7.4.1 Mean and Minimum Surface Energies

The mean underground energy of a muon is given by the solution to the differential equation for the energy loss, given in Equation (4.24). This is:

$$\langle E^s(X) \rangle = \left(E^s + \varepsilon_\mu\right) e^{-bX} - \varepsilon_\mu, \tag{7.20}$$

where $\varepsilon_\mu = a/b$ is the critical energy of muons defined in Equation (4.25), and a and b are the energy loss parameters defining the fractions of energy lost to continuous and catastrophic losses respectively, as in Equations (4.24) to (4.26) [5, 57].

Using the surface fluxes from MCEQ, the median surface energy of the muons reaching a certain depth underground can be calculated. This relation is shown in Figure 7.11.

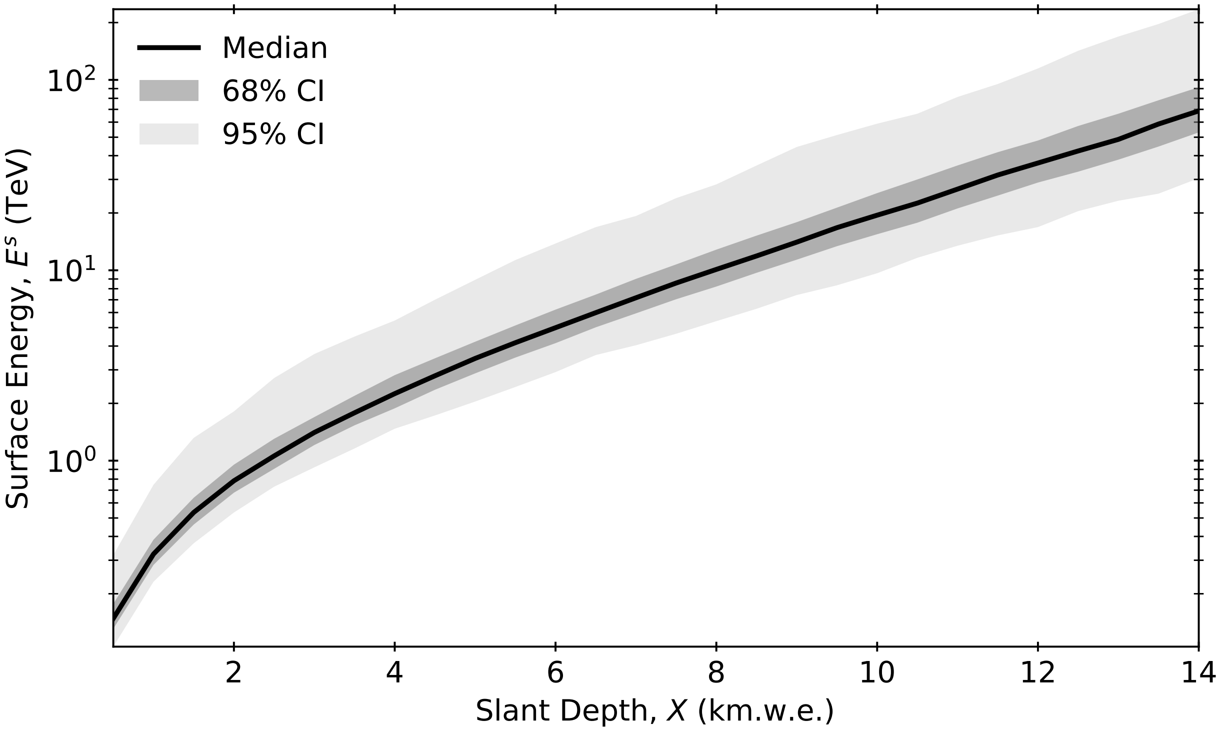

Figure 7.11: Surface energy vs slant depth, showing the median energy a muon needs at the surface to reach a given depth underground.

Taking the case of Equation (7.20) where the muon's final energy is $E^u(h) = 0$ gives the minimum energy that a muon needs at the surface in order to reach a depth h underground [5]:

$$E^s_{\min}(X) = \varepsilon_\mu \left(e^{bX} - 1\right), \tag{7.21}$$

Results from this parameterisation with the parameters from Equation (4.26) are shown in Table 7.1.

Table 7.1: Minimum surface energies, E^s_{min}, in [TeV] required for a muon to reach the depths of laboratories underground. Values are given for the parameterisations by Lipari [105, 107] and Groom [93, 106, 107] using the parameters in Equation (4.26) as well as MUTE. The last column gives the median surface energies in [TeV] with 68% confidence intervals shown in Figure 7.11. A dagger (†) indicates that the energy value was calculated using the equivalent vertical depth computed by MUTE using DAEMONFLUX (see Table 8.2 in Chapter 8).

Laboratory	**Lipari [TeV]**	**Groom [TeV]**	MUTE	
			Minimum [TeV]	**Median [TeV]**
WIPP	0.61	0.52	0.46	$0.58^{+0.12}_{-0.08}$
Y2L	-	-	$0.48^{\dagger}$	$0.61^{+0.12}_{-0.08}$ †
Soudan	0.91	0.76	0.59	$0.83^{+0.18}_{-0.11}$
KamLAND	-	-	$0.60^{\dagger}$	$0.85^{+0.19}_{-0.12}$ †
Super-Kamiokande			$0.59^{\dagger}$	$0.84^{+0.19}_{-0.12}$ †
Boulby	1.44	1.19	0.81	$1.27^{+0.27}_{-0.18}$
SUPL	1.50	1.44	0.84	$1.32^{+0.28}_{-0.19}$
LNGS	-	-	$0.88^{\dagger}$	$1.38^{+0.28}_{-0.20}$ †
LSM	-	-	$1.46^{\dagger}$	$2.32^{+0.58}_{-0.37}$ †
SURF	3.18	2.59	1.62	$2.57^{+0.62}_{-0.41}$
SNOLAB	6.62	5.28	2.24	$4.81^{+1.17}_{-0.82}$
CJPL	-	-	$2.48^{\dagger}$	$5.43^{+1.33}_{-0.90}$ †

7.4.2 Mean and Median Underground Energies

In addition to providing information about the primary cosmic ray spectrum, the mean underground energy is useful for underground detectors, as it can provide information about the underground muon energy spectrum, which is needed to run Monte Carlo simulations in programs like GEANT4 and FLUKA for the purposes of muon-induced background studies. It is also useful for studying the ratio $R(X)$ of stopping muons to throughgoing muons in an underground detector, as the mean energy shows up in analytical formulas for this ratio in which $R(X)$ is typically proportional to some power of $\langle E^u \rangle$ [5].

Rather than using the analytical form of the mean underground energy given by Equation (7.20), in MUTE, the average muon energy is calculated from the energy spectrum, which is computed by integrating the underground flux from Equation (6.15) over the zenith and azimuthal angles:

$$\Phi^u_\Omega(E^u,X) = \frac{\mathrm{d}N^u_\mu}{\mathrm{d}A\,\mathrm{d}t\,\mathrm{d}E^u} = \int_0^{2\pi}\int_0^1 \Phi^u(E^u,X(\theta,\phi),\theta)\,\mathrm{d}\cos(\theta)\,\mathrm{d}\phi. \tag{7.22}$$

This calculation is done by the `mtu.calc_u_e_spect()` function in MUTE. The energy spectra for the underground laboratories listed in Table 5.1 are shown in Figure 7.12, where the vertical ordering of the curves corresponds to the depths of the labs, and the energy spectrum decreases as depth increases, as expected. The result for Kamioka matches closely that from [219]. The results were checked by comparing the integral of Φ_{Ω}^{u} over the underground energies to the total underground flux values calculated with the `mtu.calc_u_tot_fluxes()` function (see Chapter 8), which provides a different set of computational steps to calculate the total flux, and results matched within 1%, an error that can be attributed to the respective integration routines.

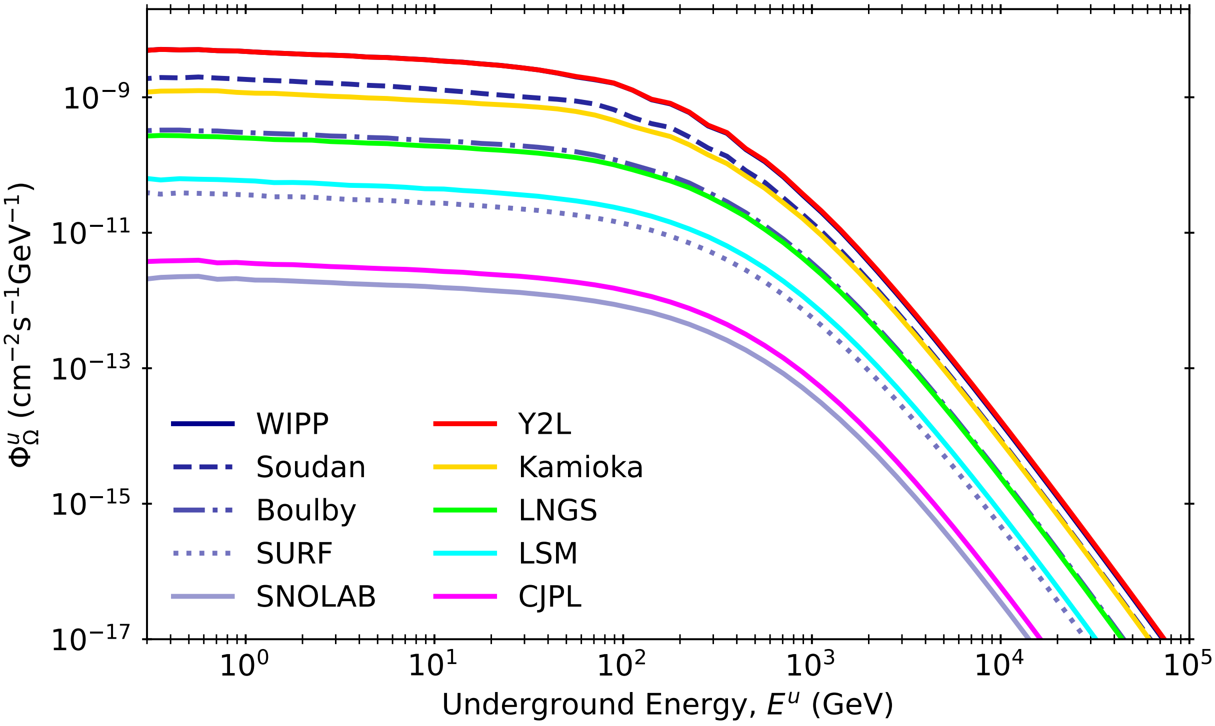

Figure 7.12: Underground muon energy spectra for labs under flat overburdens and mountains, calculated by MUTE with Equation (7.22). The curve for WIPP is behind the curve for Y2L due to their similar equivalent vertical depths.

The mean underground energy is given by the first raw moment of the spectrum:

$$\langle E^u(X)\rangle = \frac{\int_0^\infty E^u\Phi_{\Omega}^{u}(E^u,X)\mathrm{d}E^u}{\int_0^\infty \Phi_{\Omega}^{u}(E^u,X)\mathrm{d}E^u}, \tag{7.23}$$

The median energy for a given slant depth is defined as the underground energy E^u at which the fractional cumulative energy distribution is 0.5:

$$\frac{\int_0^{E^u} E^{u'}\Phi_{\Omega}^{u}(E^{u'},X)\mathrm{d}E^{u'}}{\int_0^\infty E^{u'}\Phi_{\Omega}^{u}(E^{u'},X)\mathrm{d}E^{u'}} = 0.5. \tag{7.24}$$

The mean and median energies can be calculated with the `mtu.calc_u_mean_e()` function in MUTE, which returns the mean underground energy and the median underground energy for the set vertical depth or mountain, along with the positive and negative bounds of the 68% and 95%

confidence intervals for the median energy. These values have been calculated for the underground sites listed in Table 5.1, with the results given in the fourth and fifth columns of Table 7.2. Uncertainties are not included on either set of values because the energy distribution for any given laboratory is steep and skewed, as seen in Figure 7.13, so the mean energy is usually outside the 68% confidence interval of the median.

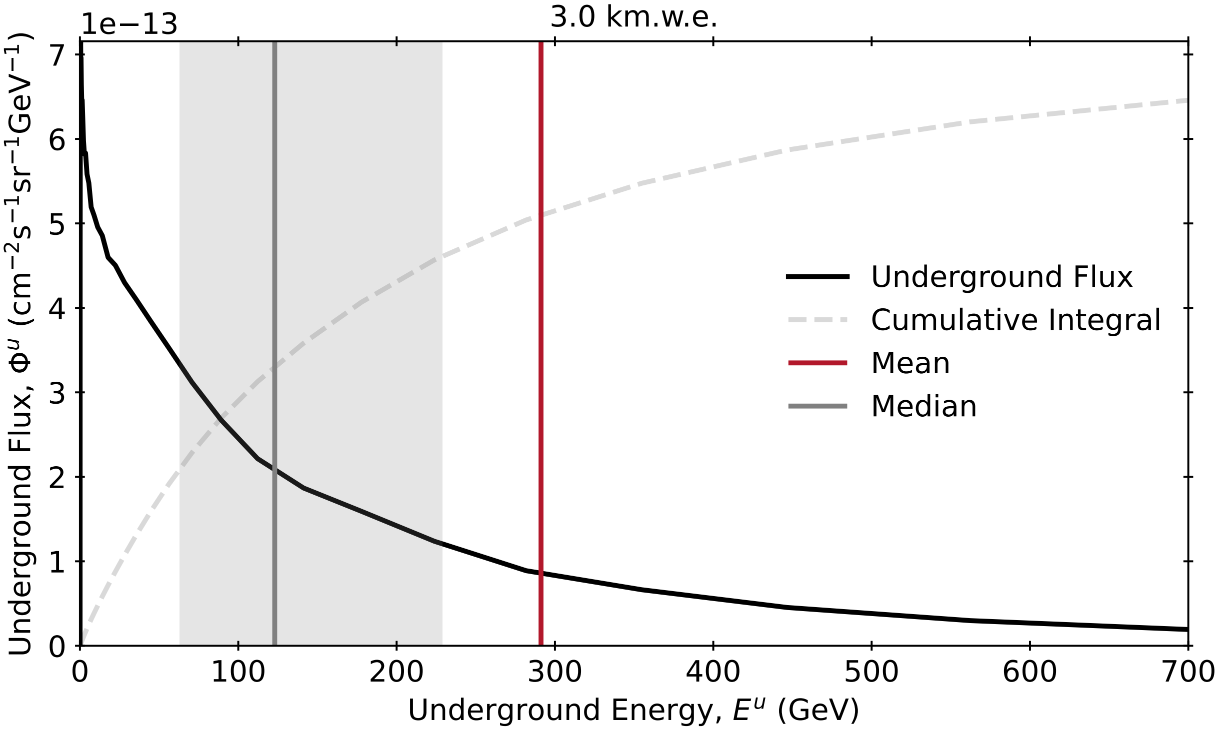

Figure 7.13: Underground flux vs underground energy for a vertical depth of 3.0 km.w.e. The flux is shown by the black curve, where low statistics in the transfer tensor at low energies cause ripples in the curve. The normalised cumulative integral of the underground fluxes, used to calculate the median energy in Equation (7.24), is shown by the dashed grey curve. The mean and median energies are shown by the solid red and grey lines at 291 GeV and 123^{+106}_{-60} GeV respectively. Because the vertical depth shown here is similar to the equivalent vertical depth of LNGS, the mean and median energies here are close to those in Table 7.2 for LNGS, though there are slight differences because a flat overburden was used here.

The values in the second and third columns of Table 7.2 were calculated with a parametric formula:

$$\langle E^u(h) \rangle = \frac{\varepsilon_\mu (1 - e^{-bh})}{\gamma_\mu - 2}. \tag{7.25}$$

As indicated, for labs for which mean energy values are not given in [107], the predicted average muon energies given these parameter sets using the equivalent vertical depths inferred from MUTE given in Table 8.2 as the h values in Equation (7.25) have been calculated.

Table 7.2: Mean and median underground muon energies in [GeV]. Values are given for the parameterisations by Lipari [105, 107] and Groom [93, 106, 107] using the parameters in Equation (4.26) as well as MUTE. A dagger (†) indicates that the energy value was calculated using the equivalent vertical depth computed by MUTE using DAEMONFLUX (see Table 8.2) because values for these labs are not given in [107].

Laboratory	Lipari [GeV]	Groom [GeV]	MUTE	
			Mean [GeV]	**Median [GeV]**
WIPP	165	184	213	102
Y2L	$171^\dagger$	$190^\dagger$	192	103
Soudan	191	212	236	115
KamLAND	198	219	265	129
Super-Kamiokande			264	128
Boulby	239	264	279	137
SUPL	$243^\dagger$	$268^\dagger$	282	138
LNGS	253	278	293	142
LSM	$287^\dagger$	$315^\dagger$	317	155
SURF	$293^\dagger$	$321^\dagger$	322	156
SNOLAB	327	356	352	172
CJPL	$330^\dagger$	$359^\dagger$	348	170

The values of the mean underground energy in Table 7.2 from Equations (7.23) and (7.25) are plotted in Figure 7.14. For shallow vertical depths, the MUTE prediction is higher than both the Lipari and Groom parameterisations, though agreement improves at deeper depths.

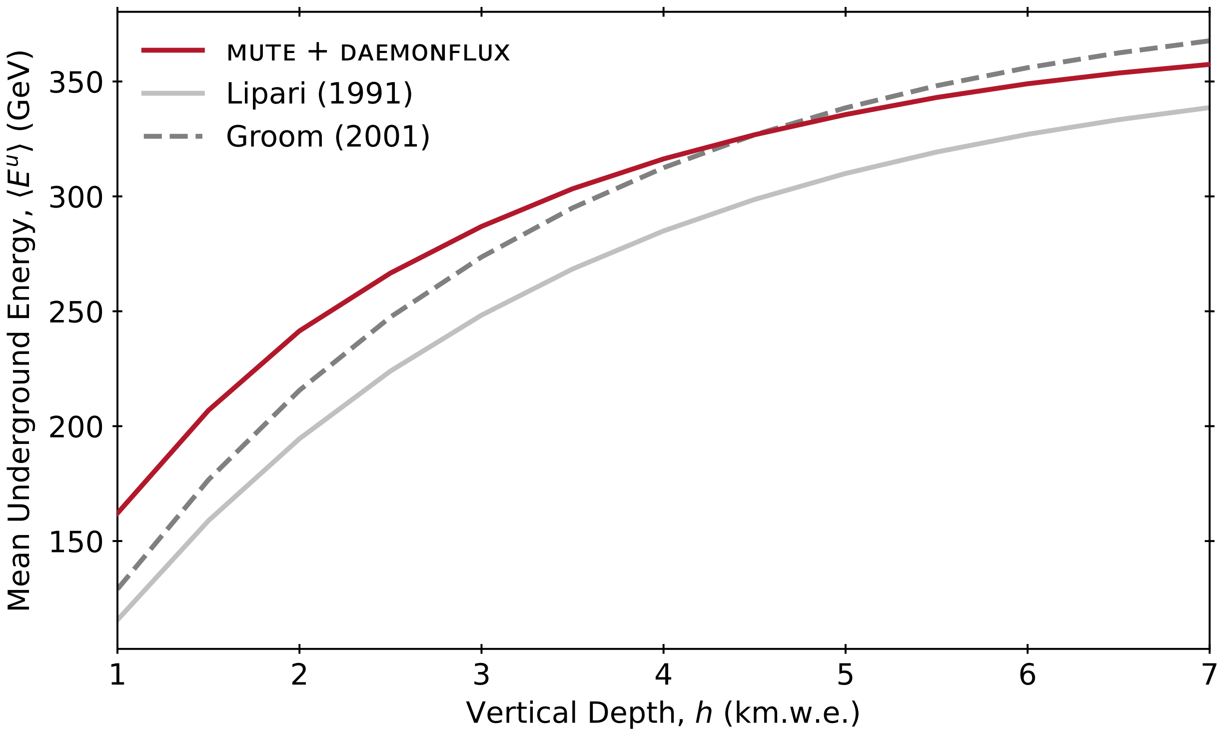

Figure 7.14: Mean underground energy vs vertical depth for standard rock, as calculated by Equation (7.23) with MUTE and by Equation (7.25) with the Lipari and Groom parameters given in Equation (4.26) from [105] and [93] respectively. Values are given in Table 7.2.

8 Total Underground Flux

The total underground muon flux, also called the omnidirectional or integrated intensity [56], is one of the main physical observables of interest for dark matter and neutrino experiments. It is defined as the number of muons underground ($\mathrm{d}N_\mu^u$) that pass through a unit of area ($\mathrm{d}A$) per unit time ($\mathrm{d}t$), and is typically measured in units of [$\mathrm{cm}^{-2}\mathrm{s}^{-1}$] [56]:

$$\Phi_{\mathrm{tot}}^u = \frac{\mathrm{d}N_\mu^u}{\mathrm{d}A\mathrm{d}t}. \tag{8.1}$$

As depth underground increases, the muon flux decreases, making it favourable for rare event search experiments to go as deep underground as possible. Comparisons between the total underground muon flux and the depth of the lab are typically shown on plots of total flux vs equivalent vertical depth, as in [5, 107, 145].

8.1 Defining Vertical Depths

In order to plot the total underground muon flux values for laboratories under flat overburdens and for those under mountains on the same plot in a meaningful way, the concept of equivalent vertical depth must be defined. For labs under flat earth, it is simple, as they have a well-defined vertical depth, h, which is the depth quoted in the literature for the given lab (for example, $h = (5.890 \pm 0.094)$ km.w.e. for SNOLAB from [89]). Labs under mountains, however, have depths that are dependent on zenith and azimuthal angle, $h(\theta, \phi)$, due to the profile of the mountain, and so do not have one single vertical depth. To deal with this, experiments have defined their depths underground in a variety of ways, including as an engineering depth, an average depth, and, as in this work, equivalent vertical depth.

8.1.1 Engineering Depth

What is sometimes referred to as the "vertical overburden depth" (see, for example, [125, 126, 145]) is actually what can be called the "engineering depth." This is simply the straight vertical amount of rock coverage directly above a laboratory, as shown in Figure 8.1.

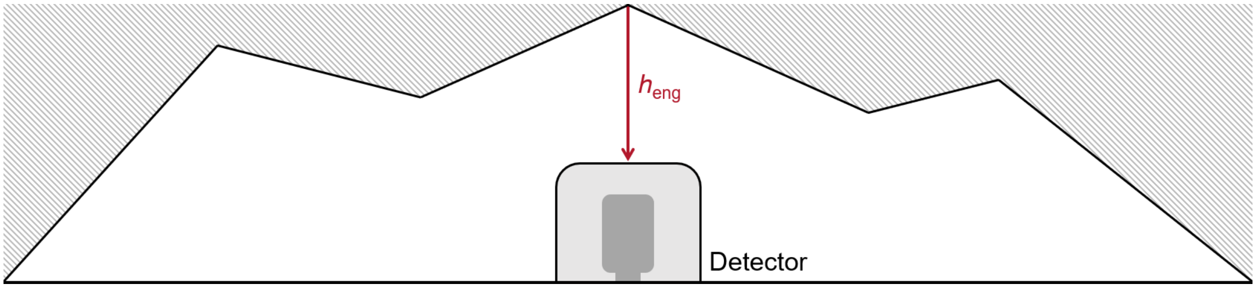

Figure 8.1: The definition of "engineering depth," h_{eng}, as being the vertical depth directly above a laboratory under a mountain (not to scale), regardless of the profile of the mountain.

Using this depth as the quoted depth of a lab, however, results in a misconception that the lab provides more coverage than it does, due to "cosmic ray leakage" through the volumes that are not covered by the mountain (shown by the grey hatched area in Figure 8.1). Therefore, if a lab under a mountain states its engineering depth is, for example, 3 km.w.e., it will provide less coverage and will thus have a higher muon flux than a lab under 3 km.w.e. of flat earth.

Some laboratories, like Y2L, Kamioka (KamLAND and Super-Kamiokande), and CJPL, quote only engineering depths in the literature. Because no other experimental depth is available, the engineering depth will be used for in tables and for plotting purposes in this chapter for these labs.

8.1.2 Average Depth

The equivalent vertical depth must also not be confused with the average depth, $\langle h \rangle$. The average depth is defined in [107] as the integral of all depth values over all angles:

$$\langle h \rangle = \int_0^{2\pi} \int_0^1 X(\theta,\phi) \mathrm{d}\cos(\theta) \mathrm{d}\phi. \tag{8.2}$$

The depths quoted by experiments at LNGS and LSM vary, but are typically minimum or average depths. The depth of LNGS is quoted in the literature as being 3.0 km.w.e. in [143, 218], 3.1 km.w.e. in [148], 3.2 km.w.e. in [144], 3.5 km.w.e. in [149], 3.8 km.w.e. in [106, 155], and 3.9 km.w.e. in [150]. For LSM, average depths are quoted as 4.8 km.w.e. in [156, 220] and 4.85 km.w.e. in [131].

Using the Gran Sasso mountain profile map from the MACRO experiment from [144], D.-M. Mei and A. Hime calculate the average depth of LNGS to be 3.65 km.w.e. in [107]. This is compared to MUTE's value of 5.23 km.w.e. with a slightly different map. Similarly, with a map of the Fréjus mountain from [131], they calculate the average depth of LSM to be 5 km.w.e., compared to MUTE's 4.97 km.w.e. Average depths will be used for plotting purposes for these labs.

8.1.3 Equivalent Vertical Depth

The definition used here for the vertical depths of labs under mountains is as given in [107], where the equivalent vertical depth is taken as the depth a lab would be at if it were under a flat overburden based on the total underground flux seen by the lab. Therefore, the vertical depth is a value that is fit by plotting the total underground flux against vertical depths for labs under flat earth as a curve, then letting the calculated total flux for a lab under a mountain float on the x-axis so it can be fit to this curve. The fitting function used in MUTE is given in Listing 8.1.

Listing 8.1: The function in MUTE used to calculate an equivalent vertical depth value given a single total underground flux value. This function takes in as input the flux value at which the equivalent vertical depth will be calculated, the model to which to fit the point (such as DAEMONFLUX), and the model error, to calculate the uncertainty of the fitted depth value.

```python
def calc_h (flux_in, model_in, model_err_in):

    def minimise (X, fluxes, root):

        spline = sciint.UnivariateSpline(depths_100[1:-1],
        ↪   np.log(fluxes[1:-1]), k = 1, s = 0)

        return (spline(X) - np.log(root))**2

    h     = scio.minimize(minimise, 1, args = (model_in, flux_in)).x[0]
    h_pos = scio.minimize(minimise, 1, args = (model_in + model_err_in,
    ↪   flux_in)).x[0] - h
    h_neg = h - scio.minimize(minimise, 1, args = (model_in - model_err_in,
    ↪   flux_in)).x[0]

    return h, h_pos, h_neg
```

8.2 Calculation of Total Underground Flux

The total underground muon flux is calculated by integrating the underground intensity from Equation (7.6) over the solid angle:

$$\Phi^{u}_{\text{tot}} = \iint_{\Omega} I^{u}(X(\theta,\phi),\theta)\mathrm{d}\Omega. \tag{8.3}$$

For the case of a flat overburden, where symmetry in the azimuthal angle is assumed, and the intensities are single-differential because of the direct correspondence between zenith angle and slant depth, this reduces to:

$$\Phi^u_{\text{tot}} = 2\pi \int_0^1 I^u_{\text{sd}}(\theta)\,\mathrm{d}\cos(\theta). \tag{8.4}$$

MUTE provides the `mtu.calc_u_tot_flux()` function for this calculation. An example call of this function is shown in Listing 8.2.

Listing 8.2: An example MUTE script which calculates the total underground muon flux under the Gran Sasso mountain using the density from Table 5.1.

```python
import mute.constants as mtc
import mute.underground as mtu

mtc.load_mountain("Gran_Sasso_Mountain.txt", density=2.72)
mtu.calc_u_tot_flux(interaction_model="DDM")
```

This calculation has been done for the sites listed in Table 5.1 for standard rock using DAEMONFLUX as the surface muon flux model, with the results given in Table 8.1. These have been plotted in Figure 8.2 against equivalent vertical depth with a MUTE curve for flat overburdens and standard rock as a reference from which the equivalent vertical depths for labs are defined.

Values calculated using MUTE for labs under mountains are shown with thick black outlines and those without outlines (with the same colours and shapes) are experimental measurements. These MUTE points have had their depth values fitted so they lie directly on the curve. These depth values are listed in Table 8.2. Their uncertainties come from the error band on the MUTE, originating from the systematic uncertainties in DAEMONFLUX, and are calculated using the function given in Listing 8.1 (although this error band results in asymmetric uncertainties, the values round similarly to the second decimal place, resulting in approximately symmetric uncertainties for the depths).

Many data points shown in Figure 8.2 are offset with respect to the MUTE result along the x-axis, as commonly seen for labs under mountains in plots presented in the literature, as in [114, 145], for example. This is due to the experiments reporting those points at an engineering depth or an average depth, as explained in Section 8.1. For example, MUTE calculates the depth of the CJPL-I lab under the Jinping mountain to be (6.22 ± 0.05) km.w.e. The value of 6.72 km.w.e. quoted in [145, 229], stated as being the result of a scaling factor F from cosmic ray leakage due to the topographic profile of the mountain, is in fact the engineering depth. The significant implications of using different conventions when talking about the depth of a laboratory under a mountain are further demonstrated in Table 8.3, where the different depth values for the Gran Sasso

Table 8.1: Total underground muon fluxes for all relevant underground laboratories. In cases where multiple measurements exist, values are listed in chronological order and the most recent measurement is taken for comparison. For LNGS, a spread of measurements covering the different halls is taken: LVD for Hall A, MACRO for Hall B, and Borexino for Hall C. A dagger (†) indicates that the value is a prediction calculated from simulation and does not come from experimental data.

Laboratory	**Experiment**	**Total Flux, Φ^u_{tot} (cm^{-2}s^{-1})**	
		Experimental	MUTE
WIPP	- (2005)	$(4.77 \pm 0.09) \times 10^{-7}$ [122]	$(4.70 \pm 0.11) \times 10^{-7}$
Y2L	KIMS (2005)	$(4.4 \pm 0.3) \times 10^{-7}$ [221]	$(3.81 \pm 0.09) \times 10^{-7}$
	COSINE-100 (2018)	$(3.98 \pm 0.39) \times 10^{-7}$ [123]	
	COSINE-100 (2020)	$(3.795 \pm 0.110) \times 10^{-7}$ [222]	
Soudan	CDMS (2005)	$(2.0 \pm 0.2) \times 10^{-7}$ [124]	$(1.44 \pm 0.04) \times 10^{-7}$
	- (2014)	$(1.65 \pm 0.10) \times 10^{-7}$ [223]	
Kamioka	KamLAND† (2006)	$(1.70 \pm 0.05) \times 10^{-7}$ [219]	$(1.54 \pm 0.04) \times 10^{-7}$
	KamLAND (2010)	$(1.49 \pm 0.11) \times 10^{-7}$ [125]	
	Super-Kamiokande† (2006)	$(1.48 \pm 0.04) \times 10^{-7}$ [219]	$(1.62 \pm 0.04) \times 10^{-7}$
	Super-Kamiokande† (2018)	$(1.54 \pm 0.31) \times 10^{-7}$ [126]	
Boulby	ZePLiN I (2003)	$(4.09 \pm 0.15) \times 10^{-8}$ [127]	$(4.40 \pm 0.14) \times 10^{-8}$
SUPL	SABRE (2021)	$(3.65 \pm 0.41) \times 10^{-8}$ [128]	$(3.88 \pm 0.12) \times 10^{-8}$
LNGS	LVD (1994)	$(2.87 \pm 0.03) \times 10^{-8}$ [224]	$(3.25 \pm 0.11) \times 10^{-8}$
	GALLEX (1999)	$(3.22 \pm 0.25) \times 10^{-8}$ [150]	
	MACRO (2003)	$(3.22 \pm 0.08) \times 10^{-8}$ [225]	
	CRESST (2004)	$(2.78 \pm 0.2) \times 10^{-8}$ [152]	
	LVD (2009)	$(3.31 \pm 0.03) \times 10^{-8}$ [226]	
	Borexino (2012)	$(3.41 \pm 0.01) \times 10^{-8}$ [227]	
	GERDA (2016)	$(3.47 \pm 0.07) \times 10^{-8}$ [149]	
	LVD (2017)	$(3.33 \pm 0.03) \times 10^{-8}$ [228]	
	Borexino (B2019)	$(3.432 \pm 0.001) \times 10^{-8}$ [154]	
	LVD (L2019)	$(3.35 \pm 0.03) \times 10^{-8}$ [148]	
LSM	Fréjus (1989)	$(5.47 \pm 0.10) \times 10^{-9}$ [131]	$(6.87 \pm 0.28) \times 10^{-9}$
	EDELWEISS (2013)	$(6.25 \pm 0.2^{+0.6}_{-1.0}) \times 10^{-9}$ [156]	
SURF	MAJORANA (2017)	$(5.31 \pm 0.17) \times 10^{-9}$ [133]	$(4.76 \pm 0.20) \times 10^{-9}$
SNOLAB	SNO (2000)	$(3.77 \pm 0.41) \times 10^{-10}$ [107]	$(3.36 \pm 0.21) \times 10^{-10}$
	SNO (2009)	$(3.31 \pm 0.10) \times 10^{-10}$ [89]	
CJPL	- (2013)	$(2.0 \pm 0.4) \times 10^{-10}$ [134]	$(3.98 \pm 0.24) \times 10^{-10}$
	JNE (2020)	$(3.53 \pm 0.29) \times 10^{-10}$ [145]	

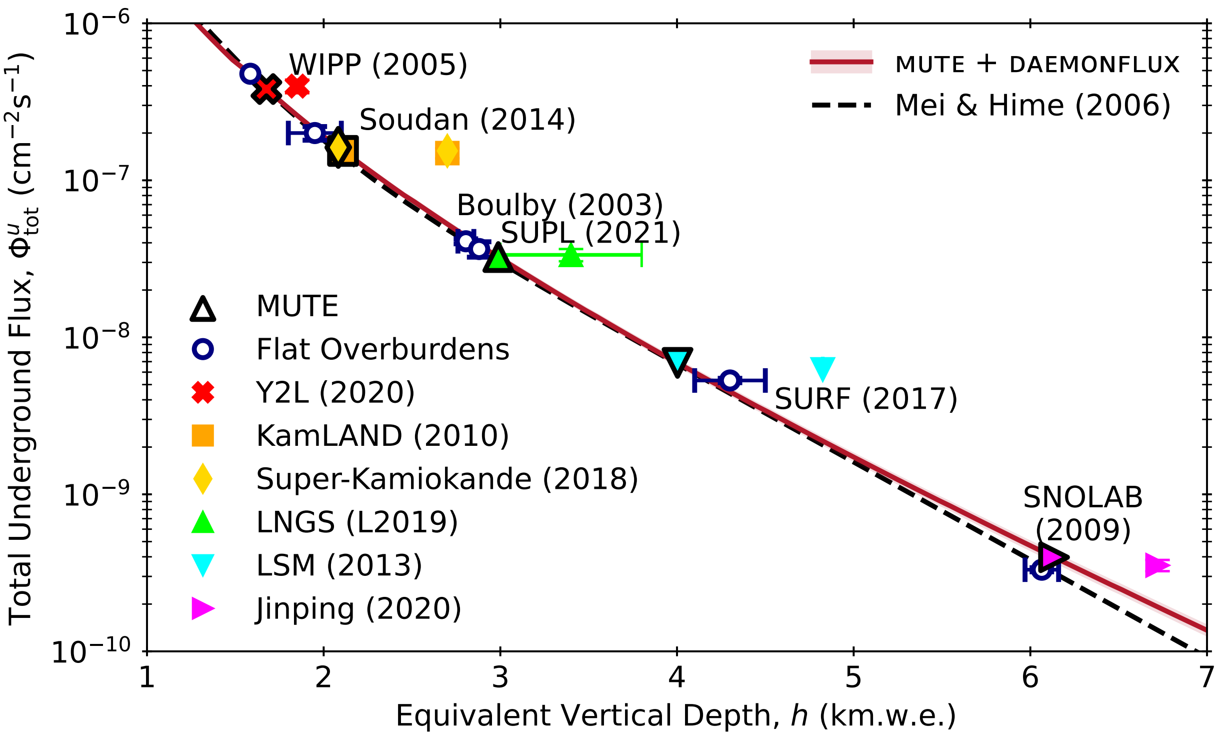

Figure 8.2: Total underground muon flux vs equivalent vertical depth underground. The curve for DAEMONFLUX was calculated using MUTE with a flat overburden and standard rock, and the points with thick black outlines were calculated using MUTE with mountain maps. The latter have had their depth values fitted to lie on the DAEMONFLUX curve using the function in Section 8.1.3, giving the laboratory's equivalent vertical depth, as opposed to the engineering or average depth as used in the literature by some experiments (see Section 8.1.1). Data points are shown for the experimental flux values listed in Table 8.1.

mountain were used in MUTE to calculate total underground fluxes for flat overburdens. There is a resulting ratio of 28 between the highest and lowest values. Confusion arising from the lack of a consistent convention across the community can therefore result in published measurements that are difficult to compare amongst each other.

Because of these inconsistencies in the definition of the depth of labs under mountains explained in Section 8.1 and visible in Table 8.3 and Figure 8.2, in order to eliminate the element of depth to make the comparison between points clearer, Figure 8.3 shows the ratio of the observed experimental data for the total muon flux to the predicted results in Figure 8.2 with DAEMONFLUX, independent of lab depth.

The first main source of systematic uncertainty comes from the uncertainties on the surface flux model, DAEMONFLUX, represented by the red error bands in Figure 8.2 and Figure 8.3 and contributing an error of ∼7% for deep depths (higher energies) and less than 1% for shallow depths. The second main source is from the limited knowledge of the density of the overburden

Table 8.2: Equivalent vertical depths for all underground laboratories with respect to standard rock (SR). Experimental depth values marked with a dagger (†) for laboratories under mountains are not equivalent vertical depths but are either engineering depths or average depths, and so a direct comparison between the experimental and MUTE values is not possible in these cases.

Laboratory	**Equivalent Vertical Depth, h_{SR} (km.w.e.)**	
	Experimental	MUTE
WIPP	$1.585^{+0.011}_{-0.006}$ [122]	1.58 ± 0.01
Y2L	$1.85^\dagger$ [123]	1.68 ± 0.01
Soudan	2.09 [124]	2.07 ± 0.01
KamLAND	$2.7^\dagger$ [125]	2.11 ± 0.01
Super-Kamiokande	$2.7^\dagger$ [126]	2.08 ± 0.01
Boulby	2.805 ± 0.045 [127]	2.85 ± 0.02
SUPL	2.88 [128]	2.92 ± 0.02
LNGS	$[3.0, 3.9]^\dagger$ [143, 150]	2.99 ± 0.02
LSM	$[4.8, 4.85]^\dagger$ [131, 156]	4.00 ± 0.03
SURF	4.26 [132]	4.18 ± 0.03
SNOLAB	6.065 ± 0.095 [89]	6.28 ± 0.05
CJPL	$6.72^\dagger$ [145]	6.13 ± 0.05

Table 8.3: A comparison of total underground muon fluxes under the Gran Sasso mountain for different types of depths as discussed in Section 8.1, calculated with MUTE using DAEMONFLUX. Note that the vertical depths used here are in terms of Gran Sasso rock, not standard rock, so a value of 2.96 km.w.e. is used for the equivalent vertical depth, rather than 2.99 km.w.e. as listed for LNGS in Table 8.2.

Depth Type	**Depth, h (km.w.e.)**	**Total Flux, Φ_{tot}^{u} (cm^{-2}s^{-1})**
Mountain Map	-	$(3.25 \pm 0.11) \times 10^{-8}$
Equivalent Vertical Depth	2.96	$(3.25 \pm 0.10) \times 10^{-8}$
Minimum Depth	3.04	$(2.85 \pm 0.93) \times 10^{-8}$
Engineering Depth	3.80	$(8.67 \pm 0.34) \times 10^{-9}$
Average Depth	5.23	$(1.16 \pm 0.06) \times 10^{-9}$

(the uncertainties on the rock density values listed in Table 5.1), represented by the horizontal red bars in Figure 8.3. The magnitudes of the uncertainties in Table 5.1 are large in many cases, leading to large uncertainties in the total flux seen in Figure 8.3. The mountain maps cited for Table 5.1 are assumed to be exact, and so no uncertainty on the slant depth values was considered. Error bars are not shown for labs for which there is no uncertainty on the rock density found in the literature or for labs for which the vertical depth or mountain profile map is already given in units of [km.w.e.]. These two systematic errors are shown separately in order to emphasise their independence from each other in the sense that the interaction model uncertainties are an unavoidable uncertainty

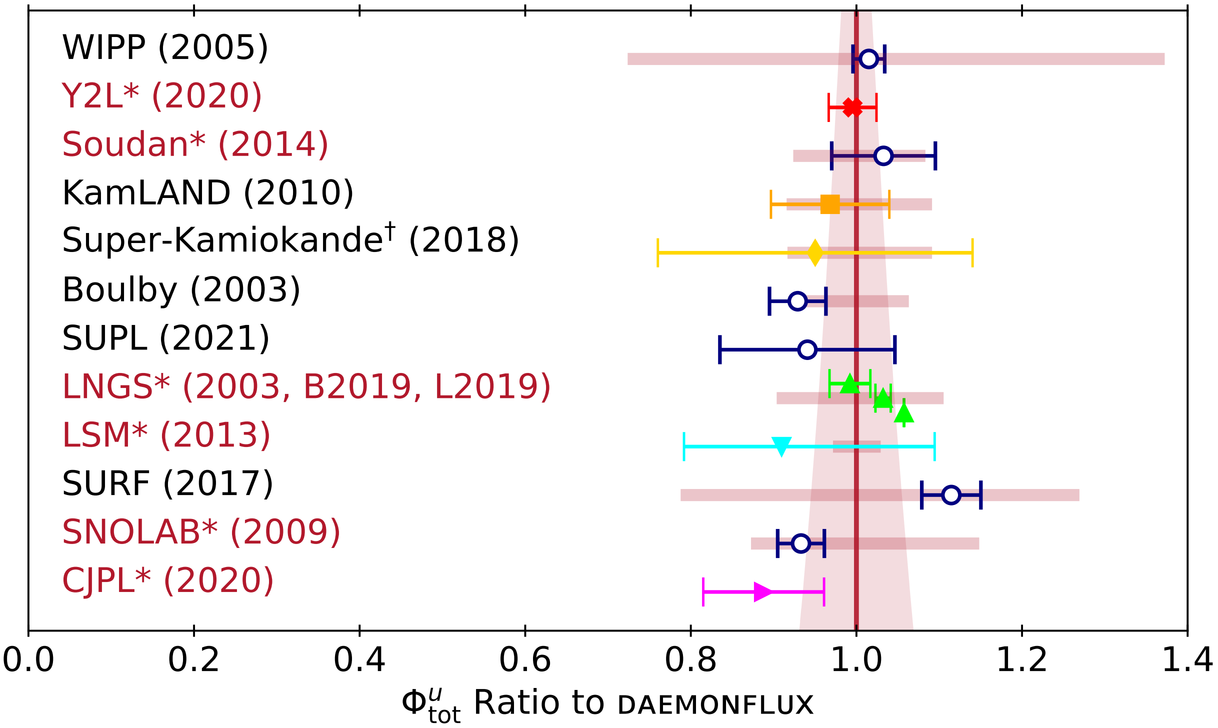

Figure 8.3: The ratio of experimental total underground muon flux measurements to MUTE results using DAEMONFLUX. The error band represents the uncertainty in the hadronic interaction model, while the thick red horizontal bars represent uncertainty coming from the rock density values given in Table 5.1. Data points are shown for the experimental flux values listed in Table 8.1. An asterisk (*) and red text means the calculation was done using the $\langle Z/A \rangle$ and $\langle Z^2/A \rangle$ values for the rock above that lab, as given in Table 6.5, whereas no asterisk and black text means standard rock was used. A dagger (†) indicates that the point used is a prediction calculated from simulation and does not come from experimental data. Comparisons to additional hadronic interaction models are shown in Figure B.2 in Appendix B.

appearing in the results from MUTE and are independent of the lab, whereas the rock density uncertainties are not included in the code but are dependent on the precision of the knowledge of a certain lab's overburden. Lastly, the PROPOSAL Monte Carlo simulations in MUTE were performed with $N = 10^6$ events per energy and zenith angle bin. Increasing the number of muons per bin from 10^5 to 10^6 results in a decrease in the total flux of 0.5% at shallow depths and less than 4% at 14 km.w.e., and further increases to the number of muons are not expected have significant effects. For this reason, the statistical uncertainty across all calculations is considered negligible.

When taking both main sources of systematic uncertainty into account, MUTE results using DAEMONFLUX agree with experimental results to the percent level in almost all cases. It can be noted that the precision of the calculations of the total underground flux in Table 8.1 and the equivalent vertical depth in Table 8.2 are good enough to resolve the difference in location between the KamLAND and Super-Kamiokande detectors under the Kamioka mountain, which are about 150 m apart according to Figure 5.6. One notable exception to the agreement, however, may be SURF. Although detailed information exists for the composition and distribution of the rock types above SURF (see [132, 230, 231, 232]), the large range of different rock types, as well as the variation in elevation of nearly 0.57 km.w.e. (see Figure 5 in [133]), which may be significant for the total underground flux, cause the uncertainty in the rock density to remain high, and it is only because of this uncertainty that MUTE finds agreement. Simulating the rock above SURF in PROPOSAL may result in better agreement between the values, though the $\langle Z/A\rangle$ and $\langle Z^2/A\rangle$ values are not directly available from the literature for inclusion in Table 6.5.

One additional case that must be commented on is the measurement for SNOLAB. Although the MUTE prediction agrees with the SNO measurement within systematic uncertainties, this agreement is achieved only when considering a depth of 6.225 km.w.e. for SNOLAB. The SNO Collaboration gives the vertical depth of the SNO detector as 6.225 km.w.e. and the total measured muon flux as $(3.31\pm0.10)\times10^{-10}$ cm^{-2}s^{-1} in [89]. The calculation in MUTE in Table 8.1, however, used a vertical depth of 6.065 km.w.e., because this is consistent with the measured vertical depth of 5.890 km.w.e. according to SNO's empirical conversion formula between X_{SNO} and X_{SR} (see Equation (6.10)). The explanation for these differing values might lie in the fact that the units of [km.w.e.] can be different with respect to different rock types, and [89] does not state which rock type the value of 5.890 km.w.e. is with respect to. When considering SNOLAB norite, as defined in Table 6.5, and a vertical depth of 6.065 km.w.e., MUTE calculates a value of $(3.36\pm0.21)\times10^{-10}$ cm^{-2}s^{-1}, as listed in Table 8.1. When considering standard rock and a vertical depth of 6.225 km.w.e., MUTE calculates a value of $(3.55\pm0.22)\times10^{-10}$ cm^{-2}s^{-1}. Both of these are in agreement with the measurement from [89], but that using SNOLAB norite is in better agreement. Simulating SNOLAB rock with its proper $\langle Z/A\rangle$ and $\langle Z^2/A\rangle$ values is likely a better characterisation of the rock than using the empirical conversion formula, and $h_{\mathrm{SR}}=6.225$ km.w.e. is likely an underestimated depth of SNOLAB. This is supported by the fact that the vertical depth obtained by fitting the experimental total flux value to the MUTE curve for standard rock is (6.28 ± 0.05) km.w.e., as given in Table 8.2. If the first bin centre used in the SNO analysis in [89] was 6.225 km.w.e., which corresponds to a zenith angle of 13° if $h_{\mathrm{SR}}=6.065$ km.w.e., it is likely that a significant portion of the data coming from the low zenith angle, where the flux is highest, is excluded from the result. Not accounting for these binning effects would result in a large discrepancy between experimental and predicted values. An alternative set of values is referenced by D.-M. Mei and A. Hime in Table I in [107] as (6.011 ± 0.100) km.w.e. and $(3.77\pm0.41)\times10^{-10}$ cm^{-2}s^{-1}. These are themselves in tension with the values presented in [89]. For these reasons, the values from [89] are not able to be compared well to the MUTE result as they are. The agreement shown in Figure 8.3 might not be true agreement, and it remains unclear whether the MUTE calculation should use a vertical depth of 5.890 km.w.e., 6.065 km.w.e., 6.156 km.w.e., or 6.225 km.w.e. More details on the origin of the 5.890 km.w.e. and 6.225 km.w.e. depth values are not available, and a description of SNO rock in terms of the Sternheimer parameters is not found in the literature, so further investigation is not possible at the moment.

In addition to calculations for standard rock, MUTE can also provide predictions for the total muon flux underwater (and under ice). Total muon flux measurements in water can be performed by water Cherenkov detectors, such as the KM3NeT detectors [233]. The comparison between MUTE, a typical reference calculation by E. V. Bugaev from [3], and an early 2020 KM3NeT measurement is shown in Figure 8.4. It can be noted that the KM3NeT data is a factor of 2 below the prediction. This comparison may benefit from more extensive data sets from a more complete version of the detectors and analysis, such as those in Figure 6 in [234], which shows a 40% error between KM3NeT ORCA data and simulations. However, the only change in the MUTE calculation between Figure 8.2 and Figure 8.4 is to the propagation medium from standard rock to sea water in the PROPOSAL code used to generate the surface-to-underground transfer tensors. Therefore, the precision seen in the rock results in Figure 8.2 should be applicable to water as well.

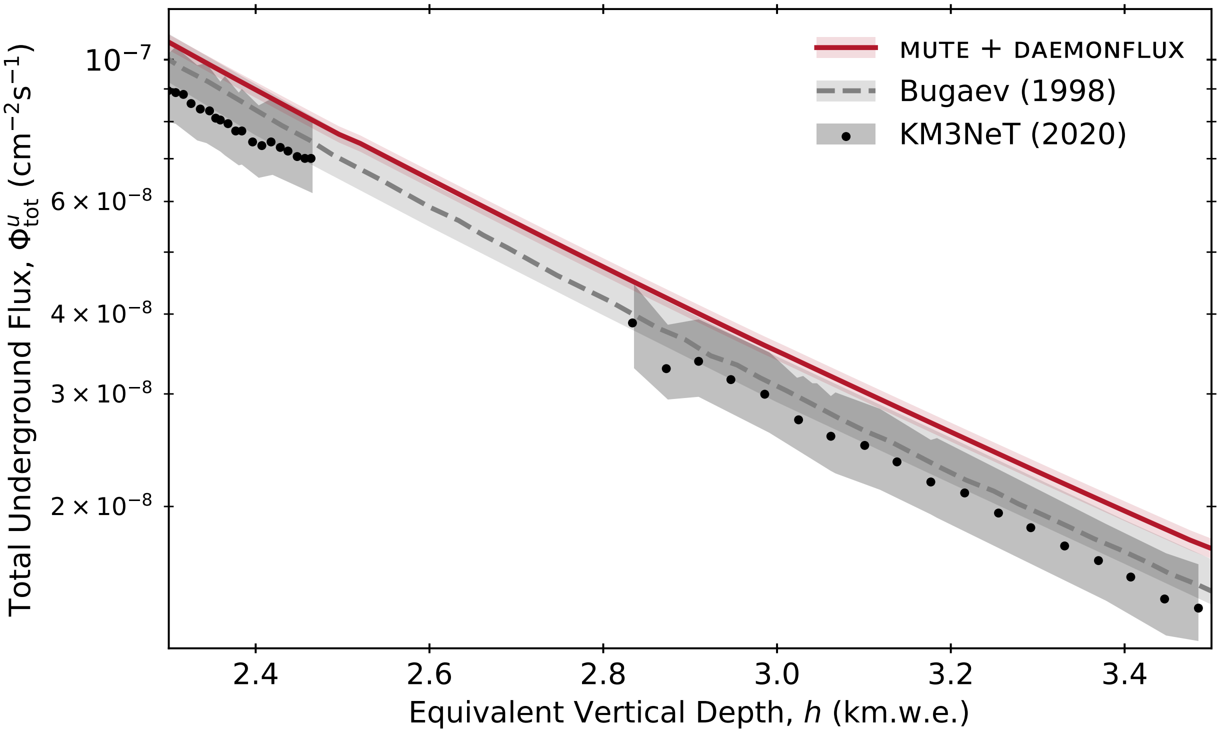

Figure 8.4: Total underwater muon flux vs slant depth. The curve for DAEMONFLUX was calculated using MUTE with a flat overburden and sea water. A curve is also included for the theoretical calculation of [3]. KM3NeT data is taken from [233].

In any case, discrepancies between measurements and calculations are not unexpected because the conditions of the measurement are not always possible to fully reproduce. Firstly, some mountain maps in Figure 5.5 were given in units of [km], but some were given in units of [km.w.e.], and so there is some ambiguity in which rock density was used to create some of the maps. In addition to this, many factors can have a significant effect on the results, including the composition (the density, the average atomic number and atomic weight, and the Sternheimer parameters) of the rock, the location of the lab under the mountain, the location of the detector in the lab, the energy threshold of the detector, the angular acceptance of the detector, and analysis decisions like energy cuts and binning choices. Differences in these factors have, for example, led to the Super-Kamiokande experiment alone reporting a wide range of measured values for its muon rate, from 1.8 Hz to 3.0 Hz (see [219, 235, 236, 237, 238, 239, 240]). More careful handling of each these factors for a specific detector may result in further improvements to the accuracy of MUTE results, and while these details were not always available for each laboratory for the present study, MUTE is provided as an open-source tool for experiments to tailor to their specific use cases.

8.3 Seasonal Variations

As stated in Section 3.2.4, underground detectors are a good probe of the seasonal variations and energy distribution of atmospheric muons. In order to investigate these seasonal variations, the interaction model in MCEq was first set through MUTE to SIBYLL-2.3c. The density model was set to use the NRLMSISE-00 model described in Section 6.3.3. MUTE was then used to calculate the total underground flux for each month of the year by looping over the months in the `month` parameter in the `mtu.calc_u_fluxes()` function, as in Listing 8.3.

Listing 8.3: An example calculation of the total underground muon flux at LNGS across the year. The surface fluxes at the location of LNGS are first calculated for each month of the year. These are then passed to the `mtu.calc_u_tot_fluxes()` function to calculate the total underground fluxes.

```python
import mute.constants as mtc
import mute.suface as mts
import mute.underground as mtu

for m in range(len(mtc.MONTHS)):
    s_fluxes = mts.calc_s_fluxes(interaction_model = "SIBYLL-2.3c",
                                 atmosphere = "MSIS00",
                                 location = (42.4, 13.5),
                                 month = mtc.MONTHS[m], force = True)
```

```
    u_tot_flux = mtu.calc_u_tot_flux(s_fluxes = s_fluxes)
```

The total flux has been calculated for each month throughout the year for a range of latitudes and longitudes spanning the planet. Using these fluxes, the amplitude of the seasonal variation in the flux underground, A^u, can be calculated as:

$$A^u = \text{sign}\left(\Phi^u_{\text{tot, Jul.}} - \Phi^u_{\text{tot, Jan.}}\right)\left(\frac{\Phi^u_{\text{tot, max}} - \Phi^u_{\text{tot, min}}}{2\left\langle\Phi^u_{\text{tot}}\right\rangle}\right), \tag{8.5}$$

where $\langle\Phi^u_{\text{tot}}\rangle$ is the mean of the total underground flux over the whole year. The sign is defined such that the amplitude is positive when the flux peaks in July and negative when it peaks in January. The definition is the same for the amplitude at the surface, A^s, but with Φ^s_{tot} used in place of Φ^u_{tot}. An example of the total muon flux at the surface and underground against month is shown in Figure 8.5 for the location and depth of SNOLAB, with the definitions of A^s and A^u shown.

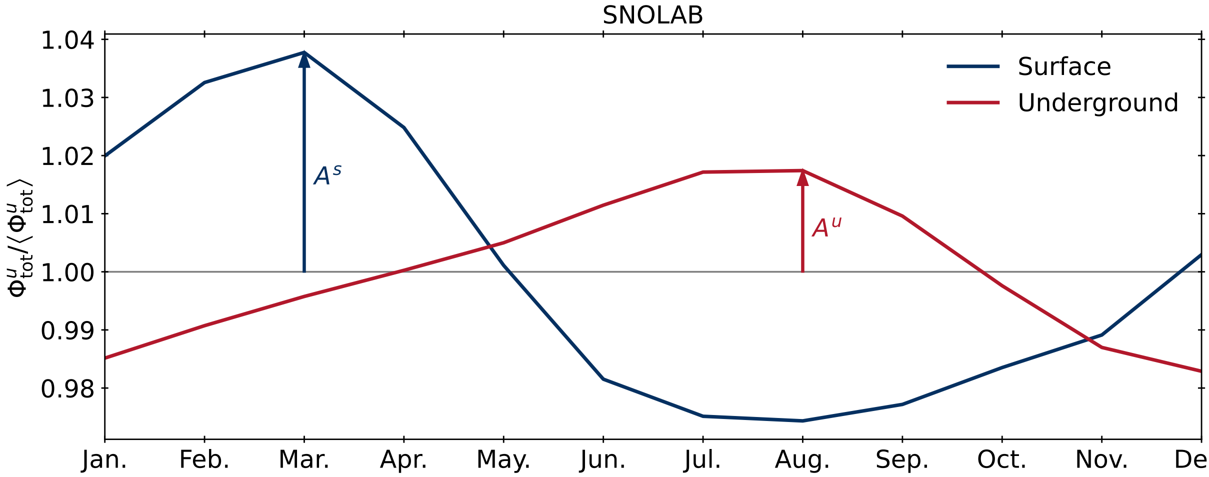

Figure 8.5: The total surface (blue) and underground (red) muon flux vs month for the location and depth of SNOLAB. The muon flux peaks at the surface in March, where the amplitude is represented by A^s, and peaks underground in August, where the amplitude is represented by A^u, showing the inversion from surface to underground.

The amplitude for each latitude-longitude bin that the calculation was performed for is plotted in Figure 8.6, for the surface of the Earth and for 3 km.w.e. underground. These plots show, first of all, the inversion of the sign of the amplitude from the northern hemisphere to the southern hemisphere, as expected from the fact that the tilt of the Earth means the two hemispheres experience summer and winter at different times. The magnitude of the amplitude increases near the poles due to violent weather conditions compared to at the equator. They also show the inversion of the sign of the amplitude from surface to underground, given by the energy dependence of the seasonal variations in the muon flux.

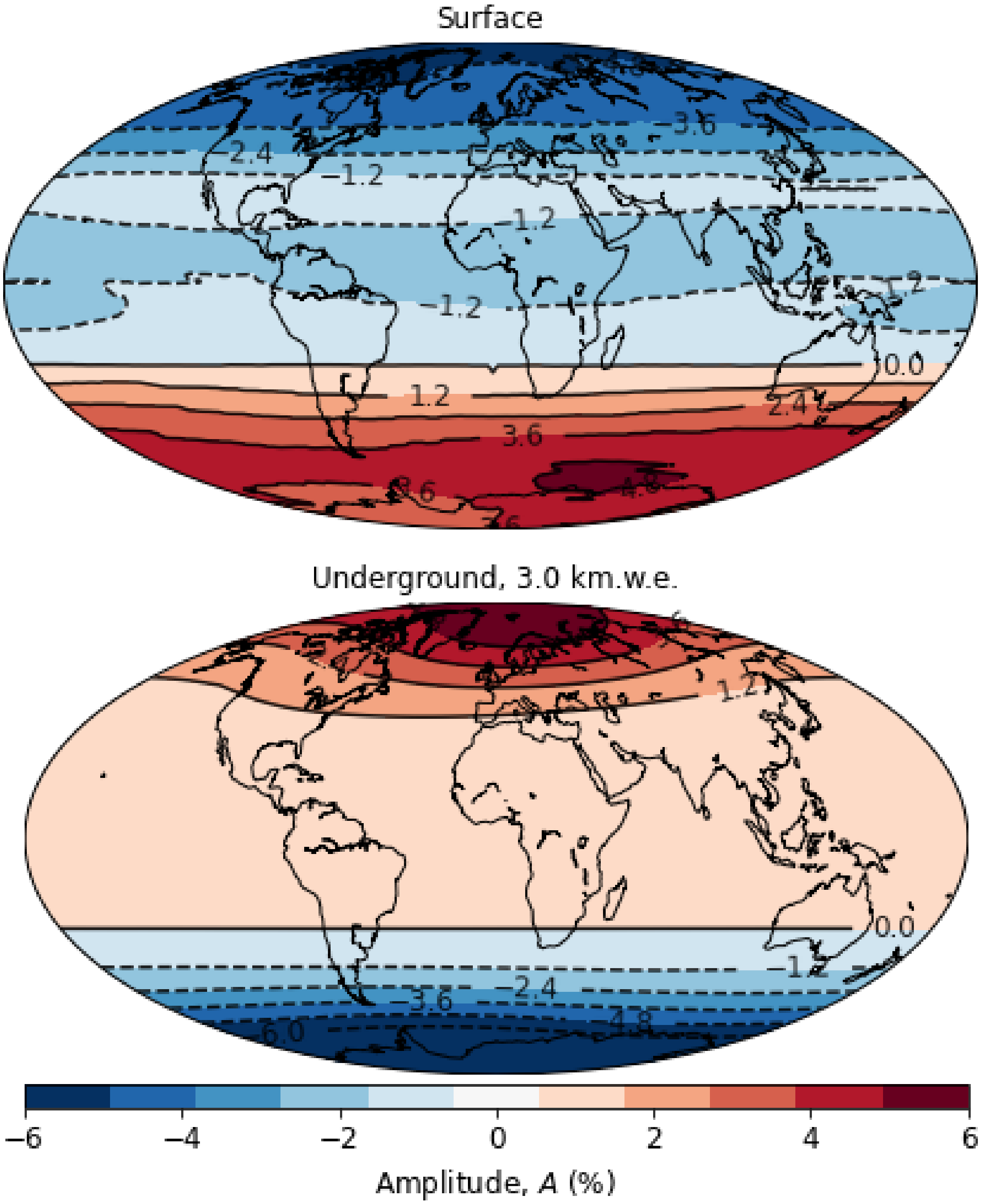
Surface

Underground, 3.0 km.w.e.

Figure 8.6: Maps (2° × 2°) of amplitudes of the seasonal variation in the muon flux at the surface of the Earth (top) and 3 km.w.e. underground (bottom). Positive amplitude (red) indicates the flux peaks around July, and negative amplitude (blue) indicates the flux peaks around January.

These maps were made for demonstrative purposes. The shapes of the contours at the surface will vary according to the altitude and the geomagnetic field (particularly because the geomagnetic field causes significant differences between the muon flux observed at the poles and at the equator), but all calculations were done for sea level without taking the geomagnetic field into account. Those underground will vary according to the density of rock, water, or ice, but calculations were done assuming standard rock for every bin, with no variations in medium or medium density.

8.3.1 Results

The amplitudes at the latitudes, longitudes, and vertical underground depths of the laboratories from Table 5.1, with the additional inclusion of the IceCube detector (for which fresh water was used as the propagation medium), were taken and are shown in Figure 8.7 compared to experimental data. The labs are arranged by depth (top) and latitude (bottom) so that both the depth and latitude dependences of the amplitude can be seen. The values of the amplitudes for all labs are given in Table 8.4.

Table 8.4: Amplitudes of seasonal variations in the total underground muon flux for all underground laboratories.

Laboratory	**Coordinates (°)**	**Amplitude, A^u (%)**	
		Experimental	MUTE
IceCube	(-90.000, 0.000)	8.58 [241]	[8.63, 9.32]
WIPP	(32.372, -103.794)	-	0.64
Y2L (COSINE-100)	(38.010, 128.543)	0.60 ± 0.20 [222]	0.53
Soudan (MINOS)	(47.823, -92.237)	2.09 [242]	1.46
Kamioka	(36.423, 137.315)	-	0.55
Boulby	(54.553, -0.825)	-	3.19
SUPL	(-37.070, 142.810)	-	0.79
LNGS (LVD)	(42.400, 13.500)	1.51 ± 0.03 [148]	1.48
LNGS (Borexino)		1.36 ± 0.04 [154]	
LNGS (OPERA)		1.55 ± 0.08 [155]	
LNGS (GERDA)		1.4 ± 0.1 [149]	
LSM	(45.179, 6.689)	-	1.92
SURF	(44.353, -103.744)	-	1.32
SNOLAB (SNO)	(46.472, -81.187)	2.4 ± 0.6 [204]	1.73
CJPL	(28.153, 101.711)	-	0.41

As seen in Figure 8.7 (bottom), there is a correspondence between latitude and amplitude, where labs closer to the equator (like CJPL and WIPP; see Figure 5.4 for the locations on a map) have small amplitudes (0.41% and 0.64% respectively), compared to those closer to the poles (like Boulby and IceCube) have large amplitudes (3.19% and a minimum of 8.63% respectively). Based on the two plots in Figure 8.7, it appears that there is a stronger correlation between latitude and amplitude than there is between depth and latitude. This is particularly interesting at the latitude of IceCube. Because the IceCube detector is located at the South Pole, where weather is

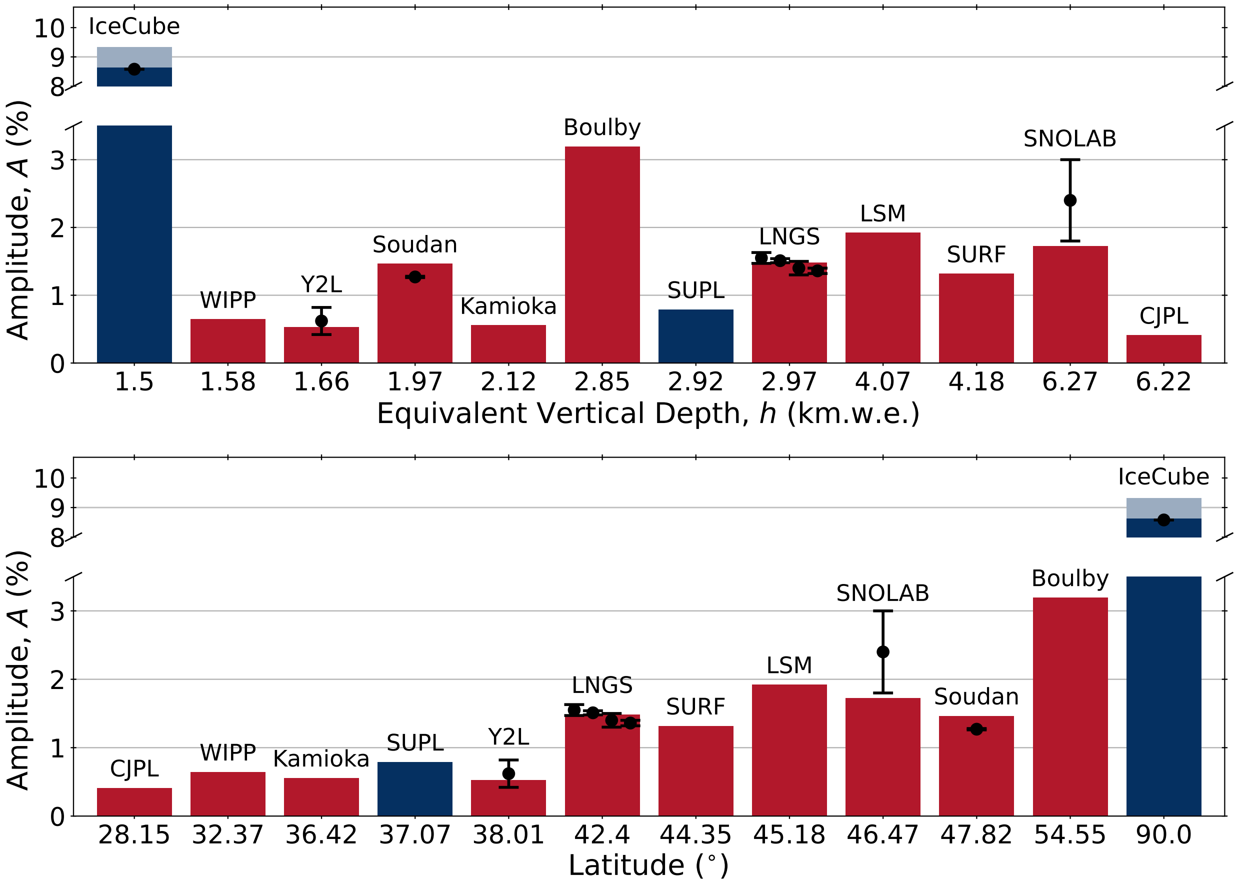

Figure 8.7: Amplitude of seasonal variations in the underground muon flux for the laboratories given in Table 5.1 against equivalent vertical depth (top) and absolute value of the latitude (bottom). Red is used for labs in the northern hemisphere, with a peak in the muon flux in July, and blue is used for labs in the southern hemisphere, with a peak in January, comparable to Figure 8.6. The dark blue bar for IceCube shows the amplitude at the top of the detector, and the lighter blue bar behind it shows the amplitude at the bottom of the detector. Experimental and calculated values are given in Table 8.4, with the calculated IceCube values shown as a range from 8.63% to 9.32%.

violent, the amplitude of the seasonal variations is much greater than that for any other laboratory. Additionally, because it spans a kilometre of vertical distance, it can measure the atmospheric muon flux at depths significantly far enough apart to be able to observe a difference in the seasonal variations. For this reason, it is presented as a range in Figure 8.7 and Table 8.4.

In general, in Figure 8.7, there is very good agreement between the MUTE predictions and the experimental measurements, with the exception of SNOLAB, possibly due to low statistics of the SNO detector. The MUTE result is more consistent with what would otherwise be expected for a lab at SNOLAB's depth and latitude, compared to the other sites, which have better agreement with the data, so it is possible that the SNO measurement is an overestimate. Despite the exclusion of systematic uncertainties in the MUTE predictions from sources like the surface flux model and the rock density due to computational constraints, MUTE is shown to be reliable with its precision, and appears suitable to provide predictions for underground sites for which seasonal variation amplitudes have not been measured. This is useful specifically for new labs under construction, but also for labs with interesting physical implications of the seasonal variations, such as IceCube at the South Pole, and SUPL in Australia, where the SABRE South experiment is located.

8.3.2 Possible Applications

These results hold many interesting physics implications which can be further explored in applications of MUTE's ability to calculate seasonal variations. An overview of some notable applications is given here.

Temperature Coefficient

The amplitude of seasonal variations is typically represented in terms of a temperature coefficient, α_T (see, for example, [2, 5, 56, 148, 154, 222, 242, 243, 244, 245, 246]). This is an energy-dependent value between 0 and 1 that describes the correlation between the muon flux and the temperature of the atmosphere, defined as:

$$\frac{\Delta R}{\langle R \rangle} = \alpha_T \frac{\Delta T_{\text{eff}}}{\langle T_{\text{eff}} \rangle}, \tag{8.6}$$

where R is the muon rate, and T_{eff} is the effective temperature of the atmosphere. This is more common in the literature than quoting the amplitude of the modulations or showing plots of the flux against time. In this case, to be able to compare to a wider range of data, it would be beneficial to be able to calculate values for the temperature coefficient with MUTE. However, this is complicated with the current implementation of the NRLMSISE-00 model, and so is outside the computational scope of this work.

Satellite Data Interfaces

Seasonal variations are currently done using the NRLMSISE-00 atmospheric model, as described in Section 6.3.3. There are interfaces available to use atmospheric satellite data, which could give daily variations in local weather patterns (including interesting phenomena like hurricanes and typhoons). Using local weather variations could give more precise predictions of the seasonal variations for a given lab because daily variations would appear in the data at the surface and underground, and so taking a ratio of the prediction to the data could cancel out detector effects coming from things like detector exposure, lifetime, and acceptance. Another possible application would be to study climate change in the upper atmosphere over time. Using MCEQ with archival satellite data, such as that from the Atmospheric Infrared Sounder (AIRS) on NASA's Aqua satellite, long-term seasonal variations could be computed and compared to the 10 and 24 years of underground muon flux data from Borexino [154] and LVD [148] respectively. The relationship between mean muon energy and the observed muons' underground depths could be used to study different parts of the atmosphere, thereby quantifying warming events and helping to improve climate forecasting models. However, although satellite data interfaces exist, they are not very advanced at the moment, and their interfacing with or implementation into MUTE would require a great deal of work.

Seasonal Variations in IceCube

Because the IceCube detector spans a kilometre of vertical distance from 1.5 km.w.e. to 2.5 km.w.e., it is unique in that it can measure the atmospheric muon flux over a range of depths. The vertical depth can easily be adjusted in MUTE with the `mtc.set_vertical_depth()` setter function. This can be used to illustrate the expected variation in the amplitude against depth, which could then be compared against IceCube data. A preliminary plot of this is shown in Figure 8.8, with a single data point from S. Tilav, et al. [241]. This preliminary comparison suggests that the atmospheric muons that IceCube observes are located primarily near the top of the instrumented volume. This is consistent with the muon veto system in place in the IceCube detector, which triggers when outer digital optical modules (DOMs) detect events, rather than inner DOMs near the detector's core. There could be interesting physics concerning the anti-correlation property (phase shift) of the surface-to-underground modulation differences to extract from Figure 8.8. For example, the shape of the curve may be a function of $\langle h \rangle$ or $\langle X \rangle$. A more in-depth study, however, would require the IceCube Collaboration to publish data for muon seasonal variation rates against depth, as well as a rigorous analysis of the errors.

Implications for DAMA/LIBRA Results

It was first theorised by A. K. Drukier, K. Freese, and D. N. Spergel in [247] that cold dark matter would have an annual modulation in its signal due to the Earth's movement through the galactic dark matter halo, with a peak in the signal in late spring.

The Dark Matter Large sodium Iodide Bulk for Rare processes (DAMA/LIBRA) experiment, located at LNGS, is made up of a detector of $5 \times 5 = 25$ NaI(Tl) crystal scintillators aiming to measure the theorised annual modulation signature of dark matter. DAMA/LIBRA published its first results in 2008 in [153], showing an annual modulation of single-hit scintillation events which were fit to a cosinusoidal function with an amplitude of (0.0131 ± 0.0016) kg^{-1}keV^{-1} (results combined with earlier DAMA/NaI data for a 2–6 keV energy interval), a period of one year, and

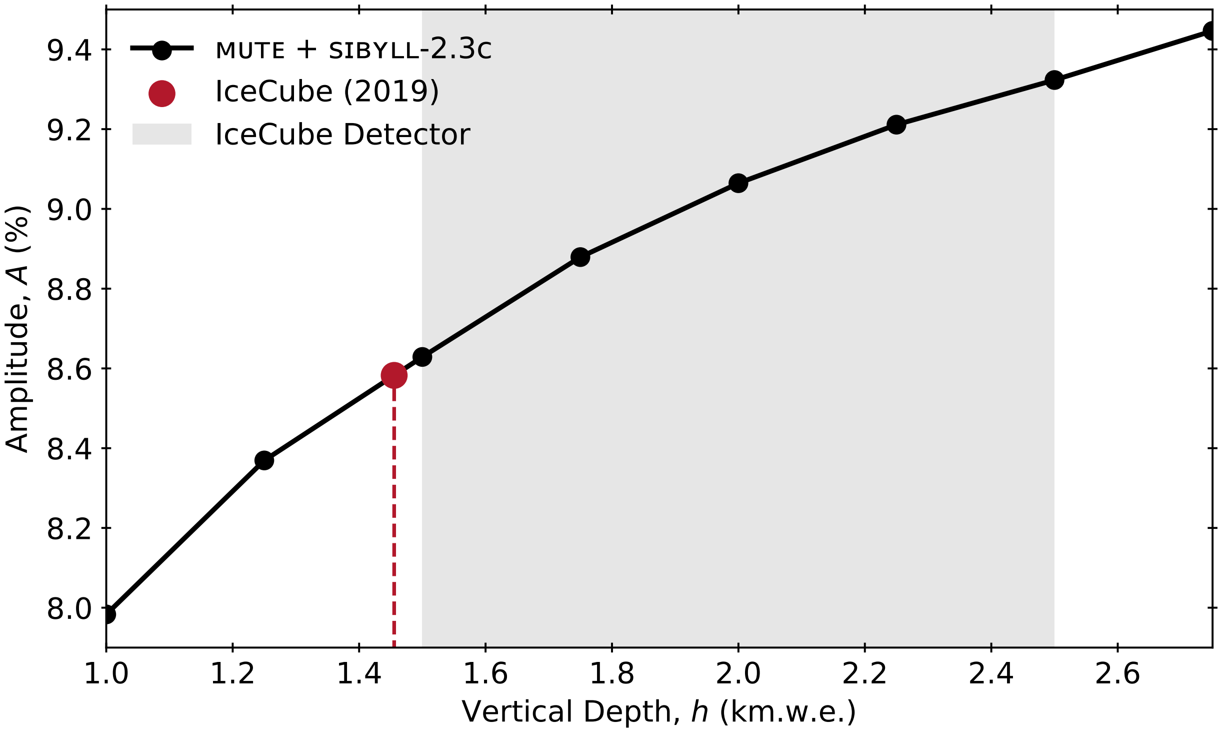

Figure 8.8: The variation of the amplitude of seasonal variations in the underground muon flux against different depths under ice at the South Pole spanning the depths covered by the IceCube detector (represented by the grey shaded region). The black points were calculated by MUTE using the SIBYLL-2.3C hadronic interaction model. The red point is a measurement taken from [241], whose depth has been fit to the black curve, giving 1.46 km.w.e.

a phase of 152.5 days, placing the peak at 2 June. This signal is consistent with what would be expected for dark matter. The DAMA/LIBRA results have long been contested because several other experiments have repeatedly excluded the DAMA/LIBRA parameter space from their WIMP search results (see, for example, the spin-independent cross-section vs WIMP mass exclusion curves in Figure 3 in [248]), though the DAMA Collaboration in [153] holds that any comparison is not model-independent and is therefore arbitrary. For this reason, additional experiments using the same NaI crystal target material have been commissioned, including ANAIS-112 at LSC [249], COSINUS at LNGS [250], COSINE-100 at Y2L [222], and, most recently, SABRE at LNGS and SUPL. However, as of yet, none of these experiments have been able to reproduce the DAMA/LIBRA observation.

Some have suggested that neutrons induced by atmospheric muons and neutrinos could be the cause of these annual modulations (see [251, 252, 253] and unpublished papers [254, 255, 256]). However, the DAMA/LIBRA signal and that which would be caused by muons are shown repeatedly to vary in their power spectrum, phase (as shown in Figure 8.5, the muon flux underground in the northern hemisphere reaches a maximum in summer, not in late spring, as is the case with WIMPs), and amplitude. Although the phase shift can be reconciled by considering solar neutrino-induced neutrons, as in [251], the amplitude of the modulations from the DAMA/LIBRA data cannot be matched. After correcting for neutrino-induced neutron cross-sections as well as event rejection, the amplitude of the signal resulting from muon- and neutrino-induced neutrons would be orders of magnitude smaller than that of the data, meaning atmospheric muons are not a possible candidate for the modulation, as asserted by a comment [257] to [251], as well as [258]. The COSINE-100 Collaboration has suggested that the observed modulation may be introduced by analysis artefacts when considering a time-dependent background, but they find a phase almost opposite to that of DAMA/LIBRA [259].

For careful analysis of these data sets, it is important to understand modulation effects of every environmental parameter to high precision, including that of atmospheric muons. The results presented in Figure 8.7 show the strong ability of MUTE to predict the amplitude of muon flux variations across the seasons. This predictive power can be of particular value to the SABRE experiment, which aims to test the dark matter seasonal modulation result reported by DAMA/LIBRA, with twin detectors located at LNGS in the northern hemisphere and SUPL in the southern hemisphere.

9 Conclusion and Outlook

This work discussed the development of MUTE, a program to calculate atmospheric muon fluxes and intensities underground and underwater, and the physical results obtained with this program. The program (Chapter 6) combines the codes MCEQ and DAEMONFLUX (Section 6.3), which provide the muon flux at the surface of the Earth, with PROPOSAL (Section 6.4), which is a Monte Carlo lepton propagation code optimised for large ranges of matter.

MUTE is able to provide a full description of surface, underground (for laboratories under both flat overburdens and mountains), and underwater muons, independent of data, as it can calculate intensities (Chapter 7), energy spectra (Section 7.4), angular distributions (Section 7.3), and total fluxes (Chapter 8) as forward predictions based on analytical and stochastic calculations alone. Additionally, the phenomenon of seasonal variations in the total muon flux was explored, and an inverse relationship in the amplitude of the variation between surface and underground was demonstrated (Section 8.3).

In all cases, MUTE has been shown to agree with experimental measurements with precision down to the percent level for even the deepest labs, thus providing substantial improvement over previous methods. On top of this, optimisations of the data structures and algorithm have allowed for the program to perform its calculations within fractions of a second, reducing the computational intensity on the user's end. Lastly, the most recent models are available for use for the primary cosmic ray flux, hadronic interactions, the atmospheric density, and interaction cross-sections for energy loss, and the modular design of the program allows for future models to be easily incorporated into the code. In conclusion, the goals of MUTE (Section 6.1.1) were for it to be precise, data-independent, flexible, easy to use, efficient, and complete, all of which have been achieved.

MUTE has wide potential for application across multiple fields of physics and beyond. By successfully cross-checking angular distribution data from the LVD experiment (Section 7.3.1), MUTE has shown to be reliable in validating data analyses, for example. Its potential to provide insights to the IceCube and DAMA/LIBRA experiments in the context of seasonal variations was also discussed (Section 8.3.2). The first version of MUTE was publicly released on 19 December 2021, and it has since already been successfully used by multiple dark matter and neutrino experiments around the world, showing its functionality in the field of astroparticle physics. Although the goals of the program have been met, however, the outlook for MUTE is wide, as there are many future possibilities still left to be explored.

9.1 Future Possibilities with MUTE

Despite the major fundamental observables of interest for underground and underwater detectors being provided by MUTE, there is still room for its utility to be expanded, especially in its application in other scientific fields that make use of atmospheric muons. The following sections provide a non-exhaustive list of additional possibilities for expansions or applications of the MUTE code that are considered out of the scope of this work but are still useful.

9.1.1 Optimisations of the Convolution

The PROPOSAL Monte Carlo simulations used for the generation of new transfer tensors in MUTE are the biggest bottleneck in terms of computation time (it takes approximately one week for 1000 jobs to run on a computer cluster to get a statistics level of 10^6 muons per bin). There is a possibility that the structure of the transfer tensor might lend itself to being calculated in a much more efficient way. In the current version of MUTE, PROPOSAL is used to calculate the survival probability matrix for each of the 28 default slant depths in `mtc._SLANT_DEPTHS`. However, there might be a linear algebraic relation between matrices for different depths such that the matrix need only be calculated for 0.5 km.w.e., and then that result could be used to derive the survival probabilities at a deeper depth by successively multiplying it into the surface flux matrix a set number of times. The general formula for a vertical depth d would be:

$$\Phi^u(E^u, X = d, \theta) = (U(E^s, E^u, X = 0.5))^{2d} \otimes \Phi^s(E^s, \theta), \tag{9.1}$$

where $\otimes$ represents the convolution in Equation (6.15). Therefore, for a depth of 3 km.w.e., for example, instead of $\Phi^u(X = 3) = U(X = 3) \otimes \Phi^s$, which is what is currently done, one could possibly do $\Phi^u(X = 3) = (U(X = 0.5))^6 \otimes \Phi^s$. This would reduce the time required for the production of new transfer tensors significantly, as well as greatly scale down the memory and disk space required to run MUTE, further improving the efficiency of the program. However, its feasibility requires more careful investigation into the structure of the transfer tensor in order to determine if a relation like the one in Equation (9.1) exists.

9.1.2 Charge Separation

Currently, MUTE provides results for muon fluxes and intensities underground for the combination of both positively and negatively charged muons. However, MCEQ and DAEMONFLUX can provide surface fluxes for μ^+ and μ^- individually. Because of this, charge separation between μ^+ and μ^- could be implemented into MUTE, which would aid in studying the underground muon charge ratio. This could provide an additional observable to compare to underground muon data, and it would be particularly relevant for muon-induced neutron studies, because positively charged muons can interact in the rock differently compared to negatively charged muons, leading to different neutron yields between the two polarities. A new global constant could be introduced in MUTE to select between calculations for μ^-, μ^+, or $\mu^- + \mu^+$.

9.1.3 Muon-Induced Neutrons

Muon-induced neutrons (or "external neutrons," as opposed to internal neutrons that are produced in radioactive decays of detector components) are an important source of background for dark matter and neutrino detectors. In order to correctly estimate the expected neutron background rates in a given experiment, highly detailed and precise simulations must be done. Simulations for muon-induced neutrons typically involve three components [95]:

1. **Generator:** A piece that models the primary cosmic ray flux and the development of the air shower down to the generation of the muon flux at sea level. In the case of MUTE, this is handled by MCEQ and DAEMONFLUX.
2. **Propagator:** A piece that handles the propagation of the muons through matter, calculating their energy losses. In the case of MUTE, this is handled by PROPOSAL.
3. **Detector Interaction:** A piece that defines the specific geometry of the laboratory setting and the detector and simulates and records the particle interactions that lead to the production of neutrons through cosmogenic activation. This is typically done using a general particle transport code, such as GEANT4 or FLUKA.

MUTE acts as a wrapper that combines the generator and propagator into one code. The energy and angular spectra output by the MUTE `mtu.calc_u_e_spect()` and `mtu.calc_u_ang_dist()` functions can be passed into general particle transport codes like GEANT4 or FLUKA in order to calculate muon-induced neutron rates. Although it is outside the scope of this work, integration with the detector interaction piece is possible. For example, neutron yields from muons could be calculated as a tensor $Y_n(E_\mu^u, E_n)$ using FLUKA [260]:

$$Y_n(E_\mu, E_n) = \frac{\mathrm{d}N_n(E_n)}{\mathrm{d}N_\mu(E_\mu)} \frac{\rho}{\rho_{\mathrm{ref}}}, \tag{9.2}$$

where $N_n(E_n)$ is the number of neutrons that fall within a certain neutron energy bin ΔE_n, $N_\mu(E_\mu)$ is the number of muons in a given muon energy bin, and ρ is the density of the medium. This neutron yield tensor could be convolved with the underground muon fluxes already provided by MUTE from Equation (6.15) to provide underground neutron fluxes:

$$\begin{aligned}\underbrace{\Phi_n(E_n,X,\theta)}_{\text{MUTE}} &= \underbrace{\Phi_\mu^s(E_\mu^s,\theta)}_{\text{MCEQ}} \otimes \underbrace{U(E_\mu^s,E_\mu^u,X)}_{\text{PROPOSAL}} \otimes \underbrace{Y_n(E_\mu^u,E_n)}_{\text{FLUKA}} \\ &= \Phi_\mu^u(E_\mu^u,X,\theta) \otimes Y_n(E_\mu^u,E_n).\end{aligned} \tag{9.3}$$

If the detector's vertical length is short enough that the entirety of the detector can be approximated to be at the same depth h, then dependence on X can be neglected. In this case, integrating this neutron flux over all variables and multiplying by the detector surface area, A, would give the neutron rate in the detector:

$$R_n = A \iint \Phi_n(E_n,X(\theta,\phi),\theta)\mathrm{d}E_n\mathrm{d}\Omega. \tag{9.4}$$

If this approximation cannot be made, as would likely be the case for both IceCube and Hyper-Kamiokande, a more complicated analysis would have to be performed. One option is to consider an effective area of the detector, as is often done for IceCube, and weight the values of N_n by Φ_μ^u. Options to deal with these different cases could be implemented into the MUTE calculations to keep the code flexible.

9.1.4 Correcting Density Profiles

As shown in Table 5.1, some laboratories have large uncertainties on their rock densities, and some have no uncertainty at all. MUTE could potentially be used to make predictions for these labs' rock densities by calculating the total muon flux for a range of densities and fitting the experimental flux to the results. If an experiment has incorrectly judged the density of the rock above their lab, this could be found by MUTE and could be corrected by adjusting the depths in the calculations. For flat overburdens, this can be done by scaling the vertical depth, h, by the ratio of the densities:

$$h_{\text{scaled}} = \left(\frac{\rho_{\text{corr}}}{\rho}\right)h, \tag{9.5}$$

where ρ_{corr} is the correction density and ρ is the original density. For mountains, this adjustment can be made manually to the mountain map provided to the `mtc.load_mountain()` function, or it can be made by passing the `density` parameter into the function.

This method was carried out for the Gran Sasso mountain above LNGS by plotting the total underground muon flux for a range of densities, and the result is shown in Figure 9.1. When comparing to the measurement from LVD, this figure suggests the rock density should be closer to

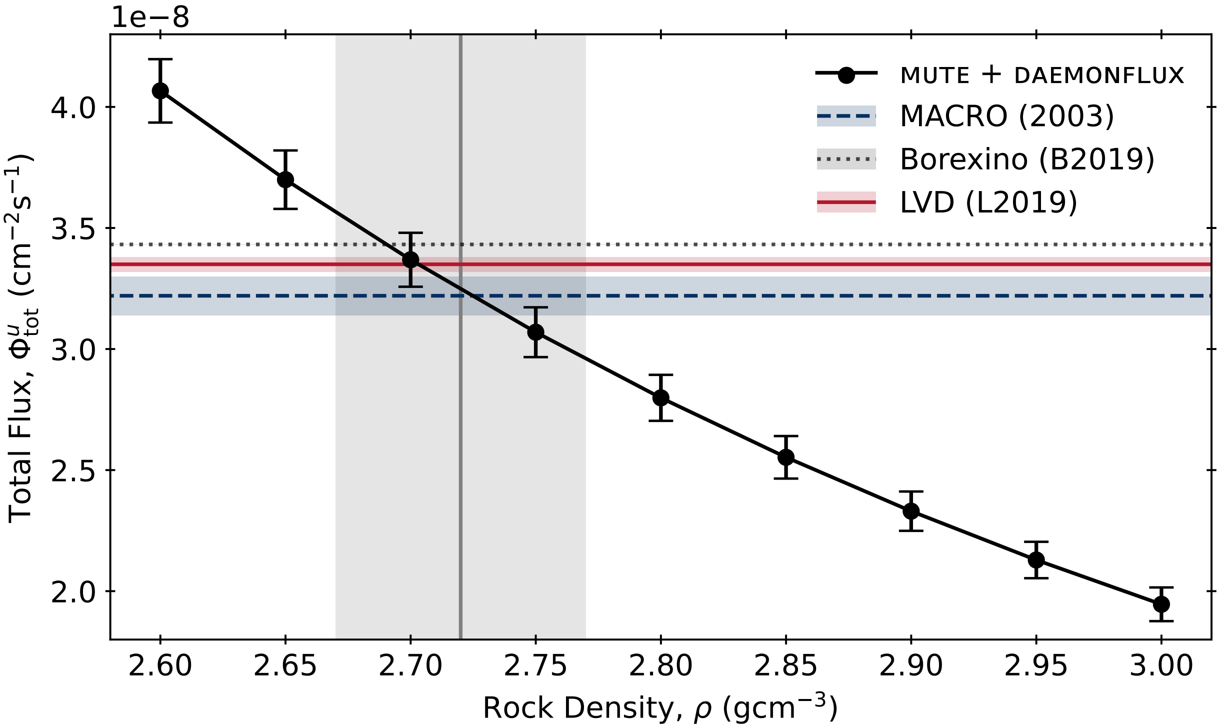

Figure 9.1: Total underground muon fluxes as a function of rock density under the Gran Sasso mountain as calculated by MUTE using the DAEMONFLUX model. The error bars represent the hadronic interaction model uncertainty. The horizontal lines and their error bands represent the experimental total fluxes from MACRO [225], Borexino [154], and LVD [148], as given in Table 8.1. The vertical line and its error band represent the measured rock density of (2.72 ± 0.05) gcm^{-3} given in Table 5.1.

(2.70 ± 0.05) gcm^{-3}, and that the value of (2.72 ± 0.05) gcm^{-3} might be slightly overestimated, though this latter value agrees well with the measurement from MACRO [225].

The limitation of using this method is that large uncertainties on both the MUTE prediction and the experimental measurement will lead to large uncertainties in the predicted density, so more precise density predictions require more precise experimental measurements. However, this can still be useful for laboratories that have no uncertainty for their densities, or for those that have significantly over- or underestimated their rock density.

9.1.5 Muon Tomography

Muon tomography refers to the use of cosmic-ray muons to produce detailed images of objects and structures in two or three dimensions in a non-invasive manner. The measurement of muon fluxes, and, in particular, the way they scatter off objects and are absorbed, can provide insight into the structure, density, and composition of those objects, similar to X-ray technology but with particles that are far more penetrating. Techniques that focus on the scattering of muons are referred to as muon scattering tomography (MST), and those that focus on the absorption of muons are referred to as muography. These techniques are useful in cases where the scanned object is inaccessible, such as in geological or archaeological surveying, or where the object is dangerous to approach, such as in investigating nuclear waste leaks.

The difficulties with muon tomography stem from the fact that the distances involved are so short, typically on the scale of metres or tens of metres. At these short distances, it can be difficult for detectors to differentiate between muons and electrons, and so results are not always precise. MUTE could find application in helping cross-check muon fluxes observed by muography detectors. However, at the moment, the minimum slant depth in MUTE is 0.5 km.w.e. due to limitations related to the optimisation of PROPOSAL for large distances. Therefore, for MUTE to provide any significant amount of contribution to muon tomography studies, more work would have to be done.

9.1.6 Muon Paleotopometry

Muon paleotopometry is an emerging geochronological method that uses cosmogenic nuclides to quantify timelines of relief formation in the Earth. It is a common question in earth sciences to ask how old certain geographical features are and how fast they formed, and atmospheric muons can help answer this question. When muons travel through the rock near the surface of the Earth, they undergo spallation processes, as explained in Section 5.1.1. This is referred to as cosmogenic activation, and it can lead to the production of rare but long-lived radioisotopes, such as ^{26}Al ($t_{1/2} = 0.7$ Ma), ^{14}C ($t_{1/2} = 5.7$ ka), and ^{10}Be ($t_{1/2} = 1.4$ Ma). These all have half-lives much shorter than the age of the Earth (4.5 Ga). Therefore, their presence in the Earth's crust is evidence of spallation from cosmic rays, and their concentrations reveal information about the exposure age of the feature to cosmic rays [261]. While a similar technique with cosmogenic neutrons has been in use for many decades, the novelty of muon paleotopometry is in using the fact that muons are more highly penetrating particles than neutrons, and so deeper and therefore older reliefs can be analysed with higher precision, addressing a methodological gap in characterising relief formation in the field.

MUTE, in combination with a general particle transport code like GEANT4 or FLUKA, as described in Section 9.1.3, can be used to obtain computed concentrations of cosmogenic nuclides. Erosion rates can then be calculated as the difference between these computed concentrations and measured concentrations that are collected from rock samples using a series of experimental techniques. The erosion rates along with the abundance of the radioisotopes can then be used to determine the age of the relief. This is work that is currently underway at Dalhousie University in Halifax, Nova Scotia by Lauren MacLellan, Marie-Cécile Piro, and John Gosse.

9.1.7 Muon Bundles

At the moment, MUTE deals only with single muons. However, atmospheric muons occasionally reach the Earth's surface in clusters called "muon bundles." These can be interesting tools of study for research into astrophysics, the composition of cosmic rays, or atmospheric physics.

Measurements of muon bundles have been performed by many experiments, including GRAPES-3 [262], NEVOD-DECOR [263], MINOS [242], NOνA [246, 264], IceCube [265], KM3NeT [120], LVD [266], MACRO [267, 268], and Fréjus [131, 269], as well as by the ALICE detector at CERN [270]. An upcoming experiment that may provide insightful muon bundle data is the Hyper-Kamiokande water Cherenkov neutrino observatory being assembled at the Kamioka Observatory. This experiment will have particular sensitivity to muon bundles during their fill procedure when the tank is partially filled with water, as photomultiplier tubes at the base of the detector will have better spatial resolution for the Cherenkov radiation showing the bundles' lateral spread.

Muon bundles are especially important for underwater detectors, which often observe muon bundles, and where atmospheric muons serve both as a background (as explained in Section 5.1.1), as a tool to check the performance of the detector and the validity of simulations [271]. Proper simulation of muon bundles is important to cross-check data analyses, since muon bundles have complex event signatures and reconstruction is often difficult [120, 272]. Furthermore, an interesting phenomenon is observed with multiple muons in that the amplitude of their seasonal variations is inverted compared to single muons: while single muons are expected to see a peak in their flux at the surface in summer according to [264], many experiments have observed multiple muons with a peak at or near the surface in the winter, such as MINOS [242], GRAPES-3 [262], NEVOD-DECOR [263], and NOνA [264]. This cannot be explained by current models. The MINOS Collaboration gives a summary and description of four possible explanations for this phenomenon: a geometric effect from the production layer of the muons in the atmosphere that affects the lateral distribution of the muons underground; muon bundles being produced at different altitudes which have different temperature profiles compared to single muons and are therefore affected by the seasons differently; conventional mesons being more likely to decay than interact in summer and therefore producing fewer muons overall; and prompt mesons that have opposite seasonal variations to conventional mesons producing more muons in the winter, when they are more likely to interact than decay [242]. An in-depth study into simulating muon bundles could reveal interesting physics.

The observables of interest for multiple muons are usually the muon multiplicity, which increases as cosmic ray energy per nucleon increases, and the lateral spread of the muons in the bundle, which decreases as cosmic ray energy per nucleon increases. While not native to the current MUTE framework, simulations of muon bundles can be achieved by using MUTE as a toolkit. The `set_single_particle_energy()` function in MCEQ can be used to set the energy of a single primary cosmic ray nucleus, and MCEQ can solve the cascade equations for muon production as normal. This returns a surface flux, which can be convolved with MUTE transfer tensors. Integrating the resultant underground flux over energy will give the mean muon multiplicity, $\left\langle N_{\mu}^{u} \right\rangle$. A plot of this for various depths underground is shown in Figure 9.2.

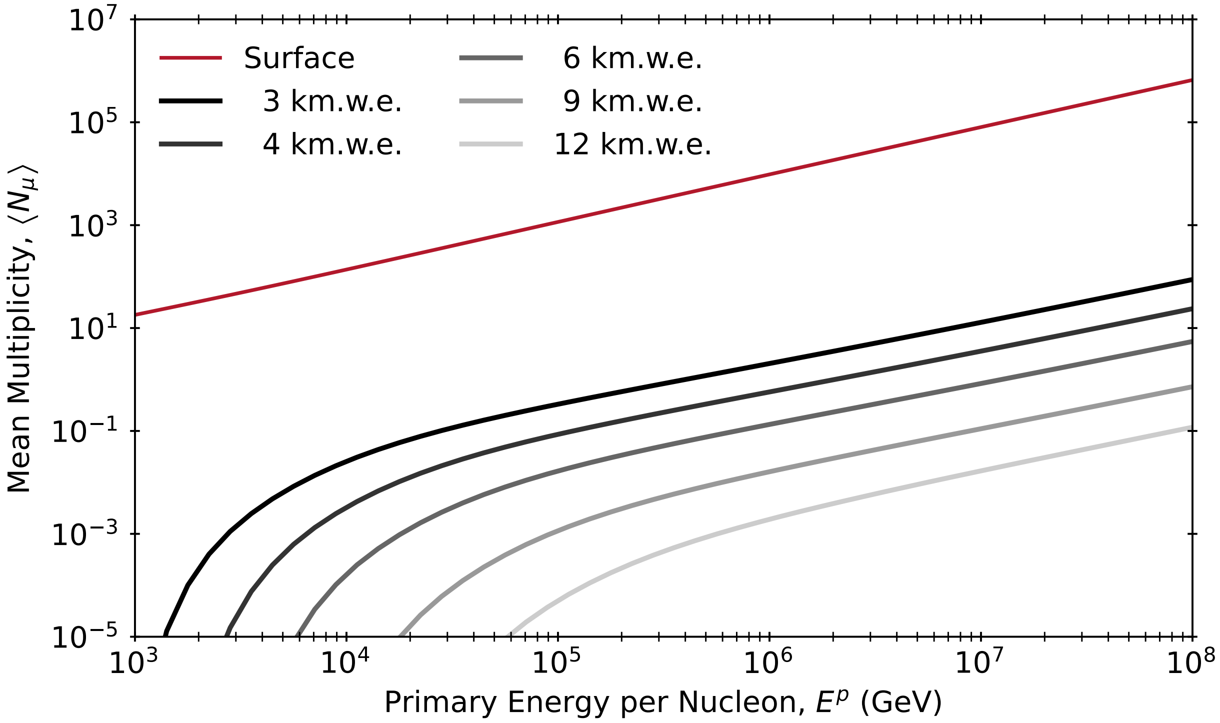

Figure 9.2: Mean muon bundle multiplicity vs cosmic ray energy per nucleon for various depths.

A new global constant could be introduced in MUTE to select between calculations for single muons or multiple muons. However, while preliminary results suggest that MUTE could be used to calculate muon bundle multiplicities, because multiple scattering is not turned on in MUTE (see Section 6.4), the lateral spread would not be able to be simulated without further changes to the propagation functions.

9.1.8 Propagation to Shallow Depths

At the moment, the minimum slant depth available in MUTE is 0.5 km.w.e. Lower depths can be set by turning on the `mtc.shallow_extrapolation` flag; however, this relies on extrapolation and does not produce smooth results. Although PROPOSAL is optimised for large depths, propagation of as little as a few centimetres is possible, so there is potential for the minimum depth in MUTE to be decreased, though the quality of results at these shallow depths must be verified.

There is great motivation behind lowering the minimum slant depth in MUTE, as it would allow for underground muon flux and intensity calculations to be carried out for shallow labs, such as Daya Bay and JUNO. It would also be useful for muon tomography, muon paleotopometry, and muon bundle studies, in particular for the comparison to the ALICE data in [270], and may be useful for astrobiology studies similar to [273].

9.1.9 Neutrino Flux Uncertainties

Because atmospheric neutrinos are produced by the same hadronic interactions as atmospheric muons, precise muon flux data can be used to perform cross-calibrations to neutrino fluxes. The DAEMONFLUX code has successfully reduced atmospheric neutrino uncertainties from 40% to less than 10% up to 1 TeV by calibrating to surface muon data in [80]. A next step is to use MUTE to calibrate to the underground intensity and flux data shown in Figures 7.3 and 8.2 to further reduce the uncertainties. When fitting to underground muon data in order to constrain uncertainties on surface flux models, the total underground muon flux may be one of the most robust observables to use because the results are model-independent. However, because of the magnitudes of the systematic uncertainties coming from the rock density errors in Figure 8.3, they may not contribute much to a fit to experimental data. If successful, however, this would have significance for direct dark matter searches, as better knowledge of the neutrino flux can reduce the neutrino fog that future ton-scale dark matter detectors will eventually reach as they increase their sensitivity [274]. This is work that is currently underway at Academia Sinica in Taipei, Taiwan by Maheen Tariq and Anatoli Fedynitch.

References

[1] A. Fedynitch, W. Woodley and M.-C. Piro, *On the Accuracy of Underground Muon Intensity Calculations*, *Astrophys. J.* **928** (2022) 27 [`2109.11559`].

[2] P.H. Barrett, L.M. Bollinger, G. Cocconi, Y. Eisenberg and K. Greisen, *Interpretation of Cosmic-Ray Measurements Far Underground*, *Rev. Mod. Phys.* **24** (1952) 133.

[3] E.V. Bugaev, A. Misaki, V.A. Naumov, T.S. Sinegovskaya, S.I. Sinegovsky and N. Takahashi, *Atmospheric Muon Flux at Sea Level, Underground and Underwater*, *Phys. Rev. D* **58** (1998) 054001 [`hep-ph/9803488`].

[4] J.S. Rigden, *Building Blocks of Matter: A Supplement to the Macmillan Encyclopedia of Physics*, Macmillan Reference USA. (2003).

[5] T.K. Gaisser, R. Engel and E. Resconi, *Cosmic Rays and Particle Physics: 2nd Edition*, Cambridge University Press (June, 2016).

[6] M. Thomson, *Modern Particle Physics*, Cambridge University Press, New York (2013), 10.1017/cbo9781139525367.

[7] D. Griffiths, *Introduction to Elementary Particles*, John Wiley & Sons (2008).

[8] PARTICLE DATA GROUP, *Review of Particle Physics*, *Ptep* **2022** (2022) 083c01.

[9] B. D'Ettorre Piazzoli et al., *Chapter 4 Cosmic-Ray Physics*, *Chin. Phys. C* **46** (2022) 030004.

[10] T.K. Gaisser, T. Stanev and S. Tilav, *Cosmic Ray Energy Spectrum from Measurements of Air Showers*, *Front. Phys. (Beijing)* **8** (2013) 748 [`1303.3565`].

[11] R. Diehl et al., *Radioactive Al-26 and Massive Stars in the Galaxy*, *Nature* **439** (2006) 45 [`astro-ph/0601015`].

[12] E. Fermi, *On the Origin of the Cosmic Radiation*, *Phys. Rev.* **75** (1949) 1169.

[13] K. Greisen, *End to the Cosmic Ray Spectrum?*, *Phys. Rev. Lett.* **16** (1966) 748.

[14] G.T. Zatsepin and V.A. Kuzmin, *Upper Limit of the Spectrum of Cosmic Rays*, *JETP Lett.* **4** (1966) 78.

[15] M. Nagano and A.A. Watson, *Observations and Implications of the Ultrahigh-Energy Cosmic Rays*, *Rev. Mod. Phys.* **72** (2000) 689.

[16] BESS, *Measurement of Cosmic-Ray Spectra with the BESS/BESS-TeV*, *Nucl. Phys. B Proc. Suppl.* **145** (2005) 132.

[17] S. Haino et al., *Measurements of Primary and Atmospheric Cosmic-Ray Spectra with the BESS-TeV Spectrometer*, *Phys. Lett. B* **594** (2004) 35 [`astro-ph/0403704`].

[18] PIERRE AUGER, *The Pierre Auger Cosmic Ray Observatory*, *Nucl. Instrum. Meth. A* **798** (2015) 172 [`1502.01323`].

[19] LHAASO, *The LHAASO Experiment: From Gamma-Ray Astronomy to Cosmic Rays*, *Nucl. Part. Phys. Proc.* **279-281** (2016) 166 [`1602.07600`].

[20] HAWC, *All-Particle Cosmic Ray Energy Spectrum Measured by the HAWC Experiment from 10 to 500 TeV*, *Phys. Rev. D* **96** (2017) 122001 [`1710.00890`].

[21] C. Grupen and I. Buvat, *Handbook of Particle Detection and Imaging*, Springer Science & Business Media (2011).

[22] A. Haungs et al., *KCDC - The KASCADE Cosmic-Ray Data Centre*, *J. Phys. Conf. Ser.* **632** (2015) 012011 [`1504.06696`].

[23] F.G. Schröder, *Radio Detection of Cosmic-Ray Air Showers and High-Energy Neutrinos*, *Prog. Part. Nucl. Phys.* **93** (2017) 1 [`1607.08781`].

[24] T.K. Gaisser and M. Honda, *Flux of Atmospheric Neutrinos*, *Ann. Rev. Nucl. Part. Sci.* **52** (2002) 153 [`hep-ph/0203272`].

[25] T.K. Gaisser, *Spectrum of Cosmic-Ray Nucleons, Kaon Production, and the Atmospheric Muon Charge Ratio*, *Astropart. Phys.* **35** (2012) 801 [`1111.6675`].

[26] V.I. Zatsepin and N.V. Sokolskaya, *Three Component Model of Cosmic Ray Spectra from 100 GeV up to 100 PeV*, *Astron. Astrophys.* **458** (2006) 1 [`astro-ph/0601475`].

[27] H.P. Dembinski, R. Engel, A. Fedynitch, T. Gaisser, F. Riehn and T. Stanev, *Data-Driven Model of the Cosmic-Ray Flux and Mass Composition from 10 GeV to 10^{11} GeV*, *PoS* **ICRC2017** (2018) 533 [`1711.11432`].

[28] P. Auger, P. Ehrenfest, R. Maze, J. Daudin and R.A. Fréon, *Extensive Cosmic-Ray Showers*, *Reviews of modern physics* **11** (1939) 288.

[29] W. Heitler, *The Quantum Theory of Radiation*, vol. 5 of *International Series of Monographs on Physics*, Oxford University Press, Oxford (1936).

[30] S. Hauser, *Measurement of Seasonal Variations of the Atmospheric Neutrino Flux with IceCube Using an Unbinned Likelihood*, Master's thesis, RWTH Aachen University, 2020.

[31] R. Bellotti et al., *A Measurement of the Negative Muon Spectrum Between 0.3-GeV/c and 40-GeV/c in the Atmosphere*, *Phys. Rev. D* **53** (1996) 35.

[32] WIZARD/MASS2, *Balloon Measurements of Cosmic Ray Muon Spectra in the Atmosphere along with those of Primary Protons and Helium Nuclei over Mid-Latitude*, *Phys. Rev. D* **60** (1999) 052002 [`hep-ex/9905012`].

[33] WIZARD/CAPRICE, *Measurement of the Flux of Atmospheric Muons with the CAPRICE94 Apparatus*, *Phys. Rev. D* **62** (2000) 032007 [`hep-ex/0004014`].

[34] M. Boezio et al., *Energy Spectra of Atmospheric Muons Measured with the CAPRICE98 Balloon Experiment*, *Phys. Rev. D* **67** (2003) 072003.

[35] S. Coutu et al., *Energy Spectra, Altitude Profiles, and Charge Ratios of Atmospheric Muons*, *Phys. Rev. D* **62** (2000) 032001 [`hep-ex/0004010`].

[36] H.M. Kluck, *Measurement of the Cosmic-Induced Neutron Yield at the Modane Underground Laboratory*, Ph.D. thesis, KIT, Karlsruhe, 2013. 10.1007/978-3-319-18527-9.

[37] A. Fedynitch, R. Engel, T.K. Gaisser, F. Riehn and T. Stanev, *Calculation of Conventional and Prompt Lepton Fluxes at Very High Energy*, *EPJ Web Conf.* **99** (2015) 08001 [`1503.00544`].

[38] P.K. Grieder, *Extensive Air Showers: High-Energy Phenomena and Astrophysical Aspects - A Tutorial, Reference Manual and Data Book*, Springer Science & Business Media (2010).

[39] M. Spurio, *Probes of Multimessenger Astrophysics: Charged Cosmic Rays, Neutrinos, γ-Rays, and Gravitational Waves*, Astronomy and Astrophysics Library, Springer (2018), 10.1007/978-3-319-96854-4.

[40] A. Fedynitch, *Cascade Equations and Hadronic Interactions at Very High Energies*, Ph.D. thesis, KIT, Karlsruhe, Dept. Phys., November, 2015. 10.5445/ir/1000055433.

[41] S.J. Brodsky, P. Hoyer, C. Peterson and N. Sakai, *The Intrinsic Charm of the Proton*, *Phys. Lett. B* **93** (1980) 451.

[42] P. Gondolo, G. Ingelman and M. Thunman, *Charm Production and High-Energy Atmospheric Muon and Neutrino Fluxes*, *Astropart. Phys.* **5** (1996) 309 [`hep-ph/9505417`].

[43] S. Matsuno et al., *Cosmic Ray Muon Spectrum up to 20 TeV at 89 Degrees Zenith Angle*, *Phys. Rev. D* **29** (1984) 1.

[44] L3, *Measurement of the Atmospheric Muon Spectrum from 20 GeV to 3000 GeV*, *Phys. Lett. B* **598** (2004) 15 [`hep-ex/0408114`].

[45] MINOS, *Measurement of the Atmospheric Muon Charge Ratio at TeV Energies with MINOS*, *Phys. Rev. D* **76** (2007) 052003 [`0705.3815`].

[46] CMS, *Measurement of the Charge Ratio of Atmospheric Muons with the CMS Detector*, *Phys. Lett. B* **692** (2010) 83 [`1005.5332`].

[47] OPERA, *Measurement of the TeV Atmospheric Muon Charge Ratio with the Complete OPERA Data Set*, *Eur. Phys. J. C* **74** (2014) 2933 [`1403.0244`].

[48] HIRES, *Measurement of the Flux of Ultrahigh Energy Cosmic Rays from Monocular Observations by the High Resolution Fly's Eye Experiment*, *Phys. Rev. Lett.* **92** (2004) 151101 [`astro-ph/0208243`].

[49] HIRES, *First Observation of the Greisen-Zatsepin-Kuzmin Suppression*, *Phys. Rev. Lett.* **100** (2008) 101101 [`astro-ph/0703099`].

[50] HIRES, *Measurement of the Flux of Ultra High Energy Cosmic Rays by the Stereo Technique*, *Astropart. Phys.* **32** (2009) 53 [`0904.4500`].

[51] PIERRE AUGER, *Observation of the Suppression of the Flux of Cosmic Rays above* $4\times10^{19}eV$, *Phys. Rev. Lett.* **101** (2008) 061101 [`0806.4302`].

[52] PIERRE AUGER, *Measurement of the Energy Spectrum of Cosmic Rays above* 10^{18} *eV Using the Pierre Auger Observatory*, *Phys. Lett. B* **685** (2010) 239 [`1002.1975`].

[53] TELESCOPE ARRAY, *The Cosmic Ray Energy Spectrum Observed with the Surface Detector of the Telescope Array Experiment*, *Astrophys. J. Lett.* **768** (2013) L1 [`1205.5067`].

[54] D.J. Bird et al., *Detection of a Cosmic Ray with Measured Energy Well Beyond the Expected Spectral Cut-off Due to Cosmic Microwave Radiation*, *Astrophys. J.* **441** (1995) 144 [`astro-ph/9410067`].

[55] P. Evenson, *Time Variation of Galactic Cosmic Rays*, in *Jet Propulsion Lab, California Inst. of Tech., Interplanetary Particle Environment. Proceedings of a Conference*, 1988.

[56] P.K.F. Grieder, *Cosmic Rays at Earth: Researcher's Reference, Manual, and Data Book*, Elsevier, Amsterdam (2001).

[57] F. Schroder, W. Rhode and H. Meyer, *Muon Flux Simulation and Comparison with Fréjus Measurements*, in *27th International Cosmic Ray Conference*, August, 2001.

[58] S. Miyake, *Rapporteur Paper On Muons And Neutrinos*, in *13th International Cosmic Ray Conference*, 1973.

[59] A. Okada, *On the Atmospheric Muon Energy Spectrum in the Deep Ocean and its Parameterisation*, *Astropart. Phys.* **2** (1994) 393.

[60] L.V. Volkova and G.T. Zatsepin, *Fluxes of Cosmic Ray Muons and Atmospheric Neutrinos at High Energies*, *Phys. Atom. Nucl.* **64** (2001) 266.

[61] L. Volkova, G. Zatsepin and L. Kuz'michev, *Cosmic-Ray Muon Spectrum at Sea Level and the Primary Cosmic-Ray Nucleon Spectrum*, *Sov. J. Nucl. Phys. (Engl. Transl.); (United States)* **29** (1979) .

[62] P. Lipari, *Lepton Spectra in the Earth's Atmosphere*, *Astropart. Phys.* **1** (1993) 195.

[63] A.A. Alves Jr., M. Reininghaus, J.-M. Alameddine, J. Albrecht, J. Alvarez-Muniz, L. Arrabito et al., *Hadron Cascades in CORSIKA 8*, *PoS* **ICRC2021** (2021) 474.

[64] A. Ferrari, P.R. Sala, A. Fasso and J. Ranft, *FLUKA: A Multi-Particle Transport Code (Program Version 2005)*, Tech. Rep. (October, 2005), DOI.

[65] G. Battistoni et al., *Overview of the FLUKA Code*, *Annals Nucl. Energy* **82** (2015) 10.

[66] T. Pierog, I. Karpenko, J.M. Katzy, E. Yatsenko and K. Werner, *EPOS LHC: Test of Collective Hadronisation with Data Measured at the CERN Large Hadron Collider*, *Phys. Rev.* **C92** (2015) 034906 [`1306.0121`].

[67] H.J. Drescher, M. Hladik, S. Ostapchenko, T. Pierog and K. Werner, *Parton Based Gribov-Regge Theory*, *Phys. Rept.* **350** (2001) 93 [`hep-ph/0007198`].

[68] N.N. Kalmykov, S.S. Ostapchenko and A.I. Pavlov, *Quark-Gluon String Model and EAS Simulation Problems at Ultra-High Energies*, *Nucl. Phys. B Proc. Suppl.* **52** (1997) 17.

[69] A.B. Kaidalov and K.A. Ter-Martirosian, *Pomeron as Quark-Gluon Strings and Multiple Hadron Production at SPS Collider Energies*, *Phys. Lett. B* **117** (1982) 247.

[70] A. Capella, U. Sukhatme, C.-I. Tan and J. Tran Thanh Van, *Dual Parton Model*, *Phys. Rept.* **236** (1994) 225.

[71] S. Roesler, R. Engel and J. Ranft, *The Monte Carlo Event Generator DPMJET-III*, in *International Conference on Advanced Monte Carlo for Radiation Physics, Particle Transport Simulation and Applications (MC 2000)*, pp. 1033–1038, December, 2000, DOI [`hep-ph/0012252`].

[72] S. Roesler, R. Engel and J. Ranft, *The Event Generator DPMJET-III at Cosmic Ray Energies*, in *27th International Cosmic Ray Conference*, August, 2001.

[73] J. Ranft, *The Dual Parton Model at Cosmic Ray Energies*, *Phys. Rev. D* **51** (1995) 64.

[74] R.S. Fletcher, T.K. Gaisser, P. Lipari and T. Stanev, *SIBYLL: An Event Generator for Simulation of High-Energy Cosmic Ray Cascades*, *Phys. Rev. D* **50** (1994) 5710.

[75] F. Riehn, R. Engel, A. Fedynitch, T.K. Gaisser and T. Stanev, *Hadronic Interaction Model SIBYLL-2.3d and Extensive Air Showers*, *Phys. Rev. D* **102** (2020) 063002 [`1912.03300`].

[76] A. Fedynitch and M. Huber, *Data-Driven Hadronic Interaction Model for Atmospheric Lepton Flux Calculations*, *Phys. Rev. D* **106** (2022) 083018 [`2205.14766`].

[77] NA49, *Inclusive Production of Charged Pions in p+C Collisions at 158-GeV/c Beam Momentum*, *Eur. Phys. J.* **C49** (2007) 897 [`hep-ex/0606028`].

[78] NA49, *Inclusive Production of Charged Kaons in p+p Collisions at 158-GeV/c Beam Momentum and a New Evaluation of the Energy Dependence of Kaon Production up to Collider Energies*, *Eur. Phys. J. C* **68** (2010) 1 [`1004.1889`].

[79] NA61/SHINE, *Measurements of $\pi^{\pm}$, $K^{\pm}$, K^0_S, Λ, and Proton Production in Proton-Carbon Interactions at 31 GeV/c with the NA61/SHINE Spectrometer at the CERN SPS*, *Eur. Phys. J. C* **76** (2016) 84 [`1510.02703`].

[80] J.P. Yañez and A. Fedynitch, DAEMONFLUX*: DAta-drivEn MuOn-calibrated Neutrino Flux*, *Phys. Rev. D* **107** (2023) 123037 [`2303.00022`].

[81] G.D. Barr, T.K. Gaisser, S. Robbins and T. Stanev, *Uncertainties in Atmospheric Neutrino Fluxes*, *Phys. Rev. D* **74** (2006) 094009 [`astro-ph/0611266`].

[82] W.H. Barkas, W. Birnbaum and F.M. Smith, *Mass-Ratio Method Applied to the Measurement of L-Meson Masses and the Energy Balance in Pion Decay*, *Phys. Rev.* **101** (1956) 778.

[83] H. Bichsel, *Barkas Effect and Effective Charge in the Theory of Stopping Power*, *Physical Review A* **41** (1990) 3642.

[84] H.H. Andersen and J.F. Ziegler, *Hydrogen: Stopping Powers and Ranges in All Elements*, in *The Stopping and Range of Ions in Matter*, vol. 3 (1977).

[85] D. Semrad, P. Mertens and P. Bauer, *Reference Proton Stopping Cross-Sections for Five Elements Around the Maximum*, *Nuclear Instruments and Methods in Physics Research Section B: Beam Interactions with Materials and Atoms* **15** (1986) 86.

[86] Y. Boudouma, A. Chami, H. Beaumevieille and M. Boudjema, *Stopping Power of Protons in He at Low Energies*, *Journal de Physique I* **2** (1992) 1803.

[87] R. Golser and D. Semrad, *Observation of a Striking Departure from Velocity Proportionality in Low-Energy Electronic Stopping*, *Physical review letters* **66** (1991) 1831.

[88] W. Lohmann, R. Kopp and R. Voss, *Energy Loss of Muons in the Energy Range 1–10000 GeV*, Tech. Rep. European Organisation for Nuclear Research (1985).

[89] SNO, *Measurement of the Cosmic Ray and Neutrino-Induced Muon Flux at the Sudbury Neutrino Observatory*, *Phys. Rev. D* **80** (2009) 012001 [`0902.2776`].

[90] M. Menon and P.R. Murthy, *Cosmic Ray Intensities Deep Underground*, *Progress in Elementary Particle and Cosmic Ray Physics* **9** (1967) 163.

[91] Y.-S. Tsai, *Pair Production and Bremsstrahlung of Charged Leptons*, *Rev. Mod. Phys.* **46** (1974) 815.

[92] M.J. Berger and S.M. Seltzer, *Tables of Energy Losses and Ranges of Electrons and Positrons*, Tech. Rep. (1964).

[93] D.E. Groom, N.V. Mokhov and S.I. Striganov, *Muon Stopping Power and Range Tables 10 MeV to 100 TeV*, *Atom. Data Nucl. Data Tabl.* **78** (2001) 183.

[94] B.B. Rossi, *High-Energy Particles*, Prentice-Hall physics series, Prentice-Hall, New York, NY (1952).

[95] J.-H. Koehne, K. Frantzen, M. Schmitz, T. Fuchs, W. Rhode, D. Chirkin et al., *PROPOSAL: A Tool for Propagation of Charged Leptons*, *Computer Physics Communications* **184** (2013) 2070.

[96] H. Bethe, *Theory of the Passage of Fast Corpuscular Rays Through Matter*, *Annalen Phys.* **5** (1930) 325.

[97] R.M. Sternheimer, *The Density Effect for Ionisation Loss in Materials*, *Phys. Rev.* **88** (1952) 851.

[98] S.R. Kelner and Y.D. Kotov, *Pair Production by Muons in the Field of Nuclei*, *Canadian Journal of Physics* **46** (1968) S387.

[99] R.P. Kokoulin and A.A. Petrukhin, *Analysis of the Cross-Section of Direct Pair Production by Fast Muons*, in *Proceedings of the 11th International Conference on Cosmic Rays, held in Budapest, 25 August-4 September, 1969. Edited by A. Somogyi, Vol. 4. Acta Physica, Supplement to Volume 29. Muons and Neutrinos, Techniques., p. 277*, vol. 4, p. 277, 1970.

[100] L. Bezrukov and E. Bugaev, *Nucleon Shadowing Effects in Photonuclear Interactions*, *Sov. J. Nucl. Phys. (Engl. Transl.)* **33** (1981) .

[101] A.V. Butkevich and S.P. Mikheev, *The Cross-Section of Muon Photonuclear Interaction*, in *28th International Cosmic Ray Conference*, pp. 1471–1474, July, 2003.

[102] H. Abramowicz, E. Levin, A. Levy and U. Maor, *A Parameterisation of $\sigma_T(\gamma^* p)$ above the Resonance Region for $Q^2 \geq 0$*, *Physics Letters B* **269** (1991) 465.

[103] H. Abramowicz and A. Levy, *The ALLM Parameterisation of $\sigma_{\mathrm{tot}}(\gamma^* p)$: An Update*, `hep-ph/9712415`.

[104] R.P. Kokoulin, *Uncertainties in Underground Muon Flux Calculations*, *Nucl. Phys. B Proc. Suppl.* **70** (1999) 475.

[105] P. Lipari and T. Stanev, *Propagation of Multi-TeV Muons*, *Phys. Rev. D* **44** (1991) 3543.

[106] MACRO, *Study of Photonuclear Interaction of Muons in Rock with the MACRO Experiment*, *Italian Phys. Soc. Proc.* **65** (1999) 419 [`hep-ex/9809006`].

[107] D. Mei and A. Hime, *Muon-Induced Background Study for Underground Laboratories*, *Phys. Rev. D* **73** (2006) 053004 [`astro-ph/0512125`].

[108] J.A. Formaggio and C. Martoff, *Backgrounds To Sensitive Experiments Underground*, *Annual Review of Nuclear and Particle Science* **54** (2004) 361.

[109] M.J. Dolinski, A.W.P. Poon and W. Rodejohann, *Neutrinoless Double-Beta Decay: Status and Prospects*, *Ann. Rev. Nucl. Part. Sci.* **69** (2019) 219 [`1902.04097`].

[110] M. Schumann, *Direct Detection of WIMP Dark Matter: Concepts and Status*, *J. Phys. G* **46** (2019) 103003 [`1903.03026`].

[111] KamLAND-Zen, *Search for the Majorana Nature of Neutrinos in the Inverted Mass Ordering Region with KamLAND-Zen*, *Phys. Rev. Lett.* **130** (2023) 051801 [`2203.02139`].

[112] Exo-200, *Search for Neutrinoless Double-β Decay with the Complete EXO-200 Dataset*, *Phys. Rev. Lett.* **123** (2019) 161802 [`1906.02723`].

[113] nEXO, *nEXO: Neutrinoless Double Beta Decay Search Beyond 10^{28}-Year Half-Life Sensitivity*, *J. Phys. G* **49** (2022) 015104 [`2106.16243`].

[114] Darwin, *Cosmogenic Background Simulations for Neutrinoless Double Beta Decay with the DARWIN Observatory at Various Underground Sites*, *Eur. Phys. J. C* **84** (2024) 88 [`2306.16340`].

[115] A. Ianni, *Considerations on Underground Laboratories*, *J. Phys. Conf. Ser.* **1342** (2020) 012003.

[116] A. Bettini, *New Underground Laboratories: Europe, Asia, and the Americas*, *Phys. Dark Univ.* **4** (2014) 36.

[117] A. Bettini, *The World Deep Underground Laboratories*, *Eur. Phys. J. Plus* **127** (2012) 114.

[118] A. Bettini, *The World Underground Scientific Facilities: A Compendium*, `0712.1051`.

[119] R. Adam et al., *Paarl Africa Underground Laboratory (PAUL)*, `2306.12083`.

[120] KM3NeT, *Letter of Intent for KM3NeT 2.0*, *J. Phys. G* **43** (2016) 084001 [`1601.07459`].

[121] KM3NeT, *Status of the KM3NeT Project*, *Jinst* **9** (2014) C04020 [`1408.1132`].

[122] E.-I. Esch, T.J. Bowles, A. Hime, A. Pichlmaier, R. Reifarth and H. Wollnik, *The Cosmic-Ray Muon Flux at WIPP*, *Nucl. Instrum. Meth. A* **538** (2005) 516 [`astro-ph/0408486`].

[123] Cosine-100, *Muon Detector and Muon Flux Measurement at Yangyang Underground Laboratory for the COSINE-100 Experiment*, *PoS* **ICRC2017** (2018) 883.

[124] S. Kamat, *Extending the Sensitivity to the Detection of WIMP Dark Matter with an Improved Understanding of the Limiting Neutron Backgrounds*, Ph.D. thesis, Case Western Reserve U., 2005. 10.2172/15017230.

[125] KamLAND Collaboration, *Production of Radioactive Isotopes Through Cosmic Muon Spallation in KamLAND*, *Phys. Rev. C* **81** (2010) 025807 [`0907.0066`].

[126] Hyper-Kamiokande, *Hyper-Kamiokande Design Report*, `1805.04163`.

[127] M. Robinson, V.A. Kudryavtsev, R. Luscher, J.E. McMillan, P.K. Lightfoot, N.J.C. Spooner et al., *Measurements of Muon Flux at 1070 Metres Vertical Depth in the Boulby Underground Laboratory*, *Nucl. Instrum. Meth. A* **511** (2003) 347 [`hep-ex/0306014`].

[128] W.D. Melbourne, *SABRE South at the Stawell Underground Physics Laboratory*, *J. Phys. Conf. Ser.* **2156** (2021) 012064.

[129] P. Urquijo, *Searching for Dark Matter at the Stawell Underground Physics Laboratory*, *EPJ Web Conf.* **123** (2016) 04002 [`1605.03299`].

[130] P. Capuano, G. De Luca, F. Di Sena, P. Gasparini and R. Scarpa, *The Density of the Rock Covering Gran Sasso Laboratories in Central Apennines, Italy by Underground Gravity Measurements*, *Journal of Applied Geophysics* **39** (1998) 25.

[131] Fréjus, *Experimental Study of Muon Bundles Observed in the Fréjus Detector*, *Phys. Rev. D* **40** (1989) 2163.

[132] J. Heise, *The Sanford Underground Research Facility*, *J. Phys. Conf. Ser.* **1342** (2020) 012085 [`1710.11584`].

[133] Majorana, *Muon Flux Measurements at the Davis Campus of the Sanford Underground Research Facility with the Majorana Demonstrator Veto System*, *Astropart. Phys.* **93** (2017) 70 [`1602.07742`].

[134] Y.-C. Wu et al., *Measurement of Cosmic Ray Flux in China JinPing underground Laboratory*, *Chin. Phys. C* **37** (2013) 086001 [`1305.0899`].

[135] Baikal-GVD, *High-Energy Neutrino Astronomy – Baikal-GVD Neutrino Telescope in Lake Baikal*, *Symmetry* **13** (2021) 377.

[136] IceCube, *Preliminary Design Document*, Tech. Rep. (2001).

[137] Antares, KM3NeT, *ANTARES and KM3NeT: The Latest Results of the Neutrino Telescopes in the Mediterranean*, *Universe* **5** (2019) 65.

[138] P-ONE, *The Pacific Ocean Neutrino Experiment*, *Nature Astron.* **4** (2020) 913 [2005.09493].

[139] E.G. Anassontzis et al., *Water Transparency Measurements in the Deep Ionian Sea*, *Astropart. Phys.* **34** (2010) 187.

[140] D. Real, A. Sánchez Losa, A. Díaz, F. Salesa Greus and D. Calvo, *The Neutrino Mediterranean Observatory Laser Beacon: Design and Qualification*, *Appl. Sciences* **13** (2023) 9935.

[141] SUPER-KAMIOKANDE, *The Super-Kamiokande Detector*, *Nucl. Instrum. Meth. A* **501** (2003) 418.

[142] W. Rhode, *Study of Ultra High Energy Muons with the Fréjus Detector*, *PhD diss., Bergische Universität Gesamthochschule Wuppertal* (1993) 93.

[143] LVD, *Muon 'Depth intensity' Relation Measured by LVD Underground Experiment and Cosmic-Ray Muon Spectrum at Sea Level*, *Phys. Rev. D* **58** (1998) 092005 [hep-ex/9806001].

[144] MACRO, *Vertical Muon Intensity Measured with MACRO at the Gran Sasso Laboratory*, *Phys. Rev. D* **52** (1995) 3793.

[145] JNE, *Muon Flux Measurement at China Jinping Underground Laboratory*, *Chinese Physics C* **45** (2021) 025001 [2007.15925].

[146] G. Pronost, M. Ikeda, T. Nakamura, H. Sekiya and S. Tasaka, *Development of New Radon Monitoring Systems in the Kamioka Mine*, *Ptep* **2018** (2018) 093h01 [1807.11142].

[147] M. Haffke, L. Baudis, T. Bruch, A.D. Ferella, T. Marrodan Undagoitia, M. Schumann et al., *Background Measurements in the Gran Sasso Underground Laboratory*, *Nucl. Instrum. Meth. A* **643** (2011) 36 [1101.5298].

[148] LVD, *Characterisation of the Varying Flux of Atmospheric Muons Measured with the Large Volume Detector for 24 Years*, *Phys. Rev. D* **100** (2019) 062002 [1909.04579].

[149] GERDA, *Flux Modulations Seen by the Muon Veto of the GERDA Experiment*, *Astropart. Phys.* **84** (2016) 29 [1601.06007].

[150] M. Cribier et al., *The Muon-Induced Background in the GALLEX Experiment*, *Astropart. Phys.* **6** (1999) 129.

[151] COSINUS, *Deep-Underground Dark Matter Search with a COSINUS Detector Prototype*, `2307.11139`.

[152] H. Wulandari, J. Jochum, W. Rau and F. von Feilitzsch, *Neutron Background Studies for the CRESST Dark Matter Experiment*, `hep-ex/0401032`.

[153] DAMA, *First Results from DAMA/LIBRA and the Combined Results with DAMA/NaI*, *Eur. Phys. J. C* **56** (2008) 333 [`0804.2741`].

[154] BOREXINO, *Modulations of the Cosmic Muon Signal in Ten Years of Borexino Data*, *JCAP* **02** (2019) 046 [`1808.04207`].

[155] OPERA, *Measurement of the Cosmic-Ray Muon Flux Seasonal Variation with the OPERA Detector*, *JCAP* **10** (2019) 003 [`1810.10783`].

[156] EDELWEISS, *Muon-Induced Background in the EDELWEISS Dark Matter Search*, *Astropart. Phys.* **44** (2013) 28 [`1302.7112`].

[157] S.I. Nikolsky, I.N. Stamenov and S.Z. Ushev, *Composition of Cosmic Radiation at Energies Approximately 10^{15} eV and Above*, *Sov. Phys. JETP* **60** (1984) 10.

[158] A.A. Lagutin and A.V. Yushkov, *Sea-Level Muon Spectrum in the Energy Range 1 TeV–10 TeV from the Data of Underground Experiments*, *Phys. Atom. Nucl.* **69** (2006) 460.

[159] M. Crouch, *An Improved World Survey Expression for Cosmic Ray Vertical Intensity vs Depth in Standard Rock*, in *International Cosmic Ray Conference*, vol. 6 of *International Cosmic Ray Conference*, p. 165, January, 1987.

[160] MACRO, *Study of Penetrating Cosmic Ray Muons and Search for Large-Scale Anisotropies at the Gran Sasso Laboratory*, *Phys. Lett. B* **249** (1990) 149.

[161] S. Miyake, *Empirical Formula for Range Spectrum of Cosmic Ray μ Mesons at Sea Level*, *J. Phys. Soc. Jap.* **18** (1963) 1093.

[162] GEANT4, *Geant4 – A Simulation Toolkit*, *Nucl. Instrum. Meth. A* **506** (2003) 250.

[163] J.F. Briesmeister et al., *MCNP™ – A General Monte Carlo N-Particle Transport Code*, Tech. Rep. LA-13709-M, Los Alamos National Laboratory, Los Alamos, NM, USA (December, 2000).

[164] N.V. Mokhov and C.C. James, *The MARS Code System User's Guide Version 15 (2016)*, Tech. Rep. (February, 2017), DOI.

[165] T. Sato et al., *Features of Particle and Heavy Ion Transport code System (PHITS) version 3.02*, *J. Nucl. Sci. Tech.* **55** (2018) 684.

[166] I.A. Sokalski, E.V. Bugaev and S.I. Klimushin, *Accuracy of Muon Transport Simulation*, in *2nd Workshop on Methodical Aspects of Underwater/Ice Neutrino Telescopes*, pp. 7–14, January, 2002 [`hep-ph/0201122`].

[167] A. Sandrock, R.P. Kokoulin and A.A. Petrukhin, *Theoretical Uncertainties of Muon Transport Calculations for Very Large Volume Neutrino Telescopes*, *J. Phys. Conf. Ser.* **1690** (2020) 012005.

[168] D. Chirkin and W. Rhode, *Muon Monte Carlo: A High-Precision Tool for Muon Propagation Through Matter*, `hep-ph/0407075`.

[169] G. Carminati, A. Margiotta and M. Spurio, *Atmospheric MUons from PArametric Formulas: A Fast GEnerator for Neutrino Telescopes (MUPAGE)*, *Comput. Phys. Commun.* **179** (2008) 915 [`0802.0562`].

[170] Y. Becherini, A. Margiotta, M. Sioli and M. Spurio, *A Parameterisation of Single and Multiple Muons in the Deep Water or Ice*, *Astropart. Phys.* **25** (2006) 1 [`hep-ph/0507228`].

[171] P. Antonioli, C. Ghetti, E.V. Korolkova, V.A. Kudryavtsev and G. Sartorelli, *A Three-Dimensional Code for Muon Propagation Through the Rock: MUSIC*, *Astropart. Phys.* **7** (1997) 357 [`hep-ph/9705408`].

[172] V.A. Kudryavtsev, *Muon Simulation Codes MUSIC and MUSUN for Underground Physics*, *Comput. Phys. Commun.* **180** (2009) 339 [`0810.4635`].

[173] W. Woodley and A. Fedynitch, *wjwoodley/mute: MUTE 2.0.0*, July, 2022. 10.5281/zenodo.6841971.

[174] W. Woodley, *wjwoodley/mute: MUTE 1.0.1*, December, 2021. 10.5281/zenodo.5803936.

[175] A. Fedynitch, F. Riehn, R. Engel, T.K. Gaisser and T. Stanev, *Hadronic interaction model sibyll 2.3c and inclusive lepton fluxes*, *Phys. Rev. D* **100** (2019) 103018 [`1806.04140`].

[176] G. van Rossum, B. Warsaw and N. Coghlan, *Style Guide for Python Code*, Pep 8 (2001).

[177] D. Heck, J. Knapp, J.N. Capdevielle, G. Schatz and T. Thouw, *CORSIKA: A Monte Carlo Code to Simulate Extensive Air Showers*, Tech. Rep. (February, 1998).

[178] R. Engel, D. Heck, T. Huege, T. Pierog, M. Reininghaus, F. Riehn et al., *Towards a Next Generation of CORSIKA: A Framework for the Simulation of Particle Cascades in Astroparticle Physics*, *Comput. Softw. Big Sci.* **3** (2019) 2 [`1808.08226`].

[179] T. Bergmann, R. Engel, D. Heck, N.N. Kalmykov, S. Ostapchenko, T. Pierog et al., *One-Dimensional Hybrid Approach to Extensive Air Shower Simulation*, *Astropart. Phys.* **26** (2007) 420 [`astro-ph/0606564`].

[180] S.J. Sciutto, *AIRES: A System for Air Shower Simulations*, `astro-ph/9911331`.

[181] T.K. Gaisser, D. Soldin, A. Crossman and A. Fedynitch, *Precision of Analytical Approximations in Calculations of Atmospheric Leptons*, *PoS* **ICRC2019** (2020) 893 [`1910.08676`].

[182] T. Kozynets, A. Fedynitch and D.J. Koskinen, *A Numerical Approach to Angular Distributions in Hadronic Cascades*, *PoS* **ICRC2021** (2021) 1209.

[183] A. Fedynitch, J. Becker Tjus and P. Desiati, *Influence of Hadronic Interaction Models and the Cosmic Ray Spectrum on the High Energy Atmospheric Muon and Neutrino Flux*, *Phys. Rev. D* **86** (2012) 114024 [`1206.6710`].

[184] S.P. Knurenko et al., *Spectrum of Cosmic Rays with Energy above* 10^{17} *eV*, *Int. J. Mod. Phys. A* **20** (2005) 6878 [`astro-ph/0411484`].

[185] PAMELA, *PAMELA Measurements of Cosmic-Ray Proton and Helium Spectra*, *Science* **332** (2011) 69 [`1103.4055`].

[186] A. Fedynitch, H. Dembinski, R. Engel, T.K. Gaisser, F. Riehn and T. Stanev, *A State-of-the-Art Calculation of Atmospheric Lepton Fluxes*, *PoS* **ICRC2017** (2018) 1019.

[187] R. Engel, F. Riehn, A. Fedynitch, T.K. Gaisser and T. Stanev, *The Hadronic Interaction Model SIBYLL – Past, Present and Future*, *EPJ Web Conf.* **145** (2017) 08001.

[188] F. Riehn, R. Engel, A. Fedynitch, T.K. Gaisser and T. Stanev, *A New Version of the Event Generator SIBYLL*, *PoS* **ICRC2015** (2016) 558 [`1510.00568`].

[189] E.-J. Ahn, R. Engel, T.K. Gaisser, P. Lipari and T. Stanev, *Cosmic Ray Interaction Event Generator SIBYLL-2.1*, *Phys. Rev. D* **80** (2009) 094003 [`0906.4113`].

[190] S. Ostapchenko, *Monte Carlo Treatment of Hadronic Interactions in Enhanced Pomeron Scheme: QGSJET-II Model*, *Phys. Rev.* **D83** (2011) 014018 [`1010.1869`].

[191] National Oceanic and Atmospheric Administration, *U.S. Standard Atmosphere, 1976*, Tech. Rep. ADA035728 (October, 1976).

[192] J.M. Picone, A.E. Hedin, D.P. Drob and A.C. Aikin, *NRLMSISE-00 Empirical Model of the Atmosphere: Statistical Comparisons and Scientific Issues*, *Journal of Geophysical Research: Space Physics* **107** (2002) Sia 15.

[193] J.C. Moreno and S. Sciutto, *Characterisation of the Atmospheric Depth Profile Using the Ground-Level Temperature: The Case of Malargüe, Argentina*, *Eur. Phys. J. Plus* **128** (2013) 10.

[194] M. Dunsch, J. Soedingrekso, A. Sandrock, M. Meier, T. Menne and W. Rhode, *Recent Improvements for the Lepton Propagator PROPOSAL*, *Comput. Phys. Commun.* **242** (2019) 132 [`1809.07740`].

[195] D. Groom, *Energy Loss in Matter by Heavy Particles*, *Particle Data Group Notes* **93** (1993) .

[196] V. Chazal, B. Chambon, M. De Jesus, D. Drain, C. Pastor, L. Vagneron et al., *Neutron background measurements in the underground laboratory of Modane*, *Astropart. Phys.* **9** (1998) 163.

[197] Y.S. Yoon, J. Kim and H. Park, *Neutron Background Measurement for Rare Event Search Experiments in the Yangyang Underground Laboratory*, *Astropart. Phys.* **126** (2021) 102533 [`2102.07205`].

[198] S. Bussino, C. Chiera, E. Lamanna, H. Bilokon and L. Miller, *Muon Survival Probabilities in Gran Sasso Rock*, Tech. Rep. (February, 1994).

[199] Cdex, *Studies of the Earth Shielding Effect to Direct Dark Matter Searches at the China Jinping Underground Laboratory*, *Phys. Rev. D* **105** (2022) 052005 [`2111.11243`].

[200] K. Mizukoshi et al., *Measurement of Ambient Neutrons in an Underground Laboratory at the Kamioka Observatory*, *PTEP* **2018** (2018) 123C01 [`1803.09757`].

[201] G.T. Ewan et al., *Sudbury Neutrino Observatory Proposal*, Tech. Rep. (October, 1987).

[202] D.W. Powers, S.J. Lambert, S.E. Shaffer, L.R. Hill and W.D. Weart, *Geological Characterisation Report, Waste Isolation Pilot Plant (WIPP) Site, Southeastern New Mexico*, Tech. Rep. (August, 1978), DOI.

[203] K. Ruddick, *Underground Particle Fluxes in the Soudan Mine*, *MINOS internal note NuMI-L-210* (1996) .

[204] C.C.M. Kyba, *Measurement of the Atmospheric Neutrino Induced Muon Flux at the Sudbury Neutrino Observatory*, Ph.D. thesis, University of Pennsylvania, 2006.

[205] S.R. Kelner, *Pair Production in Collisions Between Muons and Atomic Electrons*, *Phys. Atom. Nucl.* **61** (1998) 448.

[206] S.R. Kelner, R.P. Kokoulin and A.A. Petrukhin, *About Cross-Section for High-Energy Muon Bremsstrahlung*, Tech. Rep. Fprint-95-36 (1995).

[207] O.M. Horn, *Simulations of the Muon-Induced Neutron Background of the EDELWEISS-II Experiment for Dark Matter Search*, master's thesis, June, 2008.

[208] S. Yamamoto, A. Iyono, S. Tsuji, K. Okei, H. Matsumoto and T. Nakatsuka, *Survival Probability of Charged Particles Dissipating Their Energies by Radiation and Ionisation*, *PoS* **ICRC2017** (2018) 565.

[209] T. Nakatsuka, A. Iyono, S. Yamamoto, S. Tsuji, K. Okei and H. Matsumoto, *An Analytical Derivation of the Survival Probability of Muon Penetrating Through Matters*, *PoS* **ICRC2019** (2020) 925.

[210] Y.M. Andreyev, V.I. Gurentsov and I.M. Kogai, *Muon Intensity from the Baksan Underground Scintillation Telescope*, in *International Cosmic Ray Conference*, vol. 6 of *International Cosmic Ray Conference*, p. 200, January, 1987.

[211] PARTICLE DATA GROUP, *Review of Particle Physics*, *Ptep* **2020** (2020) 083c01.

[212] T.S. Sinegovskaya and S.I. Sinegovsky, *Prompt Muon Contribution to the Flux Underwater*, *Phys. Rev. D* **63** (2001) 096004 [`hep-ph/0007234`].

[213] ANTARES, *Measurement of the Atmospheric Muon Flux with the ANTARES Detector*, `0911.3055`.

[214] NEMO, *Measurement of the Atmospheric Muon Depth Intensity Relation with the NEMO Phase-2 Tower*, *Astropart. Phys.* **66** (2015) 1 [`1412.0849`].

[215] X. Bai et al., *Response of AMANDA-II to Cosmic Ray Muons*, in *28th International Cosmic Ray Conference*, pp. 1373–1376, May, 2003.

[216] I.A. Sokalski, E.V. Bugaev and S.I. Klimushin, *MUM: Flexible Precise Monte Carlo Algorithm for Muon Propagation Through Thick Layers of Matter*, *Phys. Rev. D* **64** (2001) 074015 [hep-ph/0010322].

[217] E.V. Bugaev, V.A. Naumov, S.I. Sinegovsky and E.S. Zaslavskaya, *Prompt Leptons in Cosmic Rays*, *Nuovo Cim. C* **12** (1989) 41.

[218] LVD, *Upper Limit on the Prompt Muon Flux Derived from the LVD Underground Experiment*, *Phys. Rev. D* **60** (1999) 112001 [hep-ex/9906021].

[219] A. Tang, G. Horton-Smith, V.A. Kudryavtsev and A. Tonazzo, *Muon Simulations for Super-Kamiokande, KamLAND and CHOOZ*, *Phys. Rev. D* **74** (2006) 053007 [hep-ph/0604078].

[220] NEWS-G, *First Results from the NEWS-G Direct Dark Matter Search Experiment at the LSM*, *Astropart. Phys.* **97** (2018) 54 [1706.04934].

[221] Z. Jing-Jun, K. Ke-Jun, L. Yuan-Jing and L. Jin, *Study on the Muon Background in the Underground Laboratory of KIMS*, *Chinese Physics C* **29** (2005) 721.

[222] COSINE-100, *Measurement of the Cosmic Muon Annual and Diurnal Flux Variation with the COSINE-100 Detector*, *JCAP* **02** (2021) 013 [2005.13672].

[223] C. Zhang and D.M. Mei, *Measuring Muon-Induced Neutrons with Liquid Scintillation Detector at Soudan Mine*, *Phys. Rev. D* **90** (2014) 122003 [1407.3246].

[224] M. Aglietta et al., *Single Muon Angular Distributions Observed in the LVD Particle Astrophysics Experiment*, *Astropart. Phys.* **2** (1994) 103.

[225] MACRO, *The Search for the Sidereal and Solar Diurnal Modulations in the Total MACRO Muon Data Set*, *Phys. Rev. D* **67** (2003) 042002 [astro-ph/0211119].

[226] M. Selvi, L. collaboration et al., *Analysis of the Seasonal Modulation of the Cosmic Muon Flux in the LVD Detector During 2001-2008*, in *the proceedings of the 31st International Cosmic Ray Conference (ICRC), July*, pp. 7–15, 2009.

[227] BOREXINO, *Cosmic-Muon Flux and Annual Modulation in Borexino at 3800 m Water-Equivalent Depth*, *JCAP* **05** (2012) 015 [1202.6403].

[228] LVD, *Underground Flux of Atmospheric Muons and its Variations with 25 Years of Data of the LVD Experiment*, *PoS* **ICRC2017** (2018) 291.

[229] JINPING, *Simulation and Sensitivity Studies for Solar Neutrinos at Jinping*, in *Proceedings, 5th International Solar Neutrino Conference: Dresden, Germany, June 11-14, 2018*, M. Meyer and K. Zuber, eds., pp. 381–389 (2019), DOI.

[230] S.W. Caddey et al., *The Homestake Gold Mine, an Early Proterozoic Iron-Formation-Hosted Gold Deposit, Lawrence County, South Dakota*, no. 1857, US Government Printing Office (1991), 10.3133/b1857J.

[231] K. Hart, T. Trancynger, W. Roggenthen and J. Heise, *Topographic, Geologic, and Density Distribution Modelling in Support of Physics Experiments at the Sanford Underground Research Facility (SURF)*, in *Proceedings of the South Dakota Academy of Science*, vol. 93, 2014.

[232] D.-M. Mei, C. Zhang, K. Thomas and F. Gray, *Early Results on Radioactive Background Characterisation for Sanford Laboratory and DUSEL Experiments*, *Astropart. Phys.* **34** (2010) 33 [`0912.0211`].

[233] KM3NET, *Dependence of Atmospheric Muon Flux on Seawater Depth Measured with the First KM3NeT Detection Units: The KM3NeT Collaboration*, *Eur. Phys. J. C* **80** (2020) 99 [`1906.02704`].

[234] KM3NET, *Comparison of the Atmospheric Muon Flux Measured by the KM3NeT Detectors with the CORSIKA Simulation Using the Global Spline Fit Model*, *PoS* **ICRC2023** (2023) 338.

[235] Y. Koshio, *Study of Solar Neutrinos at Super-Kamiokande*, Ph.D. thesis, Tokyo U., 1998. 10.11501/3162311.

[236] SUPER-KAMIOKANDE, *Measurement of the Flux and Zenith Angle Distribution of Upward Throughgoing Muons by Super-Kamiokande*, *Phys. Rev. Lett.* **82** (1999) 2644 [`hep-ex/9812014`].

[237] SUPER-KAMIOKANDE, *Search for* $\overline{\nu}_e$ *from the Sun at Super-Kamiokande I*, *Phys. Rev. Lett.* **90** (2003) 171302 [`hep-ex/0212067`].

[238] SUPER-KAMIOKANDE, *First Measurement of Radioactive Isotope Production Through Cosmic-Ray Muon Spallation in Super-Kamiokande IV*, *Phys. Rev. D* **93** (2016) 012004 [`1509.08168`].

[239] SUPER-KAMIOKANDE, *An Indirect Search for WIMPs with Super-Kamiokande*, in *27th International Cosmic Ray Conference*, June, 2001 [`hep-ex/0106024`].

[240] S.W. Li and J.F. Beacom, *First Calculation of Cosmic-Ray Muon Spallation Backgrounds for MeV Astrophysical Neutrino Signals in Super-Kamiokande*, *Phys. Rev. C* **89** (2014) 045801 [1402.4687].

[241] IceCube, *Seasonal Variation of Atmospheric Muons in IceCube*, *PoS* **ICRC2019** (2020) 894 [1909.01406].

[242] Minos, *Observation of Seasonal Variation of Atmospheric Multiple-Muon Events in the MINOS Near and Far Detectors*, *Phys. Rev. D* **91** (2015) 112006 [1503.09104].

[243] Macro, *Seasonal Variations in the Underground Muon Intensity as Seen by MACRO*, *Astropart. Phys.* **7** (1997) 109.

[244] E.W. Grashorn, J.K. de Jong, M.C. Goodman, A. Habig, M.L. Marshak, S. Mufson et al., *The Atmospheric Charged Kaon/Pion Ratio Using Seasonal Variation Methods*, *Astropart. Phys.* **33** (2010) 140 [0909.5382].

[245] IceCube, *Atmospheric Variations as Observed by IceCube*, in *Proceedings of the 31st ICRC, Lodz, Poland, July 2009*, January, 2010 [1001.0776].

[246] NOvA, *Observation of Seasonal Variation of Atmospheric Multiple-Muon Events in the NOvA Near Detector*, *Phys. Rev. D* **99** (2019) 122004 [1904.12975].

[247] A.K. Drukier, K. Freese and D.N. Spergel, *Detecting Cold Dark Matter Candidates*, *Phys. Rev. D* **33** (1986) 3495.

[248] J. Billard et al., *Direct Detection of Dark Matter – APPEC Committee Report*, *Rept. Prog. Phys.* **85** (2022) 056201 [2104.07634].

[249] J. Amaré et al., *First Results on Dark Matter Annual Modulation from the ANAIS-112 Experiment*, *Phys. Rev. Lett.* **123** (2019) 031301 [1903.03973].

[250] G. Angloher et al., *The COSINUS Project - Perspectives of a NaI Scintillating Calorimeter for Dark Matter Search*, *Eur. Phys. J. C* **76** (2016) 441 [1603.02214].

[251] J.H. Davis, *Fitting the Annual Modulation in DAMA with Neutrons from Muons and Neutrinos*, *Phys. Rev. Lett.* **113** (2014) 081302 [1407.1052].

[252] S. Chang, J. Pradler and I. Yavin, *Statistical Tests of Noise and Harmony in Dark Matter Modulation Signals*, *Phys. Rev. D* **85** (2012) 063505 [1111.4222].

[253] E. Fernandez-Martinez and R. Mahbubani, *The Gran Sasso Muon Puzzle*, *JCAP* **07** (2012) 029 [1204.5180].

[254] K. Blum, *DAMA vs the Annually Modulated Muon Background*, 1110.0857.

[255] J.P. Ralston, *One Model Explains DAMA/LIBRA, CoGENT, CDMS, and XENON*, 1006.5255.

[256] D. Nygren, *A Testable Conventional Hypothesis for the DAMA-LIBRA Annual Modulation*, 1102.0815.

[257] P.S. Barbeau, J.I. Collar, Y. Efremenko and K. Scholberg, *Comment on "Fitting the Annual Modulation in DAMA with Neutrons from Muons and Neutrinos"*, Phys. Rev. Lett. **113** (2014) 229001 [1409.3185].

[258] J. Klinger and V.A. Kudryavtsev, *Can Muon-Induced Backgrounds Explain the DAMA Data?*, J. Phys. Conf. Ser. **718** (2016) 042033.

[259] COSINE-100, *An Induced Annual Modulation Signature in COSINE-100 Data by DAMA/LIBRA's Analysis Method*, Sci. Rep. **13** (2023) 4676 [2208.05158].

[260] SUPER-KAMIOKANDE, *Measurement of the Cosmogenic Neutron Yield in Super-Kamiokande with Gadolinium Loaded Water*, Phys. Rev. D **107** (2023) 092009 [2212.10801].

[261] G. Raab, J. Gosse and A. Hidy, *Muon Paleotopometry – Measuring Crustal Thickness Variations with Muons?*, Tech. Rep. Copernicus Meetings (2023), DOI.

[262] K.P. Arunbabu et al., *Dependence of the Muon Intensity on the Atmospheric Temperature Measured by the GRAPES-3 Experiment*, Astropart. Phys. **94** (2017) 22.

[263] E.A. Yurina, A.G. Bogdanov, A.N. Dmitrieva, R.P. Kokoulin and V.V. Shutenko, *Variations in the Intensity of Cosmic-Ray Muon Bundles According to DECOR Data 2012–2017*, J. Phys. Conf. Ser. **1189** (2019) 012010.

[264] NOvA, *Seasonal Variation of Multiple-Muon Cosmic-Ray Air Showers Observed in the NOvA Detector on the Surface*, Phys. Rev. D **104** (2021) 012014 [2105.03848].

[265] ICECUBE, *Cosmic Ray Spectrum and Composition from PeV to EeV Using 3 Years of Data from IceTop and IceCube*, Phys. Rev. D **100** (2019) 082002 [1906.04317].

[266] G. Anzivino et al., *Single and Multiple Muon Events in LVD Detector*, Nucl. Instrum. Meth. A **295** (1990) 466.

[267] MACRO, GRACE, *Coincident Observations of Air Cherenkov Light by a Surface Array with Deep Underground Muon Bundles*, in *23rd International Cosmic Ray Conference*, May, 1993.

[268] MACRO, *Measurement of the Residual Energy of Muons in the Gran Sasso Underground Laboratories*, *Astropart. Phys.* **19** (2003) 313 [hep-ex/0207043].

[269] C. Berger and F. Collaboration, *Recent Results from the Fréjus Experiment*, *Nuclear Instruments and Methods in Physics Research Section A: Accelerators, Spectrometers, Detectors and Associated Equipment* **264** (1988) 24.

[270] ALICE, *Study of Cosmic Ray Events with High Muon Multiplicity Using the ALICE Detector at the CERN Large Hadron Collider*, *JCAP* **01** (2016) 032 [1507.07577].

[271] KM3NET, *Comparison of the Measured Atmospheric Muon Flux with Monte Carlo Simulations for the First KM3NeT Detection Units*, *PoS* **ICRC2019** (2020) 927 [2101.00907].

[272] KM3NET, *Muon Bundle Reconstruction with KM3NeT/ORCA Using Graph Convolutional Networks*, *PoS* **ICRC2021** (2021) 1048.

[273] N. Globus, A. Fedynitch and R.D. Blandford, *Polarised Radiation and the Emergence of Biological Homochirality on Earth and Beyond*, *Astrophys. J.* **910** (2021) 85 [2101.00530].

[274] C.A.J. O'Hare, *New Definition of the Neutrino Floor for Direct Dark Matter Searches*, *Phys. Rev. Lett.* **127** (2021) 251802 [2109.03116].

[275] J. Xu et al., *A Study of the Residual* ^{39}*Ar Content in Argon from Underground Sources*, *Astropart. Phys.* **66** (2015) 53 [1204.6011].

[276] X. Bertou, *The ANDES Underground Laboratory*, *Eur. Phys. J. Plus* **127** (2012) 104.

[277] K. Park, *The New Underground Facility in Korea, Yemilab*, *J. Phys. Conf. Ser.* **2156** (2021) 012171.

[278] V. Dadykin, V. Yakushev, P. Korchagin, V. Korchagin, A. Malgin, F. Ryassny et al., *The Research Programme of the Liquid Scintillation Detector (LSD) in the Mont Blanc Laboratory*, in *19th Intern. Cosmic Ray Conf-Vol. 8*, no. He-5.3-6, 1985.

[279] J. Evans, D.G. Gamez, S.D. Porzio, S. Söldner-Rembold and S. Wren, *Uncertainties in Atmospheric Muon-Neutrino Fluxes Arising from Cosmic-Ray Primaries*, *Phys. Rev. D* **95** (2017) 023012 [1612.03219].

[280] O.C. Allkofer, H. Jokisch, G. Klemke, Y. Oren, R. Uhr, G. Bella et al., *Cosmic-Ray Muon Spectra at Sea Level up to 10 TeV*, *Nucl. Phys. B* **259** (1985) 1.

Appendix A Additional Underground Sites

While Table 5.1 lists the laboratories relevant for this study, there are additional underground labs around the world, listed in Table A.1, hosting some of the experiments mentioned in this work. These labs are not included in Table 5.1 because there is either not enough information about them to do a full set of MUTE calculations (the depth, the rock density, the coordinates, and the mountain map for labs under mountains are needed in order to calculate the underground intensity, total muon flux, and seasonal variations), or the labs are not in use anymore (like IMB and KGF) or are still being planned (like PAUL and ANDES), and so there is not enough data to compare predictions to. There are also single-experiment labs, such as Daya Bay and Jiangmen Underground Neutrino Observatory (JUNO) in China, and Neutrinos at the Main Injector Off-Axis ν_e Appearance (NOνA) at Fermilab in the United States, which are not covered in this work, as they only service single experiments and are often too shallow for MUTE to perform calculations for.

Table A.1: Additional underground laboratories not under consideration for this study.

Acronym	Laboratory	Location	Depth (km.w.e.)
SUL	Solotvina Underground Laboratory	Ukraine	1
-	Otō Cosmo Observatory	Japan	1.4
KURF	Kimballton Underground Research Facility	United States	1.45 [275]
IMB	Irvine-Michigan-Brookhaven detector	United States	1.57 [5]
ANDES	Agua Negra Deep Experiment Site	Argentina, Chile	1.75 [276]
-	Yemilab	South Korea	1.9 [277]
ARF	Astroparticle Research Laboratory	South Korea	2
PAUL	Paarl Africa Underground Laboratory	South Africa	2.4 [119]
LSC	Laboratorio Subterráneo de Canfranc	Spain	2.45
CUPP	Centre for Underground Physics in Pyhäsalmi	Finland	2.7
INO	India-Based Neutrino Observatory	India	4
-	Callio Lab	Finland	4.1
BNO	Baksan Neutrino Observatory	Russia	4.8
-	Mont Blanc	France	5.2 [278]
KGF	Kolar Gold Fields Mine	India	7 [5]
-	East Rand Property Gold Mine	South Africa	8.89

Appendix B Further Comparisons Between Hadronic Interaction Models

There are multiple parameters that can be set regarding the calibration data sets in DAEMONFLUX. The curves in Figures 7.3 and 7.4 use DAEMONFLUX results that have been calibrated to muon flux and charge ratio data, but exclude the high-energy muon flux data from the DEIS experiment [80]. In order to compare, the ratio panel from Figure 7.3 was plotted again in Figure B.1, using DAEMONFLUX results that have been fully calibrated including DEIS data (first panel), completely uncalibrated to muon data (second panel), and with the DDM (third panel) and SIBYLL-2.3D (fourth panel) hadronic interaction models. DDM is nearly identical to the uncalibrated DAEMONFLUX result, as should be the case, since DAEMONFLUX is essentially DDM calibrated to surface muon data. It more accurately describes data taken at shallower slant depths, roughly corresponding to surface energies below 1 TeV, whereas SIBYLL-2.3D is better for deeper slant depths that sample surface energies from TeV to tens of TeV scales.

The error bands of the DDM and SIBYLL calculations include only hadronic uncertainties in Figure 7.3. The dominant sources are pion and kaon production yields at small scattering angles, as described in Section 3.3.4. Limited knowledge of the cosmic ray nucleon flux is expected to add an additional uncertainty of up to 20% [27, 186, 279].

To assess the impact of the choice of hadronic interaction model on the total underground flux, Figure B.2 shows the ratio of observed to predicted total muon fluxes using additional models available in MUTE: DAEMONFLUX uncalibrated to muon data, DAEMONFLUX calibrated to muon data including DEIS data from [280], DDM, and SIBYLL-2.3D. The uncalibrated DAEMONFLUX result is very similar to DDM, as expected. While the errors are smallest on the calibrated DAEMONFLUX result including DEIS data, the agreement to the experimental fluxes is worse, supporting the decision to exclude DEIS data from the calibration by default in DAEMONFLUX [80]. Almost no systematic shift with respect to the total flux data with the DAEMONFLUX model in Figure 8.3 is observed, whereas with all other displayed models in Figure B.2, there are noticeably larger errors and the prediction appears systematically lower than data. Therefore, MUTE in combination with DAEMONFLUX provides a satisfactory description of the data within the uncertainties of the data, and while other models remain available for use with MUTE, DAEMONFLUX will remain the default.

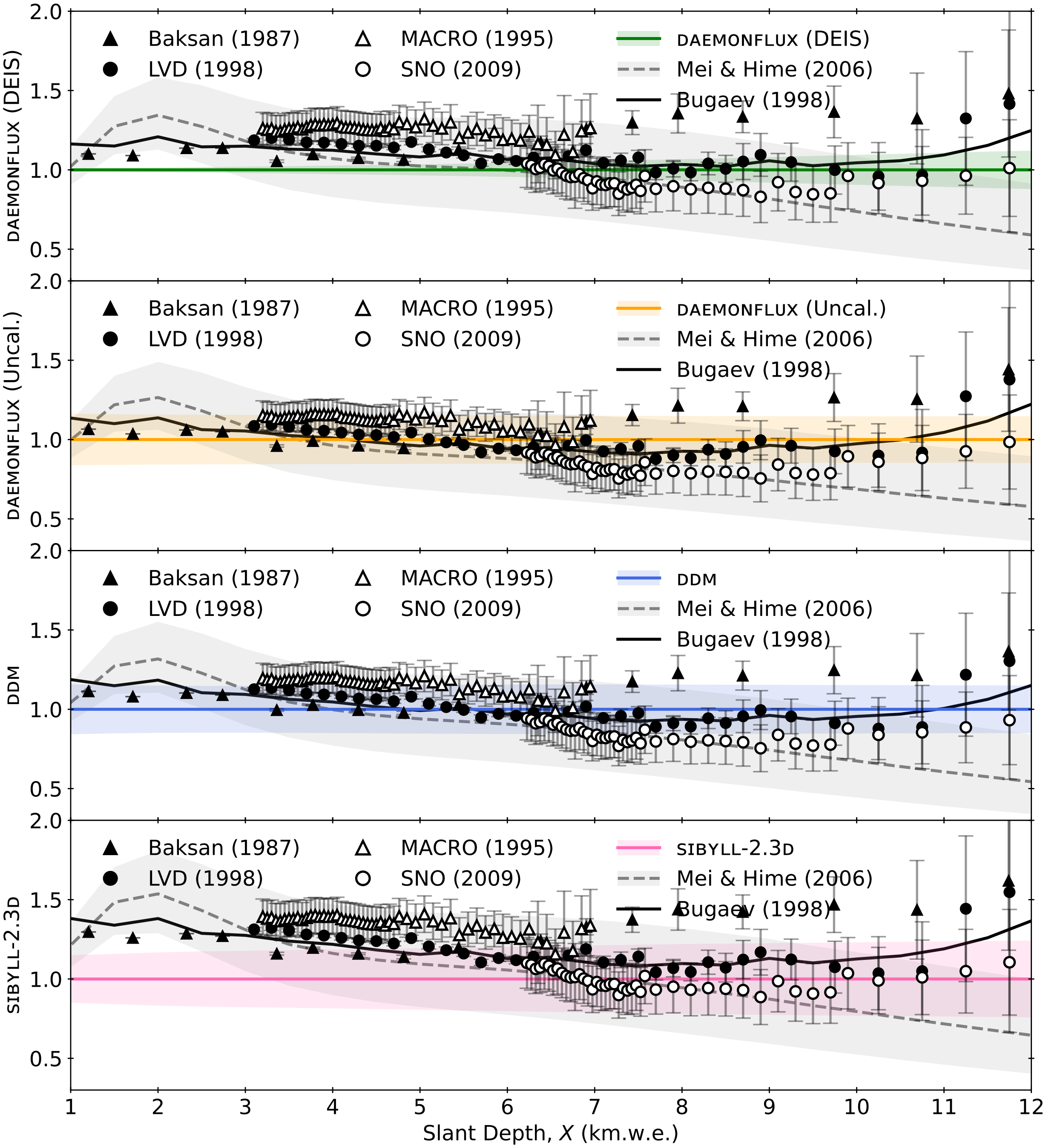

Figure B.1: The ratio to MUTE results for standard rock using DAEMONFLUX uncalibrated, DAEMONFLUX calibrated with DEIS data, DDM, and SIBYLL-2.3D, in order, of the experimental data, including the [107] fit, and the [3] calculation. All experimental data is referenced in Figure 7.3.

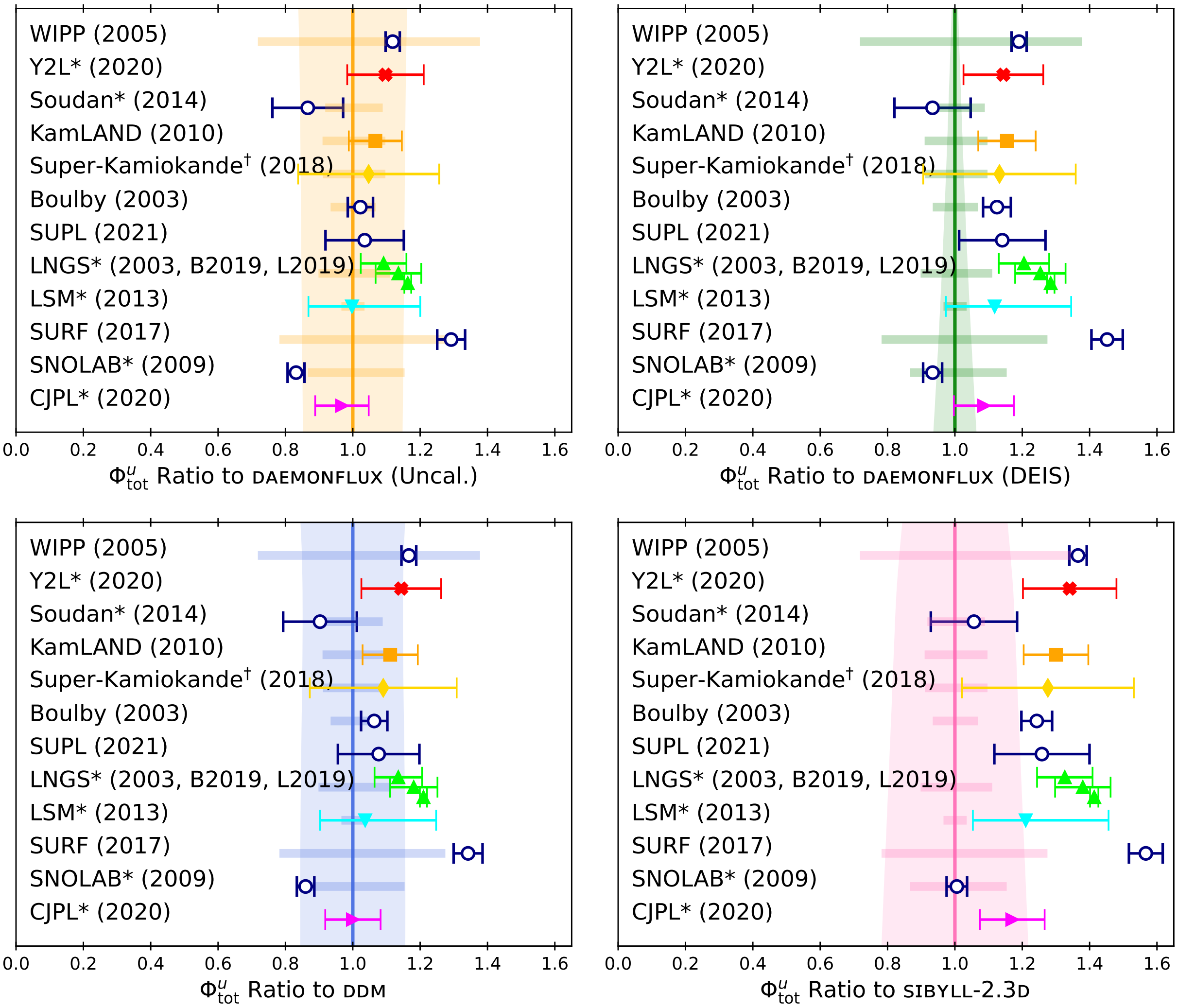

Figure B.2: The ratio of experimental total underground muon flux measurements to MUTE results using DAEMONFLUX uncalibrated (top left), DAEMONFLUX calibrated with DEIS data (top right), DDM (bottom left), and SIBYLL-2.3D (bottom right). An asterisk (*) means the calculation was done using the $\langle Z/A \rangle$ and $\langle Z^2/A \rangle$ values for the rock above that lab, as given in Table 6.5, whereas no asterisk means standard rock was used. A dagger (†) indicates that the point used is a prediction calculated from simulation and does not come from experimental data.

Appendix C Further Comparison Between Intensity Types

To further understand how the different types of intensities (single-differential, vertical-equivalent, and true vertical) compare to each other when varying vertical depth, these intensities have been plotted against slant depth for standard rock in Figure C.1. The single-differential intensity curve increases above the true vertical curve as slant depth increases due to contribution of non-vertical muons. This feature is also present in the vertical-equivalent curves, though it is masked by the multiplication of $\cos(\theta)$, which acts to lower the curves on the plot, since, from Equation (4.1), $\cos(\theta)$ decreases as X, and therefore θ, increases. In the true vertical curve, the shape of the curve is reproduced by all vertical depths. The effects of the difference displayed here between vertical-equivalent and true vertical intensities is shown in Figures 7.5 and 7.6.

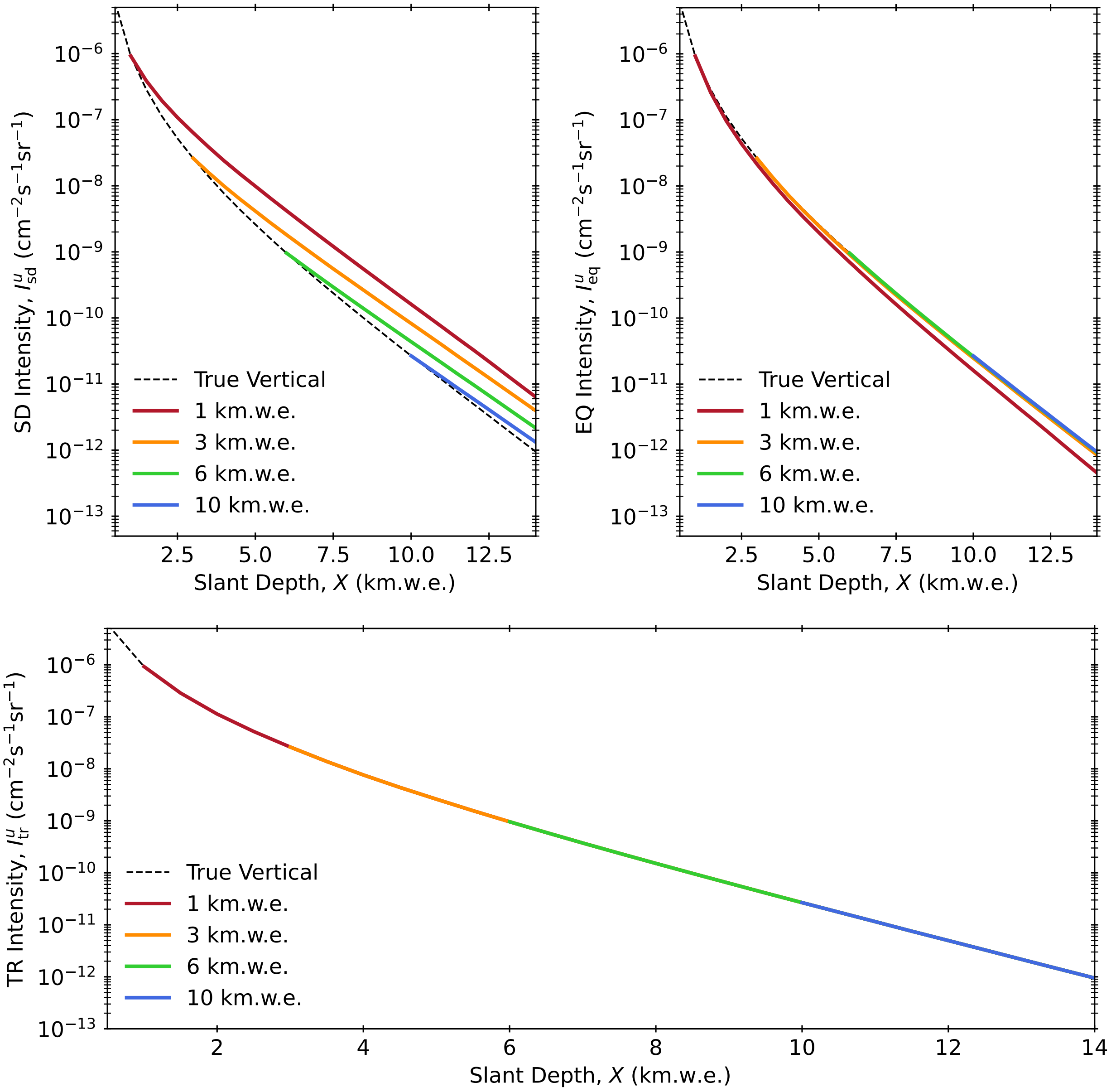

Figure C.1: Underground intensity vs slant depth for various vertical depths, showing the difference in behaviour of the curve when changing the vertical depth between single-differential intensities (top left), vertical-equivalent intensities (top right), and true vertical intensities (bottom). A dashed curve for true vertical intensities for $h = 0.5$ km.w.e. is shown on each plot to emphasise the divergence of the single-differential and vertical-equivalent intensities from true vertical intensity as the slant depth increases.